



Università degli Studi Roma Tre

Mathematics and Physics Department

Doctoral School in Physics

XXXVI Cycle

**Electromagnetic characterization of lunar
soil simulants and Ground Penetrating
Radar measurements for water ice
detection within the shallow lunar
subsurface.**

PhD Candidate:
Chloe Helenè Martella

Supervisor:
Elena Pettinelli

Academic Year 2023/2024

Contents

| | |
|--|-----------|
| Introduction | i |
| 1 The Moon | 1 |
| 1.1 General characteristics | 2 |
| 1.2 The interior of the Moon | 5 |
| 1.3 The lunar geology | 6 |
| 1.3.1 Basins | 7 |
| 1.3.2 Maria | 8 |
| 1.4 Lunar Rocks | 9 |
| 1.4.1 Highland rocks | 10 |
| 1.4.2 Mare basalts | 11 |
| 1.5 Lunar regolith | 11 |
| 1.5.1 Classification system | 14 |
| 1.6 Water ice on the Moon | 16 |
| 2 The Electromagnetic Theory | 23 |
| 2.1 The wave equation | 24 |
| 2.2 Propagation, Phase and Attenuation constants | 25 |
| 2.3 Electromagnetic Properties of Materials | 27 |
| 2.3.1 Dielectric Properties | 27 |
| 2.3.1.1 Polarization Mechanisms | 27 |
| 2.3.2 Electric Susceptibility | 28 |
| 2.3.3 The complex dielectric permittivity | 30 |
| 2.3.4 Conductivity | 31 |
| 2.3.5 Magnetic Properties | 32 |
| 2.4 Frequency dependance of permittivity | 33 |
| 2.4.1 The Debye model | 33 |
| 2.5 Temperature dependance of permittivity | 35 |
| 2.6 Dielectric behavior of geomaterials | 36 |
| 2.6.1 Rocks | 36 |
| 2.6.2 Soils | 38 |
| 2.6.3 Water ice | 39 |
| 3 Radar theory and application for explorations | 43 |
| 3.1 Introduction | 43 |
| 3.2 Ground Penetrating Radar | 43 |
| 3.2.1 Timing and resolution | 45 |
| 3.3 Antennas design | 48 |
| 3.3.1 Directivity - TE, TM patterns | 49 |

| | | |
|----------|---|-----------|
| 3.3.2 | Shielding | 50 |
| 3.4 | Energy losses and attenuation | 52 |
| 3.5 | Survey acquisitions | 54 |
| 3.6 | Data visualization | 54 |
| 3.7 | Radar for space exploration | 55 |
| 3.8 | Moon radar missions | 56 |
| 4 | Electromagnetic mixing models | 59 |
| 4.1 | Maxwell-Garnett | 60 |
| 4.2 | Mixing bounds | 61 |
| 4.3 | Power-laws | 62 |
| 4.3.1 | $\beta = 1$ (Linear) | 62 |
| 4.3.2 | $\beta = 1/2$ (CRIM) | 63 |
| 4.3.3 | $\beta = 1/3$ (LLL) | 63 |
| 4.3.4 | $\beta = 0$ (Lichteneker rule) | 63 |
| 5 | Chemical and mineralogical characterization of lunar regolith analogues | 64 |
| 5.1 | Lunar regolith analogues | 64 |
| 5.2 | Chemical and mineralogical composition | 69 |
| 5.3 | Grain density analysis | 70 |
| 5.4 | Grain size distribution analysis | 71 |
| 5.5 | Mineralogical analysis | 72 |
| 5.6 | Discussion | 74 |
| 6 | Assessing the effect of porosity and mineralogy on dielectric properties of regolith analogues | 76 |
| 6.1 | Introduction | 76 |
| 6.2 | VNA set-up | 76 |
| 6.2.1 | Coaxial transmission-reflection line method | 78 |
| 6.2.2 | Nicolson-Ross-Weir algorithm | 80 |
| 6.3 | Porosity estimation | 81 |
| 6.4 | Sample preparation | 82 |
| 6.5 | Measurement results | 82 |
| 6.5.1 | Frequency spectra | 82 |
| 6.5.2 | Magnetic permeability | 84 |
| 6.5.3 | Bulk density effect | 85 |
| 6.6 | Discussion | 87 |
| 6.6.1 | Models and mixing formulas | 87 |
| 6.6.2 | The effect of $(FeO + TiO_2)\%$ content on loss tangent | 89 |
| 6.6.3 | The effect of mineralogy on dielectric losses | 91 |
| 6.6.4 | Attenuation models vs depth | 92 |
| 6.7 | Conclusions | 96 |
| 7 | Dielectric measurements in function of temperature on dry and saturated regolith analogues | 99 |
| 7.1 | Introduction | 99 |
| 7.2 | LCR meter set-up | 99 |
| 7.2.1 | Capacitive cell dielectric measurements | 101 |

| | | |
|----------|--|------------|
| 7.3 | Samples preparation | 103 |
| 7.4 | Temperature cycles | 105 |
| 7.5 | Measurement results | 107 |
| 7.5.1 | Dielectric properties as a function of frequency | 107 |
| 7.5.2 | The effect of temperature | 110 |
| 7.5.3 | Attenuation estimation | 112 |
| 7.6 | Discussion | 113 |
| 7.6.1 | Activation energy | 113 |
| 7.6.2 | Ice/regolith mixing formula and models | 115 |
| 7.7 | Conclusions | 119 |
| 8 | GPR investigation for water ice detection within the lunar regolith layer | 120 |
| 8.1 | Introduction | 120 |
| 8.2 | Experimental set-up | 120 |
| 8.3 | Environment material: Glass-beads | 122 |
| 8.4 | Frozen targets | 123 |
| 8.5 | Experimental results | 125 |
| 8.5.1 | Background acquisition | 126 |
| 8.5.2 | Ice lens | 126 |
| 8.5.3 | Ice/glass-beads mixture | 127 |
| 8.6 | Inversion approach | 128 |
| 8.6.1 | Frequency content analysis | 131 |
| 8.7 | Discussion | 132 |
| 8.8 | Conclusions | 133 |
| 9 | Summary and conclusions | 135 |
| | Bibliography | 138 |

List of Figures

| | | |
|------|--|----|
| 1.1 | Giant impact hypothesis. | 1 |
| 1.2 | Moon's orbit around the Earth. | 3 |
| 1.3 | Mean global temperature of the Moon. | 4 |
| 1.4 | Cross-section of the interior of the Moon. | 5 |
| 1.5 | Schrödinger crater. | 6 |
| 1.6 | Formation stages of simple crater. | 7 |
| 1.7 | South pole-Aitken basin. | 8 |
| 1.8 | Lunar maria on the near side. | 9 |
| 1.9 | Radar section and interpretation of the Von Karman Crater. | 13 |
| 1.10 | Cross sectional diagram of the upper lunar crust. | 14 |
| 1.11 | Lunar soil classification. | 16 |
| 1.12 | Evidence of exposed water ice at the lunar South Pole. | 18 |
| 1.13 | Lunar surface anomaly reflectance associated to water ice. | 19 |
| 1.14 | Evolution of vertical ice distribution in PSR. | 20 |
| 1.15 | Map of water ice stability depth at the Lunar poles. | 21 |
| 1.16 | Map of current and past extent of PSRs. | 22 |
| | | |
| 2.1 | Transverse electromagnetic propagation (TEM). | 26 |
| 2.2 | Polarization mechanisms. | 28 |
| 2.3 | Flat capacitor filled by a dielectric material. | 29 |
| 2.4 | Equivalent circuit system of a flat capacitor powered by an alternating current. | 30 |
| 2.5 | Vectorial currents diagram in the capacitive cell filled with a dielectric material. | 31 |
| 2.6 | Debye model. | 34 |
| 2.7 | Cole-Cole diagram. | 35 |
| 2.8 | Effect of temperature on dielectric properties. | 36 |
| 2.9 | Complex permittivity of rock samples at 450 MHz and 35 GHz. | 37 |
| 2.10 | Complex permittivity of selected rock samples | 38 |
| 2.11 | Complex permittivity of powdered rocks versus density | 39 |
| 2.12 | Complex permittivity of lunar regolith | 39 |
| 2.13 | Pure water ice Debye model. | 40 |
| 2.14 | Effect of impurities on energy losses of water ice. | 41 |
| 2.15 | Dielectric properties of sea ice. | 42 |
| | | |
| 3.1 | GPR sketch. | 44 |
| 3.2 | GPR radargram acquisition. | 44 |
| 3.3 | GPR time resolution. | 46 |
| 3.4 | Transmitter blanking and pulses overlaps. | 47 |

| | | |
|------|---|-----|
| 3.5 | GPR depth and lateral resolution. | 48 |
| 3.6 | GPR system resolution designs. | 48 |
| 3.7 | Antenna directivity. | 50 |
| 3.8 | TE TM dipole patterns. | 50 |
| 3.9 | Radar system. | 51 |
| 3.10 | Scattering attenuation. | 53 |
| 3.11 | Radar signals incident angles with surface roughness. | 53 |
| 3.12 | GPR visual presentations. | 55 |
| 4.1 | Simple two-phase mixture. | 60 |
| 4.2 | Wiener and HS mixing rules boundaries. | 62 |
| 5.1 | Morpho-grainsizer MGS. | 71 |
| 5.2 | Grain size distribution. | 72 |
| 5.3 | SEM-EDS instrument. | 73 |
| 6.1 | VNA set-up. | 77 |
| 6.2 | Coaxial transmission line. | 77 |
| 6.3 | VNA set-up scheme. | 79 |
| 6.4 | NRW algorithm transmission line scheme set-up. | 81 |
| 6.5 | Frequency spectra of ϵ' and ϵ'' of LHS-1 tested with VNA. | 83 |
| 6.6 | Frequency spectra of ϵ' and ϵ'' of LMS-1 tested with VNA. | 83 |
| 6.7 | Frequency spectra of ϵ' and ϵ'' of OPRH2N tested with VNA. | 83 |
| 6.8 | Frequency spectra of ϵ' and ϵ'' of OPRL2NT tested with VNA. | 84 |
| 6.9 | μ' and μ'' of analogues. | 85 |
| 6.10 | ϵ' vs density. | 86 |
| 6.11 | ϵ'' vs density. | 86 |
| 6.12 | Probability density functions (Lichtenecker formula). | 88 |
| 6.13 | Comparison of ϵ' with literature. | 89 |
| 6.14 | Loss tangent results and comparison with literature. | 90 |
| 6.15 | Loss tangent vs pyroxene and plagioclase. | 92 |
| 6.16 | Loss tangent vs olivine and ilmenite. | 92 |
| 6.17 | Density profile vs depth and loss tangent curves for regolith simulants and Lunar data. | 94 |
| 6.18 | Attenuation curves vs depth for regolith simulants and apollo data at 60 and 500 MHz. | 95 |
| 7.1 | LCR equivalent electric circuit. | 99 |
| 7.2 | LCR set-up. | 101 |
| 7.3 | LCR set-up dielectric measurement. | 101 |
| 7.4 | Samples preparation for dry measurements | 103 |
| 7.5 | samples preparation for ice/regolith mixtures | 105 |
| 7.6 | Temperture cycles applied with the climatic chamber | 106 |
| 7.7 | Ascent e descent stages of temperature cooling cycle. | 106 |
| 7.8 | Complex permittivity of dry analogues vs frequency. | 107 |
| 7.9 | ϵ' of saturated mixtures vs frequency. | 108 |
| 7.10 | ϵ'' of saturated mixtures vs frequency. | 109 |
| 7.11 | Electrical conductivity | 110 |
| 7.12 | Complex permittivity of dry analogues vs temperature | 111 |

| | | |
|------|---|-----|
| 7.13 | Phase angle of saturated mixtures vs frequency. | 112 |
| 7.14 | Complex permittivity of saturated mixtures vs temperature | 112 |
| 7.15 | Attenuation of dry samples and ice/regolith mixtures. | 113 |
| 7.16 | Activation energy. | 115 |
| 7.17 | Ice/regolith mixtures and mixing formulas Off Planet Research samples (ϵ'). | 116 |
| 7.18 | Ice/regolith mixtures and mixing formulas Exolith and LCATS-1 (ϵ'). . . | 117 |
| 7.19 | Ice/regolith mixtures and mixing formulas (ϵ''). | 117 |
| 8.1 | GPR experimental set-up sketch. | 121 |
| 8.2 | Dielectric box set-up. | 122 |
| 8.3 | Glass beads dielectric permittivity test. | 123 |
| 8.4 | Icy targets. | 124 |
| 8.5 | Distilled water ice dielectric permittivity. | 125 |
| 8.6 | Ice/glass-beads mixture dielectric permittivity. | 125 |
| 8.7 | Radargram of the background: dielectric box filled with glass beads. . . | 126 |
| 8.8 | Radargram water ice target. | 126 |
| 8.9 | Radargram of melted water ice target. | 127 |
| 8.10 | Radargram of ice/glass-beads mixture target. | 127 |
| 8.11 | Radargram of melted ice/glass-beads mixture target. | 128 |
| 8.12 | Envelopes of free run test over the ice lens target. | 129 |
| 8.13 | Envelopes of free run test over the ice/glass-beads mixture target. . . . | 129 |
| 8.14 | Inversion methods to estimate permittivity of the frozen target. | 130 |
| 8.15 | Selection of reflection peaks for the FFT analysis. | 131 |
| 8.16 | Variation of FFT peaks with frequency for the water-ice lens target. . . | 132 |
| 8.17 | Variation of FFT peaks with frequency for the ice/glass-beads mixture. . | 132 |

List of Tables

| | | |
|-----|--|-----|
| 1.1 | Planetary properties of the Moon and the Earth [122]. | 3 |
| 1.2 | Chemical composition of lunar meteorites. | 10 |
| 1.3 | Mean superficial regolith thickness [94]. | 14 |
| 1.4 | Lunar missions designated to find evidences of presence of water. | 17 |
| 3.1 | Characteristics of obiter radar sounders. | 56 |
| 3.2 | Characteristics of GPR on space rovers. | 56 |
| 5.1 | Lunar analogue list tested in this work. | 65 |
| 5.2 | Updated list of the existing lunar simulants from CSM Database. | 67 |
| 5.3 | Dielectric measurements conducted on other lunar regolith simulants. | 68 |
| 5.4 | Chemical composition of lunar regolith analogues. | 69 |
| 5.5 | General composition of the regolith simulants. | 70 |
| 5.6 | Grain density measurements. | 70 |
| 5.7 | SEM-EDS mineralogical composition | 73 |
| 5.8 | Average bulk chemical composition of samples after SEM-EDS. | 74 |
| 6.1 | Complex magnetic permeability of analogues. | 84 |
| 6.2 | Least square regression results (Lichtenecker formula). | 87 |
| 6.3 | Lunar rocks dielectric data from Apollo landing sites. | 91 |
| 7.1 | Cooling cycle measurements preparation for the dry analogues tests. | 104 |
| 7.2 | Heating cycle measurements preparation for the dry analogues tests. | 104 |
| 7.3 | Ice/regolith mixtures preparation. | 105 |
| 7.4 | Activation energy of dry regolith samples. | 114 |
| 7.5 | Activation energy of ice/regolith mixtures. | 115 |
| 7.6 | ϵ' ice/regolith mixtures measured at 200 K and 1 MHz. | 118 |
| 7.7 | ϵ'' ice/regolith mixtures measured at 200 K and 1 MHz. | 118 |
| 8.1 | Permittivity of the water-ice lens target. | 124 |
| 8.2 | Permittivity of the ice/glass-beads mixture target. | 124 |
| 8.3 | Inversion parameters results for water ice target. | 130 |
| 8.4 | Inversion parameters results for ice/glass-beads mixture target. | 130 |

Introduction

The purpose of this thesis is to provide support for the exploration of Permanently Shadowed Regions (PSR) of the Moon for the search of water ice utilizing radar methodology. Understanding the origin, age and distribution of water ice in the subsurface of the lunar polar and sub-polar regions for future in situ resource utilization (ISRU) requires the use of in-situ geophysical methods capable to measure depth, lateral and vertical extent, physical distribution (i.e., mixed in the regolith or as lens/layers of pure ice) and volume of the ice. Among all geophysical techniques, Ground Penetrating Radar (GPR) is by far the most suitable method for planetary shallow subsurface exploration, as it does not require any direct and permanent contact between the antennas and the surface, it is light, non-destructive, has a low power consumption and can easily operate on board a rover.

The analysis and interpretation of radar data can provide a vertical section of the investigated area based on the electromagnetic response of the material present at depth. The electromagnetic response of material is linked to the constitutive parameters. Such parameters can be investigated in laboratory, to examine how they change as a function of physical parameters like temperature, porosity, water content.

The key point of this thesis is to improve our understanding of how geo-materials interact with radio waves by carrying out laboratory measurements on regolith analogues and modeling the experimental data at varying physical conditions. In this work are also presented and discussed some GPR lab scale experiments where lens of ice or pockets of regolith/ice mixtures are embedded in a layer of a regolith simulant.

The laboratory measurements are carried out at the Earth and Planetary Physics Laboratory at the Mathematics and Physics Department of Roma Tre University. Such a facility is designed to operate dielectric spectroscopy investigation on a variety of terrestrial material that may be constitute the surface and subsurface of several Planets and Satellites of the Solar System.

Dielectric spectroscopy data lead to the estimation of parameters crucial for radar applications, namely the propagation velocity and the signals attenuation along the propagation path. The former is a parameter that allows to determine the permittivity of buried structures hence the hypothesis of compositional interpretation of the subsurface features. The latter gives information regarding the depth at which possible reflectors/features are buried.

The following manuscript, in Chapter 1, provides a thorough summary of lunar physical/geophysical properties, spanning from internal structure, surface morphology and crater formation to lunar regolith features and water ice in PSRs. Chapter 2 covers electromagnetic theory, starting with Maxwell's equations, addressing electromagnetic polarization, dielectric permittivity, and how this parameter is related to the propagation of electromagnetic waves within various materials. Chapter 3 explores Ground Penetrating Radar, its theory, and planetary applications. Chapters 4 and 5 discuss the

characterization of lunar simulant samples used in this research and the electromagnetic mixing models employed to estimate the dielectric properties of biphasic mixtures. Finally, from Chapter 6 onward, the results of the laboratory experimental activity are presented. This research work encompasses a diverse set of laboratory activities aimed at characterizing the dielectric properties of lunar regolith analogues and evaluating the potential of GPR for subsurface exploration of the Moon. The dielectric properties of nine analogues were measured under varying compaction conditions, employing a Vector Network Analyzer (VNA) connected to multiwire electrodes. Measurements spanned a frequency range of 100 kHz to 3 GHz, with compaction adjustments facilitated by a vibration plate (Chapter 6). Temperature-dependent dielectric behavior was studied in Chapter 7 using a capacitive measurement cell connected to an LCR meter, spanning a frequency spectrum of 20 Hz to 1 MHz. Integration with a climatic chamber enabled exploration across temperatures ranging from 200 K to 350 K. Dry conditions and scenarios involving mixtures with distilled water ice were investigated. The investigation extended to Ground Penetrating Radar measurements in a laboratory setting, utilizing a dielectric box filled with a synthetic mixture of glass beads mimicking lunar regolith properties (Chapter 8). Summary and conclusions are found in Chapter 9.

Chapter 1

The Moon

The Moon is the Earth's only natural satellite, the fifth largest in the Solar System and the most visible object from our planet. It is a rather simple world, but it also plays a major role in the comprehension of the evolution of the Solar System; and it is a crucial first step towards human space exploration. As a matter of fact, the Moon has witnessed the existence of the Solar System over the past 4.5 billion years.

In relation to the Moon's genesis and origin, the so-called gigantic impact hypothesis has gained considerable relevance in the scientific community after the Apollo missions. The Moon formed when the proto-Earth and a Mars-sized asteroid collided. According to this hypothesis, both objects must have already differentiated. After the collision most of the dense material was incorporated into the Earth's core and mantle, while the outer layers of the Earth (the crust and the upper mantle) were ejected into orbit where accreted to form the Moon. According to this theory, its primary source of material is the impactor rather than the Earth. It explains the Moon's lack of iron and water, the large angular momentum and mass; but despite this model is widely accepted it is far from being perfect [91].

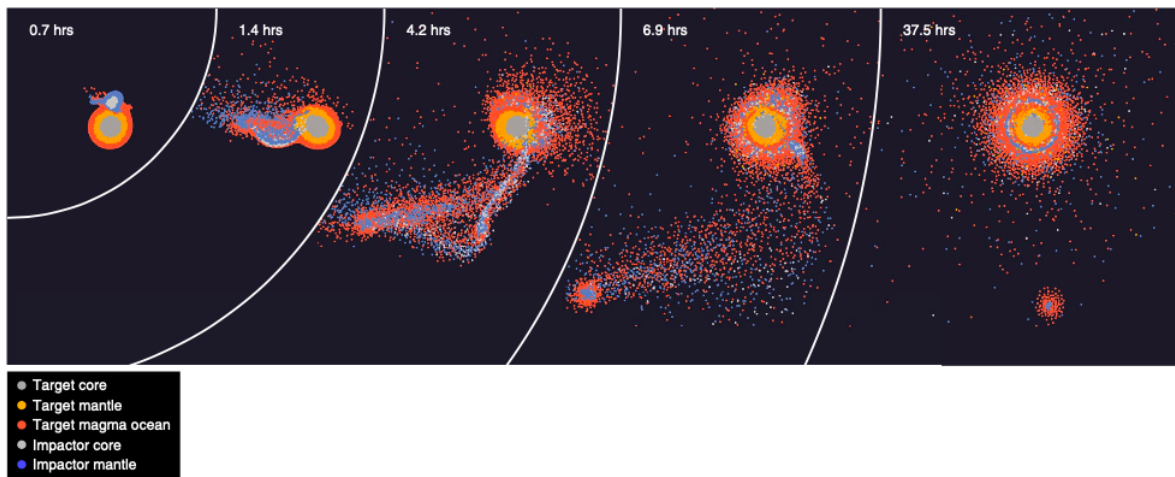


Figure 1.1: *Mathematical simulation of the giant impact theory between the proto-Earth and a Mars-size object [91].*

1.1 General characteristics

The Moon revolves counterclockwise around the Earth, just as the Earth and the other planets do around the Sun. It takes an average of 27.32166 days to revolve around the Earth, due to the tidal friction which slows down the lunar rotation. The elliptical orbit exhibits an eccentricity $e = 0.0549$, and the average distance from the Earth is around 384.100 km . The Moon is locked into a synchronous rotation with respect to the Earth, the average period of revolution around its principal axis is equal to the period of revolution around the Earth. Doing so, it maintains the same face oriented toward the Earth, which is the reason why we refer to the *near side* and the *far side* of the Moon.

Besides the synchronous orbit, tidal effects cause the Moon to recede from Earth at a rate 3.79 cm/year . The orbit of the Moon is inclined by 5.15° with respect to the ecliptic and the inclination of the lunar orbit to the Earth's equatorial plane varies between 18.4° and 28.6° . The orientation of its rotation axis is tilted by 1.53° relative to the ecliptic pole.

The exact synchronism between the Earth and the Moon is only given at two specific points along the orbit: near perigee and near apogee, where the rotational angular velocity exhibits a delay compared to the orbital angular velocity. This is due to the orbital eccentricity and the variation of the angular velocity. This scenario leads to geometric librations in longitude of about $\pm 8.6^\circ$ while the inclination of the Moon's orbit with the respect to the ecliptic plane causes the latitudinal libration of about 6.9° . As a result of these geometric librations we can only see the 60% of the lunar surface from the Earth.

In terms of geophysical parameters, the Moon shows a surface gravity of 1.622 m/s^2 , which is nearly the 17% of the gravity on the Earth. The average lunar bulk density is assessed to be around $3345.56 \pm 0.40\text{ kg/m}^3$ [48], considerably smaller compared to the Earth (5.52 g/cm^3), pointing out that the Moon and the Earth interior structures are different. Also, the moment of inertia that is 0.3932 ± 0.0002 indicates a small increase of density with depth.

Temperatures at the equator varies from $350 - 400\text{ K}$ at noon to $70 - 100\text{ K}$ around midnight; these extremes conditions are due to the absence of atmosphere and free water to moderate the temperatures. At the lunar polar regions the surface temperatures are much colder, varying between $150 - 200\text{ K}$ and $50 - 100\text{ K}$, because of the low incident angle of sunlight [143][122], see Fig.(1.3).

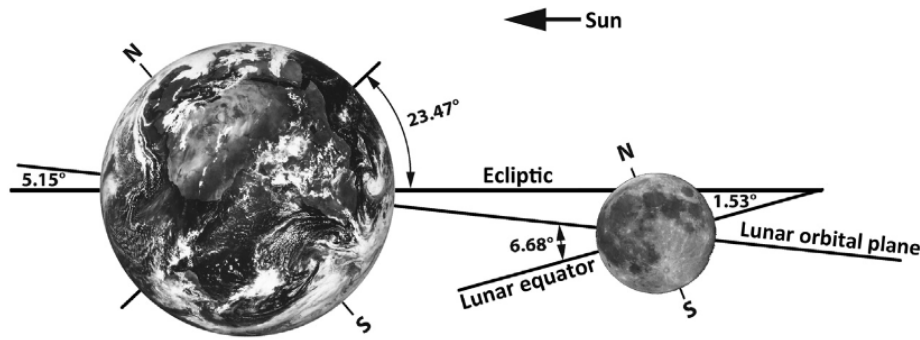


Figure 1.2: The Moon revolves counterclockwise around the Earth and it takes an average of 27.32166 days. The orbit has an eccentricity $e = 0.0549$, and the average distance from the Earth is $R = 384.100$ km. The Moon is locked into a synchronous rotation with respect to the Earth, keeping the same face turned toward the Earth.

| | Moon | Earth |
|----------------------------------|--|--|
| Mass | 0.7×10^{23} kg | 59.8×10^{23} kg |
| Equatorial radius | 1.738 km | 6.378 km |
| Density | 3.34 g/cm ³ | 5.515 g/cm ³ |
| Diameter | 3.476 km | 12.756 km |
| Obliquity of rotation axis | 6.68° | 23.45° |
| Inclination of orbit to ecliptic | 5.145° | |
| Eccentricity of orbit | 0.0549 | 0.01671 |
| Gravitational acceleration | 1.622 m/s ² ($\frac{1}{6}$ Earth normal) | 9.8 m/s ² |
| Mean orbital velocity | 1.023 km/s ⁻¹ | 29.79 km/s ⁻¹ |
| Length of day | ~ 709 hours (29.5 Earth days) | 24 hours |
| Distance from Earth | ~ 356.000 km - ~ 406.000 km | |
| Temperature range at equator | $-173^{\circ}\text{C} \div 127^{\circ}\text{C}$ | $0^{\circ}\text{C} \div 60^{\circ}\text{C}$ |
| Temperature range at poles | $-258^{\circ}\text{C} \div -113^{\circ}\text{C}$ | $-89^{\circ}\text{C} \div -18^{\circ}\text{C}$ |
| Escape velocity | 2 km/s | 11 km/s |
| Atmospheric pressure at surface | 1×10^{-12} torr | 760 torr |

Table 1.1: Planetary properties of the Moon and the Earth [122].

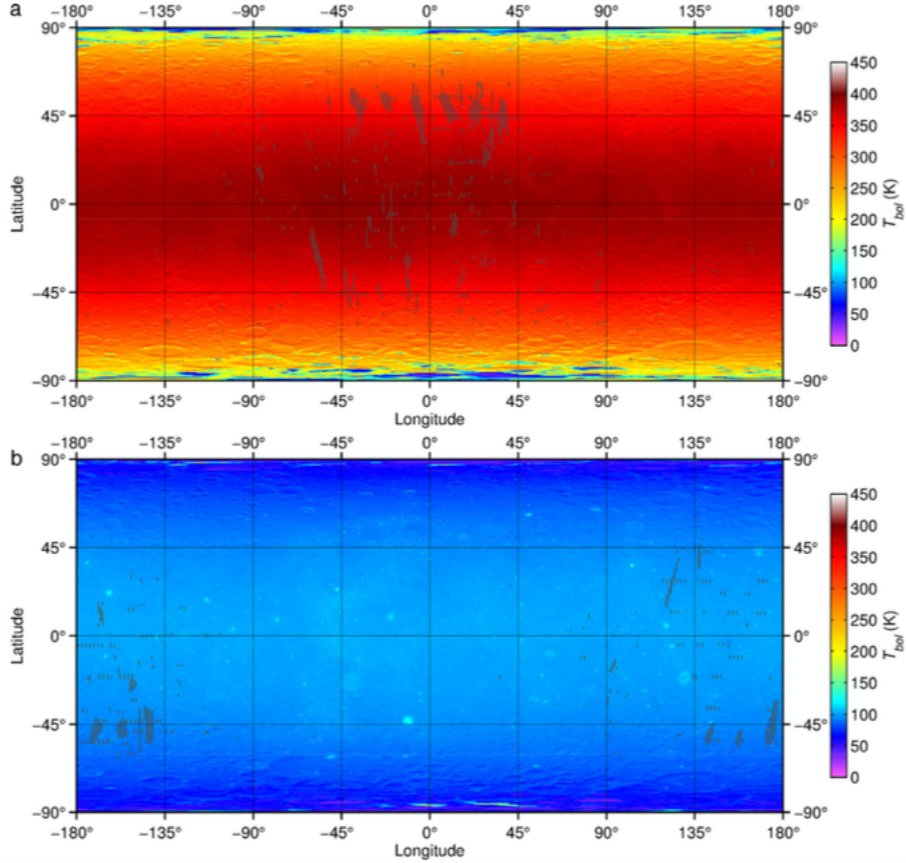


Figure 1.3: Superficial mean bolometric temperature of the Moon inferred from Diviner data. Figure a) shows the mean temperature for one hour at noon and figure b) at midnight. Figure from [143].

The Moon does not exhibit an internally generated magnetic field but the crust shows some regions of weak remanent magnetization. The magnetic field data inferred from orbit and from lunar rocks analyses show that the Moon once had a global magnetic field powered by a core dynamo [140]. The dynamo operated during the first 100 million years following the crust formation, the paleomagnetic data provided evidence that the dynamo was active from about $4.25 Ga$ to $1 \div 2.5 Ga$ and the absence of a core-generated field implies that the dynamo ceased to operate after that time. Several dynamo mechanism models were proposed, core thermal convection, core crystallization, mantle precession and impact that could have changed the rotation rate of the mantle.

During the Apollo era, astronauts installed a network of four three-component, long period seismometers in a nearly equilateral triangle array (with corner distance of $\sim 1100 km$), which detected roughly 13000 seismic events for almost 8 years [48]. In such a scenario, the Moon turned out to be an "active" body, in fact at that time only meteoroid impacts were expected to be recorded.

The recorded moonquakes can be divided in four categories: *thermal moonquakes* that are caused by the diurnal temperature changes, *deep moonquakes* that are originated from the zone between $700 \div 1200 km$ inside the Moon, whose magnitude is less than 3 on the Richter scale. The origin of these events is unclear but tidal influences due to the interaction between the Moon and the Earth is a plausible hypothesis. For this reason, deep moonquakes occur in so-called *nests*, which repeatedly release

seismic energy. *Seismic events caused by meteoroid impacts* were recorded over 1700 times. *Shallow moonquakes*, the hypocenter is located between $50 \div 200 \text{ km}$ from the surface. Signals produced by those events are stronger than the other events and their magnitude is greater than 5 on the Richter scale [66].

The lunar seismic signals were found to be of surprisingly long duration and high frequency content compared to the events on the Earth. These characteristics are related to intense scattering due to an highly heterogeneous, dry and porous lunar regolith and a low intrinsic attenuation of the lunar interior.

1.2 The interior of the Moon

The deep structure of the Moon is a key point to assess the formation and evolution processes of the Earth-Moon System. Despite the large amount of data provided by the Apollo experiments and other recent spacecraft missions, the deep lunar structure as mantle and core, remain largely unknown. Data suggest that the Moon differentiated into crust, mantle and possibly a small core, as well as the other terrestrial bodies in the Solar System. The low lunar average density outlines the presence of a iron core smaller than the other terrestrial planets. Other geophysical data suggests a solid inner core surrounded by a molten core, which is characterized by high electrical conductivity and higher density than the overlying mantle. The chemical composition of the core is not well constrained but, the values of moment of inertia, the k_2 Love number, the quality factor Q as well as many other parameters, suggest a core radius ranging between 300 and 400 km composed of $Fe - FeS - C$, metallic alloy or molten silicates [48]. The hypothesis of a solid inner core is also inferred by thermal models, which indicate that some portions of the core should have crystallized over the past 4.5 Ga . Seismic data also support the presence of a small inner core and a partially molten layer at the base of the mantle ($\sim 300 \text{ km}$ deep) [93].

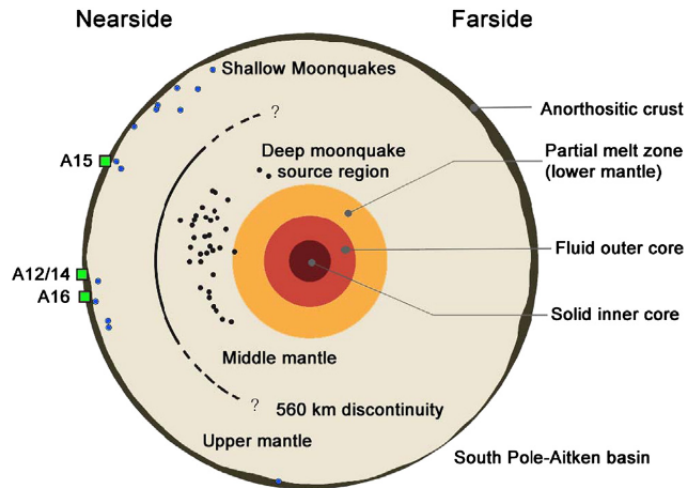


Figure 1.4: Cross-section of the interior of the Moon. Inferred by geophysical investigations the Moon is believed to be differentiated in crust, mantle, a small solid inner core and a fluid outer core. From [141].

1.3 The lunar geology

The surface of the Moon is almost completely covered by craters, that are the results of meteorites and comets bombardment. Since the Moon has virtually no atmosphere, the impacts generates craters that are ten to twenty times larger than the colliding projectile itself.

Most of lunar craters have radial symmetry and the size determines how they formed. Craters with diameter $< 15 \text{ km}$, consist of smoothly contoured bowl-shaped or cone-shaped depressions that considerably deeper than the surrounding terrain. Crater morphology becomes more complex when impact energy and crater size increase. Medium sized craters (20 km to 175 km) are featured by roughly flat floors, a central peak or peak rings, and terraced walls. When the diameter is $> 175 \text{ km}$ they can present more intricate center features, and central peaks are replaced by rings. The exterior deposits that slope downward from the rim crest are present immediately in the surrounding of the craters; and about one radius from the rim crest there are secondary craters that dominate the deposits outermost region. These features are generated by the material ejected from the crater that follow a parabolic path and land in the nearby terrain. The ejecta from large craters and basins also creates a vast number of secondary craters, which are located even hundreds of kilometers away from the major ones. This fact outlines that the process involved is extremely energetic, and the velocity of the ejecta approaches the lunar escape velocity. The material that is not ejected during the impact is drastically altered. The surface is sometime broken into rubble and then welded together by the material that has been melted because of the high energy of the impact. The result of this kind of process goes under the name of breccia. Analyzing deeper below the surface, rocks are cracked and deformed but clearly the deformation is less severe at depth [142] [122].

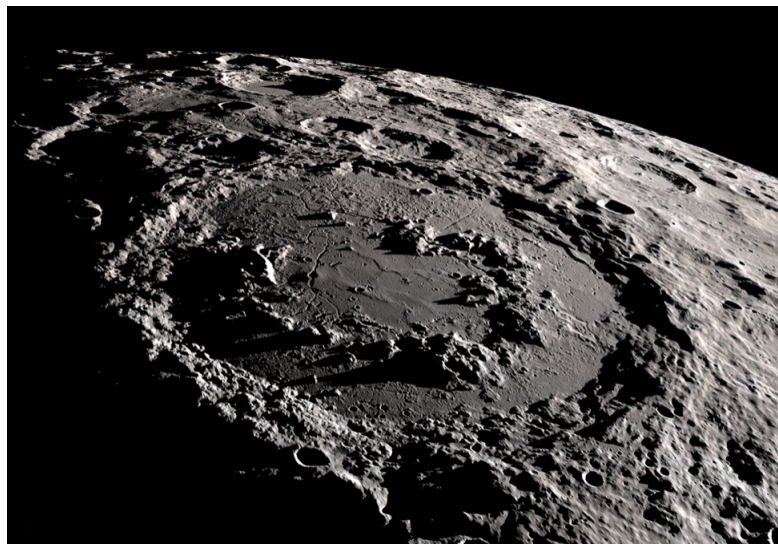


Figure 1.5: *Schrödinger crater, diameter of 320 km, the inner ring is about 150 km in diameter. Unknown depth. Location: near south lunar pole 75.0° S 132.4° E .*

Shock waves generated by the impact projectile rapidly propagate into both surface and the impactor. This produces an intense compression and melted material is subsequently shot out from the contact area. Due to the decompression along the free surface, a much greater amount of the surface and the impactor material are ejected

along the cavity walls as it expands. The first material ejected reaches the highest velocity and it is the last to impact to the surface. When the maximum depth has been reached, the cavity continues to grow laterally and the material from the upper wall is the last to be shot out. The material near the contact zone is melted and large blocks are weakly fractured. Ejecta material often generate mixed zones, that may be ejected in a later stage of the cavity expansion. For a simple crater, ejecta are deposited in reverse order from the ejection, so the later derived material is pushed out at lower velocity and land near the rim. When the attraction of gravity overcomes the force of injection, the cavity growth ceases, shock waves decay and turn into elastic waves fracturing the rocks around the cavity. When the induced stress by decompression fall below the tensile strength of the surrounding rocks, the deformation ends. At this point, the crater walls drop and the remaining melts flow down at the bottom of the depression [142] [122].

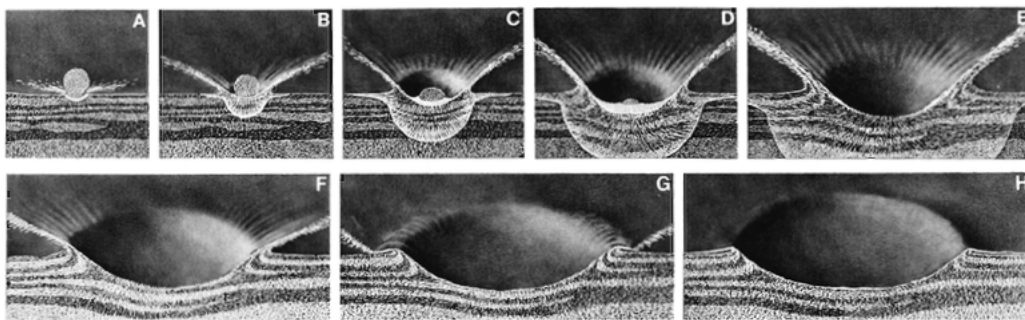


Figure 1.6: *Formation stages of simple craters. A. first stage, highly shocked material ejected. B. C. D. E. shock waves propagate outward, cavity grows while and after the impactor is consumed. F. maximum crater size is reached. G. a curtain of debris continues the outward expansion after the cavity growth ceased and overturned flap of ejecta comes to rest. H. final configuration [142].*

1.3.1 Basins

Basins are generated from very large impactors that produced an excavation with a diameter of at least 300 km up to thousands of kilometers. They represent the oldest geologic features on the lunar surface, more than 50 basins are present and some of them were afterwards filled with lava flows. Craters and basins are marked by a very similar formation process, while they differ for the dimensions. Basins are characterized by at least one internal ring inside the rim, peaks and secondary craters. Among all, there are three major basins that have to be mentioned: the Orientale, the Imbrium and the South Pole-Aitken basin.

The Orientale basin was not filled by lava, which means that its interior structure is visible, also it better displays the geological features due to less degradation and flooding than the other basins. Inside this basin 4 major rings are found, the outermost is Montes Cordillera that has a diameter of 930 km , the second one called Montes Rook is about 620 km , the third and fourth are 480 km and 320 km respectively.

The Imbrium basin was the first to be studied because of its favorable position on the lunar near side for telescopic observations. Conversely to the case of Orientale, the Imbrium basin was then filled by lava flows.

The South Pole-Aitken basin is the largest known impact crater in the Solar System with a diameter of 2500 km and 13 km deep. It is located in the south polar region

between the Aitken crater and the south pole as shown in Fig.(1.7). Its real extension was known after imaging data provided by the Lunar Orbiter Satellite and it is believed that the impact may have exposed the upper mantle [122] [142] [92].

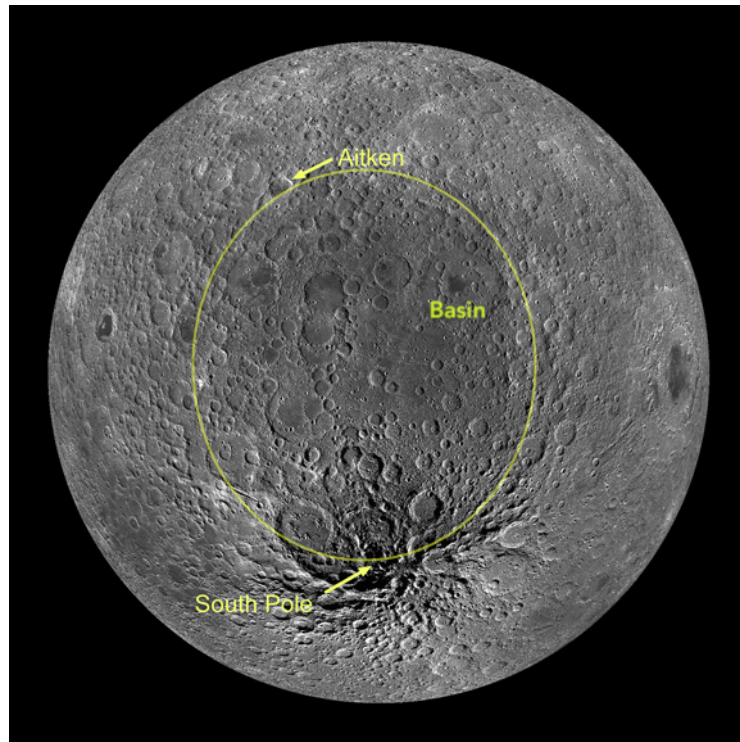


Figure 1.7: The South pole-Aitken basin.

1.3.2 Maria

Maria are the round, dark areas that cover about 30% of the lunar near side. They are located inside basins that were later filled with lava when volcanic activity began. Nevertheless, we can find other areas on the surface of the Moon that are characterized by the same type of rocks, but that have been blanketed by the ejecta produced by later impactors. These areas are so called *cryptomare*.

Many lunar maria are outlined by strong gravity anomalies called *mascons*¹. The strongest anomaly is associated with Mare Imbrium but also other significant anomalies occur with Serenitatis, Crisium and mare Nectaris. These features were first discovered by tracking data of lunar orbiters and then confirmed by Apollo and Clementine missions. As a matter of fact, spacecraft would accelerate as they flown over the maria and then decelerate as they left the area [122] [142].

¹Mascons: short term for mass concentrations.

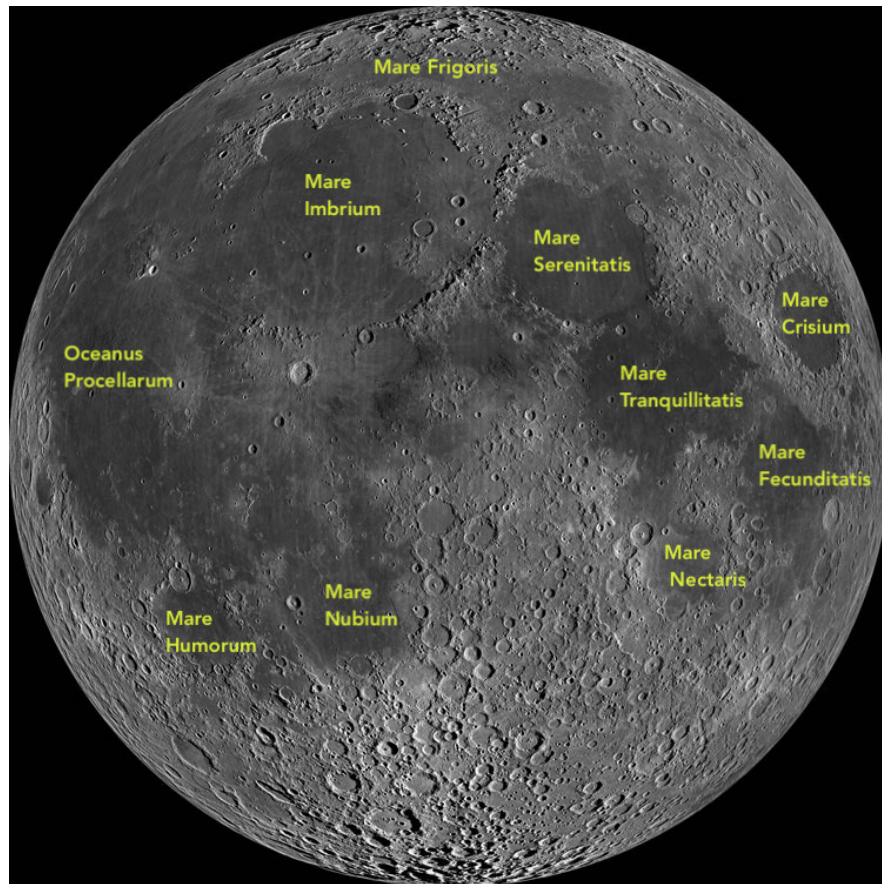


Figure 1.8: Lunar Maria located on the near side.

1.4 Lunar Rocks

Direct analysis of lunar samples returned from Apollo missions have provided information about the chemical and mineralogical composition of the Moon, the age but also essential details about the origin of the Moon and the evolution of the crust. The results of these studies can be used to study larger areas of the lunar surface, including regions that have never been directly sampled. Other significant data regarding chemical composition were also acquired with natural X -ray and γ -ray analysis from orbit by the Apollo command modules. For this reason, the compositions of lunar rocks are typically compared to the chondritic meteorites that are supposed to represent the primordial composition of the Solar System.

Lunar rocks can be divided in four distinct groups: *basaltic volcanic* rocks, which include lava flows and volcanic ash rocks (pyroclastic deposits). *Pristine* rocks from lunar highlands, complex *polymict breccias* that were formed by impacts and *lunar regolith* that covers the lunar surface. The present and the following sections provide a brief description of the lunar rocks, among others, the lunar regolith is analyzed in more detail as it represents the main objective of this work.

Resulting from the Apollo 11 samples analysis, mare basalts revealed a strong depletion of volatile elements such as Na , K , Pb , Rb , H_2O and many trace elements that are conversely present in the chondrites. By contrast, lunar rocks seem enriched in refractory elements (Al , Ba , Ca , Hf , Sr , U , Th , Zr , and others). Data provided by Surveyor mission, other samples analysis and remote sensing, showed a terra compo-

sition high in *Al*, where especially the far side terra seems richer. There are three major minerals that characterize the composition of the lunar terre: plagioclase, low-*Ca* pyroxene and olivine. Sometimes, rocks classification is made using anorthosite, norite and troctolite (ANT), which are the predominant material of the lunar terra crust. The basaltic regolith samples provided by Apollo 11 included small fragments of plagioclase and anorthosite, which are presumably ejected fragments from an impact object and these results seems to agree with similar samples collected at the Apollo 12 landing site.

A compositional class of terra material called KREEP (*K* = potassium, REE = rare Earth elements, *P* = phosphorus) appeared very abundantly in the Apollo 14 landing site, Mare Imbrium and Oceanus Procellarum. These elements characterize regolith and bedrock breccias. KREEP and other trace elements like *U*, *Th*, *Zr*, *Ba*, *Rb* are not considered most common lunar minerals, therefore are concentrated in the first partial melts or in the last residual liquids of fractionating magna systems. The presence of trace elements *U*, *Th* and ^{40}K make KREEP much more radioactive than ANT suite, thus γ -ray spectrometers carried on Apollo 15 and 16 could detect them [142] [59].

| <i>Meteorites</i> | | | | | | |
|--|---------|---------|---------|--------------|-----------|---------|
| <i>Components</i> | Dho 280 | Dho 730 | NWA 482 | Asuka 881757 | EET 87521 | NWA 773 |
| <i>SiO</i> ₂ | 44.4 | 43.7 | 43.9 | 46.2 | 47.9 | 44.7 |
| <i>TiO</i> ₂ | 0.19 | 0.17 | 0.16 | 2.06 | 1.00 | 0.57 |
| <i>Al</i> ₂ <i>O</i> ₃ | 30.7 | 27.6 | 29.4 | 10.7 | 13.0 | 6.79 |
| <i>Cr</i> ₂ <i>O</i> ₃ | 0.04 | 0.09 | 0.09 | 0.26 | 0.21 | 0.36 |
| <i>FeO</i> | 3.40 | 4.13 | 3.78 | 23.3 | 18.6 | 18.8 |
| <i>MnO</i> | 0.05 | 0.06 | 0.05 | 0.30 | 0.24 | 0.26 |
| <i>MgO</i> | 2.53 | 6.90 | 4.28 | 6.36 | 7.38 | 20.0 |
| <i>CaO</i> | 18.2 | 15.9 | 17.8 | 11.9 | 11.3 | 7.90 |
| <i>Na</i> ₂ <i>O</i> | 0.39 | 0.35 | 0.38 | 0.30 | 0.38 | 0.17 |
| <i>K</i> ₂ <i>O</i> | 0.02 | 0.02 | 0.04 | 0.04 | 0.05 | 0.09 |
| <i>P</i> ₂ <i>O</i> ₅ | 0.06 | 0.05 | 0.04 | - | - | 0.08 |
| <i>H</i> ₂ <i>O</i> | 0.05 | - | - | - | - | - |

Table 1.2: Major elements composition given in wt% of some lunar meteorites. Dho280, Dho 730 and NWA 482 are samples of lunar highland rocks. Asuka 881757, EET 87521 and NWA 773 are mare basalts [64].

1.4.1 Highland rocks

The pristine highland rocks can be divided in two distinct chemical groups that differ in their molar abundance of $Ca/(Ca + Na + K)$ and $Mg/(Mg + Fe)$. Resulting from radiometric analysis regarding age determinations, the ferroan anorthosite rocks result extremely old ($4.56 \div 4.29 Ga$). The magnesian suite rocks, that are high in Mg/Fe are also very old ($4.46 \div 4.18 Ga$), overlapping with the ferroan anorthosites, which is an issue to explore. By contrast, the alkali suite rocks, which include alkali anorthosite,

norite, gabbro-norite, granite and quartz, result younger ($4.37 \div 3.80 \text{ Ga}$). Accordingly with age determinations, the formation of some ferroan anorthosites occurred in parallel with the earliest *Mg* suite magmatism. Nevertheless, the simultaneous crystallization of the latter is not consistent with the Lunar Magma Ocean (LMO) hypothesis. In fact, in the LMO models, the ferroan anorthosites crystallized first and formed the oldest crust that was later intruded by the younger *Mg* suite rocks. For this reason, an alternative crust building mechanism was initially hypothesized, the so called global magma ocean or serial magmatism. Later analysis showed the presence of highly pure anorthosites in many regions where fresh rocks from depth are exposed, which is a sign of plagioclase accumulation from a magma ocean.

It is well known that anorthosite is very common in highland rocks with plagioclase composition of typically An_{96} , by contrast the plagioclase in terrestrial rocks range from An_{35} to An_{65} and the higher anorthitic contents clearly reflect the depletion in volatile elements such as *Na*. Most of the rocks that are found in the lunar highlands were presumably formed during the differentiation of a magma ocean, when buoyant plagioclase accumulated in the upper crust and produced a thick anorthositic crust. The magnesian suite rocks were thought to make up a significant proportion of the crust but then, resulting from more accurate analysis, may instead be more localized products of intrusive activity in the Procellarum KREEP terrain (PKT) or other regions characterized by the overturn of the mantle cumulates that have brought magnesian rocks to the upper mantle, producing hybrid magnesian magma [61].

1.4.2 Mare basalts

The largest amounts of mare basalts were provided by Apollo 11, 12, 15 and 17, which landed on maria. Geochemically, these basalts are rich in FeO , TiO_2 , depleted in Al_2O_3 and show an higher CaO/Al_2O_3 ratios than highland rocks. Moreover, compared with the highland rocks, mare basalts contain more olivine and/or pyroxene and less plagioclase. Mare basalts are thought to be the results of partial melting of mantle cumulates generated during the early differentiation of the Moon. Typically, mare basalts are categorized using their TiO_2 contents that led to three different kind of basalt types: very low-*Ti* ($< 1.5 \text{ wt}\% TiO_2$), low-*Ti* ($< 1.5 - 6 \text{ wt}\% TiO_2$) and high-*Ti* basalts ($> 6 \text{ wt}\% TiO_2$). The results of radiometric analysis showed *Ti*-rich basalts are generally older than *Ti*-poor basalts, which led to the develop of models where lunar mare volcanism began with high TiO_2 content decreasing with time. However, recent remote sensing analysis revealed the existence of young basalts with high TiO_2 contents. Also, orbital data of *Fe* and *Ti* concentrations seems to reveal no correlation between mare ages and their composition. In fact, the concentrations of FeO and TiO_2 vary independently with time, thus, these early interpretations were probably biased because the six Apollo landing sites are high-*Ti* basalts areas [61] [142].

1.5 Lunar regolith

Lunar regolith is the uppermost surface layer made of fragmental and unconsolidated rock material that overlies or covers the bedrock. The lack of atmosphere allows meteorites and micrometeorites to strike the surface producing breccias and agglutinates of small grain size. It also represents a boundary layer between the free surface and the solid Moon. Thus, crucial information about these two regions can be retrieved

studying its chemical and physical properties. For instance, trapped in the solid fragments, atoms from the Sun and cosmic-ray particles were found, making the lunar regolith highly susceptible to electrostatic charging [30]. Solar-wind particles normally consist of ionized atoms with energies of 1000 eV per nuclear particle (mainly H, He, C, N). This energy is sufficient to implant numerous particles into the surfaces (around 10^{-4} mm) of exposed mineral grains. Particles accelerated by solar flares have energies ranging from $1 \text{ MeV}/amu$ to $> 100 \text{ MeV}/amu$, and they can penetrate several millimeters to several centimeters to trigger nuclear reactions with specific materials. In addition, these particles cause lattice damage tracks and trapped-electron anomalies in crystals [59].

Owing to its complexity, lunar regolith can be divided in three major layers as follows: *superficial regolith*, *upper megaregolith* and *lower megaregolith* [114]. A schematic representation of megaregolith structure is shown in Fig.(1.10).

The superficial regolith layer is characterized by high degree of overturn, mixing and subsequent comminution due to small meteoritic impacts. It consists of loose, unconsolidated fines and breccia. Regarding its thickness, it can be determined using different approaches. Worthy of mention are the seismic refraction experiments (*Active Seismic Experiments* ASE) performed during the Apollo 14,16 and 17 missions that have led to the characterization of the lunar near surface structure. The results of these experiments, together with the passive recordings of Apollo Lunar Module (LM) ascent stage impacts, brought to an interpretation of the seismic velocity structure of the shallow layers. At the Apollo 14 landing site the uppermost seismic velocity layer ($\sim 0.1 \text{ km s}^{-1}$) results to be 8.5 m thick [31], while at the Apollo 16 landing site they have found a depth of 12.2 m [36]. In 2013 the Chinese Chang'è-3 mission collected a radar section of $\sim 110 \text{ m}$ on the far side of the Moon, revealing a complex vertical structure of 20 m made of reworked zones, ejecta, paleoregolith, transition zones and the basaltic bedrock [40]. More recently, the thickness of the regolith has been measured in the South Pole-Aitken basin using the Ground Penetrating Radar of Chang'e 4 mission and such thickness resulted to be about 12 m [81]. The radar section highlights how the subsurface is composed of loose soil, which is very transparent to the radar signals, overlying a second layer of nearly 28 m made of ejecta deposit outlined by rocks and boulders of various sizes and a mixture of fine materials, Fig.(1.9) [86]. Compared to the far side, this section suggests that this area is more homogeneous and made of fine-grained soil. The Chang'è-4 data reveals different units of various thicknesses made by multiple subsurface layers [46].

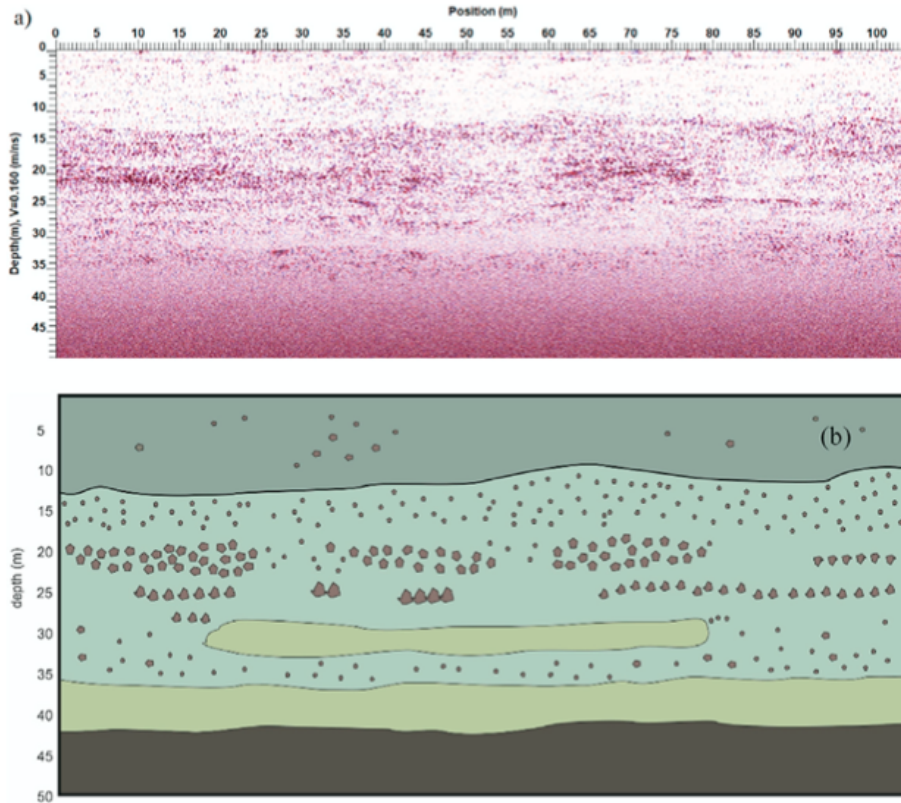


Figure 1.9: (a) *Chang'e 4* Radar section collected with the 500 MHz antennas. (b) Von Karman Crater subsurface sketch based on the radar section interpretation and tomographic reconstruction from [81]. Image from [86].

The upper megaregolith consists of depositional layers of brecciated and/or melted material, that are characterized by transport and deposition of material by means of either impact ejecta sedimentation or transient crater gravitational collapse. The thickness of this layer is thought to range between $1 \div 3 \text{ km}$ and it can be inferred by modeling the correlations between crater population and the total volume of ejecta in a certain area. The GRAIL mission provided some data that are consistent with the existence of this upper layer, assuming a bulk density of 2600 kg m^{-3} with large surface porosity of $0.30 \div 0.35$ in a thin porous layer limited to the top 3 km of the crust [56].

The bottom megaregolith layer is about $20 \div 25 \text{ km}$ in depth. It mostly consists of bedrock fractured by impacts but not transported like the other cases mentioned above. The fracture-density and fragment-size distribution decrease sharply with increasing depth. The study of this lower layer was made possible by the analysis of the lunar Passive Seismic Experiment (PSE) data, which provided significant information. Moreover, the recent GRAIL data assumes a bulk density of 2400 kg m^{-3} and surface porosity of about $0.10 \div 0.20$ that decrease exponentially with depth [56][122][59].

One of the main reasons why the lunar regolith is so crucial for our understanding of the Moon is because almost all direct measurements of physical and chemical properties of lunar material were made on samples collected from regolith. Furthermore, most of the experiments, both conducted by astronauts and remotely monitored from Earth, were done on or within the regolith layer.

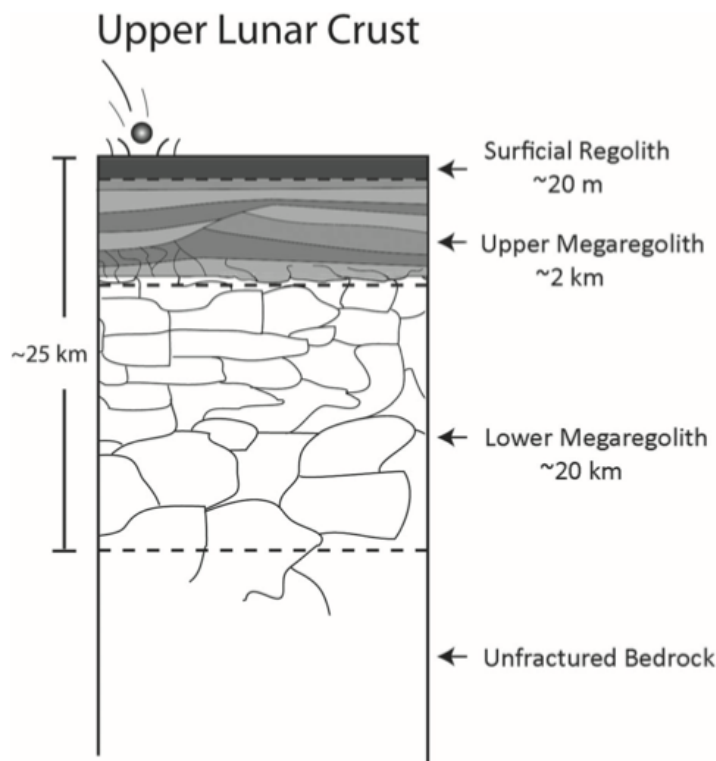


Figure 1.10: Cross sectional diagram of the upper lunar crust. Three distinct regolith layers are found: superficial regolith, upper megaregolith and lower megaregolith [114].

| <i>Location</i> | Photogeology | Seismometer |
|-------------------------|--------------|-------------|
| Flamsteed Ring | 3.3 m | - |
| NE of Wichmann Crater | 3.3 m | - |
| Apollo 12 site | 4.6 m | 3 to 5 m |
| Apollo 15 site | ≈ 7 m | 5 m |
| Apollo 11 site | 4.6 m | 3 to 6 m |
| SE Mare Tranquillitatis | 7.5 m | - |
| Apollo 17 site | ≈ 8 m | ≈ 8 m |
| Apollo 16 site | ≈ 8 to 10 m | 12 to 15 m |
| Highland Plains | 16 m | - |
| Apollo 14 site | - | 10 to 20 m |

Table 1.3: Mean superficial regolith thickness [94].

1.5.1 Classification system

The characterization of lunar regolith has primarily centered on particle size, composition, and space weathering effects. Particle size is commonly expressed using metrics like mean particle size, while distributions are often fitted with power laws or log-normal distributions. Rocks can be classified using terrestrial igneous rock schemes, and detailed mineralogical composition is best determined through methods like X-ray diffraction (XRD). Remote sensing techniques aim to identify pure minerals, but assumptions and uncertainties exist, especially due to resolution constraints. Elemen-

tal chemistry is described in weight percent oxides, with distinctions between basaltic mare and anorthositic to noritic highland terrains. Space weathering effects, including maturity indices like Is/FeO ratio and Optical Maturity (OMAT), influence regolith properties over time. Despite the variety of metrics, there is a lack of a cohesive system combining these factors, with existing studies primarily focused on lunar geological history without practical applications in mind.

To be widely adopted and practically applicable in lunar resource utilization, a lunar soil classification system must possess key attributes. It should primarily show real-world ramifications, where discriminating various soil groups has practical effects for certain activities. The classification should be quantifiable, clear, and measurable using remote sensing or low-cost in-situ approaches, with no need for sophisticated sample return or isotopic analyses. Furthermore, the approach should be consistent with existing measurements and descriptors for lunar regolith in order to preserve familiarity and avoid the introduction of extra expressions [17]. A new classification system is introduced by [17] that contains nine groups from particle size distribution and elemental composition of lunar soil. Fig.(1.11) shows the proposed classification where a very first distinction between highland and maria terrain can be made based on the FeO content. This point is particularly useful considering that some of the Apollo landing sites and thus some Apollo samples collected come from transition zones between highland and maria, leading to uncertainties on the classification of such samples.

| Major divisions | | Group symbol | Group name |
|--|--|--------------|---|
| Highland composition FeO < 8.6 wt% | Coarse grained regolith more than 50% retained on No. 120 sieve (125 μm) | HC | Highland coarse-grained soils |
| | Medium grained regolith | HM | Highland medium grained soils |
| | Fine grained regolith more than 50% passes No. 270 sieve (53 μm) | HF | Highland fine-grained soils |
| Intermediate composition FeO 8.6–15.9 wt% | Coarse grained regolith more than 50% retained on No. 120 sieve (125 μm) | IC | Intermediate composition coarse soils |
| | Medium grained regolith | IM | Intermediate composition medium-grained soils |
| | Fine grained regolith more than 50% passes No. 270 sieve (53 μm) | IF | Intermediate composition fine-grained soils |
| Mare composition FeO > 15.9 wt% | Coarse grained regolith more than 50% retained on No. 120 sieve (125 μm) | MC | Mare coarse-grained soils |
| | Medium grained regolith | MM | Mare medium-grained soils |
| | Fine grained regolith more than 50% passes No. 270 sieve (53 μm) | MF | Mare fine-grained soils |

Figure 1.11: Lunar soil classification proposed in [17] for future ISRU of the lunar soil.

1.6 Water ice on the Moon

Several observations have indicated the presence of water ice and volatiles in the lunar polar regions [45][29][82]. The impact of carbonaceous asteroids and comets, the outgassing caused by volcanic activity and the Solar wind along with micrometeoroid impacts are thought to be the primary source of water ice at the lunar poles [18][84].

The Moon's rotation axis is tilted of about 1.5° relative to the ecliptic, producing permanently shadowed regions (PSR). Topographic depressions in the PSR like impact craters present extremely cold surface temperatures ($< 110\text{K}$) in which water and volatiles deposited over billions of years [139]. These areas are also called *cold traps* and are estimated to be around $17,000\text{ km}^2$ at South pole from 80° latitude [121]. Direct evidence of PSR and cold traps mechanism is also known on other airless body in the Solar System such as Ceres and Mercury [11].

The delivery of volatiles (e.g. H_2O , CO_2 , SO_2) can occur at any latitude and molecules can migrate via ballistic hopping until they are captured in the cold traps or lost.

Multiple mechanisms, such as photodestruction (both photodissociation and photoionization), chemical reactions in the atmosphere and on the surface, thermal escape, radiation pressure escape and the solar wind interactions, can result in the depletion of volatiles during the migration [11]. According to simulations of cometary impacts on the lunar surface, $\sim 6.5\%$ of the impactor mass is retained on the Moon. Taking into account the cometary impact flux and the post-impact processes that deplete the water concentration, the total water mass that survives to the migration to the poles is about $1.3 \cdot 10^8$ to $4.3 \cdot 10^9$ metric tons over $1 Ga$, which agrees with the Lunar Prospector neutron flux measurements [104]. A parallel simulation that used asteroids as the impactor, resulted in a water delivery mass on the Moon that is six times higher than that of comets.

The water cycle can be triggered by the interaction between solar wind and the lunar regolith that forms H_2O and OH molecules [69]. These molecules are associated to the observed $2.8 - 3 \mu m$ absorption band in the reflected sunlight. The solar wind implants $-OH$ groups into the regolith that react and produce H_2O when the surface temperature is higher than $348 K$. Water molecules will then move through the ballistic hopping. The two current mechanisms for delivering water to the Moon are the solar wind implantation and the gardening process, although it is also believed that past lunar volcanic activity contributed to this process. A transient atmosphere was produced $3.8 - 1 Gyr$ ago by the volcanism, water vapor outgassed from cracks in the lunar crust and migrated to the poles [134].

In Tab.(1.4) can be found a list of lunar missions that carry on-board several scientific instruments that have been designated to detect and give evidences about the presence of volatiles and water/ice abundance on the Moon. The evidences of water ice were made also combining data from different missions as will be discussed in this section.

| Mission | launch year | Ref. |
|---|-------------|---------------|
| Clementine | 1994 | [98][97] |
| Lunar Prospector (LP) | 1998 | [43][44][45] |
| Kaguya (SELENE) | 2007 | [71] |
| Chandrayaan-1 | 2008 | [54] |
| Lunar Reconnaissance Orbiter (LRO) | 2009 | [22][85] |
| Lunar Crater Observation and Sensing Satellite (LCROSS) | 2009 | [123][29][28] |
| Lunar Polar Hydrogen Mapper (LunaH Map) | 2022 | [57] |

Table 1.4: Lunar missions designated to find evidences of presence of water/ice/hydrogen abundances on the Moon.

Surface temperature data from LRO's Diviner combined with UV albedo spectra from LAMP data provided some evidences of exposed water ice at the lunar South Pole, Fig(1.12) [58]. Based on the estimations of both annual maximum temperature and the annual average temperature, the cold traps are distinctly marked by $T_{max} = 100 K$ and $T_{avg} = 70 K$ whereas the surround areas show temperature peaks of $T_{max} = 230 K$ and $T_{avg} = 120 K$, yielding nearly $1.1 \cdot 10^4 km^2$ of cold traps area at latitudes $> 82^\circ$. For locations identified by $T_{max} < 100 K$ there is a spectral evidence for water ice at

the surface of $>\sim 1\text{nm}$ thickness. If the water ice is mixed with the lunar regolith the concentration is expected to be $\sim 0.1\%$ to 2.0% by mass and it can reach up to 10% of the surface when it is exposed. These assumptions are true when pure water ice is involved in the process but the presence of additional volatiles can not be ruled out. CO_2 ice may also be present in cold traps where $T_{max} < 60\text{K}$ [11].

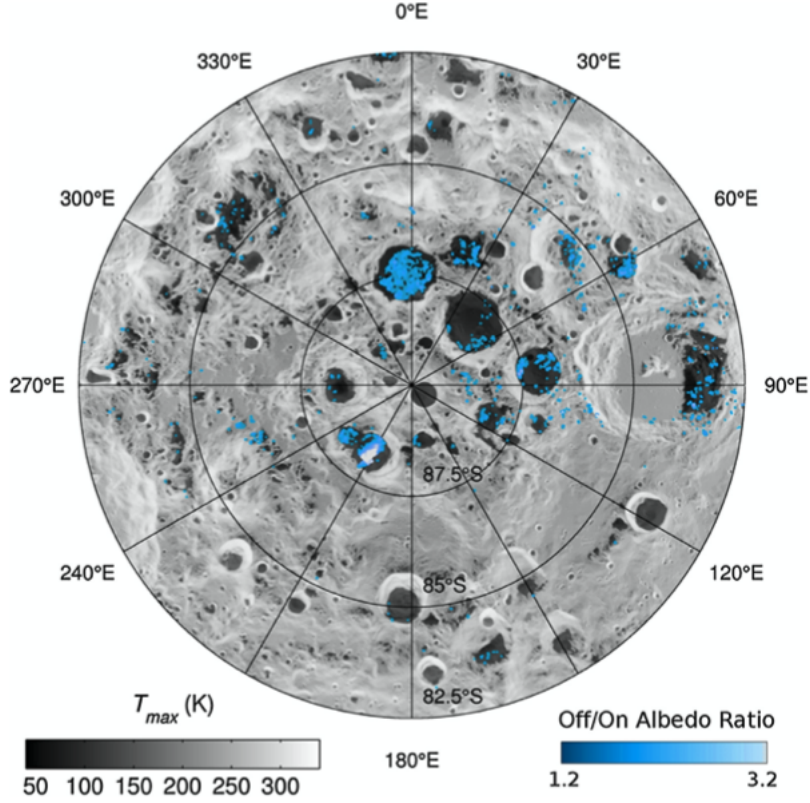


Figure 1.12: Evidence of exposed water ice at the lunar South Pole inferred from surface temperature Diviner data and UV albedo spectra from LAMP. The map shows the location of anomalous UV albedo that is consistent with water ice [58].

An other evidence that further support this finding is given by the relationship found between a rapidly increasing reflectance, measured by the Lunar Laser Altimeter, and a decreasing lunar surface temperature (from Diviner data), towards the pole [47]. This is observed in locations where the surface temperature is compatible with the existence of water ice also noted by [58]. The South Pole shows a temperature-reflectance trend that is consistent with the presence of water ice in the areas characterized by surface temperature below 110K . On the contrary, the North Pole does not show a sharp increase in reflectance when the temperature is below 110K but the steady increase of reflectance is still present, and it may indicate a limited water ice exposure compared to the South Pole. The bright pixels shown in Fig.(1.13) outline the reflectance anomalies that are unlikely caused by geologic process and water ice may be present in these areas.

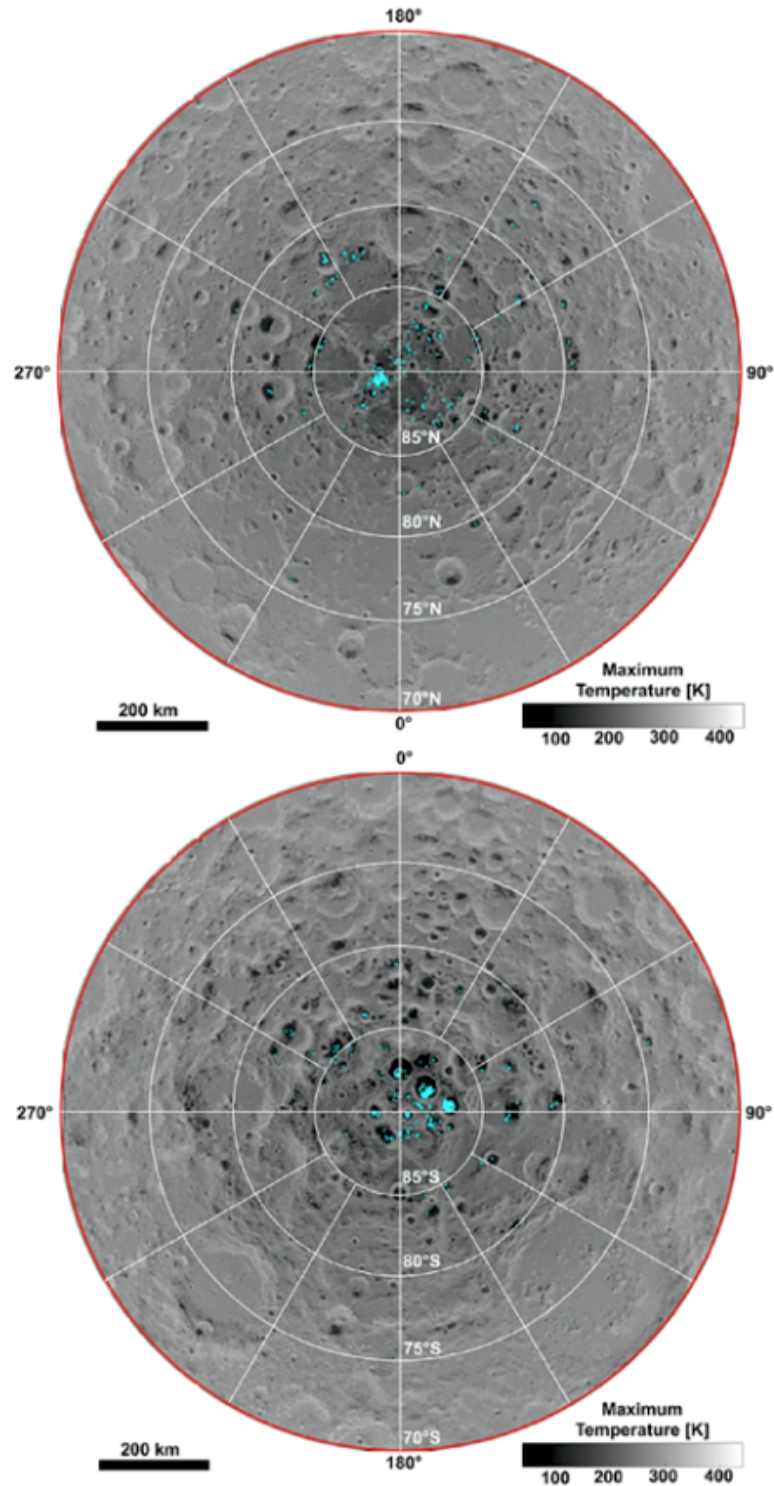


Figure 1.13: Lunar surface anomaly reflectance found at the Lunar Poles (North Pole on the left and south Pole on the right) that are consistent with decreasing temperature below 110 K [47]. Water ice may be present in the area highlighted by bright pixels. Reflectance is measured by the Lunar Laser Altimeter and the surface temperature data are acquired by the Diviner Lunar Radiometer Experiment. Picture taken from [47].

The gardening process is the main responsible for the ice distribution at depth in the PSR [18]. Superficial ice layers are comminuted and overturned with regolith by

impacts, part of the ice vaporizes and escapes from the cold traps and some of that is re-deposited in the surrounding area [42]. Secondary impacts push down and mix the ice grains, regolith and rocks, Fig.(1.14). There is still an open debate concerning whether the water ice is predominantly present in thick layers (superficial or buried), fractured and mixed within the regolith or in the form of icy soil in permafrost conditions. Regarding its lattice structure, ice might be either crystalline or amorphous in nature, depending on the temperature at which it was deposited in lunar cold traps [121]. Given all the factors presented above, the PSR are considered prime targets for detecting water ice, especially for the preservation of water ice from sublimation, the absence of solar radiation, and extremely and constant low temperatures [82]. The detection and precise estimation of water ice volumes might be more difficult of what expected due to the morphology and accumulation processes on the Moon [116]. Several reasonable explanations exist for the difficulty in finding water ice across vast lunar polar regions. These include the chance of fine-grained frost, burial depths more than 1 m and instrumental limitations [44][85][116]. An other problem in terms of clear detection of water ice within the dry regolith is given by radar observations. In fact, the dielectric characteristics of these two elements are very similar and it might be hard to see water ice within the regolith just using radar investigations [27]. This fact is one of the main topics of this thesis and it will be further discussed and deepen in the following chapters.

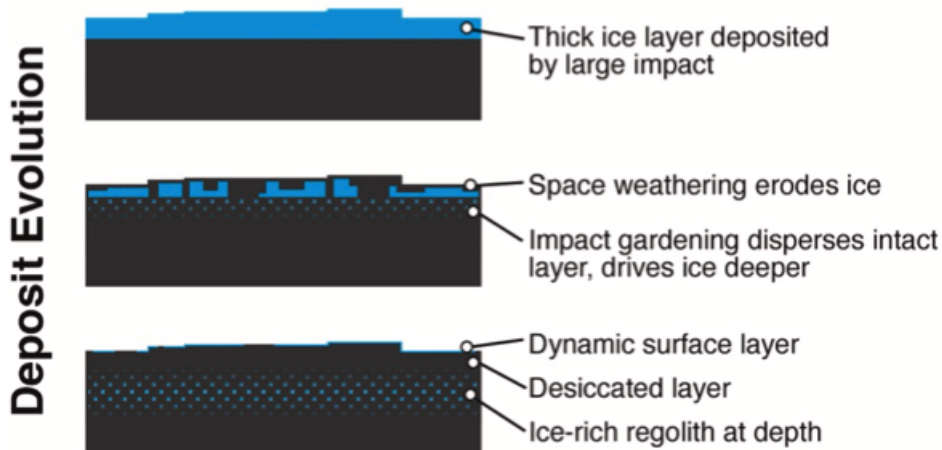


Figure 1.14: *The evolution of vertical ice distribution in PSR. The gardening process is the main driver of the vertical distribution of ice in the cold traps. Ice layers present at the surface is comminuted and mixed with the regolith due to impacts. Figure from [18].*

In Fig.(1.15) is reported a map of water ice stability depth for the North and the South pole inferred from polar hydrogen abundances and true polar wander [125]. According to this study, the maximum ice stability depth would be up to 3 m for the North polar region and 2.4 m for the South polar region.

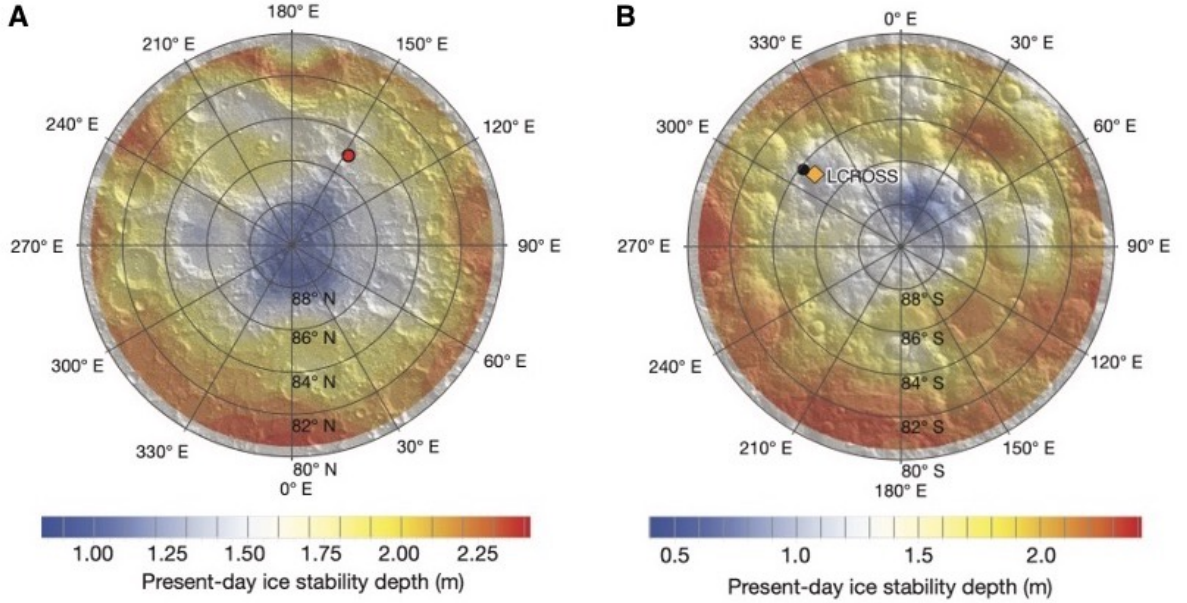


Figure 1.15: Map of water ice stability depth at the North pole (A) and South pole (B) inferred by polar hydrogen abundance and true polar wander [125]. Modified picture from [125].

A further topic of discussion is if water ice may also be mixed with other volatile species delivered by comets and outgassing, depending on the surface physical conditions. The presence of water and other volatiles is strongly dependent on surface and near-surface temperature and ultimately on the sublimation rate. The sublimation rate of water ice in vacuum can be expressed by the Hertz-Knudsen formula as follow:

$$E = \alpha p_s(T) \sqrt{\frac{\mu}{2\pi R_\mu T}} \quad (1.1)$$

where α is the sublimation coefficient ranging from 0 to 1, $p_s(T)$ is the equilibrium water pressure of ice, $\mu = 18.015$ is the molar mass and R_μ is the universal gas constant. Given that, at $T = 104 K$, $109 K$ and $120 K$ the sublimation rate of hexagonal ice is $10 kg m^2 Gyr^{-1}$, $100 kg m^2 Gyr^{-1}$ and $1.3 \cdot 10^4 kg m^2 Gyr^{-1}$ respectively [121]. This is true for exposed superficial ice but subsurface ice would experience a significant decrease in the sublimation rate due to the presence of a regolith layer which act as a diffusion barrier. It's estimated that at $1 m$ depth the sublimation rate is lower by a factor 10^4 , hence a loss rate of $100 kg m^2 Gyr^{-1}$ occurs at $T = 131 K$ instead of $109 K$ at the surface.

In a recent study, researchers have downwardly revised the overall estimates of cold-trapped ices on the Moon [120]. The Moon experienced a major reorientation of its spin axis as it moved further away from Earth. The PSRs started to form on the lunar surface following the transition known as the Cassini state and water ice started to grow and accumulate since then. In this study they calculated the spin axis orientation and the extent of lunar PSRs also taking into account the the advancements in modeling the Moon-Earth's distance over time. The discussion is about the age discrepancies between large craters and the PSR they host, indicating that the PSRs are generally younger, Fig.(1.16). According to this analysis, the majority of lunar water sources existed prior to the formation of present cold traps, forcing a large downward revision in predicted ice volumes within these locations. Between 4.25 and 3.75 billion years

ago, impacts and outgassing supplied far more ice to polar areas than following periods. During the Imbrian era, PSRs were somewhat rare, and volcanic outgassing coincided with the early stages of PSR development. Solar wind-generated water may still play a role in ice preservation. The key findings underline the relatively recent age of lunar PSRs, which may explain the discrepancies.

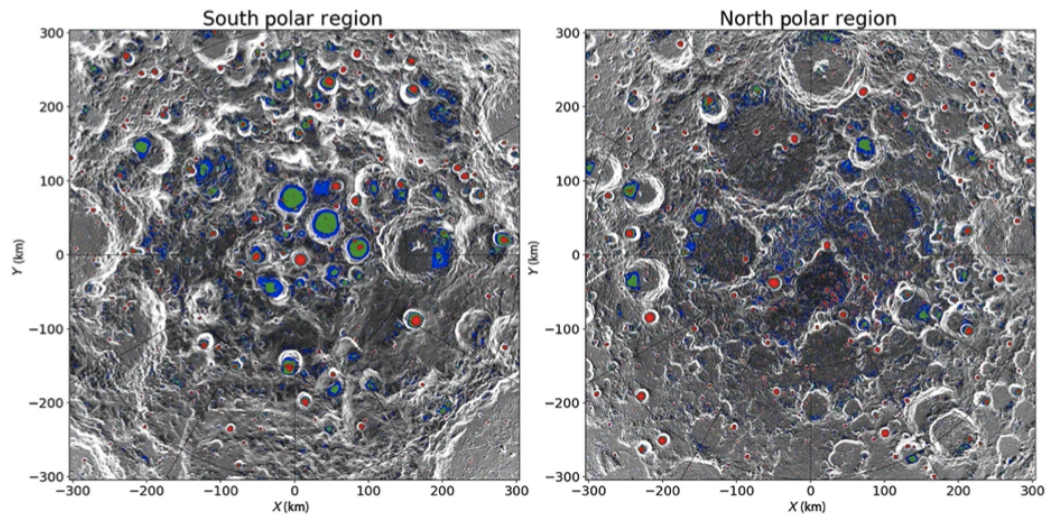


Figure 1.16: Map of current and past extent of PSRs at the lunar poles. Colored patches depict the area of PSRs in polar stereographic projection for the south and north polar regions with current topography at maximum solar declinations of 1.5° (blue, close to current), 3° (green, 2.1 Ga ago), and 6° (red, 3.3 Ga ago). Picture from [120].

Chapter 2

The Electromagnetic Theory

Maxwell's equations describe the propagation of electromagnetic radiation through the vacuum defining the relations between the electric and magnetic fields. Such partial differential equations are expressed as follows:

$$\nabla \times \vec{E} = -\frac{\partial \vec{B}}{\partial t} \quad (2.1)$$

$$\nabla \times \vec{H} = \vec{J} + \frac{\partial \vec{D}}{\partial t} \quad (2.2)$$

$$\nabla \cdot \vec{D} = q \quad (2.3)$$

$$\nabla \cdot \vec{B} = 0 \quad (2.4)$$

where \vec{E} is the electric field intensity (V/m), q is electric charge density (C/m^3), \vec{B} is the magnetic flux density (T), \vec{J} is the current density (A/m^2), \vec{D} is the electric flux density (or electric displacement) (C/m^2), \vec{H} is the magnetic field intensity (A/m) and t is time (s).

These equations describe the physics of the electromagnetic fields and are supplemented by the constitutive relations that further describe the macroscopic interaction between matter and EM field, relating flux densities to the fields.

$$\vec{J} = \sigma \vec{E} \quad (2.5)$$

$$\vec{D} = \varepsilon \vec{E} \quad (2.6)$$

$$\vec{B} = \mu \vec{H} \quad (2.7)$$

σ is the electrical conductivity and describes the free charge movement under the influence of an external electric field. ε is the dielectric permittivity and characterizes the displacement of charge particles within an insulator when an electric field is applied. μ is the so called magnetic permeability and describes the interaction of magnetic field and the magnetic moments of atoms and molecules. Such quantities σ, ε, μ are called constitutive parameters and are generally complex quantities. These equations remain true in the ideal scenario of uniform, homogeneous material with no losses. The response of a material to an external field can also be non-linear and time dependent,

which means that the material properties can also depend on the history of the interaction with the applied field. Furthermore, the physical properties of materials can also exhibit some dispersive behavior. For these reasons, eq.(2.5), (2.6) and (2.7) should be written in the following form:

$$\vec{J}(t) = \int_0^\infty \sigma(\tau) \cdot \vec{E}(t - \tau) d\tau \quad (2.8)$$

$$\vec{D}(t) = \int_0^\infty \varepsilon(\tau) \cdot \vec{E}(t - \tau) d\tau \quad (2.9)$$

$$\vec{B}(t) = \int_0^\infty \mu(\tau) \cdot \vec{H}(t - \tau) d\tau \quad (2.10)$$

2.1 The wave equation

Combining the constitutive equations with the Maxwell's equations, we obtain:

$$\nabla \times \vec{E} = -\mu \frac{\partial \vec{H}}{\partial t} \quad (2.11)$$

$$\nabla \times \vec{H} = \sigma \vec{E} + \varepsilon \frac{\partial \vec{E}}{\partial t} \quad (2.12)$$

$$\nabla \cdot \vec{E} = \frac{q}{\varepsilon} \quad (2.13)$$

$$\nabla \cdot \vec{H} = 0 \quad (2.14)$$

Let's consider a region of space with no sources ($\vec{J} = 0$ and $q = 0$), eq.(2.11) and (2.12) can be written in a more homogeneous form evaluating the left side curl.

$$\nabla \times \nabla \times \vec{X} = \nabla(\nabla \cdot \vec{X}) - \nabla^2 \vec{X} \quad (2.15)$$

$$\nabla(\nabla \cdot \vec{E}) - \nabla^2 \vec{E} = -\mu \nabla \times \frac{\partial \vec{H}}{\partial t} \quad (2.16)$$

$$\nabla(\nabla \cdot \vec{H}) - \nabla^2 \vec{H} = \varepsilon \nabla \times \frac{\partial \vec{E}}{\partial t} \quad (2.17)$$

Since there are no sources in the region of interest ($\nabla \cdot \vec{E} = 0$), ($\nabla \cdot \vec{H}) = 0$ we obtain:

$$\nabla^2 \vec{E} = \mu \varepsilon \frac{\partial^2 \vec{E}}{\partial t^2} \quad (2.18)$$

$$\nabla^2 \vec{H} = \varepsilon \mu \frac{\partial^2 \vec{H}}{\partial t^2} \quad (2.19)$$

Eq.(2.18) and (2.19) are called wave equations and outline the propagation of EM waves through a material.

2.2 Propagation, Phase and Attenuation constants

A possible solution for the wave equation can be expressed in the form of the plane wave:

$$E = E_0 \exp(j\omega t - \gamma x) \quad (2.20)$$

$$H = H_0 \exp(j\omega t - \gamma x) \quad (2.21)$$

where we expressed the solution in time harmonic form by assuming that each field varies in time according to $e^{j\omega t}$. In this way we have $j\omega = \partial/\partial t$, where $j^2 = -1$. The plane wave is characterized by a period equal to:

$$f = \omega/2\pi \quad (2.22)$$

The plane wave propagates parallel to the $+x$ direction and the propagation constant γ , a complex quantity, that depends on the dielectric properties of the investigated material.

$$\gamma = j\omega\sqrt{\varepsilon\mu} = \alpha + j\beta \quad (2.23)$$

The quantity α is the attenuation constant and describes the attenuation of the electromagnetic wave during the propagation. This can be also expressed in unit of decibels:

$$\alpha(dB) = 20\log_{10}(e^{\alpha(Np/m)}) = 8.686\alpha(Np/m) \quad (2.24)$$

The EM wave's energy decreases when it travels through a material as a result of attenuation.

β is the phase-propagation constant that defines the phase velocity at which the EM wave propagates. Since the permittivity and permeability are complex quantities, we can write:

$$\gamma = j\omega\sqrt{\varepsilon\mu} = j\omega\sqrt{(\varepsilon' - j\varepsilon''_e)(\mu' - j\mu'')} = \alpha + j\beta \quad (2.25)$$

The attenuation and the phase-propagation constants can be expressed as a function of the material parameters:

$$\alpha = \frac{\omega}{\sqrt{2}} \left[\sqrt{\mu'^2 + \mu''^2} \sqrt{\varepsilon'^2 + \varepsilon_e''^2} - \varepsilon'\mu' + \varepsilon_e''\mu'' \right]^{1/2} \quad (2.26)$$

$$\beta = \frac{\omega}{\sqrt{2}} \left[\sqrt{\mu'^2 + \mu''^2} \sqrt{\varepsilon'^2 + \varepsilon_e''^2} + \varepsilon'\mu' - \varepsilon_e''\mu'' \right]^{1/2} \quad (2.27)$$

where $\varepsilon_e'' = \varepsilon'' + \frac{\sigma_s}{\omega}$ is called effective permittivity and σ_s identifies the static conductivity of the medium.

Considering the eq.(2.23), the wave equation can be expressed in terms of the attenuation and phase-attenuation constant.

$$E = E_0 \exp(-\alpha x) \exp(j2\pi(\nu t - \beta x/2\pi)) \quad (2.28)$$

$$H = H_0 \exp(-\alpha x) \exp(j2\pi(\nu t - \beta x/2\pi)) \quad (2.29)$$

where $\nu = dx/dt$ is the phase velocity, which is defined as:

$$\frac{dx}{dt} = \nu = \frac{\omega}{\beta} = \frac{\lambda}{T} \quad (2.30)$$

where $T = 1/f$ is the time period and $\lambda = 2\pi/\beta$ is the spatial period.

To further illustrate the coupling of \vec{E} and \vec{H} , since the wave equation only depends on x and t , all the other derivatives are equal to zero:

$$\frac{\partial E}{\partial y} = \frac{\partial E}{\partial z} = \frac{\partial H}{\partial y} = \frac{\partial H}{\partial z} = 0 \quad (2.31)$$

Consequently, we may write:

$$0 = \varepsilon \frac{\partial E_x}{\partial t} \quad 0 = -\mu \frac{\partial H_x}{\partial t} \quad (2.32)$$

$$-\frac{\partial H_z}{\partial x} = \varepsilon \frac{\partial E_y}{\partial t} \quad -\frac{\partial E_z}{\partial x} = -\mu \frac{\partial H_y}{\partial t} \quad (2.33)$$

$$\frac{\partial H_y}{\partial x} = \varepsilon \frac{\partial E_z}{\partial t} \quad \frac{\partial E_y}{\partial x} = -\mu \frac{\partial H_z}{\partial t} \quad (2.34)$$

Since we presupposed there were no sources in the region of interest, the divergence is zero. Therefore:

$$\frac{\partial E_x}{\partial x} = 0 \quad \frac{\partial H_x}{\partial x} = 0 \quad (2.35)$$

The EM waves that are generated can be defined as superposition of plane waves which propagate as transverse electromagnetic modes (TEM).

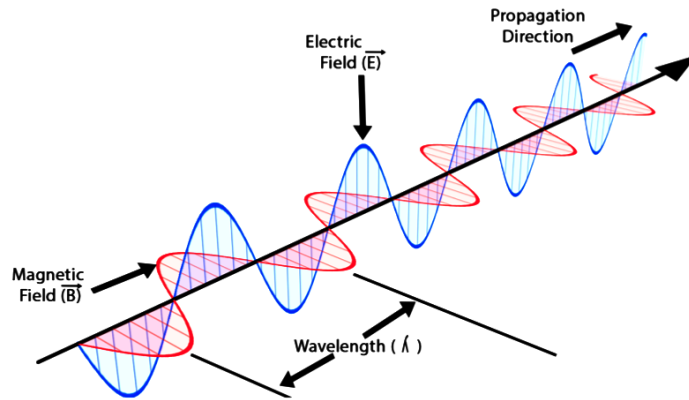


Figure 2.1: With transverse electromagnetic (TEM) propagation, the electric and magnetic field lines are all constrained to travel in directions that are normal the direction of propagation.

2.3 Electromagnetic Properties of Materials

Terrestrial materials, including rocks, soils, and fluids, can exhibit a variety of electromagnetic behaviors, which are governed by the material's varying physical-chemical properties. The EM behaviors can be described in terms of the constitutive parameters: the complex dielectric permittivity and the complex magnetic permeability. Such quantities serve as the key parameters for the macroscopic description of an electromagnetic field-exposed dielectric material.

2.3.1 Dielectric Properties

As insulators with tightly bonded electrons in their atoms, dielectric materials don't conduct electricity. In the presence of an external electric field, they may also store energy. Such materials are electrically neutrals but they can present some electric polarization phenomena under the influence of an external field. The electric field tends to distort or polarize atoms and molecules to form an electrical dipole. The local redistribution of bound charges causes both storage and dissipation of energy. We may use the concept of electric polarization \vec{P} to explain this phenomenon. It is defined as the dipole moment per unit volume ΔV of the dielectric material, where ΔV is the volume, N_e the number of dipole per unit volume and $d\vec{p}_i$ are the induced moment inside the volume.

$$\vec{P} = \lim_{\Delta V \rightarrow 0} \frac{1}{\Delta V} \sum_{i=1}^{N_e \Delta V} d\vec{p}_i \quad (2.36)$$

When an applied electric field is present, many forms of charge separation and, consequently, dipole moments, can appear in a material. These rely on the atomic, molecular, polar characteristics, and the frequency of the applied field [62].

2.3.1.1 Polarization Mechanisms

There are several polarization mechanisms that take place, marked by different length scales, [101] and [49]. The frequency of applied field governs the establishment of dipoles, whether there is enough time before the field direction is inverted. The different processes involved are summarized below:

Electronic polarization: the cloud of electrons around the atomic nuclei is distorted by the electric field. The induced displacement produces dipoles that tend to orient in a direction opposite to the field. It rapidly establishes and resists at high frequency ($< 10^{24} Hz$).

Ionic or molecular polarization: the electrical field produce a slight separation of positive and negative charges that generate dipoles, resulting in a distortion of molecules. Materials with positive and negative ions that repel each other when an external field is applied are significantly more likely to exhibit this process. This mechanism can undergoes at frequencies up to $< 10^{14} Hz$.

Orientational polarization: it is also called dipole mechanism and occurs in

materials characterized by randomly oriented dipole that tend to orient in the direction of the electric field, ($< 10^{12} Hz$).

Maxwell-Wagner polarization: this process is also referred as space charge polarization or interfacial polarization and is only established for low frequencies ($< 10^6 Hz$). It locally causes the migration of charges particles. This mechanism is frequently present during experimental measurements between the capacitor cell and the tested material.

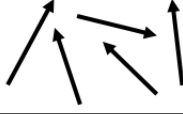
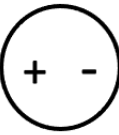
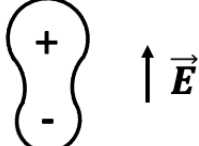
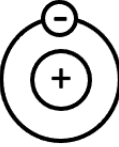
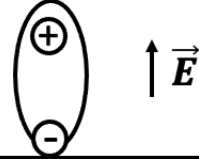
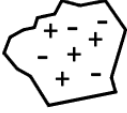
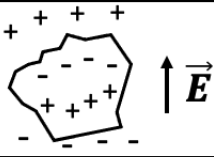
| Mechanism | No applied field | Applied field |
|---|---|---|
| Electronic polarization |  |  |
| Ionic or molecular polarization |  |  |
| Orientational or dipole polarization |  |  |
| Interfacial polarization |  |  |

Figure 2.2: Polarization mechanisms that take place when a dielectric material is under the influence of an external electric field. Modified from [49].

It may takes some time for a general material under the effect of an external field to reach the steady state. This delay is known as "relaxation time" τ . In light of this, we can distinguish between an almost immediate polarization caused by the deformation of atoms and molecules and a secondary, time-dependent polarization. The application of external field arises a second effect inside the material which is the electric conduction that also cause energy dissipation. The electrical conduction arises when free charges are present. Both polarization and conduction phenomena can be discussed in terms of permittivity and permeability.

2.3.2 Electric Susceptibility

We can introduce the susceptibility χ_e to quantitatively assess the polarization induced in the material by the external electric field. The susceptibility is also useful to define the relative dielectric constant.

Let us consider a flat capacitor filled by a dielectric homogeneous material, under the influence of an external field, Fig(2.3). The resulting electric flux density is given by the sum of two terms.

$$\vec{D} = \varepsilon_0 \vec{E} + \vec{P} \quad (2.37)$$

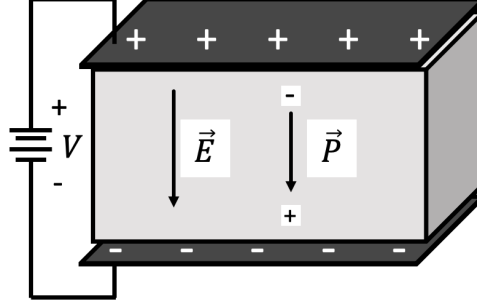


Figure 2.3: Flat capacitor filled by a dielectric material. The polarization induced inside the material is directly proportional to the electric field. The relation between \vec{E} and \vec{P} is given by the susceptibility χ_e .

The electric flux density can be directly linked to the applied field and so the polarization.

$$\vec{P} = \varepsilon_0 \chi_e \vec{E} \quad (2.38)$$

The quantity χ_e defines the dimensionless electric susceptibility that it is generally expressed in the following way:

$$\chi_e = \frac{1}{\varepsilon_0} \frac{\vec{P}}{\vec{E}} \quad (2.39)$$

For the majority of linear dielectric materials, the polarization is directly proportional to the average electric field strength. The ratio P/E is a constant that describes an intrinsic attribute of the material. Substituting the eq.(2.38) in the flux density we can obtain the operative definition of the relative permittivity also known as dielectric constant.

$$\vec{D} = \varepsilon_0 \vec{E} + \varepsilon_0 \chi_e \vec{E} = \varepsilon_0 (1 + \chi_e) \vec{E} = \varepsilon_s \vec{E} \quad (2.40)$$

The parameter ε_s defines the static permittivity of a given material but it is commonly expressed divided by the permittivity of the vacuum, which gives the relative permittivity ε_r .

$$\varepsilon_r = \frac{\varepsilon_s}{\varepsilon_0} = 1 + \chi_e \quad (2.41)$$

The relative dielectric constant is a complex quantity and it is convenient to highlight its real and imaginary part.

$$\varepsilon_r = \varepsilon'_r - j\varepsilon''_r \quad (2.42)$$

2.3.3 The complex dielectric permittivity

The complex dielectric permittivity can be discussed through the equivalent circuit approach, illustrated in Fig.(2.4) [62]. Let's consider an empty flat capacitor connected to a circuit powered by alternating current. The circuit system is characterized by an alternating voltage V and the capacitor by the stored charge Q . The charging current that flows through the capacitor has a phase angle of 90° against the voltage V and it can be calculated by eq.(2.43), where C_0 is the vacuum capacitance and $\omega = 2\pi f$ is the angular frequency. When the capacitor is filled by a dielectric material, its capacitance depends on the dielectric properties of the substance. This fact is highlighted in eq.(2.44) by the factor ϵ'_r that is the real part of the relative dielectric permittivity previously defined in eq.(2.41).

$$I_c = \frac{dQ}{dt} = j\omega C_0 V = I_0 e^{j(\omega\tau + \pi/2)} \quad (2.43)$$

$$C = C_0 \frac{\epsilon'}{\epsilon_0} = C_0 \epsilon'_r \quad (2.44)$$

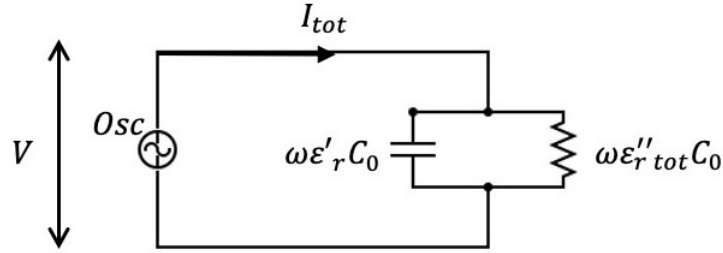


Figure 2.4: Equivalent circuit system of a flat capacitor powered by an alternating current. The resolution of the system provides the operative definition for the complex permittivity.

In addition to the charging current component, a loss current I_r can occur, which is proportional to the conductance G of the dielectric material and it is in phase with the applied voltage. The total current is then expressed in eq.(2.46). The angle between the charge current and the total current, in Fig.(2.5), is called the loss angle δ and it is used to illustrate the frequency response of the circuit, the dissipation factor D or loss tangent, eq.(2.47).

$$I_r = GV \quad (2.45)$$

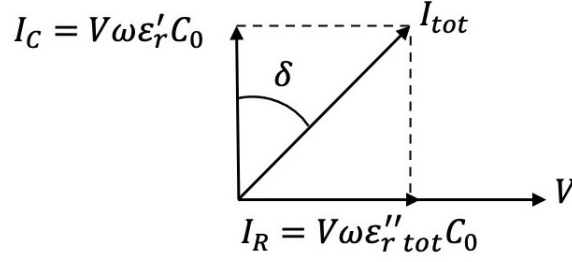


Figure 2.5: Vectorial currents diagram in the capacitive cell filled with a dielectric material. The total current that flows in the circuit is given by two terms: a charge current and a loss current. The angle δ is the loss angle.

$$I_{tot} = I_c + I_r = V(j\omega C + G) \quad (2.46)$$

$$D = \tan\delta = \frac{I_r}{I_c} = \frac{1}{\omega RC} \quad (2.47)$$

Since the dissipation process may account for multiple causes that are related not only to the RC circuit itself but also to the dielectric properties of the material inserted into the capacitor, it's more convenient to introduce the complex dielectric permittivity to outline the capacitance and conductance. The equation (2.46) becomes:

$$I_{tot} = I_c + I_r = V(j\omega\epsilon' + \omega\epsilon'') \frac{C_0}{\epsilon_0} = j\omega C_0 \epsilon_r V \quad (2.48)$$

Doing so the loss tangent is given by the ratio between the imaginary and real part of the permittivity.

$$D = \tan\delta = \frac{\epsilon''}{\epsilon'} \quad (2.49)$$

2.3.4 Conductivity

The equation (2.48) can be written in a different form to show the relation of permittivity and conductivity. For a parallel plate capacitor the capacitance can be expressed as a function of the geometry of the cell, eq.(2.50), where A is the area, d the plates separation and the electric field $E = V/d$.

$$C = \frac{A}{d} \epsilon_0 \quad (2.50)$$

In light of this, we can write the total density current using the eq.(2.48).

$$J = \frac{\partial I_{tot}}{\partial A} = \frac{\partial}{\partial A} (j\omega\epsilon' + \omega\epsilon'') AE = (j\omega\epsilon' + \omega\epsilon'') E \quad (2.51)$$

The total density current can also be expressed in terms of the electric displacement from eq.(2.2) and taking into account the equations (2.5) and (2.6) we can extract the relation between permittivity and conductivity.

$$J = (j\omega\epsilon' + \omega\epsilon'') E = \epsilon \frac{\partial E}{\partial t} \quad (2.52)$$

The product of the angular frequency and the imaginary part of permittivity constitutes the dielectric conductivity $\sigma = \omega\varepsilon''$. The quantity σ takes into account all the variety of effects that cause the dissipation, the ohmic conductivity, the conduction due to the charge migration and it is frequency dependent.

To further illustrate the relation of permittivity and conductivity, we can identify the effective conductivity which is given by the sum of two terms: the static conductivity σ_s and the one caused by the alternating field $\sigma_a = \omega\varepsilon''$, eq.(2.53) [49]. The complex dielectric permittivity can now be expressed in terms of the conductivity, as shown in eq.(2.54) and (2.55).

$$\sigma_e = \sigma_s + \omega\varepsilon'' = \sigma_s + \sigma_a \quad (2.53)$$

$$\varepsilon = \varepsilon' - j\varepsilon'' = \varepsilon' - j\frac{\sigma_e}{\omega} = \varepsilon' - j\frac{\sigma_s + \omega\varepsilon''}{\omega} \quad (2.54)$$

$$\varepsilon = \varepsilon' - j\left(\varepsilon'' + \frac{\sigma_s}{\omega}\right) \quad (2.55)$$

The equation (2.55) is the most common way to show the permittivity since it takes into account both the dielectric loss and the conductive loss. Similarly, the loss tangent, eq.(2.49) can also be expressed as a function of conductivity:

$$\tan\delta = \frac{\varepsilon'' + \sigma_s/\omega}{\varepsilon'} \quad (2.56)$$

2.3.5 Magnetic Properties

Materials that present magnetic polarization when exposed to an external magnetic field are called magnetic materials. In complete analogy to the dielectric case, the magnetization is given by the alignment of intrinsic magnetic dipoles to the external field. The macroscopic description of the phenomena is given by the magnetization vector which is defined as the dipole moment per unit volume ΔV of the material; the equivalent of polarization for the dielectric case. Linear material are non-magnetic and in this work it's always implied that $\mu_r \sim 1$.

$$\vec{M} = \lim_{\Delta V \rightarrow 0} \frac{1}{\Delta V} \sum_{i=1}^{N_m \Delta V} d\vec{m}_i \quad (2.57)$$

The magnetization and the magnetic field are related by the so called magnetic susceptibility which is a complex and dimensionless quantity:

$$\vec{M} = \chi_m \vec{H} \quad (2.58)$$

The magnetic flux density can be then expressed as the sum of two terms, the magnetic field and the magnetization vector, yielding to the definition of the complex magnetic permeability μ .

$$\vec{B} = \mu_0(\vec{M} + \vec{H}) = \mu_0(1 + \chi_m)\vec{H} = \mu\vec{H} \quad (2.59)$$

$$\mu = \mu_0(1 + \chi_m) \quad (2.60)$$

$$\mu_r = \frac{\mu}{\mu_0} = (1 + \chi_m) \quad (2.61)$$

where μ_r is the relative magnetic permeability which describes the magnetization of a material when exposed to an external magnetic field.

2.4 Frequency dependence of permittivity

As was introduced in section 2.3.1, the dielectric behavior and the polarization mechanisms are strongly governed by the oscillation of the electromagnetic field. However, it is more fascinating to examine the dielectric characteristics in the frequency domain since no geo-material is free from dielectric losses, and as a result, free from dispersion. The potential energy is transformed into kinetic energy when the dipoles are established by rotating and moving charges in space. This fact is reflected in the decrease of the real part of permittivity and the increase of the imaginary part. The coupling of real and imaginary part is well described by the Kramers-Kronig relations,[126]:

$$\varepsilon'(\omega) = 1 + \frac{2}{\pi} \int_0^{\infty} \frac{\omega' \varepsilon_r''(\omega')}{(\omega')^2 - \omega^2} d\omega' \quad (2.62)$$

$$\varepsilon''(\omega) = \frac{2\omega}{\pi} \int_0^{\infty} \frac{1 - \varepsilon_r'(\omega')}{(\omega')^2 - \omega^2} d\omega' \quad (2.63)$$

2.4.1 The Debye model

In this regard, several models were proposed to describe the permittivity as a function of frequency, in order to obtain a better comprehension of the phenomenon. The Debye model is one of the most common mathematical approach that was developed to describe the polarization of pure polar molecules, which also describes the dielectric behavior of several geo-materials [34].

$$\varepsilon_e(\omega) = \varepsilon_{\infty} + \frac{(\varepsilon_s - \varepsilon_{\infty})}{1 + j\omega/\omega_{rel}} - j \frac{\sigma_s}{\omega \varepsilon_0} \quad (2.64)$$

$$\varepsilon_e'(\omega) = \varepsilon_{\infty} + \frac{(\varepsilon_s - \varepsilon_{\infty})}{1 + (\omega/\omega_{rel})^2} \quad (2.65)$$

$$\varepsilon_e''(\omega) = \frac{(\varepsilon_s - \varepsilon_{\infty})\omega}{\omega_{rel} \left(1 + (\omega/\omega_{rel})^2\right)^2} + \frac{\sigma_s}{\omega \varepsilon_0} \quad (2.66)$$

The quantity $\omega_{rel} = 1/\tau$ is the relaxation angular frequency, inversely proportional to the relaxation time τ , ε_s and ε_{∞} are the static permittivity and the high frequency permittivity respectively. A general material can present multiple polarization mechanisms that occur at different frequencies, hence it can show N relaxation frequencies. The equation (2.64) can be rewritten in a more general form:

$$\varepsilon_e(\omega) = \varepsilon_{\infty} + \sum_{n=1}^N \frac{(\varepsilon_s - \varepsilon_{\infty})}{1 + j\omega/\omega_{rel_n}} - j \frac{\sigma_s}{\omega \varepsilon_0} \quad (2.67)$$

Once the relaxation frequency is noted, the equation (2.53) can also be expressed in terms of ω_{rel} :

$$\sigma_e = \sigma_\infty - \sigma_s \frac{\omega^2}{\omega^2 + \omega_{rel}^2} \quad (2.68)$$

where the conductivity at high frequencies σ_∞ can also be expressed in terms of the static conductivity σ_s , static permittivity ϵ_s and ω_{rel} :

$$\sigma_\infty = \sigma_s + \epsilon_0(\epsilon_s - \epsilon_\infty)\omega_{rel} \quad (2.69)$$

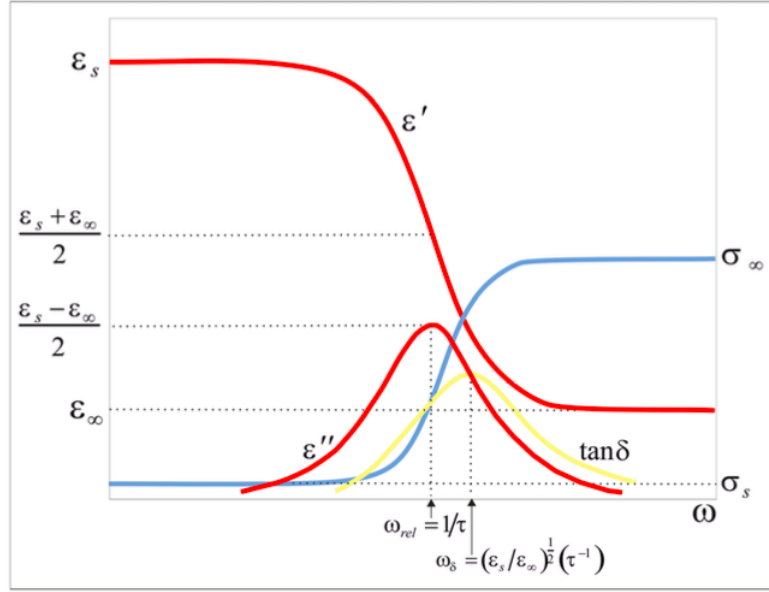


Figure 2.6: The Debye model describes the behavior of complex dielectric permittivity in the frequency domain. Figure taken from [110].

If the static conductivity is negligible, the relaxation frequency can be found at the maximum of the imaginary part as shown in Fig.(2.6), while the real part of permittivity exhibits an inflection:

$$\frac{d\epsilon_e''(\omega)}{d\omega} = 0 \rightarrow \omega/\omega_{rel} = 1 \quad (2.70)$$

$$\epsilon_e''_{MAX} = \frac{\epsilon_s - \epsilon_\infty}{2} \quad (2.71)$$

$$\epsilon_e' = \frac{\epsilon_s + \epsilon_\infty}{2} \quad (2.72)$$

These results can be easily visualized in the "Cole-Cole diagram" where ϵ'' vs ϵ' produces a circle where only the positive region has physical meaning, Fig.(2.7).

$$\left(\epsilon' - \frac{\epsilon_s + \epsilon_\infty}{2}\right)^2 + \epsilon''^2 = \left(\frac{\epsilon_s - \epsilon_\infty}{2}\right)^2 \quad (2.73)$$

The circle equation is determined by combining the real and imaginary part, eq.(2.65) and (2.66).

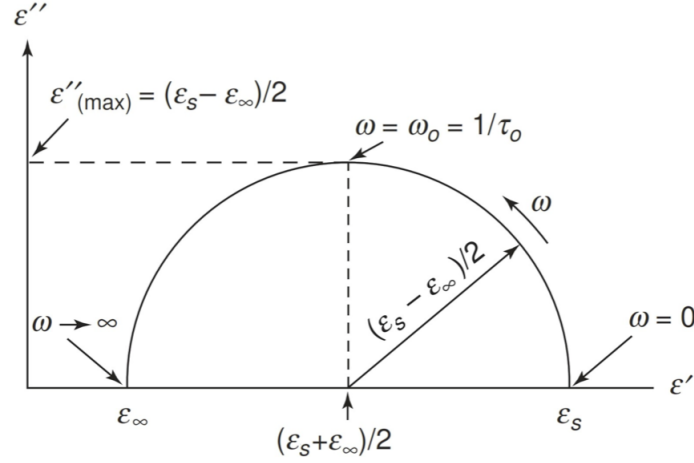


Figure 2.7: The Cole-Cole diagram also known as Argand diagram for one relaxation frequency Debye model where the static conductivity is negligible.

2.5 Temperature dependance of permittivity

Once the Debye model is noted, it is important to highlight that the relaxation frequency also change at varying temperature according to exponential law, eq.(2.74) where E is the activation energy, k_b the Boltzmann constant, ω_0 is a constant value and T the temperature in Kelvin. Similarly, for dipolar material, the gap between static and infinite permittivity varies with temperature as highlighted in eq.(2.74) [62].

$$\omega_{rel} = \omega_0 e^{-E/k_b T} \quad (2.74)$$

$$\varepsilon_s - \varepsilon_\infty = \frac{A}{T} \quad (2.75)$$

Substituting eq.(2.74) and (2.75) into the Debye model, and neglecting the static conductivity, it yields to the description of permittivity also in terms of temperature:

$$\varepsilon'_e(\omega) = \varepsilon_\infty + \frac{A/T}{1 + (\omega/\omega_0)^2 \exp(2E/k_b T)} \quad (2.76)$$

$$\varepsilon''_e(\omega) = \frac{(A/T) \omega \exp(E/k_b T)}{\omega_0 \left[1 + (\omega/\omega_0)^2 \exp(2E/k_b T) \right]} \quad (2.77)$$

These two equations illustrate an inverse proportionality relationship with temperature. As the temperature decreases, the value of real part increases and the peak of imaginary part moves towards lower frequency values. The same also applies for the static conductivity that is related to the temperature according to the Arrhenius formula, eq.(2.78). The effect of temperature on dielectric parameters is depicted in Fig.(2.8).

$$\sigma_s = \sigma_{s0} \exp(-E/k_b T) + \frac{A}{T} \omega_0 \exp(-E/k_b T) \frac{\omega^2 \exp(2E/k_b T)}{\omega_0^2 + \omega^2 \exp(2E/k_b T)} \quad (2.78)$$

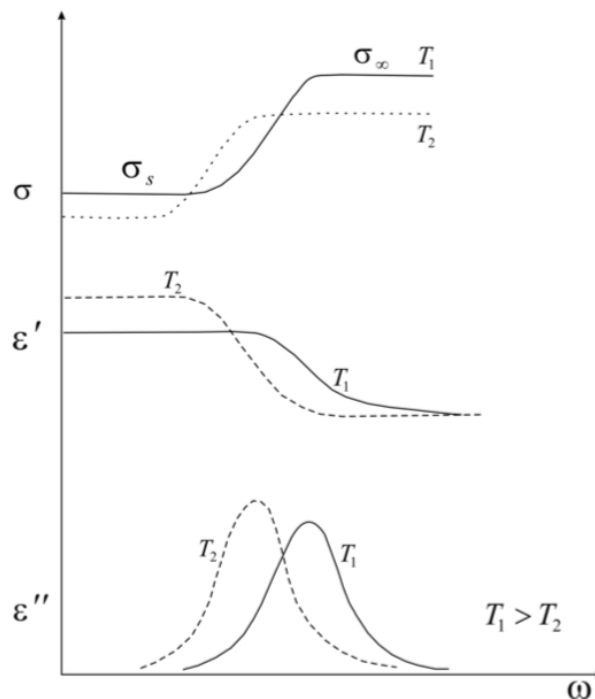


Figure 2.8: Effect of temperature on dielectric properties. For higher temperature values, the permittivity and conductivity move towards lower relaxation frequency values. Modified from [110].

2.6 Dielectric behavior of geomaterials

The intent of this paragraph is to summarize the dielectric properties and behavior of geomaterials relevant to planetary explorations, such as rocks, soil, and ice. Data from the literature, graphs, and tables are presented for comparison with laboratory measurements.

2.6.1 Rocks

Rocks are composite material made up of one or more minerals. However, because of the possibility of non-mineral components, including water, the physical properties of a rock may not be a simple sum of the attributes of its constituent minerals. Two electrical characteristics are important in the petrophysical characterization of rocks: the electrical resistivity and the dielectric permittivity. Most minerals in rocks, particularly silicates and carbonates, have very high specific resistivity, exceeding $10^9 \Omega m$ (or specific conductivity $\sigma < 10^{-9} S/m$), making them insulators. Conductive minerals, such as sulfides and certain oxides, are uncommon in the Earth's crust, with graphite being a notable example [119]. The relative permittivity of the most abundant rock-forming minerals tends to lie in the range of 4 to 10, but some minerals, particularly those in the sulfide and oxide groups, show greater values. Variations in electrical characteristics can be attributed to impurities and unique crystalline structures, which also contribute to electrical anisotropy within the same mineral class or group.

Campbell and Ulrichs (1969) [16] undertook a comprehensive investigation of the dielectric properties of rocks and powders. Their study involved measurements on 36 distinct rock types, examining both their solid and powdered forms, at frequencies of 450

MHz and 35 GHz. According to the data in Fig.(2.9), the relative dielectric permittivity of 36 solid rock types ranges from 2.5 to 9.6. Interestingly, there are not any significant variations between the values obtained at 450 MHz and 35 GHz, demonstrating that ϵ_r remains stable across the microwave spectrum, implying a frequency-independent behavior. This observation is supported by the spectra given in Fig.(2.10), which exhibit the behavior of four representative rock types. In particular, dielectric investigations at various temperatures show that ϵ_r has temperature-independent trends. Other electric measurements and properties of rocks and terrestrial material can be found in [107].

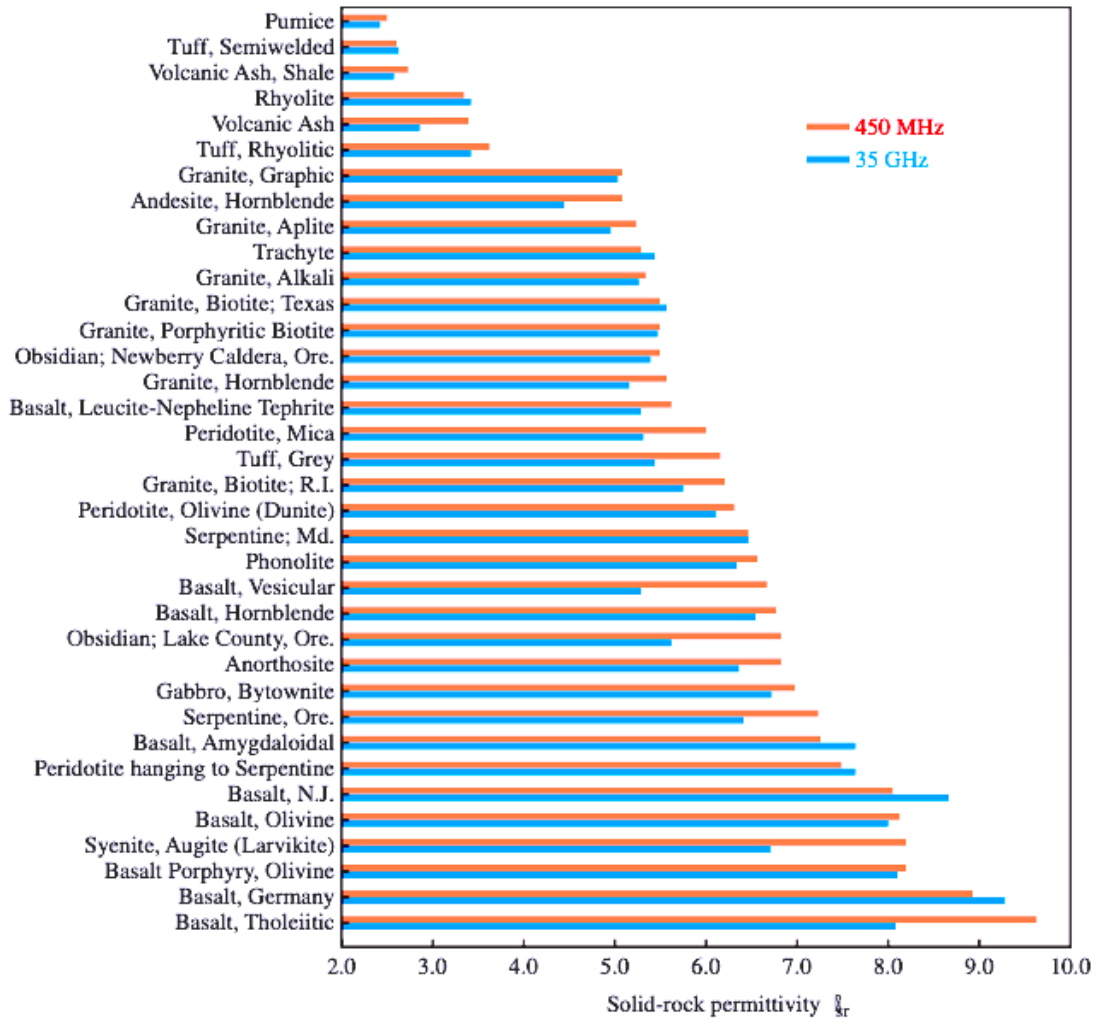


Figure 2.9: Complex permittivity of 36 rock samples measure at 450 MHz and 35 GHz in the work of Campbell and Ulrichs (1969) [16]. Modified from [83].

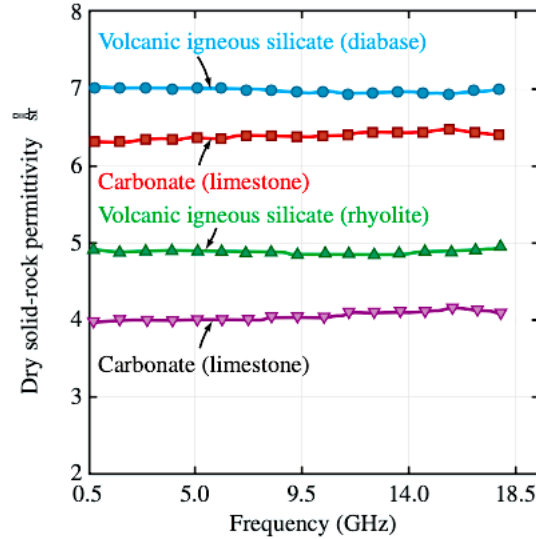


Figure 2.10: Complex permittivity of selected rock samples measure at varying frequency from [83].

2.6.2 Soils

The anhydrous powders consist of grains derived from various rocks and minerals, blended with enclosed air volumes residing within the pores. Due to this composition, they are generally treated as heterogeneous mixtures whose dielectric properties are described by mixing formulas. The microwave dielectric constant of soil, is nearly constant throughout a wide range of temperatures and frequencies in the absence of liquid water. It is shown that the real part of permittivity ranges between 2 and 4 and the imaginary part is lower than 0.05. The main variation is given by variation of bulk density (or porosity) and several models were proposed. Eq.(2.79) is general model from [35] for dry soil while eq.(2.80) is empirical formula identical to the Lichteneker rule discussed in the mixing formula chapter that is also shown in Fig.(2.11).

$$\epsilon'_{soil} = (1 + 0.44\rho_b)^2 \quad (2.79)$$

$$\epsilon'_{soil} = 2^{\rho_b} \quad (2.80)$$

An extensive work of dielectric measurements was carried out on lunar regolith samples [59], whose dielectric properties endorse the constant behavior of general dry soil. Fig.(2.12) reports the real part of permittivity and loss tangent of several Apollo regolith samples as a function of density. Eq.(2.81) gives the empirical trend obtained on moon data for dry regolith as a function of density [59].

$$\epsilon'_{regolith} = 1.871^{\rho_b} \quad (2.81)$$

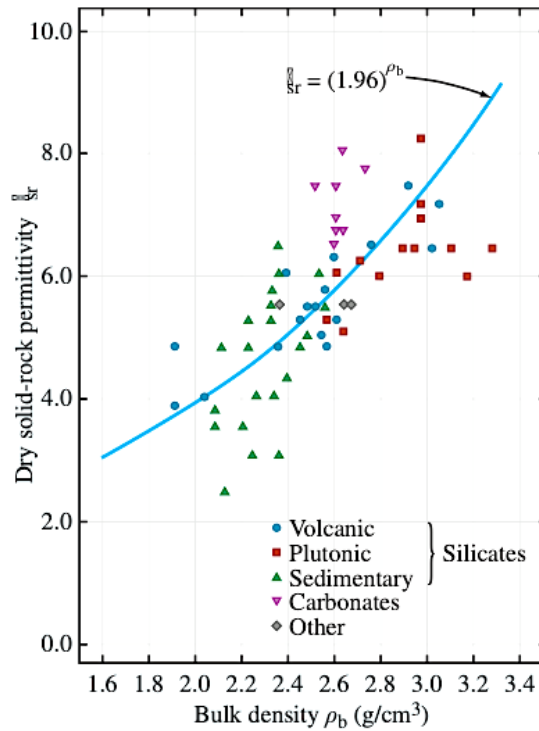


Figure 2.11: Complex permittivity of powdered rock samples in function of bulk density [83].

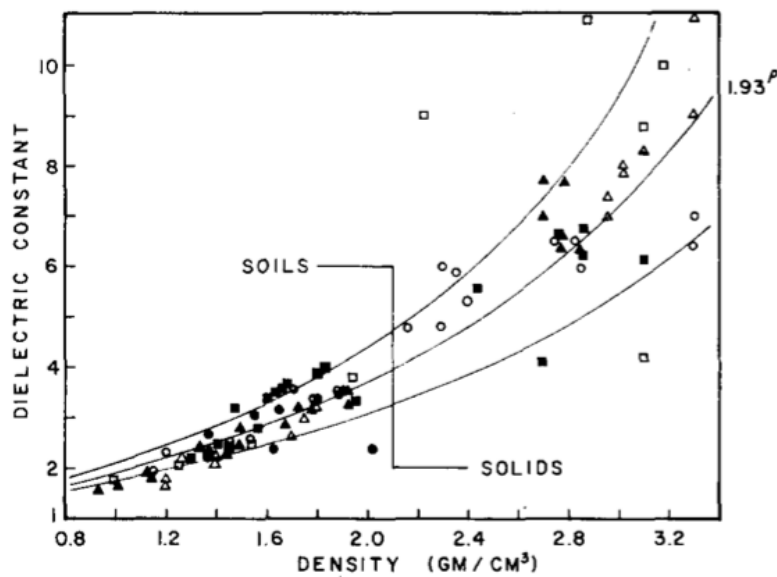


Figure 2.12: Complex permittivity of lunar regolith in function of bulk density [100].

2.6.3 Water ice

Water exhibits a high degree of polarizability due to the polar nature of its molecules. The distribution of dipoles in liquid water will essentially align with the supplied electric field. As a result of this phenomena, water has a relative permittivity of about 80 and it strongly varies with temperature, [4]. Water, as a polar molecule, has the ability to dissolve ionic compounds. Ionic compounds dissociate in water, creating positively

and negatively charged ions that can move freely throughout the water, resulting in electrical conductivity. Therefore, while water is a poor conductor of electricity in its pure form, the level of conductivity directly increases with the concentration of ions that are dissolved in it. Laboratory investigations of pure water ice have covered a broad spectrum of temperatures and frequencies and the experimental results show that the dielectric properties of pure water ice adhere to the Debye model; which is already discussed in the prior section. This behavior is primarily caused by proton hopping polarization and has been extensively studied by numerous researchers, and more details can be found in [8], [67], and [20]. There are several aspects that can modify the dielectric response of the sample as crystal orientations, cracks and inclusions of impurities or gas bubbles, and many others [110]. Furthermore, the ice growth and cooling procedure may accidentally affect the integrity of the ice-to-electrode interface, perhaps generating air gaps or cracks. This is further complicated by the materials' different thermal expansion coefficients. These characteristics, taken together, have the ability to significantly modify the expected Debye behavior of pure water ice. They have the ability to introduce new relaxation phenomena, shorten relaxation durations, and broaden the bell-shaped dielectric response curve. Fig.(2.13) reports the Debye curves of pure water ice.

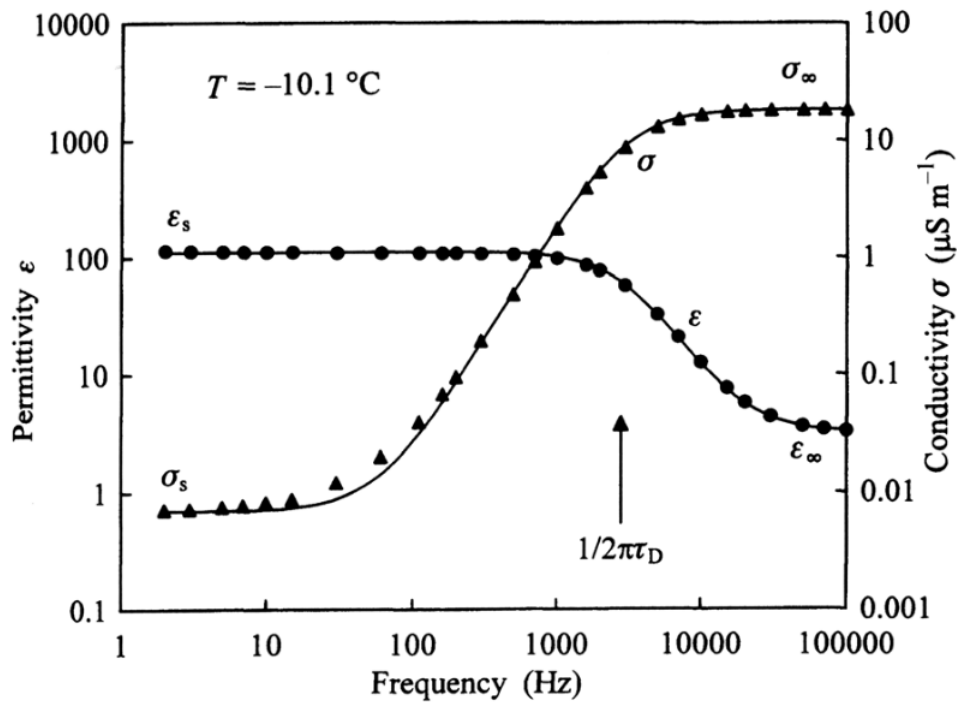


Figure 2.13: Pure water ice Debye model measured at 263 K in function of frequency. Left Y-axis reports the complex permittivity, right Y-axis shows the conductivity. Taken from [108].

In the frequency range 10 MHz to 300 GHz the water ice permittivity is frequency independent and presents weak variation with temperature that can be modeled as eq.(2.82), [90]. In practical applications, the temperature dependence can be disregarded, and a constant value of real part of nearly 3.2 can be employed consistently throughout the entire microwave frequency range.

$$\epsilon' = 3.1884 + 9.1 \times 10^{-4} T \quad (\text{when } -40^\circ \leq T \leq 0^\circ) \quad (2.82)$$

The pure water ice is often contaminated with ionic impurities like salts, that give rise to the permittivity of the sample, particularly the imaginary part that is related to the energy losses. Water ice is extremely sensitive to very small quantities of impurities, since they have the ability to replace the existing oxygen atoms and therefore modify the lattice structure. Fig.(2.14) shows a notable variation of the imaginary part, varying the salinity S of water ice samples [83]. Such impurities can become integrated into the hydrogen-bonded network and cause the creation of protonic point defects [74]. H^+ , OH^- , NH_4^+ , Cl^- , and F^- are among the most common ions that can be hosted within the ice lattice [108].

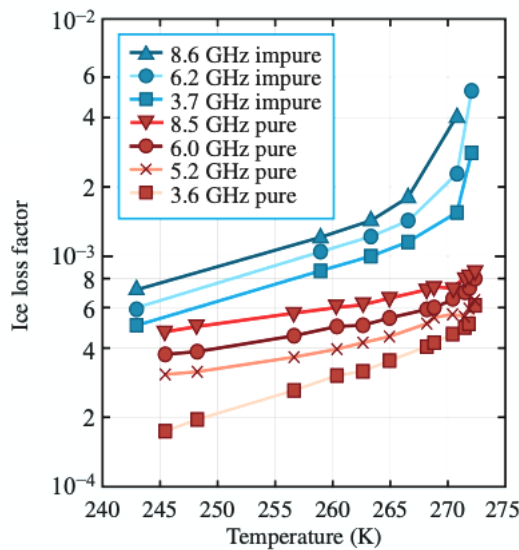


Figure 2.14: How impurities affects the energy losses of water ice samples. Modified from [83]

When compared to pure water ice, sea ice is a much more complicated medium in terms of structure and electromagnetic properties. Sea ice has a complicated composition, with liquid brine inclusions and air pockets distributed throughout the ice matrix. The brine inclusions, which contain a salt-water mixture, have a significant impact on the composite's complex dielectric characteristics. This is primarily due to their significantly higher complex dielectric constants than ice. The rate of ice layer formation has a significant impact on the shape and concentration of these brine inclusions. Sea ice is commonly classified into three major types based on its age: (a) young ice, which is typically less than 30 cm thick, (b) first-year ice, which is typically 30 cm to 2 meters thick, and (c) multiyear ice, which is thicker than 2 meters [138]. Several main parameters influence the complex dielectric constant of sea ice: the dielectric constant of pure ice; the dielectric constant of the brine pockets or inclusions; the volume fraction of brine within the ice; the distribution and geometry of the brine pockets and inclusions relative to the direction of the external electric field. Other factors that can influence the dielectric behavior are the ice temperature and the salinity S that also influence the volume fraction [83]. The salinity parameter is primarily governed by temperature and several models describe its trends as a function of temperature [5]. The empirical

models for salinity expressed below are also plotted as a function of temperature in Fig.(2.15).

$$S_b = 1.725 - 18.756T - 0.3964T^2 \quad \text{for } -8.2 \leq T \leq -2^\circ\text{C} \quad (2.83)$$

$$S_b = 57.041 - 9.929T - 0.16204T^2 - 0.002396T^3 \quad \text{for } -22.9 \leq T \leq -8.2^\circ\text{C} \quad (2.84)$$

$$S_b = 242.94 + 1.5299T + 0.0429T^2 \quad \text{for } -36.8 \leq T \leq -22.9^\circ\text{C} \quad (2.85)$$

$$S_b = 508.18 + 14.535T + 0.2018T^2 \quad \text{for } -43.2 \leq T \leq -36.8^\circ\text{C} \quad (2.86)$$

The complex permittivity of sea ice is plotted as a function of frequency in Fig.(2.15) modeled by Stogryn in 1971 [128] as follow:

$$\varepsilon'_b = \varepsilon_{W\infty} + \frac{\varepsilon_{b0} - \varepsilon_{W\infty}}{1 + (2\pi f\tau_b)^2} \quad (2.87)$$

$$\varepsilon''_b = (2\pi f\tau_b)^2 \frac{\varepsilon_{b0} - \varepsilon_{W\infty}}{1 + (2\pi f\tau_b)^2} + \frac{\sigma_b}{2\pi f\varepsilon_0} \quad (2.88)$$

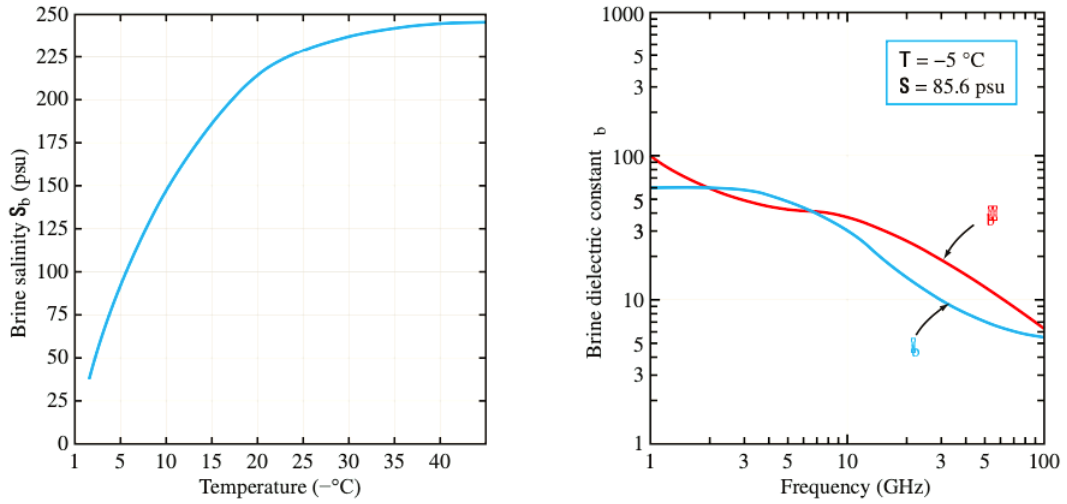


Figure 2.15: Dielectric properties of sea ice. On the left panel is reported the variation salinity in function of ice temperature. On the right panel is reported the dielectric constant of liquid brine at varying frequency that is calculated using the Stogryn's model [128]. The red curve is the real part of permittivity while the blue line is the imaginary part. Modified from [83]

Chapter 3

Radar theory and application for explorations

3.1 Introduction

The radar remote sensing is non-invasive technique based on the electromagnetic wave propagation. The remote sensing techniques cover the whole electromagnetic spectrum from low-frequency radio waves through the microwave, submillimeter, infrared, visible, ultraviolet, x-ray, and gamma-ray regions of the spectrum. Among all geophysical methodology of investigations, they are considered one of the most powerful tool since they are non-destructive and high-resolution methods. Remote sensing is become a standard tool in the field of Earth observation for mapping the vegetation, land use, glaciers monitoring and many other applications; but it is also widely employed in space explorations for the mapping the surface of planets and to detect subsurface features, discontinuities natural reservoirs without probing and drilling [32]. Radar stands for Radio Detection and Ranging, it's a system designed for the detection and location of objects by radiating EM energy into space and detecting the echo signal reflected from objects. The intent of this chapter is to give a brief introduction to the radar instruments, basic principles and applications in the context of space explorations.

3.2 Ground Penetrating Radar

The (GPR), also known as georadar, is a high-resolution EM technique used to assess buried objects' location and depth, as well as investigate natural subsurface conditions and features without direct access to it. It's a class of radar in the ultrawideband UWB that operates in the frequency range $10MHz - 10GHz$. It is employed for various purposes: engineering, archeology, glaciology, geology, ground water, and many other applications [68] where the target is usually located only a few wavelengths from the antenna system.

A very common GPR design comprises a transmitter and receiver antennas in a fixed geometry that moves along the surface. It operates by transmitting EM energy pulses that propagate into the ground. When the EM energy encounter an interface between two material it is partially reflected back and registered by the receiver antenna. The reflections occur due to abrupt changes in the dielectric properties. GPR units consist of a control unit that generates trigger pulses to the antennas for transmitting and

receiving signals, along with a computer for data collection, Fig.(3.1). The collection of GPR reflected signals can be visualized in a two dimensional representation called radargram, shown in Fig.(3.2) where on the vertical axis is reported the two-wave travel time of the EM pulses, while the position of the GPR is reported on the horizontal axis.

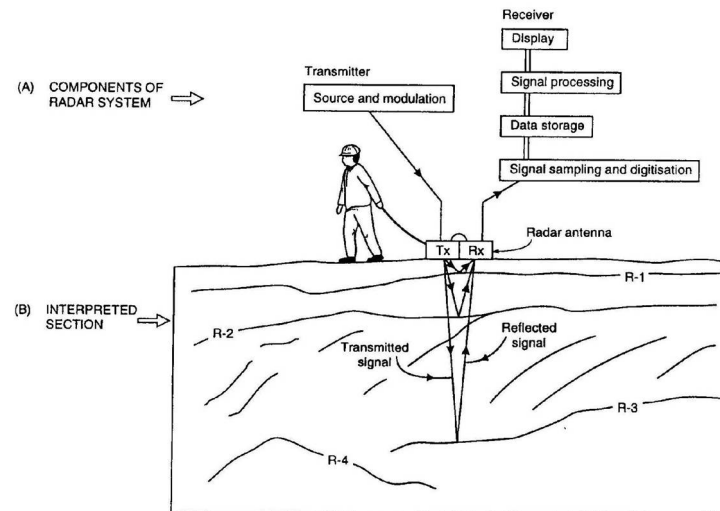


Figure 3.1: Ground penetrating radar sketch that illustrates the basic principles of this survey technique. (image taken from [1])

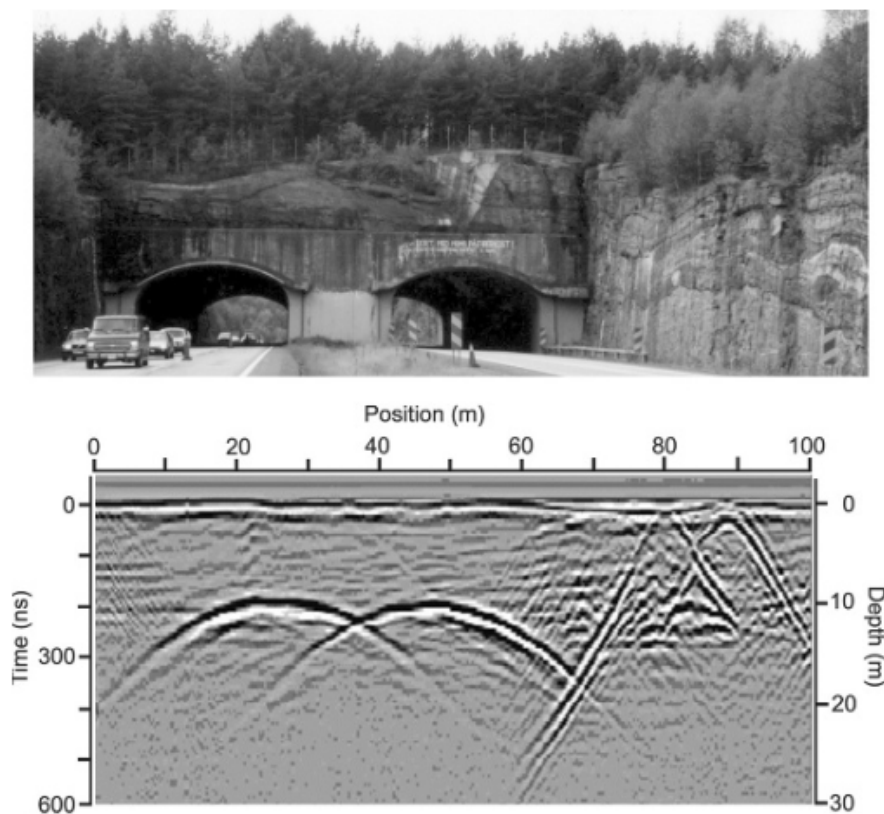


Figure 3.2: Recorded returned signal obtained by GPR surveys, also known as radargram image. (taken from [68]).

The performance of GPR depends on surface and subsurface conditions, and the instrument design is strongly applications-oriented, depending on target-type and EM properties of the "environment" that retain the target. Generally, the GPR design is made considering two fundamental aspects in order to detect a target: adequate spatial-depth resolution of the target; adequate signal to noise ratio and clutter ratio.

For the following discussion, is important to highlight and introduce the concepts of bandwidth B and central frequency. The GPR can be described in terms of B and central frequency f_c of operation which are strongly related to W , i.e. the EM pulse width generated by the instrument.

$$W = \frac{1}{B} = \frac{1}{f_c} \quad (3.1)$$

$$\lambda_c = \frac{v}{f_c} \quad (3.2)$$

where λ_c is the center frequency wavelength. It is important to underline that the bandwidth B doesn't define the central frequency of the GPR. However, the ratio B/f_c is a quantity that characterizes the GPR signal.

$$R = \frac{B}{f_c} \quad (3.3)$$

With R having an appropriate upper limit equal to one, the intent is always to maximize B and minimize f_c for optimal GPR design.

3.2.1 Timing and resolution

The GPR is employed for the detection of objects that can be found in the first one hundred meters below the surface and thus resolution, times and frequency band are important aspects to consider. We can determine the time range resolution of the GPR using the two wave travel time delay time formula, eq.(3.4) considering min-max survey depth of $0.01 - 100\text{ m}$ and velocity range $0.033 - 0.3\text{ m/ns}$ typically encountered in the GPR surveys (water and air velocity propagation respectively).

$$\tau = \frac{2 \cdot d}{v} \quad (3.4)$$

Substituting the depths and velocities it's easy to evaluate that the GPR time range correspondes to $67\text{ ps} - 6060\text{ ns}$.

An other crucial aspect is the resolution and the ability to discriminate the presence of multiple targets at a depth. This translates into the ability to record multiple distinct pulses and not a one larger event as shown in Fig.(3.3). When the direct signal from the transmitter to the receiver overlaps with the reflected signals in time, transmitter blanking happens. If two targets produce equal route lengths, the changes in travel times may be minimal, resulting in the overlap of the reflected pulses. (Note that the route lengths can be even different if the velocities are also different, resulting in similar travel times). Two separated events/objects are resolved only if the pulses are separated in time by a factor $W/2$, where W is the pulse width, see Fig.(3.4).

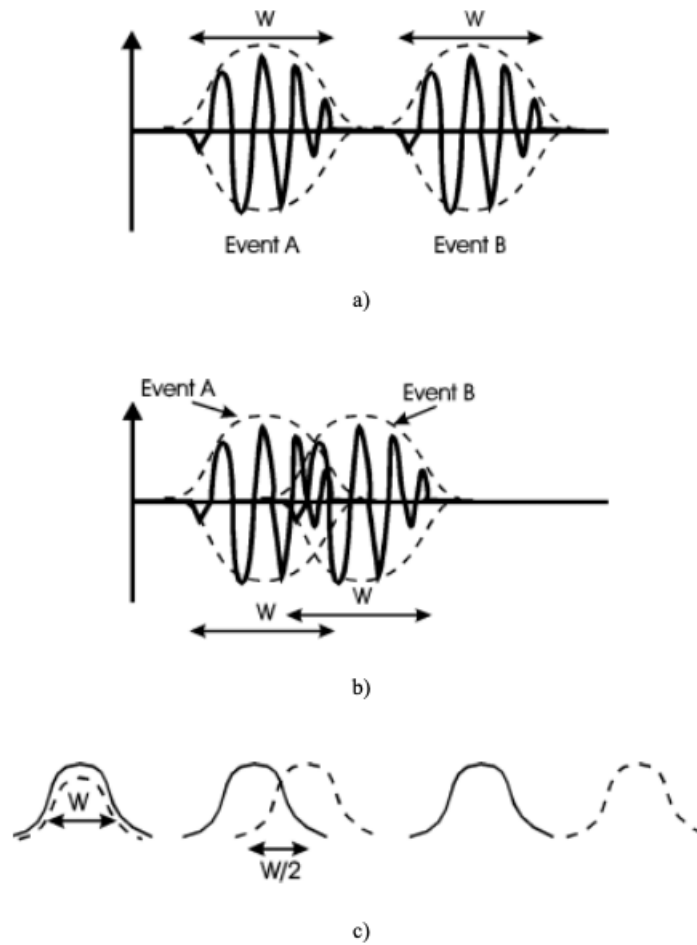


Figure 3.3: A) Two distinct pulses registered by the GPR that are separated in time. The dotted lines represent the signal envelope that are completely separated and resolved. B) The two events are not distinguishable since the two envelopes partially or totally overlaps. C) Two events are resolved only if are separated in time by a factor $W/2$ where W is the pulse width. Picture taken from [4].

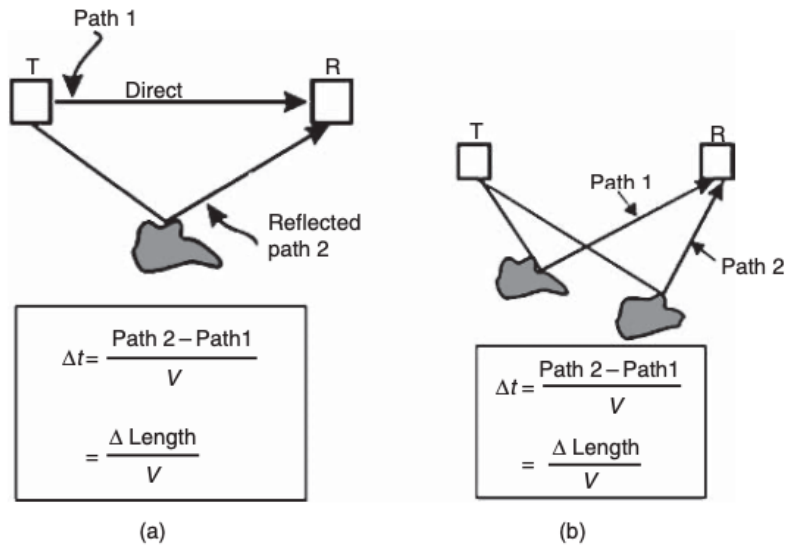


Figure 3.4: A) Transmitter blanking happens when the direct signal from the transmitter to the receiver overlaps with time reflected signals. B) If two targets have comparable path lengths, travel time variations might be small, causing reflected pulses to overlap. From [68].

The resolution in space is a result of the temporal pulse separation concept and is determined by pulse width W and material EM propagation velocity v . For radar purposes we can distinguish between depth resolution, eq.(3.5) (logitudinal) and angular resolution, eq.(3.6) (lateral) as reported in Fig.(3.5). The radial resolution is influenced by pulse attenuation and dispersion. The distance from the system, the pulse width, and the velocity all affect lateral resolution. The lateral resolution decreases with distance. ([68]) Lateral resolution is related to the first Fresnel zone, in fact in eq.(3.6) the equality operation is given by considering eq.(3.1) and (3.2).

$$\Delta r \geq \frac{Wv}{4} \quad (3.5)$$

$$\Delta l \geq \sqrt{\frac{Wvr}{2}} = \sqrt{\frac{d\lambda_c}{2}} \quad (3.6)$$

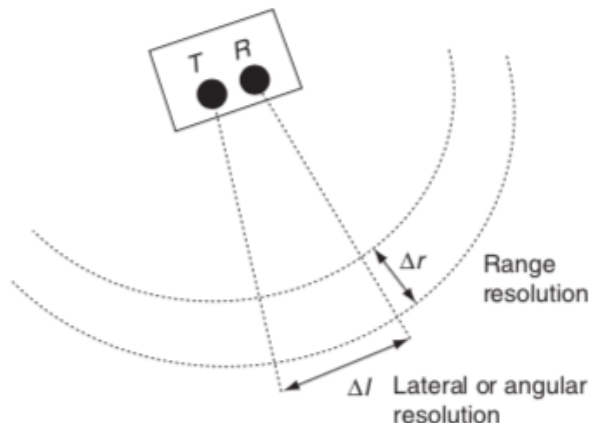


Figure 3.5: The resolution length is determined by the pulse width and propagation velocity. In an ideal environment, the radial resolution length is independent of distance from the source. In actuality, pulse dispersion and attenuation will affect radial resolution at greater distances. The lateral resolution is determined by the velocity, pulse width, and distance from the system. The lateral resolution length increases with increasing distance. Image taken from [68].

Typical GPR designs with bandwidth resolution and depth of investigation is reported in Fig.(3.6) from [4]. A basic guideline is that the resolution should be on the order of the greatest depth of exploration divided by 100.

$$\Delta r \approx \frac{h_{max}}{100} \quad (3.7)$$

| Maximum Depth (m) | Resolution Required(m) | Envelope Width in (ns) | Required Bandwidth (MHz) |
|-------------------|------------------------|------------------------|--------------------------|
| 0.1 | 0.001 | 0.02 | 50000 |
| 1.0 | 0.010 | 0.20 | 5000 |
| 10.0 | 0.100 | 2.00 | 500 |
| 100.0 | 1.000 | 20.00 | 50 |

Figure 3.6: Summary of GPR design with typical depth, resolution and bandwidth required. Table from [4].

3.3 Antennas design

Antennas play a crucial role in GPR applications, as they both generate and detect electromagnetic (EM) fields. The transmit antenna is responsible for converting the excitation voltage into a spatially and temporally distributed field. On the other hand, the receiving antenna detects the temporal variation of a vector component of the EM field and converts it into a recordable signal.

To meet the desired antenna characteristics, several requirements must be addressed. Firstly, it is crucial to precisely define the source and detection locations.

Secondly, the transmitter and receiver responses must remain consistent over time and space, ensuring their invariance. Additionally, the vector character linking the source voltage and received voltage must be quantifiable for accurate measurement and analysis. Lastly, the antennas bandwidth should be appropriate for the system application needs. Fulfilling these requirements is challenging; field generation and detection demand the use of finite-size antennas, where the antenna dimensions should be comparable to the wavelength of the signals. Finite-size antennas possess the following characteristics:

- **Spatially Distributed Field:** Field creation and detection occur over a distributed region, resulting in imprecise source and detection points.
- **Ground-Dependent Response:** The field transit time (or wavelength) is not invariant in GPR applications due to the host environment, making the antenna response not perfectly invariant.
- **Less-Precise Vector Characterization:** Spatially distributed antennas make it difficult to isolate response to a single vector component, leading to less precise vector characterization.
- **Bandwidth Maximization:** Damping the antenna improves bandwidth, but it may make the antenna less efficient and less sensitive to its surroundings.

3.3.1 Directivity - TE, TM patterns

Among various antenna types, short electric dipoles have demonstrated effectiveness in GPR applications. The relative electric field amplitude at a considerable distance from the source is donut-shaped when the dipole is in a uniform medium, as shown in Fig.(3.7B). There is no energy emitted from the antenna's ends, but energy is radiated uniformly in the plane perpendicular to the dipole axis. The cross sections through the donut commonly referred to as the TE and TM patterns [68], Fig.(3.7C). The pattern changes dramatically when the dipole antenna is put on the ground, Fig.(3.8). The refractive focusing associated with the impedance change at the air-ground contact causes the change in directivity. This a good approximation in far-field case, the fields are not as well defined near the antennas, and there are secondary lateral and evanescent fields at the air-ground interface.

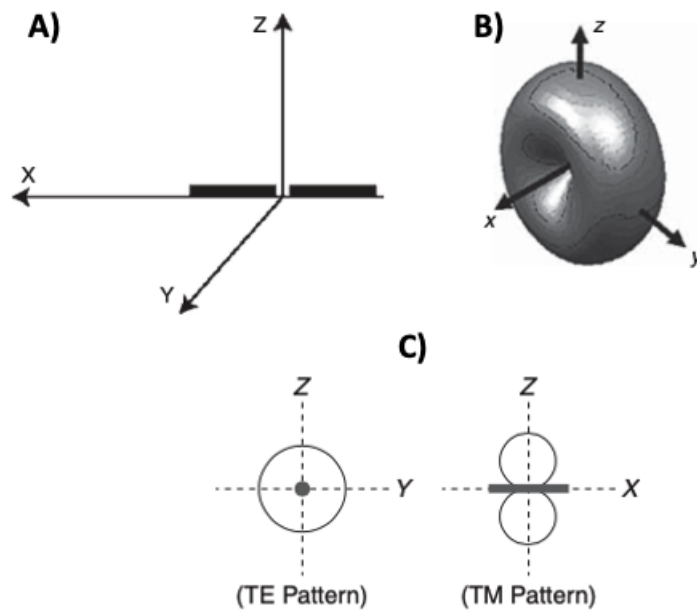


Figure 3.7: A) System geometry and coordinates for dipole antenna. X - Y plane represents the ground surface when the antenna is placed on the ground. B) 3-D model of small electric dipole. The pattern is a donut-like shape in a uniform material. No radiation is emitted from the ends of the dipole. C) Orthogonal cross sections through the 3-D dipole pattern showing the TE (H plane) or TM (E plane) directivity patterns. Modified after [68].

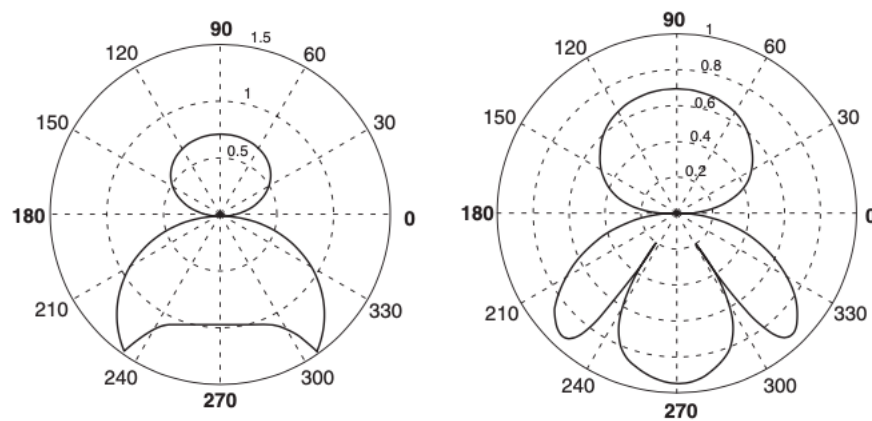


Figure 3.8: TE and TM patterns of dipole antenna that change dramatically when the dipole is put in contact with the surface. This two pattern showed here are for a general ground permittivity of 3.2. Image from [68].

3.3.2 Shielding

Ground-penetrating radar antennas are often placed near the air-ground contact, and a shield is used to surround the antenna when necessary. This shielding is dedicated to avoid the emission of energy in air and to avoid recording signals travelling in air.[4]. Referring to the Fig.(3.9), the primary goals of antenna shielding design are to maximize energy focused on path AA' to and from the subsurface target, minimize

direct transmitter-to-receiver energy on path B , minimize energy escaping into the air along path CC' , and minimize external noise indicated by signals D . Despite the numerous advantages of shielding, there are certain disadvantages to consider. The shielding involves a structure with an EM response, causing energy to travel from the transmitting antenna to both the transmitter and receiving antenna shields before reaching the receiving antenna itself. As a result, significant shielding-generated signals may reverberate for an extended period, leading to a considerable increase in the system ring-down.

In addition to these challenges, effective shielding leads to larger transducer size, increased weight, and higher manufacturing costs. Consequently, antenna shielding can sometimes introduce more issues than it resolves. As a result, many practitioners prefer unshielded antenna configurations, especially when dealing with lower frequencies where size and weight play crucial roles. In contrast, shielded antennas are more commonly utilized in higher-frequency GPR systems, typically above 100 MHz, where antennas are smaller. In these cases, tight ground coupling is integrated into the shielding design to minimize signal leakage into the air.

Practical considerations for antenna shielding are essential to keep in mind. Regardless of claims made, shielding is never perfect. Some GPR applications do not require shielding; open sites can achieve the highest fidelity and maximum depth of penetration without shielded antennas. Even with an ideally designed shield, there remains the possibility of spurious signal leakage, which may occasionally mislead even experienced GPR users in their interpretations. Thus, careful analysis and thoughtful decision-making are imperative when determining the need for and implementation of antenna shielding in GPR applications.

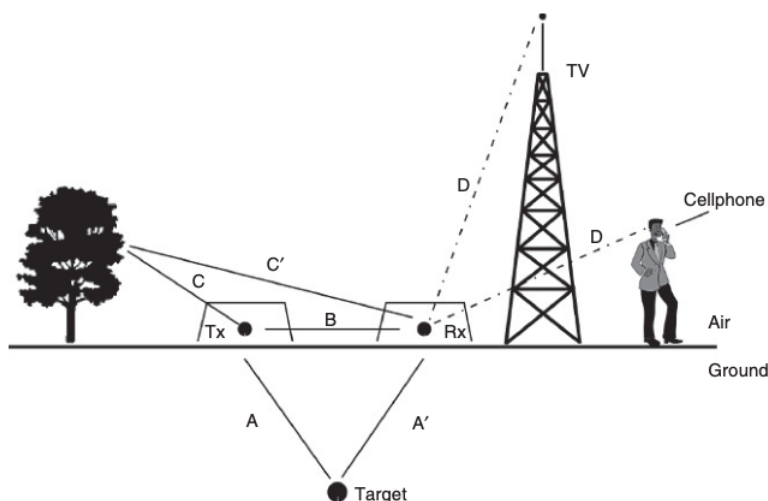


Figure 3.9: GPR system both transmits and detects radio waves. There are several different signals and routes, and the goal is to optimize the intended responses while minimizing others. Image from [4].

Without shielded antennas, open sites can achieve excellent fidelity and greatest depth of penetration. Even with the best shielding, spurious signal leakage is possible, which can occasionally deceive even experienced GPR users.

3.4 Energy losses and attenuation

The energy of EM pulses that propagate from the antennas through the medium is subjected to the attenuation process which follows an exponential law. There are two main factors that cause energy losses. The energy *absorption* of the media in which the signal propagates and the *scattering*. The first is defined as an intrinsic process since it is strongly related to the electromagnetic properties of the medium; the latter depends on dimensions and geometry of scatterers and the wavelength of the signal. Scattering attenuation is also known as volume scattering [83] since it is produced by discrete particles in a background dielectric medium that is otherwise homogeneous. In contrast with the volume scattering there is the surface scattering phenomenon that happens at a continuous surface interface between two dielectrically differing media. In the context of GPR survey the first two mechanisms of dissipation are relevant. The surface scattering plays a major role for radar applications on Earth Observations and Space Explorations.

Intrinsic attenuation (absorption): when a dielectric material is under the influence of an electric field the absorption process is a result of the conduction current and the displacement current. The first depends on the properties of the external field while the latter depends on the rate of change of the alternating field. The intrinsic attenuation is commonly described by loss tangent $\tan\delta$, that is defined as the ratio of conduction to displacement currents in a material. The intrinsic dispersion and its relation with the loss tangent is deeply discussed in chapter (2), section (2.3.4).

Scattering attenuation: The subsurface is generally a non-uniform medium that is characterized by heterogeneities that act as scatterers. The small scale scatterer generates weak reflections in all directions that are undetectable from the receiving antenna. This process dissipates part of the EM energy that is then absorbed by the medium through the ohmic dissipation. The scattering dissipation follows an exponential law as a function of distance r [12]

$$E = E_0 e^{-\alpha_s r} \quad (3.8)$$

where α_s is the scattering attenuation coefficient derived by [4] that depends on the scattering cross-section A . and the number of scatterers per unit volume N .

$$\alpha_s = \frac{NA}{2} \quad (3.9)$$

The scattering attenuation, is a highly frequency-dependent phenomenon and when the scattering is produced by small scale scatterers it is called Rayleigh scattering process, where A in eq.(3.9) is known as Rayleigh cross-section:

$$A = Ca^6 f^4 \quad (3.10)$$

where C is a constant ($1/m^4 Hz^4$), a is the radius of a sphere, the geometrical factor of the scatterers, and f is the central frequency of the radar signal [68].

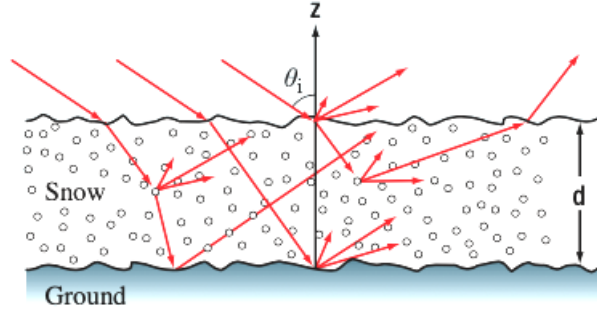


Figure 3.10: The scattering attenuation is caused by small heterogeneities present into the medium that reduce the energy of the transmitted signal. Image from [83].

Surface attenuation: In the context of radar observations the roughness of a surface is depicted in terms of statistical parameters, measured in unit of wavelength λ of the incident signal. The standard deviation of the surface height variation s (rms height) and the surface correlation length l are the main parameters to describe roughness [83]. Using the parameter s and the wavelength λ the electromagnetic roughness parameter is defined as follow:

$$k_s = \frac{2\pi}{\lambda} s \quad (3.11)$$

The roughness on a surface can be categorized by the Rayleigh criterion which allows to define when a surface is considered smooth from electromagnetic point of view. In Fig.(3.11) is shown the effect of surface roughness for normal and oblique incidence. For the first scenario, if the surface was completely flat the electric fields of the two reflected rays would have been in phase if the surface had been entirely flat, but because the rough surface is higher at point B than at point A by a height h , the field of the reflected ray at point B travels a shorter distance by $2h$. The phase difference for the case In Fig.(3.11A) is equal to $\Delta\phi = 2kh = 4\pi h/\lambda$ where $k = 2\pi/\lambda$. On the other hand, the phase difference for the oblique incidence at angle ϑ is equal to $\Delta\phi = 2kh\cos\vartheta$.

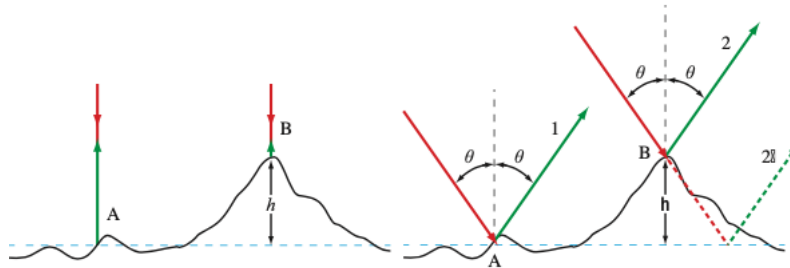


Figure 3.11: (a) normal incidence, (b) oblique incidence. Modified from [83].

According to Rayleigh roughness criteria, a surface can be considered smooth when $\Delta\phi < \pi/2$. This condition is equivalent to $h < \frac{\lambda}{8\cos\vartheta}$. For a general surface that is defined by *rms* s , the Rayleigh criterion is equal to:

$$s < \frac{\lambda}{8\cos\vartheta} ; \text{ and } k_s < 0.8 \text{ if } \vartheta = 0. \quad (3.12)$$

This criterion is valid for a first order classification roughness-smoothness but for more detailed and complex models, a more sharp criterion is required. The Fraunhofer criterion, which define the far-field distance of the antenna, requires that the maximum phase difference between electric field rays from the center and the edge of the antenna must be less than $\pi/8$ radians.

The Fraunhofer criterion is shown in eq.(3.13):

$$s < \frac{\lambda}{32\cos\vartheta} ; \text{ or } k_s < 0.2 \text{ if } \vartheta_i = 0. \quad (3.13)$$

3.5 Survey acquisitions

GPR surveys can be performed using various acquisitions modes and geometries, each designed to capture specific information about subsurface structures and features. At first, we can distinguish between two types of GPR surveys, reflection and transillumination. Here are briefly described the surveys acquisition modes that are classified as reflection surveys. The transillumination surveys are less common and are generally emplaced to study boreholes for engineering studies. The reflection data acquisition modes include:

Common offset: The transmitter and receiver are set at a fixed distance and move over the surface simultaneously in common offset mode operation. In a radargram display, the two wave travel times of the EM pulses that travel through the subsurface are presented on the vertical axis, while the distance the antennas have traveled is displayed on the horizontal axis.

Common source: this configuration comprises a fixed transmitter and a moving receiver, increasing the offset for each acquisition. This is also called wide-angle reflection and refraction sounding. This particular configuration is suitable in areas where subsurface reflectors are planar.

Common receiver: same configuration of the common source point but inverting receiver and transmitter antennas. Fixed receiver and movable source increasing the offset at each acquisition.

Common midpoint: the transmitter and receiver are positioned equidistant from the midpoint of the survey line.

3.6 Data visualization

Data visualization is a critical aspect of the GPR data analysis process, enabling the possibility to interpret and comprehend subsurface structures and features effectively. Visualization techniques play a vital role in transforming raw GPR data into informative and visually understandable representations, aiding in subsurface imaging, anomaly detection, and geophysical investigations. One-dimensional, two-dimensional,

and three-dimensional visualization techniques provide valuable insights into subsurface structures

A-scan: short for "Amplitude-scan," is a 1-D visualization technique that plots the amplitude of the received radar signal as a function of time. It represents the strength of reflections as a function of travel time and provides information about subsurface layers and objects for a single survey point. A-scan data are collected by stationary measurement, placing the antennas above the position of interest.

B-scan: also known as "Depth-slice" or "Time-slice," is a 2-D data visualization method that displays signal amplitude as a function of both time and position. It presents a cross-sectional view of the subsurface at a specific depth level, showing the variations in radar reflections along a designated line or profile.

C-scan: the GPR signal amplitude is plotted against position for a specific time window. It provides a plan view of the subsurface data, allowing researchers to visualize the distribution of reflections over an area. C-scans are commonly used to create 2-D images or maps of subsurface features, showing the spatial arrangement of anomalies and structures at a particular depth level.

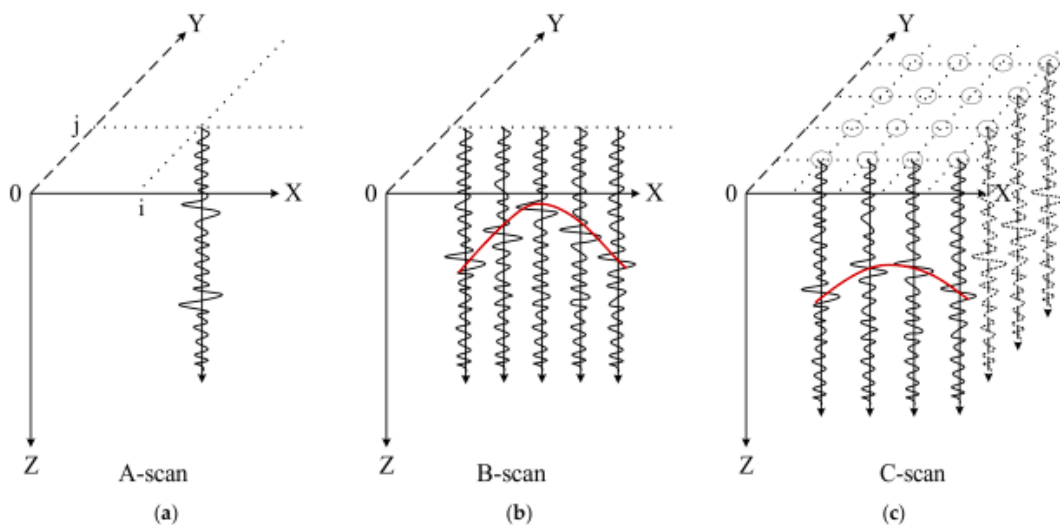


Figure 3.12: Ground Penetrating Radar different radargrams visual presentations: (a) A-scan, (b) B-scan, (c) C-scan. Image from [70].

3.7 Radar for space exploration

The remote sensing technique of investigation is by far the most suitable methodology that grant to study remote regions of the Solar System. Radar systems for planetary exploration can be mounted on satellites or, depending on current and future space mission objectives, typical ground-penetrating systems are installed on robotic rover vehicles to detect the relative shallow subsurface characteristics of planets and celestial bodies in general. The spaceborne radar can be divided into two categories: Synthetic Aperture Radar (SAR) also known as imaging radar; and sounding radar. They both

are designed on the basic principle of monostatic radar but they differ in frequency, geometry of observation and data processing algorithms. Spaceborne radar are greatly emplaced in the context of space explorations to map the surface of planets and study the subsurface features like on the Moon, Mars, Venus and the icy satellites of Jupiter. We can identify two scenarios of investigations: 1) *dry environments*: rocky crust covered in regolith like the case of Moon and Mars. 2) *non-dry and cold environments*: icy bodies like Europa, Ganymede and Callisto where the surface may present icy mixtures of regolith and grains of ice and saline ice [96]; polar and sub-polar regions of Mars and Moon where polar caps are present [45]; the lunar cold traps in the sub-polar regions [42], where water and CO_2 ice are thought to be present at the surface and buried within the regolith. Very dry and cold environments are favorable for radar explorations since radio waves can penetrate at great depths. The Earth is the only ground-truth reference for terrestrial planets, therefore surface features and processes observed on these bodies can only be interpreted using the Earth as a reference. The information obtained from missions that took place in the last decades has thus helped for the reconstruction of extremely complicated scenarios and drawn the path for future explorations.

| Radar instrument | Type of signal | Antenna central frequency (MHz) | Bandwidth (MHz) | Vertical resolution in free space (m) | Altitude (km) | Mission | Target | Year of launch |
|------------------|----------------|---------------------------------|-----------------|---------------------------------------|---------------|-----------------------------|---------------------------------|----------------|
| ALSE | chirp | 5/16 158 | 0.5/1.6 16 | 150/50 5 | 110 | Apollo 17 | Moon | 1972 |
| MARSIS | chirp | 1.8/3/4/5 | 1 | 150 | 400–800 | Mars Express | Mars | 2003 |
| SHARAD | chirp | 20 | 10 | 15 | 300 | Mars Reconnaissance Orbiter | Mars | 2007 |
| LRS | chirp | 5 | 2 | 75 | 100 | Kaguya | Moon | 2007 |
| CONCERT | impulse | 90 | 10 | 30 | 10–100 | Rosetta (orbiter/lander) | 67P/Churyumov-Gerasimenko comet | 2004 |
| MOSIR | chirp | 2.5/17.5–40 | 5–20 | 30–7.5 | 265–800 | Tianwen-1 | Mars | 2020 |
| RIME | chirp | 9 | 1/3 | 50/150 | TBD | JUICE | Jupiter icy moons | 2023 |
| REASON | chirp | 960 | 110 | 150 15 | TBD | Europa Clipper | Europa | 2024 |
| SRS | chirp | 9 | 6 | 20 | TBD | EnVision | Venus | 2031 |

Table 3.1: Characteristics of orbiter radar sounder emplaced for space explorations, from [109].

| Radar instrument | Type of signal | Antenna central frequency (MHz) | Bandwidth (MHz) | Vertical resolution in free space (m) | Step size (m) | Mission | Target | Year of launch |
|------------------|----------------|---------------------------------|---------------------|---------------------------------------|------------------|--------------------|------------------------------|----------------|
| LPR | impulse | 60 500 | 40 500 | ~ 6 ~ 0.5 | ~ 0.08 ~ 0.04 | Chang'e-3 | Moon: Mare Imbrium | 2013 |
| LPR | impulse | 60 500 | 40 500 | ~ 6 ~ 0.5 | ~ 0.08 ~ 0.04 | Chang'e-4 | Moon: Von Karman crater | 2018 |
| LRPR | impulse | 2000 | 2000 | ~ 0.1 | - | Chang'e-5 (lander) | Moon: Oceanus Procellarum | 2020 |
| RIMFAX | FMCW | 375 675 | 150–600 150–1200 | ~ 0.3 ~ 0.15 | 0.05/0.1 | Mars 2020 | Mars: Jazero crater | 2020 |
| RoPeR | chirp | 55 1300 | 15–95 450–2150 | ~ 2 ~ 0.1 | 0.5 | Tianwen-1 | Mars: Utopia Planitia | 2020 |
| WISDOM | step frequency | 500– 3000 | 2500 | 0.11 | 0.1 | ExoMars | Mars | 2022 |

Table 3.2: Characteristics of GPR mounted on rovers, from [109].

3.8 Moon radar missions

In the last 5 decades 5 missions have employed the radar instrument to study the Moon. We are on the edge of a new era of discovery thanks to sophisticated technologies and

novel data-processing methodologies. The next generation of planetary exploration geophysicists will face an interesting task in the next decades.

Apollo 17 ALSE : In 1972 during the Apollo 17 mission, the Apollo Lunar Sounder Experiment (ALSE) marked a pioneering achievement in space exploration, representing the inaugural utilization of radar sounder technology during space missions. ALSE played a pivotal role as part of the instrumentation aboard Apollo 17, facilitating a comprehensive investigation of both the lunar surface and its interior. The radar system comprised two High-Frequency (HF) bands, namely 5 MHz (HF1) and 15 MHz (HF2), as well as one Very High Frequency (VHF) band at 150 MHz, each exhibiting a 10% bandwidth with the application of a chirped signal. The ALSE system's design meticulously balanced the need for penetration depth and resolution. To fulfill the primary objective of acquiring data on the upper 2 km of the lunar crust, the radar system relied on long radar wavelengths, capitalizing on the prevailing arid lunar surface conditions. This choice facilitated enhanced radar wave penetration compared to scenarios involving wet lunar rock conditions. To mitigate interference from along-track clutter, the effective antenna footprint was skillfully narrowed through the generation of a synthetic aperture during ground processing. Additionally, surface topography knowledge enabled the identification of clutter stemming from across-track scatterers. All channels were thoughtfully equipped with an automatic gain control (AGC) feature, updating every 30 seconds, to optimize signal allocation within the receiver's dynamic range. The ALSE's capabilities unveiled subsurface structures within the lunar basins of Mare Crisium and Mare Serenitatis. These layering structures were observed in various locations within these basins, affirming their prevalence. Essentially, the basalt constituting these mare basins was inferred to contain these layered structures. Specifically, depths of 0.9 km and 1.6 km beneath the lunar surface were ascertained for Mare Serenitatis, while Mare Crisium exhibited a depth of 1.4 km. Furthermore, a total basalt thickness estimate ranging from 2.4 – 3.4 km was determined for Mare Crisium. The findings also yielded valuable insights into lunar wrinkle ridges, supporting the notion that their formation primarily resulted from fault-related motion, [112], [133].

Kaguya LRS : The Kaguya project, formally known as the Selene lunar orbiter, was launched by Japan's space agency, JAXA, in 2007. This cutting-edge spacecraft used an innovative sensor called the Lunar Radar Sounder (LRS) to probe the lunar subsurface down to a depth of around 1 – 2 km. The LRS has a central frequency of 5 MHz and a bandwidth of 2 MHz, making it ideal for determining subsurface stratification with a space resolution of 75 m. The fundamental technique of LRS apparatus is based on plasma waves and sounder experiments that have been developed through observations of the earth's magnetosphere, plasmasphere, and ionosphere, [105], [109]. The LRS on the Kaguya mission meticulously explored the Moon's surface, focusing on the Mare Imbrium region, revealing subsurface stratifications of the nearside maria, [106], the deepest reflector at a depth of about 1.05 km and opening an intense debate regarding the lava tubes detection on the moon with remote sensing techniques, [77].

Chang'è 3,4,5 LPR : In the 2013 the China National Space Administration (CNSA) launched Chang'E-3 (CE-3) mission that marked the the first attempt to employ

the GPR on a rover to explore an extraterrestrial body. The Lunar Penetrating Radar (LPR) aboard Yutu operated at frequencies of 60 MHz and 500 MHz [65]. The high-frequency GPR observations unveiled intricate subsurface details to depths of approximately 10 meters. Despite collecting some data, the rover encountered difficulties navigating lunar regolith and became immobile after covering about 100 meters.

On January 3, 2019, the Chang'E-4 (CE-4) lander executed a successful landing on the eastern floor of Von Karman crater, marking the first spacecraft to safely touch down on the Moon's far side [80]. The CE-4 mission, initially designed for a three-month duration, continues to operate effectively after more than three years, with the Yutu-2 rover having acquired approximately 1400 meters of radar data. This instrument mirrors the dual-frequency GPR system utilized by CE-3, functioning at 60 MHz (low frequency) and 500 MHz (high frequency). The frequency bandwidths for these frequencies are 40–80 MHz and 250–750 MHz, respectively [133]. Both missions share common objectives: estimating lunar regolith depth and deciphering subsurface lunar structure along the rover's path. Nonetheless, interpreting low-frequency data remains a challenge due to antenna interactions with both the rover and lunar surface, as well as the limited length of the radar profile [109].

The Chang'E 5 lunar sample return mission was launched in November 2020. A distinct variant of GPR was put to the test. The mission involved a rover landing in the Oceanus Procellarum region, comprising a lander with a primary focus on extracting lunar soil samples and facilitating their return to Earth through a modular system, including an ascender, orbiter, and returner [21]. The Lunar Regolith Penetrating Radar (LRPR), integrated into the CE-5 mission, featured a stationary array of 12 fixed high-frequency antennas positioned at the base of the lander, encircling the drilling apparatus at an elevation of approximately 90 cm above the lunar surface. Each of these antennas can both transmit and receive signals. Consequently, when one antenna was in transmission mode, the remaining 11 operated in receiving mode. The mission's objective revolved around constructing a comprehensive image of the regolith's structure within the drilling zone before commencing the sample extraction process. This was achieved by employing a multi-view and multi-static configuration. The radar effectively captured the intricate details of roughly 2 meters of lunar regolith, providing insights into the distribution of lunar fines and rock fragments [130]. The culmination of this mission resulted in the successful return of 2 kg of lunar soil to Earth on December 2020.

Chapter 4

Electromagnetic mixing models

The anhydrous powders simulants that are tested in this work are made of grain of different rocks and minerals that are mixed with volumes of air trapped within the pores. For this reason, they are also called heterogenous mixtures. The shallow subsurface of planetary bodies are mixtures that are made up of different components and fragments of different densities; and the overall mixtures volume is described with macroscopical averaged values of physical properties. For radar and remote sensing applications, the EM properties of powders that cover large portions of surfaces are quite different than the solid sample and the interaction of the EM radiation is strictly linked to several factors as the dimension of grains, shape, orientations and the incident wavelength. Dielectric investigations of heterogenous mixtures are significant for understanding the interactions of radiation with planetary mixtures and for improving the interpretation of radar data, like the detection of buried materials like water ice.

For certain physical parameters the process of homogenization is quite simple through the averaging process of physical parameters of the different phases present into the mixtures; but for others the discussion is more complicated. For EM properties as the permittivity of dielectric material we can use several mixing rules that are introduced in order to exploit an homogeneous description even for heterogeneous mixtures. With those formulas we can extract the effective parameters like ε_{eff} that are always intended as the relative complex quantity if not differently stated. In these scenario, this chapter aims to present the most common EM mixing rules used in literature that are also discussed and used in the analysis of this work. The intent of this chapter is not to rigorously derive mixing formulas, but to give a general description of them. Various mixing theories address the microstructure of the mixture, while others focus on averaging properties to minimize the impact of small fluctuations on the effective permittivity. While several equations have explicit constraints on their applicability, many exhibit similar behavior when applied to a specific mixture as they make general assumptions about the structure of a mixture. As a result of the inherent complexity at microscopic scales, choosing the best equation to describe a macroscopic system of heterogeneous mixtures is challenging. The majority of the content of this chapter is taken from [126]. In the following discussions, the powder samples present two mixture phases: the inclusion phase that is described by ε_i and volume fraction f ; while the phase environment is characterized by ε_e and volume fraction $(1 - f)$. In this context, the inclusions are the grains of regolith while the environments is the air when the regolith is anhydrous; or the liquid water/water-ice when the samples are frozen-saturated.

4.1 Maxwell-Garnett

One of the oldest and most often used mixing theories is the Maxwell-Garnett (MG) rule. Consider a simple mixture in which spherical inclusions with permittivity ε_i filling random places in the host environment of permittivity ε_e . The MG formula is also known as the Lorenz-Lorentz equation, Clausius-Mossotti formula, or the Rayleigh equation. It was developed in 1904 to explain the observed properties of metal spheres enclosed in liquid, and it was later expanded to the broader dielectric situations.

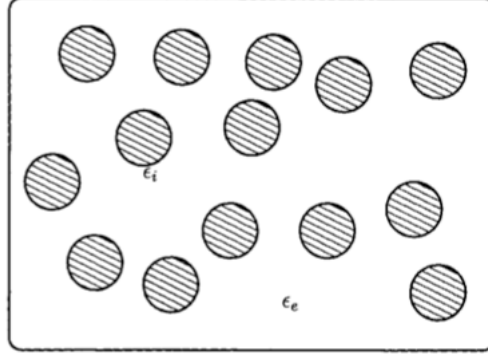


Figure 4.1: Simple two-phase mixture where spherical inclusion of permittivity ε_i are within the host matrix of permittivity ε_e .

$$\varepsilon_{eff} = \varepsilon_e + 3f\varepsilon_e \frac{\varepsilon_i - \varepsilon_e}{\varepsilon_i + 2\varepsilon_e - f(\varepsilon_i - \varepsilon_e)} \quad (4.1)$$

The effective permittivity of the mixture can be derived from the averaged volume electric flux density using the corresponding volume fraction for each phase:

$$\langle \mathbf{D} \rangle = \varepsilon_{eff} \langle \mathbf{E} \rangle \quad (4.2)$$

$$\langle \mathbf{D} \rangle = f\varepsilon_i \langle \mathbf{E}_i \rangle + (1-f)\varepsilon_e \langle \mathbf{E}_e \rangle \quad (4.3)$$

$$\langle \mathbf{E} \rangle = f \langle \mathbf{E}_i \rangle + (1-f)\varepsilon_e \quad (4.4)$$

ε_{eff} is given by the ratio between the flux density and the electric field, assuming that the quantities ε_i and E_e are constant:

$$\varepsilon_{eff} = \frac{Af\varepsilon_i + (1-f)\varepsilon_e}{Af + (1-f)} \quad (4.5)$$

where the quantity $A = 3\varepsilon_e/(\varepsilon_i + 2\varepsilon_e)$ is given by the ratio of internal and external field $\mathbf{E}_i/\mathbf{E}_e$. Eq.(4.1) is clearly asymmetric, the inclusion and environment phases do not contribute equally to the effective permittivity of the mixture.

The inclusions can also be thought as dipole moments which average into the dielectric polarization \mathbf{P} . The Clausius-Mossotti (CM) formula simply express MG rule from a microscopic point of view. Assuming that the polarizability of a spherical inclusions of volume V is expressed as eq.(4.7), the CM formula allows to express the effective permittivity of a mixture with spherical inclusions as:

$$\frac{\varepsilon_{eff} - \varepsilon_e}{\varepsilon_{eff} + 2\varepsilon_e} = \frac{\alpha n}{3\varepsilon_e} \quad (4.6)$$

where n is the number density of the dipoles, (m^{-3}).

$$\alpha = V(\varepsilon_i - \varepsilon_e) \frac{3\varepsilon_e}{\varepsilon_i + 2\varepsilon_e} \quad (4.7)$$

4.2 Mixing bounds

The MG rule established the analysis of individual free scatterer responses. In the case of mixtures, the inclusions were assumed to be influenced by the local field, which was estimated using the average polarization. However, the real mixtures often exhibit completely random structures. This might appear contradictory when applying the approach employed so far. Given the complexity of the mixture systems, it is more convenient considering loose boundaries that cannot be exceeded regardless of the volume fractions and geometries that the phases establish. In this context it is reasonable to assume that the effective permittivity of the two-phase composite mixture is included between the minimum and maximum values of the permittivities of the individual phases:

$$\min\{\varepsilon_e, \varepsilon_i\} \leq \varepsilon_{eff} \leq \max\{\varepsilon_e, \varepsilon_i\} \quad (4.8)$$

The most general boundaries are the Wiener bounds that can be retrieved with a circuitual approach, considering the two-phases as capacitors connected in parallel or series circuit:

$$\varepsilon_{eff,min} = \frac{\varepsilon_e \varepsilon_i}{f\varepsilon_e + \varepsilon_i(1-f)} \quad (4.9)$$

$$\varepsilon_{eff,max} = f\varepsilon_i + \varepsilon_e(1-f) \quad (4.10)$$

The Wiener bounds are absolute boundaries since retain the max and min character independently of the mixture type: the max value occurs for both scenarios $\varepsilon_i \leq \varepsilon_e$ and the same also applies for the min value. But other stricter bounds were proposed and they are called Hashin-Shtrikman bounds, that can be applied when assumption of isotropic mixture is made. The formal derivation of these two bounds is not given in this section but the minimum and maximum values can be obtained with MG formula for isotropic spherical inclusions switching $\varepsilon_i \rightarrow \varepsilon_e$ and $f \rightarrow (1-f)$.

$$\varepsilon_{eff,1} = \varepsilon_e + 3f\varepsilon_e \frac{\varepsilon_i - \varepsilon_e}{\varepsilon_i + 2\varepsilon_e - f(\varepsilon_i - \varepsilon_e)} \quad (4.11)$$

$$\varepsilon_{eff,2} = \varepsilon_i + 3(1-f)\varepsilon_i \frac{\varepsilon_e - \varepsilon_i}{\varepsilon_e + 2\varepsilon_i - (1-f)(\varepsilon_e - \varepsilon_i)} \quad (4.12)$$

where eq.(4.11) represents the ordinary scenario of inclusion of permittivity ε_i within the environment of permittivity equal to ε_e while eq.(4.12) is the opposite case of inclusion ε_e into a matrix of ε_i . Fig.(4.2) shows the two boundaries. The mixing bounds presented in this section are employed into the discussion of data analysis, and depending on the specific scenario, either broader or more stringent limits are applied as per the case under consideration.

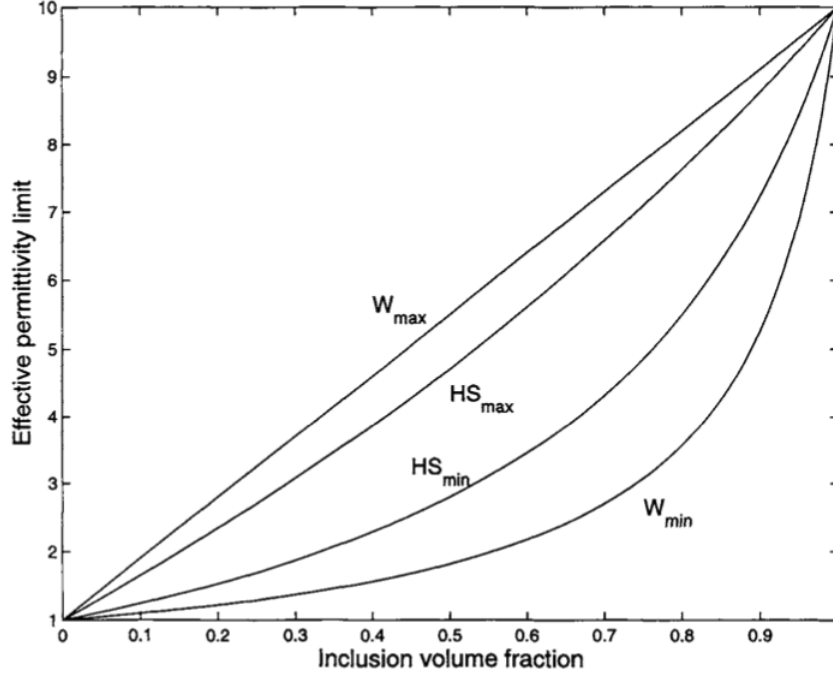


Figure 4.2: Wiener and Hashin-Shtrikman min and max boundaries presented for the effective permittivity of mixtures. Wiener bounds are wider while the HS bounds can also be expressed by MG rule exchanging inclusions and environment parameters. Figure taken from [126]

4.3 Power-laws

There is a family of mixing equations that determine the effective permittivity by averaging the contributions based on volume weights. The eq.(4.13) represents the generalized form of power laws where β is the power that changes the weights of each phase and produce different models for the description of the mixture.

$$\varepsilon_{eff}^{\beta} = f\varepsilon_i^{\beta} + (1 - f)\varepsilon_e^{\beta} \quad (4.13)$$

A common aspect of these mixing equations is that they often do not account for the exact geometrical shape of different phases within the mixture, such as the particle shape of inclusions. Because these equations do not take into account the polarization of isolated inclusions, they tend to produce greater estimates for the effective permittivity of a mixture when the volume fractions of inclusions are low.

4.3.1 $\beta = 1$ (Linear)

The linear model is the Wiener upper bound discussed above, and it is also known as Silberstein formula or Browns formula. It provides the maximum value of ε_{eff} . The composition of a mixture is generally more complex than what the linear law describes. As a result, this equation is an extreme example of first order approximation of the effective permittivity of a mixture and is rarely used to model physical systems.

$$\varepsilon_{eff} = f\varepsilon_i + (1 - f)\varepsilon_e \quad (4.14)$$

4.3.2 $\beta = 1/2$ (CRIM)

This model found its roots in optical physics, specifically aiming to describe the refractive index of a mixture composed of non-magnetic gases. A similar approach independently emerged within specific models that deal with the propagation of plane waves through materials with varying dielectric properties. In a larger sense, the CRIM equation defines the refractive index of mixtures without magnetic properties, defining it as a simple average of the refractive indices of its constituent parts. This model is also known as the "Time-Propagation model."

$$\sqrt{\varepsilon_{eff}} = f\sqrt{\varepsilon_i} + (1 - f)\sqrt{\varepsilon_e} \quad (4.15)$$

4.3.3 $\beta = 1/3$ (LLL)

The Looyenga-Landau-Lifshitz Formula (LLL), which represents the effective permittivity of a mixture, was separately developed by Looyenga in 1965 and Landau and Lifshitz in 1960. The key concept in both derivations focuses around a system composed of two components. When compared to the effective permittivity of the total combination, these components have slightly greater permittivities and slightly lower permittivities ($\pm\delta\varepsilon$). The entire mixture's effective permittivity is then determined as a volumetric average of these two constituent components, which are themselves mixtures of materials. Both derivations assume that the difference in dielectric characteristics between the phases of the mixture is modest. The equation is independent of particle shape or internal structure since the derivation does not take into account the shape or structure of the particles. The LLL model does not exhibit a percolation threshold since the arrangement and position of the mixture components with regard to each other are not considered, and the dielectric contrast is assumed to be small.

$$\varepsilon_{eff}^{1/3} = f\varepsilon_i^{1/3} + (1 - f)\varepsilon_e^{1/3} \quad (4.16)$$

4.3.4 $\beta = 0$ (Lichteneker rule)

The original derivation of the formula, proposed by Lichtenecker in 1926, is considered semi-empirical due to its poor theoretical base. The Lichtenecker-Weiss formula was then derived as a particular instance involving a uniform distribution of particles in their broader derivation of generic power law equations with inclusion shapes following a beta function distribution and it can also be derived directly from Maxwell's equations and the charge conservation principle, with random spatial distribution of inclusions. These later derivations emphasize that the effectiveness of applying the formula hinges on how well the mixture conforms to a randomly distributed inclusion pattern.

$$\varepsilon_{eff} = \varepsilon_i^f + \varepsilon_e^{(1-f)} \quad (4.17)$$

Chapter 5

Chemical and mineralogical characterization of lunar regolith analogues

This chapter aims to gather all of the general characteristics of the lunar regolith analogs that are studied in this work, as well as the manufacturer's reference datasheets for chemical and mineralogical composition. The results of measurements made in the lab, such as the samples' grain density via mean of pycnometer, are also provided here. The University of Florence graciously contributed the grain size distribution and mineralogical analyses that were achieved by means of SEM-EDS and are described here. The quality of these samples is also discussed at the chapter's final section.

5.1 Lunar regolith analogues

Lunar simulants are laboratory-created products using terrestrial and meteoritic materials to simulate one or more physical/chemical characteristics of lunar rocks or soils. Synthetic materials, such as glasses, metals, and minerals, may also be added to the final composition to achieve a product with qualities closely resembling those of lunar materials [124]. The need to create laboratory simulants arises from the necessity to conduct testing and measurements for In-Situ Resource Utilization (ISRU) and future lunar missions [131]. Approximately 13000 lunar samples have been collected during lunar missions, but they are deemed too precious to be compromised or contaminated by destructive laboratory tests. Despite the requirement for lunar simulants to be chemically similar to lunar soils in terms of mineralogy, particle size distributions, and mechanical features, large-scale production with consistent characteristics remains difficult. To date, the list of produced simulants is extensive, with several companies commercializing such products to facilitate broader dissemination and promote research and development in the field of space exploration. This work aligns with the context of the Melody project, funded by the Italian National Institute of Astrophysics (INAF), which facilitated the acquisition of 9 lunar regolith simulants for analysis in this study. The reasons behind the purchase of these products were the need for lunar highland and mare simulants, preferably with varying grain sizes. These specific products (summarized in Table 5.1) were chosen as they reflect these characteristics and were the only available options in the market in 2021. The existing list of lunar simulants is extensive, and new products are continually developed to

address the growing demand and diverse requirements for research and development. A detailed list containing all existing lunar simulants updated at December 2023 is reported in Tab.(5.2) provided by the Colorado School of Mines CSM Planetary Simulant Database at <https://simulantdatab.com/index.php>. The Database presents all the planetary simulants present on the market, all the general information about mineralogy and chemistry of the samples. It also provides the availability on the market and the fidelity. Fidelity is an arbitrary and subjective parameter, the definition and standards of which vary depending on the individual establishing them. In this specific case, the CSM Database categorizes simulants as follows:

- **Basic:** A single type of rock that has been crushed into a powder. It is possible that the chemistry or mineralogy of reference materials will not be reproduced precisely. Many of these are referred by the term "geotechnical simulants" despite though their geotechnical characteristics have not been altered to achieve great accuracy.
- **Standard:** Crushed anorthosite with or without additional elements, crushed to a representative particle size distribution, for lunar highlands. For lunar mare, a basaltic material crushed to a representative particle size distribution, with or without additional components. A basaltic feedstock (or individual silicates) combined with secondary oxides and/or salts for Mars. The mineralogy or physical properties of asteroids are extremely accurate.
- **Enhanced:** A product that fits the "Standard" specification and contains synthetic agglutinates (rather than just glass) for lunar simulants. A simulant with perfectly accurate mineralogy and a representative particle size distribution for Mars. Both the mineralogy and physical properties of asteroids are extremely precise.
- **Specialty:** This category includes dust simulants as well as simulants that replicate properties including lunar volatiles, nanophase iron, and so on.

| EXOLITH LAB | Type of analogue |
|----------------------------|---|
| LHS-1 | <i>Lunar Highland simulant</i> |
| LHS-1D | <i>Lunar Highland Dust simulant</i> |
| LMS-1 | <i>Lunar Mare simulant</i> |
| LMS-1D | <i>Lunar Mare Dust simulant</i> |
| ASTROPORT | |
| LCATS-1 | <i>Lunar Mare simulant</i> |
| OFF PLANET RESEARCH | |
| OPRH2N | <i>General Nearside Highland simulant</i> |
| OPRH3N | <i>General Farside Highland simulant</i> |
| OPRL2N | <i>General Mare simulant</i> |
| OPRL2NT | <i>Higher Titanium Mare simulant</i> |

Table 5.1: *Nine Lunar analogues dielectrically tested in this work at varying physical conditions.*

| Lunar Simulants | | |
|------------------------|--|----------------|
| Acronym | Name | Country |
| - | Oshima Simulant | Japan |
| - | Maryland-Sanders Lunar Simulant | United States |
| - | Kohyama Simulant | Japan |
| ALRS-1 | Australian Lunar Regolith Simulant | Australia |
| ALS | Arizona Lunar Simulant | United States |
| BHLD20 | Beijing Highlands Lunar Dust | China |
| BP-1 | Black Point | United States |
| CAS-1 | Chinese Academy of Sciences | China |
| CHENOBI | CHENOBI | Canada |
| CLDS-i | China Lunar Dust Simulant | China |
| CLRS-1/2 | Chinese Lunar Regolith Simulant | China |
| CMU-1 | Carnegie Mellon University | United States |
| CSM-CL | Colorado School of Mines Colorado Lava | United States |
| CSM-LHT-1 | CSM Lunar Highlands Type | United States |
| CSM-LMT-1 | CSM Lunar Mare Type | United States |
| CUG-1A | China University of Geosciences | China |
| CUMT-1 | China University of Mining and Technology Number One | China |
| DNA-1 | De NoArtri | Italy |
| EAC-1 | European Astronaut Centre | Europe |
| FJS-1/2/3 | Fuji Japanese Simulant | Japan |
| GRC-1/3 | Glenn Research Center | United States |
| GSC-1 | Goddard Space Center | United States |
| JLU-U | JLU-H Highland Simulant | China |
| JSC-1 | Johnson Space Center | United States |
| KLS-1 | Korea Lunar Simulant | Korea |
| KOHLs-1/KAUMLS | Korean Lunar Simulants | Korea |
| LCATS-1 | Lunar Caves Analog Test Sites | United States |
| LHS-1 | Lunar Highlands Simulant | United States |
| LMS-1 | Lunar Mare Simulant | United States |
| LSS | Apollo Lunar Soil Simulant | United States |
| MKS-1 | MKS-1 Lunar Simulant | Japan |
| MLS-1/1P | Minnesota Lunar Simulant | United States |
| MLS-2 | Minnesota Lunar Simulant | United States |
| Mooncastle | Mooncastle | United States |
| NAO-1 | National Astronomical Observatories | China |
| NEU-1 | Northeastern University Lunar Simulant | China |
| NU-LHT | NASA/USGS Lunar Highlands Type | United States |

Table 5.2 continued from previous page

| | | |
|--------------------|---|----------------|
| OB-1 | Olivine Bytownite | Canada |
| OPRFLCROSS1 | Off Planet Research LCROSS Simulant | United States |
| OPRH2N/H2W/H3N/H3W | Off Planet Research Highlands Simulant | United States |
| OPRL2N/L2W | Off Planet Research Mare Simulant | United States |
| TJ-1/2 | Tongji University | China |
| TLS-01 | Thailand Lunar Simulant | Thailand |
| TUBS-M | TU Braunschweig Base Simulant Mare | Germany |
| TUBS-T | TU Braunschweig Base Simulant Terrae | Germany |
| UoM-B | University of Manchester – Black | United Kingdom |
| UoM-W | University of Manchester – White | United Kingdom |

Table 5.2: List of the existing lunar simulants from the Colorado School of Mines CSM Planetary Simulant Database at <https://simulantdatab.com/index.php>. List updated at Dec 2023.

Simulants have been employed in this work for conducting dielectric measurements, necessitating a comprehensive literature analysis. Several studies have investigated the dielectric properties of lunar simulants. Some of those are present in the CSM Database, others are powder simulants created by the laboratory itself for this specific purpose. Table (5.3) provides a list of the analyzed samples, the employed frequency, the testing temperature, and the environmental conditions in which the tests were conducted. It is noteworthy that some simulants were also tested by forming mixtures with water ice, and these measurements will be revisited later for comparison with the results obtained in this study.

| Sample | Frequency | Temperature | Env. | Ref. |
|------------------------------------|----------------------------------|-----------------------|--------|-------|
| Regolith powder | 30 Hz-100 kHz | 100, 298 and 373 K | vacuum | [3] |
| JSC1A-AGGL | 1.8 – 3.5 GHz | room T | air | [7] |
| CHENOBI-AGGL | 1.8 – 3.5 GHz | room T | air | [7] |
| NU-LHT-2M-AGGL | 1.8 – 3.5 GHz | room T | air | [7] |
| JSC-1A-AGGL-DUST | 1.8 – 3.5 GHz | room T | air | [7] |
| JSC-1A (no nFe) | 1.8 – 3.5 GHz | room T | air | [7] |
| S09_23 | 1.8 – 3.5 GHz | room T | air | [7] |
| NU-LHT-2M (no nFe) | 1.8 – 3.5 GHz | room T | air | [7] |
| V2-10-146-180-750 UM | 1.8 – 3.5 GHz | room T | air | [7] |
| V2-10-146-106-180 UM | 1.8 – 3.5 GHz | room T | air | [7] |
| S11-3 | 1.8 – 3.5 GHz | room T | air | [7] |
| V2-11-109/110 | 1.8 – 3.5 GHz | room T | air | [7] |
| Synth. Basalt 4% Ti (no nFe) | 1.8 – 3.5 GHz | room T | air | [7] |
| Synth. Basalt 12% Ti (no nFe) | 1.8 – 3.5 GHz | room T | air | [7] |
| Synth. Basalt 16% Ti (no nFe) | 1.8 – 3.5 GHz | room T | air | [7] |
| JSC-1A | 1.7, 2.5, 6.6, and 31.6 GHz | 83-473K | air | [13] |
| JSC-1 | 0.9, 2.2-3.3GHz and 8-12GHz | room T | air | [39] |
| JSC-1A | 0.9, 2.2-3.3GHz and 8-12GHz | 200-316K | air | [39] |
| JSC-1A + water ice | 1 Hz-100 kHz, 20 Hz and 1 MHz | 100-200K | vacuum | [99] |
| JSC-1A + water ice | 50 MHz - 2 GHz | 243 K | air | [10] |
| TALS (from JSC -1A) + water ice | 2.38 and 7.2 GHz | 77K and 303K | air | [14] |
| Regolith powder | 1 mHz - 10 kHz | 181 K | air | [127] |
| Anorthiste | 2-6 GHz | 213, 253 and 293 K | air | [76] |
| Basalt | 2–6 GHz | 213, 253 and 293 K | air | [76] |
| Dunite | 2–6 GHz | 213, 253 and 293 K | air | [76] |
| Ilmenite | 2–6 GHz | 213, 253 and 293 K | air | [76] |

Table 5.3: Dielectric measurements conducted on other lunar regolith simulants that can be found in literature.

5.2 Chemical and mineralogical composition

From this paragraph onward, the chemical and physical properties of the nine simulant samples tested in this study will be detailed. The chemical composition of the lunar regolith simulants are provided by the laboratories that produce the analogues. The Exolith simulants LHS-1 and LHS-1D chemically simulate the lunar highland, they only differ in the grain size where the analogue with the lower grain size is indicated by the "D" that stands for *Dust*. The same goes for the two maria simulants LMS-1 and LMS-1D [79] [78]. The regolith analogues produced by Off Planet Research have a slightly different characterization [113]. The OPRH series are highland simulants, differentiated into near side highland OPRH2N and far side highland OPRH3N. Their chemical composition are not so apart, they differ in the oxide content $FeO+TiO_2$ wt.% where OPRH2N presents 4.2 wt% and OPRH3N has 3.5 wt%, which are also similar to the other highland simulants LHS-1 and LHS-1D. The OPRL series are maria simulants, their oxide content is higher compare to the simulants listed above having 11.14 wt% and 22.92 wt% OPRL2N and OPRL2NT respectively. The LCATS-1 simulant is produced by the Astroport laboratory and it represent a maria analogue. Its chemical composition doesn't show large variation when compared to the other maria analogues, its oxide content ranges between 8–9.5 wt% which is similar to the OPRL2N and quite the double compared to the LMS-1 and LMS-1D. Regarding LCATS-1, the chemical composition provided is given in a range of values which is different from the one found in the literature by the same laboratory. Particularly, the SiO_2 content from [63] is 33.47 wt% that is not reliable for basaltic material (see row six in Tab.(5.4)).

The analysis conducted on the analogues are meant to improve the interpretation of radar data since the simulants provide a wide range of different lunar terrain that can be encountered on the Moon. These investigations are also meant to verify the physical-chemical characteristics that are reported on the related documentation provided by the producers. In some cases we encounter some discrepancies on data and this led us to conduct other geo-chemical analysis to assess the causes of the discrepancies. In the following sections are reported the analysis that have been conducted on the regolith analogues.

| Chemical Composition | | | | | | | | | | | | | | | | | |
|----------------------|---------|---------|-----------|-----------|-------|-------|-------|-------|---------|--------|----------|------|--------|-------|-----------|-------|----------|
| Simulant | SiO_2 | TiO_2 | Al_2O_3 | Fe_2O_3 | FeO | MnO | MgO | CaO | Na_2O | K_2O | P_2O_5 | Cl | SO_3 | SrO | Cr_2O_3 | NiO | TOT(wt%) |
| LHS-1 | 48.1 | 1.1 | 25.8 | 3.7 | - | 0.1 | 0.3 | 18.4 | - | 0.7 | 1 | 0.4 | 0.3 | 0.1 | - | - | 100 |
| LHS-1D | 48.1 | 1.1 | 25.8 | 3.7 | - | 0.1 | 0.3 | 18.4 | - | 0.7 | 1 | 0.4 | 0.3 | 0.1 | - | - | 100 |
| LMS-1 | 40.2 | 7.3 | 14 | 13.9 | - | 0.3 | 12 | 9.8 | - | 0.6 | 1 | 0.4 | - | 0.1 | 0.3 | 0.2 | 100.1 |
| LMS-1D | 40.2 | 7.3 | 14 | 13.9 | - | 0.3 | 12 | 9.8 | - | 0.6 | 1 | 0.4 | - | 0.1 | 0.3 | 0.2 | 100.1 |
| LCATS-1 | 46 | 1 | 14.5 | 3 | 7 | 0.15 | 8.5 | 10 | 2.5 | 0.75 | 0.6 | - | - | - | 0.02 | - | 94.02 |
| | to | to | to | to | to | to | to | to | to | to | to | - | - | - | to | - | to |
| | 49 | 2 | 15.5 | 4 | 7.5 | 0.20 | 9.5 | 11 | 3 | 0.85 | 0.7 | - | - | - | 0.06 | - | 103.31 |
| | 33.47 | 3 | 8.34 | 13.93 | - | 0.17 | 12.03 | 12.66 | 2.2 | 1.32 | 1.17 | - | - | - | - | - | 88.29 |
| OPRH2N | 47.89 | 0.52 | 27.06 | - | 3.68 | 0.06 | 2.84 | 14.19 | 2.43 | 0.25 | 0.2 | - | - | - | - | - | 99.12 |
| OPRH3N | 47.98 | 0.36 | 28.67 | - | 2.69 | 0.04 | 1.96 | 14.71 | 2.36 | 0.18 | 0.14 | - | - | - | - | - | 99.09 |
| OPRL2N | 47.35 | 1.47 | 17.4 | - | 9.67 | 0.16 | 8.1 | 11.08 | 2.83 | 0.69 | 0.58 | - | - | - | - | - | 99.33 |
| OPRL2NT | 40.54 | 10.09 | 15.28 | - | 12.83 | 0.37 | 6.83 | 9.57 | 2.41 | 0.58 | 0.51 | - | - | - | - | - | 99.01 |

Table 5.4: Chemical composition of lunar regolith analogues granted by the laboratories that provided the simulants. Exolith [79][78], Astroport [63], Off Planet Research [113].

| SAMPLE | Basalt | Anorthosite | Pyroxene | Olivine | Ilmenite | TOT(%) |
|---------|--------|-------------|----------|---------|----------|--------|
| LHS-1 | 24.7 | 74.4 | 0.2 | 0.3 | 0.4 | 100 |
| LHS-1D | | | | | | |
| LMS-1 | 32 | 19.8 | 32.8 | 11.1 | 4.3 | 100 |
| LMS-1D | | | | | | |
| OPRH2N | 30 | 70 | - | - | - | 100 |
| OPRH3N | 20 | 80 | - | - | - | 100 |
| OPRL2N | 90 | 10 | - | - | - | 100 |
| OPRL2NT | 75.6 | 10 | - | - | 14.4 | 100 |

Table 5.5: General composition for 8 regolith simulants provided by the producers. For LCATS-1 this information is not provided by Astroport. Regarding the Exolith simulants, the given composition is a mix of minerals and rocks which is not reliable since the basalt emplaced could be made of plagioclase or pyroxene which would affect the mineralogical composition. For the OPR simulants, the producer provided the rocks composition which are basalt and anorthosite mixed at different proportion. For OPRL2NT, to simulate lunar area with higher % of titanium, they also added some ilmenite to the mixture.

5.3 Grain density analysis

The grain density of samples is a required parameters in order to study the dielectric behavior at varying porosity. We tested the regolith analogues with the pycnometer to retrieve ρ_g , listed in Tab.(5.6). For the analogues LMS-1 and 1-D the test was repeated to check the obtained results. According to the chemical composition provided by Exolith [79], the two simulants are the same chemical sample that only differ in terms of grain size particles. If this assumption is true, the results of the pycnometer should overlaps within the measurement uncertainties, but the grain density of LMS-1 and LMS-1D present different values. The discrepancy observed for the LMS-1 and 1-D simulants is probably caused by the sieving process that the dust simulant undergoes to obtain a finer powder, that blocks some heavier particles.

| SIMULANT | ρ_g (g/cm^3) | $\sigma\rho_g$ (g/cm^3) |
|----------|-----------------------|-----------------------------|
| LHS-1 | 2.7850 | 0.0008 |
| LHS-1D | 2.7744 | 0.0017 |
| LMS-1 | 3.0506 | 0.0013 |
| | 3.0599 | 0.0030 |
| LMS-1D | 2.8334 | 0.0021 |
| | 2.8016 | 0.0020 |
| OPRH2N | 2.8154 | 0.0014 |
| OPRH3N | 2.7844 | 0.0016 |
| OPRL2N | 2.8860 | 0.0015 |
| OPRL2NT | 3.0108 | 0.0030 |
| LCATS-1 | 3.1245 | 0.0014 |

Table 5.6: Grain density of the nine lunar regolith analogues under test in this work. We tested the grain density at the Science Department of Roma Tre University. The grain density is a fundamental parameter for the application of mixing formula later discussed in this work.

5.4 Grain size distribution analysis

The nine lunar regolith simulants were sent to the facility *vuLab* of Earth Science Department, Università di Firenze to be tested with a morpho-grainsizer (MGS) Morphologi G3SETM, Fig.(5.1). The MGS is powerful instrument that perform morphometric measurements from which we can obtain the grain size distribution of powder samples. The instrument is set to work in grain size range 1 to 180 μm ; a small volume of powder is inserted into the sample dispersion unit which sprays the particles into a chamber and the optical unit acquires up to 1.200.000 images of particles per hour. This procedure provide a very robust statistics and it also avoid the vitrification process of small particles. The grain size distribution of the simulants are reported in Fig.(5.2).

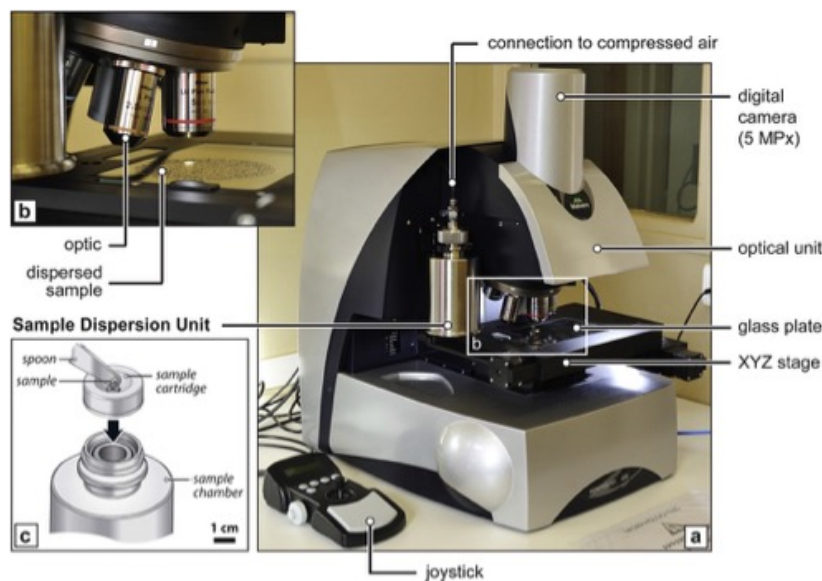


Figure 5.1: A) morpho-grainsizer (MGS) Morphologi G3SETM by Malvern InstrumentTM has been used for morphometric measurements at the *vuLab* of Earth Science Department, Università di Firenze. It requires small volume of material (5mm³). It takes up to 1.200.000 images of particles in about 1 hour. The grain size is limited to 250 μm and grant reproducible dispersion procedure with high efficiency over a wide grain size range (180 to 1 μm)

According to the data sheets provided by the Exolith Lab, the simulants LMS-1 and LHS-1 are characterized by an average grain size of 50 μm and 60 μm respectively, while for the two dust simulants we have an average grain size of 7 μm . Apart from LHS-1, the MGS analysis of the other three analogues show a slightly different average grain size. For the other simulants we can't produce a comparison since the grain size information is not provided by the producers.

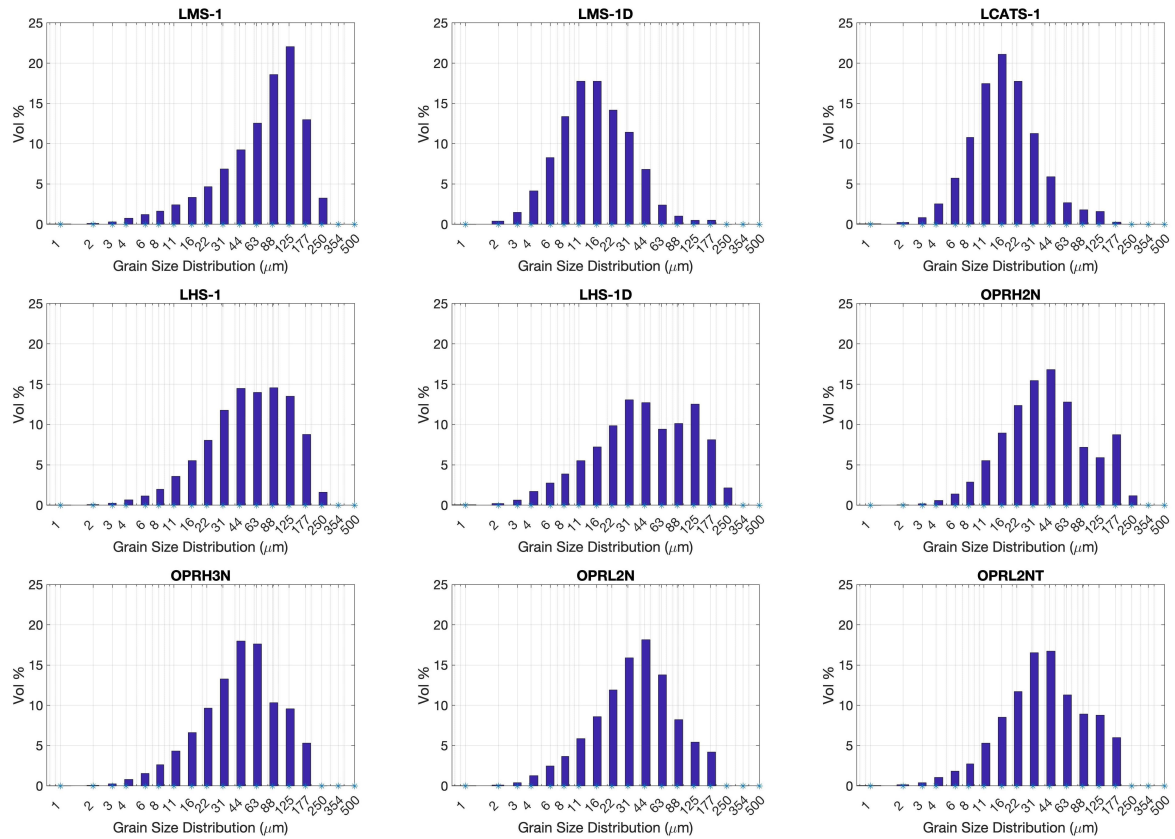


Figure 5.2: Grain size distribution of the nine regolith simulants obtained via means of the morpho-grainsizer instrument.

5.5 Mineralogical analysis

The MGS instrument emplaced for the grain size distribution analysis also allows to prepare 1 inch stab on which the powder sample is sprayed that can be used for mineralogical analysis. The nine simulants were tested with the Energy Dispersive X-Ray Spectroscopy SEM-EDS (instrument EVA MA 15) at the *MEMA* facility of the Università di Firenze.

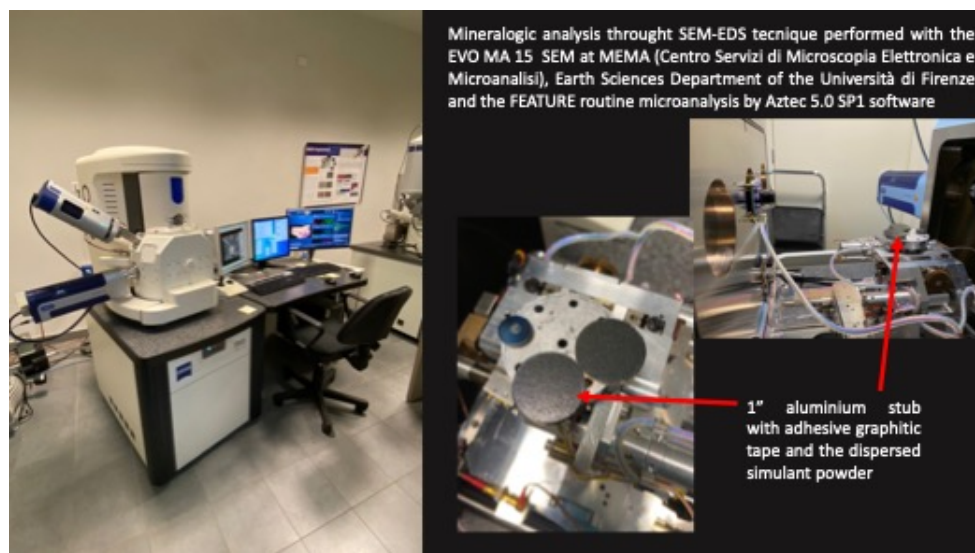


Figure 5.3: The mineralogical analysis were conducted through the SEM-EDS at the Università di Firenze. 1 inch stab of sprayed regolith analogues is prepared with the MGS instrument and then analyzed to address the elemental composition.

The instrument was set to operate in the gran size range $5\ \mu\text{m}$ to $180\ \mu\text{m}$; for each analogue were analyzed 4 areas of $4\ \text{mm}^2$ on the stab and it takes up to 1 night to complete the analysis. The software (Aztec 5.0 SP1) is able to identify between 1500 to 6000 particles in each area, selecting backscattered electron images (BSE) with an appropriate black and white image threshold. The identification of mineralogical classes is possible by setting some simple rules (i.e. ilmenite: $Ti > 20\ \text{wt}\%$, plagioclase: $Al > 20\ \text{wt}\%$, glass: $Si > 40\ \text{wt}\%$). After the feature routing is launched, the microanalysis program scans the recorded area ($2\ \text{mm} \times 2\ \text{mm}$ surface), identifying all particles and assigning each one to a mineral class, creating a morphometric and compositional database, stopping when finish to scan all fields in the selected area or reaching a maximum particles number.

| vol % | | | | | | | | |
|----------|-------------|---------|----------|----------|----------------|-------|----------------|-----|
| SIMULANT | Plagioclase | Olivine | Pyroxene | Ilmenite | Phyllosilicate | Glass | Not classified | TOT |
| LHS-1 | 76.9 | 0.04 | 16.4 | 0.3 | 0.1 | 3.6 | 2.6 | 100 |
| LHS-1D | 78.9 | 0.5 | 15.7 | 0.2 | 0.05 | 2.6 | 2.1 | 100 |
| LMS-1 | 36.1 | 12.5 | 40.5 | 3.8 | 0.5 | 2.1 | 4.5 | 100 |
| LMS-1D | 59.1 | 4.5 | 32.5 | 0.6 | 0.2 | 1.7 | 1.5 | 100 |
| OPRH2N | 74.6 | 0.4 | 19.4 | 0.002 | 3.0 | 0.6 | 2.0 | 100 |
| OPRH3N | 80.1 | 0.6 | 12.1 | 0.01 | 1.6 | 0.7 | 5.0 | 100 |
| OPRL2N | 35.2 | 2.3 | 46.7 | 0 | 12.4 | 0.3 | 3.0 | 100 |
| OPRL2NT | 23.2 | 1.1 | 31.7 | 11.1 | 19.5 | 0.5 | 12.9 | 100 |
| LCATS-1 | 16.7 | 3.1 | 38.1 | 0.9 | 17.2 | 0.4 | 23.6 | 100 |

Table 5.7: Mineralogical composition of the nine simulants obtained with SEM-EDS.

| Simulant | SiO_2 | TiO_2 | Al_2O_3 | FeO | MnO | MgO | CaO | Na_2O | K_2O | P_2O_5 | Cr_2O_3 | NiO | TOT(wt %) |
|----------|---------|---------|-----------|-------|-------|-------|-------|---------|--------|----------|-----------|-------|-----------|
| LHS-1 | 50.92 | 0.58 | 27.94 | 1.39 | 0.10 | 0.71 | 14.72 | 3.19 | 0.36 | - | 0.01 | 0.00 | 99.92 |
| LHS-1D | 50.81 | 0.49 | 27.81 | 2.25 | 0.00 | 1.18 | 14.12 | 2.93 | 0.40 | - | 0.00 | 0.00 | 99.99 |
| LMS-1 | 44.14 | 6.62 | 13.32 | 6.20 | 0.03 | 14.35 | 7.29 | 2.05 | 0.59 | - | 0.03 | 0.00 | 94.63 |
| LMS-1D | 51.71 | 1.11 | 21.86 | 4.37 | 0.01 | 6.37 | 10.77 | 2.64 | 0.45 | - | 0.06 | 0.47 | 99.82 |
| LCATS-1 | 38.85 | 4.22 | 10.76 | 11.91 | 0.07 | 11.57 | 15.00 | 3.57 | 1.93 | 2.17 | 0.04 | - | 99.60 |
| OPRH2N | 47.55 | 0.69 | 25.83 | 4.90 | 0.00 | 2.46 | 14.76 | 2.89 | 0.35 | 0.00 | - | - | 99.40 |
| OPRH3N | 47.90 | 0.34 | 28.37 | 2.40 | 0.01 | 1.27 | 15.93 | 2.90 | 0.22 | 0.00 | - | - | 99.34 |
| OPRL2N | 46.38 | 1.26 | 16.27 | 9.61 | 0.00 | 9.66 | 13.82 | 2.30 | 0.40 | 0.00 | - | - | 99.70 |
| OPRL2NT | 39.39 | 11.56 | 15.43 | 13.88 | 0.16 | 5.46 | 10.20 | 3.32 | 0.06 | 0.00 | - | - | 99.46 |

Table 5.8: Average bulk chemical composition of samples after SEM-EDS analyses.

5.6 Discussion

Results obtained from SEM-EDS analyses shows that Exolith simulants LHS-1, LHS-1D, LMS-1 and LMS-1D present discrepancies from technical reports. In particular LMS-1 and 1-D have different grain size distribution Fig.(5.2) and they also considerably differ in modal and mineral compositions. Such analogues should have the same lithology, with same compositions but different grain sizes. The samples under test present different mineral composition and modal proportions, see Tab.(5.7 and 5.8), that are substantially different from the technical reports, Tab.(5.5 and 5.4). Particularly, LMS-1D shows SiO_2 and Al_2O_3 % much higher than reference values. This fact is probably caused by a deficit in mafic component. Different modal proportions and computed mean bulk compositions are displayed by LMS-1 and LMS-1D. The Exolith technical report does not specify the exact modal mineralogy (basaltic glass and basalt components may contain varying amounts of plagioclase, pyroxene, and maybe minor amounts of olivine). This lack of information makes possible for us to compare the LMS-1 and 1-D values to the original reference values. The discrepancy between LMS-XX series was also highlighted by the difference in the grain density ρ_g directly tested and reported in Tab.(5.6). On the other hand, LHS-1 and 1-D present quite a good match in terms of modal proportion and calculated mean bulk compositions with the reference values of the Exolith reports. Also the grain density overlaps within the uncertainties, highlighting the fact that the composition of the two samples are the same.

These analyses highlighted the presence of certain mineral phases that are not listed in the manufacturer datasheet, as pyrophanite ($MnTiO_3$) which is a Mn-end member of the ilmenite group, and phyllosilicates, a hydrated minerals family that formed by weathering of silicates, mostly olivines and pyroxenes. Since the calculated proportions are very low (up to 0.5 vol% for phyllosilicates and up to 0.2 vol% for pyrophanite), the presence of these phases has no effect on the modal mineralogy and bulk composition.

Due to the similar modal proportions of ilmenite and pyrophanite in LHS-1, it's difficult to highlight whether there is an influence on dielectric properties, specifically the impact of water present in phyllosilicates (lunar minerals are highly anhydrous) and the pyrophanite dielectric properties with respect to ilmenite.

The composition of LCATS-1 simulant differs significantly from what is claimed in the datasheet. Oxide content in the estimated mean bulk composition fall outside of the target range. The finding of a notably albitic plagioclase composition, that is rare for any lunar plagioclase, is noteworthy. Lunar plagioclases are typically Ca-rich and virtually profoundly Na,K-poor. LCATS-1 also presents perovskite (a calcium

titanate, CaTiO_3) as the primary opaque phase rather than ilmenite. Perovskite has not yet been identified as a major or even a minor exogenic carbonaceous chondritic component of lunar regolith [144].

Chapter 6

Assessing the effect of porosity and mineralogy on dielectric properties of regolith analogues

6.1 Introduction

In this chapter are reported the measurements conducted at varying compaction steps for the nine regolith analogues. The dielectric parameter of dry samples are tested as a function of porosity via mean of a Vector Network Analyzer VNA (Agilent E5071C) connected to a coaxial cage multiwire electrodes. The dielectric parameters are tested in the frequency range $100\text{ kHz} - 3\text{ GHz}$ and each compaction step (i.e. for decreasing porosity) is obtained placing the coaxial cage on a vibration plate.

The characteristic of the equipment and the methodology applied to conduct the measurements are described in the following sections.

6.2 VNA set-up

The Vector Network Analyzer (VNA) is an instrument that sends an electric signal through the DUT at varying frequency and measures the output signal. It is typically employed to test DUT in the $\text{MHz} - \text{GHz}$ range. The DUT is inserted into a coaxial cage with stainless steel multiwire electrodes in a teflon box and connected to the instrument (transmission probe-line) [88]. The 2-port VNA measures the scattering parameters S_{11} , S_{12} , S_{21} , S_{22} between the port 1 and port 2 and with application of the Nicolson-Ross-Weir algorithm (NRW) we evaluate the complex dielectric permittivity and complex dielectric permeability of the tested material [95],[19].

The transmission-reflection line method is commonly used to test samples affected by medium to high energy losses, but it is also employed for the study of powder samples since the coaxial cage minimizes the low-frequency polarization effects (i.e. the interfacial polarization between the cell and the DUT). The coaxial transmission line theory is here expressed by circuital approach in order to discuss the VNA set-up.

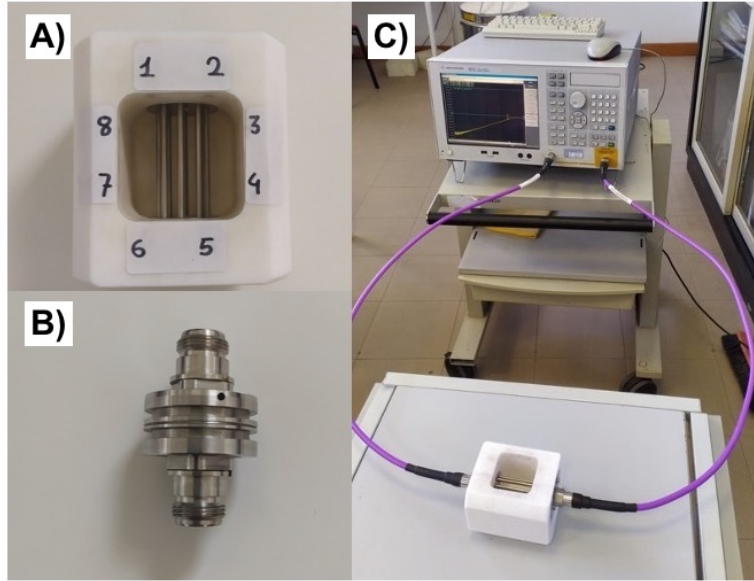


Figure 6.1: A) Coaxial cage measurement cell characterized by stainless steel multiwire electrodes in a teflon box. B) Connector calibrator that simulates the N-type connectors of the cell that we use to remove the effect of the connector from data. C) Vector Network analyzer (Agilent E5071C) connected to the coaxial cage. With this apparatus we measured the dielectric properties of regolith analogues as a function of porosity in the frequency spectrum 100kHz to 3GHz.

The transmission line is generally represented as a two-wire lines since it always presents at least two conductors in order to grant the propagation of transverse electromagnetic wave. The following approach is valid when an infinitesimal part of the transmission line is small than the wavelength ($\Delta z \ll \lambda$). In Fig.(6.2) the quantity $R (\Omega/m)$ is the resistance produced by the finite conductivity of the single conductor, $L (H/m)$ is the self-inductance of the two conductor elements, $C (F/m)$ describes the capacitance due to the proximity of the two conductors and $G (S/m)$ represents the conductance caused by the dielectric losses between the two conductor elements.

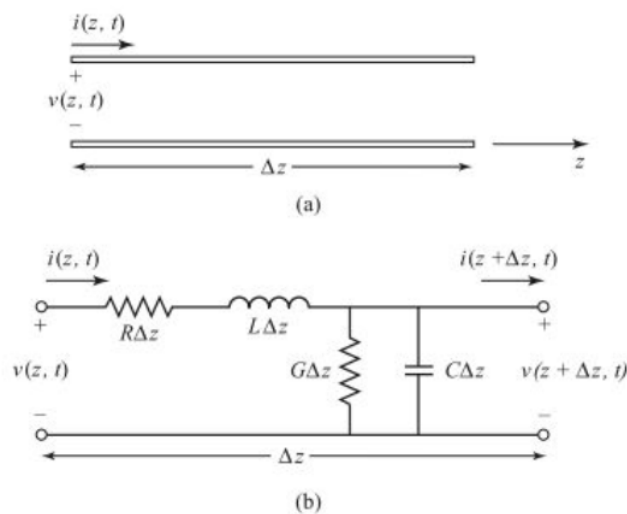


Figure 6.2: Coaxial transmission line. A) Voltage and currents of the transmission line, B) equivalent circuit of lumped-element.

The circuit shown in Fig.(6.2 B) can be resolved through the application of the

Kirchhoff's laws obtaining the telegrapher equations for current and voltage:

$$\frac{\partial I(z, \omega)}{\partial z} = -(G - i\omega C)V(z, \omega) \quad (6.1)$$

$$\frac{\partial V(z, \omega)}{\partial z} = -(R - i\omega L)I(z, \omega) \quad (6.2)$$

The two wave equations $I(z)$ and $V(z)$ can be expressed in terms of the complex propagation constant $\gamma = \sqrt{(R + i\omega L)(G + i\omega C)}$. In Chapter(2) is reported the EM theory and the relation between γ and the EM parameters, it won't be reported here to avoid redundancy.

$$I(z) = I_0^+ e^{-\gamma z} + I_0^- e^{\gamma z} \quad (6.3)$$

$$V(z) = V_0^+ e^{-\gamma z} + V_0^- e^{\gamma z} \quad (6.4)$$

In eq.(6.3) and (6.4) the term $e^{\gamma z}$ express the wave propagation on $-z$ direction and $e^{-\gamma z}$ describe the wave propagation on $+z$ direction. In the end, after few mathematical manipulations we can express the current $I(z)$ that flows through the line as a function of R, L and γ , eq.(6.5). We can also express the characteristic impedance Z_0 of the coaxial line:

$$I(z) = \frac{\gamma}{R + i\omega L} (V_0^+ e^{-\gamma z} - V_0^- e^{\gamma z}) \quad (6.5)$$

$$Z_0 = \frac{R + i\omega L}{\gamma} = \sqrt{\frac{R + i\omega L}{G + i\omega C}} \quad (6.6)$$

where the circuital parameters R, L, G and C are related to the quantities ε, μ and the geometrical factor of the system f_g as follow:

$$R = \omega C_0 \mu'' = f_g \mu_0 \mu'' \quad (6.7)$$

$$L = L_0 \mu' = f_g \mu_0 \mu' \quad (6.8)$$

$$G = \omega C_0 \varepsilon'' = 1/f_g \varepsilon_0 \varepsilon'' \quad (6.9)$$

$$C = C_0 \varepsilon' = 1/f_g \varepsilon_0 \varepsilon' \quad (6.10)$$

6.2.1 Coaxial transmission-reflection line method

Considering a two-port VNA device as shown in Fig.(6.3) the incident wave a_i where $i = 1, 2$, propagates through the DUT and the transmitted wave b_i in registered to the other port. The quantities that relate the input and output waves are the scattering parameters or simply the S-parameters. S_{ij} , ($i, j = 1, 2$) are complex quantities identified by magnitude and phase that are defined as the ratios of wave quantities. For example, the input reflection coefficient on port 1 is given by $S_{11} = b_1/a_1$ for $a_2 = 0$ and $a_1 \neq 0$, (match). In general, both incident waves can be non-zero so we express it in a more general form introducing the S-matrix:

$$\begin{pmatrix} b_1 \\ b_2 \end{pmatrix} = \begin{pmatrix} s_{11} & s_{12} \\ s_{21} & s_{22} \end{pmatrix} \begin{pmatrix} a_1 \\ a_2 \end{pmatrix} \quad (6.11)$$

$$\mathbf{b} = \mathbf{S}\mathbf{a} \quad (6.12)$$

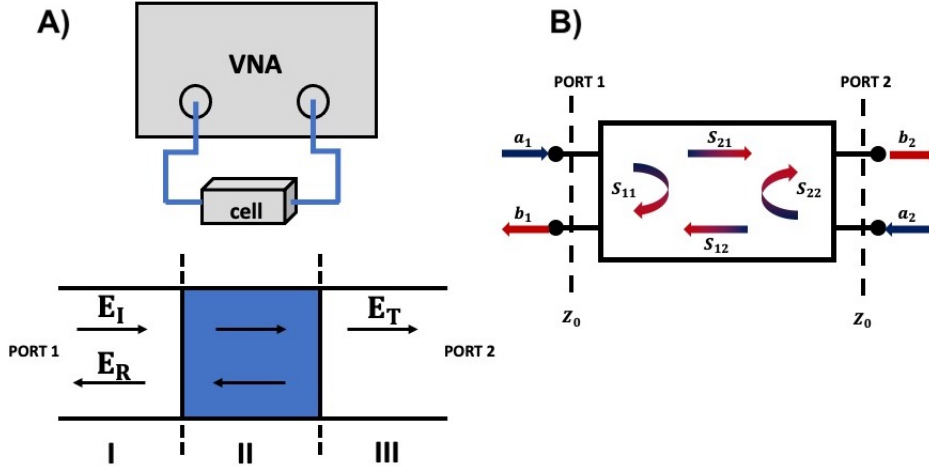


Figure 6.3: A) Scheme of the VNA set-up. The VNA measures the scattering parameters S_{11} , S_{12} , S_{21} , S_{22} between the port 1 and port 2 and with the application of the Nicholson-Ross-Weir algorithm (NRW) we evaluate the complex dielectric permittivity and complex dielectric permeability of the DUT [95]. B) shows the two-port device with its wave quantities. a_i and b_i , ($i = 1, 2$) represent the incident and transmitted waves respectively, which are related by the scattering matrix S .

By measuring this set of parameters it is possible to evaluate the complex permittivity ϵ_r and permeability μ_r of the DUT. The boundary conditions of regions I, II and III in Fig.(6.3 A) require that the electric and magnetic fields have to be equal and from that we can express the S-parameters as a function of reflection Γ and transmission T coefficients, [6]:

$$\Gamma = \frac{\frac{\mu_r}{\gamma} - \frac{\mu_0}{\gamma_0}}{\frac{\mu_r}{\gamma} + \frac{\mu_0}{\gamma_0}} \quad (6.13)$$

$$T = e^{-\gamma z} \quad (6.14)$$

$$S_{11} = S_{22} = \frac{\Gamma(1 - T^2)}{1 - \Gamma^2 T^2} \quad (6.15)$$

$$S_{21} = \frac{T(1 - \Gamma^2)}{1 - \Gamma^2 T^2} \quad (6.16)$$

where z is the length of the sample and γ_0 is the propagation constant for free space.

6.2.2 Nicolson-Ross-Weir algorithm

The complex dielectric permittivity and permeability of the sample under test are estimated from the S-parameters by the application of the NRW method. The fundamental equations are expressed as follow:

$$K = \frac{(S_{11}^2 - S_{21}^2 + 1)}{2S_{11}} \quad (6.17)$$

$$\Gamma = K \pm \sqrt{K^2 - 1} \quad (6.18)$$

$$T = \frac{(S_{11} + S_{21}) - \Gamma}{1 - (S_{11} + S_{21})\Gamma} \quad (6.19)$$

The original algorithm [95], was retrieved using a uniform air-transmission line where the impedance at the terminations is matched, like the case shown in Fig.(6.4A). For the experimental set-up in this case study, the NRW algorithm is adapted according to [88], since the cross-section of the transmission line is larger than that of the standard cables, Fig.(6.4B and 6.1C). This causes an impedance mismatch between the cables and probe. The modified algorithm takes into account the geometrical factor F_g of the probe that is defined as the ratio of impedances of coaxial cage and the probe-line. This yields to:

$$\sqrt{\varepsilon_r/\mu_r} F_g = \frac{(1 - \Gamma)}{(1 + \Gamma)} \quad (6.20)$$

$$\sqrt{\varepsilon_r\mu_r} l = jc(2\pi f)^{-1} \ln(T) \quad (6.21)$$

where c is the velocity of the light in a vacuum, f is the frequency and l is the length of the coaxial-cage line. Z_c is the impedance of the coaxial cables and Z_p the one of the probe-line in air. It is important to note that when $F_g = 1$ we obtain the original NRW algorithm. When combining eq.(6.20) and eq.(6.21) it is possible to evaluate the relative dielectric permittivity and permeability of the DUT:

$$\varepsilon_r = jc(2\pi flF_g)^{-1} \ln(T) \frac{1 - \Gamma}{1 + \Gamma} \quad (6.22)$$

$$\mu_r = jc(2\pi fl)^{-1} F_g \ln(T) \frac{1 + \Gamma}{1 - \Gamma} \quad (6.23)$$

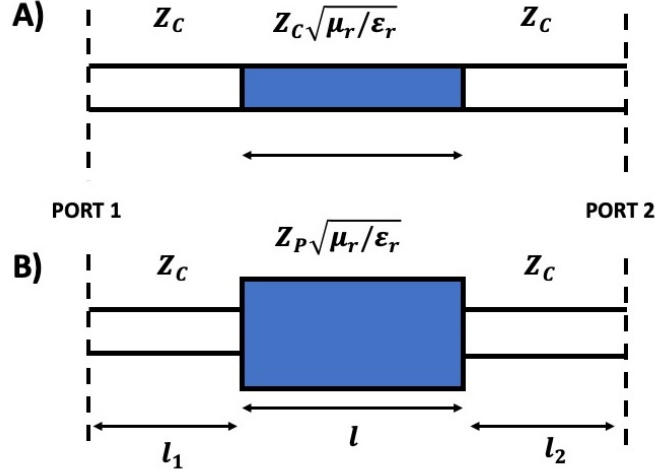


Figure 6.4: Scheme of the transmission line set-up. The white regions are the connecting cables, the blue area is the region of the DUT. A) Uniform air-transmission line emplaced for the original Nicolson-Ross-Weir algorithm. B) Modified transmission line used in this work where the contact area between the probe and the cables exhibit an impedance mismatch.

Calibration

The transmission line method is affected by three different types of measurement errors: systematic, random, and drift errors. The first type is generated by the instrumentation intrinsic noise; the systematic errors can be corrected by calibrating the VNA and applying the corrections of VNA and cables to data. The calibration procedure was taken at room temperature prior to each measurement using the SOLT technique that involves Short measurements (out of phase by 180°) and Open measurements, which replicate the ideal signal reflection from the VNA. This is followed by a Load measurement (at $50\ \Omega$), using a calibration standard that simulates a complete absence of signal reflection. The complete calibration procedure and additional details are explained in the work of Brin et al. [9].

6.3 Porosity estimation

For each regolith analogue the dielectric parameters are tested varying the porosity of the sample, collecting nearly 200 measurements. The measurements are performed with the coaxial cage reported in Fig.(6.1A). The volume of the box is known, equal to $V_{tot} = 146 \pm 3\ cm^3$. The powder sample is inserted into the box completely filling the volume and not applying any mechanical stress to the powder. In this way the powder sample is non-compacted and using eq.(6.24) and (6.25) we first estimate the bulk density and then the porosity of this first configuration.

$$\rho_b = \frac{m}{V} \quad (6.24)$$

$$\Phi = 1 - \frac{\rho_b}{\rho_g} \quad (6.25)$$

In eq.(6.24) and (6.25) m is the mass of the sample inserted into the cell, V is the volume occupied from the sample, ρ_b is the bulk density and ρ_g is the grain density of

each sample that are measured with the pycnometer and reported in Tab.(5.6). After the acquisition of the dielectric parameters with the VNA of the first configuration, the sample holder is put on a vibration plate that slightly compact the mixture. Once the powder is compacted, the volume occupied by the sample is $V_i = V_{tot} - \delta V$. Eq.(6.26) allows to estimate the new volume V_i that is then used to estimate the bulk density and the porosity of this second configuration. This procedure is iterated and applied several times in order to obtain dielectric parameters for each porosity configuration.

$$\frac{V_i}{V_{tot}} = \frac{h_i}{h_{tot}} \rightarrow V_i = V_{tot} \frac{h_{tot} - \delta h_i}{h_{tot}} \quad (6.26)$$

In eq.(6.26) V_{tot} and h_{tot} are the volume and height occupied by the non-compacted powder, V_i is the volume occupied from the sample after each compaction, and h_i is the vertical height of the powder occupied in the box for each measurement and δh_i is the difference in height that is measured with a caliber for each compaction. The lower the porosity, the lower the air content into the mixture. Ideally, when $\Phi = 0$ we should obtain the dielectric behavior of the solid material (i.e. rocks).

6.4 Sample preparation

It is very well known that the presence of remanent moisture strongly affects the dielectric response of the sample, where the complex permittivity significantly increases [118]. Therefore, it is fundamental to remove humidity from analogues before each measurement, drying each sample in a vacuum-oven at $105^\circ C$ for at least 24 hours. The temperature was set not too high in order to not modify the chemistry/mineralogy of the samples.

6.5 Measurement results

6.5.1 Frequency spectra

The following graphs show the electromagnetic properties in function of frequency measured varying the porosity, as illustrated in the previous sections. For each sample were acquired between 20 to 30 dielectric measurements at varying porosity at room temperature. Plots report real and imaginary parts at selected porosity chosen among all collected curves. In Fig.(6.5) and (6.7) data is partially distorted because of the occurrence of resonance effects between the cell and the analogue [88]. These phenomena typically happen for frequencies above $10^8 Hz$. The results of dusty analogues LHS-1D and LMS-1D are not reported since the EM behavior doesn't differ from the two samples with greater particles size. In addition to that, the imaginary part is difficult to be measured since its value is lower than 10^{-2} , which corresponds to the VNA instrument limit. The dielectric measurements were collected over the frequency spectrum $100 kHz - 3 GHz$ but data are only reported in the frequency sub-range 10^7 to $3 \cdot 10^8 Hz$ because within this range data are less affected by resonance effects and distortions [9]. Data below $10^7 Hz$ for low loss material is not reliable due to the VNA measurement limits. The real part of permittivity shows no dependence with frequency while the imaginary part slightly increases with frequency. The uncertainties of real

part of permittivity are less than few percent of the measurements and are not visible in the following plots.

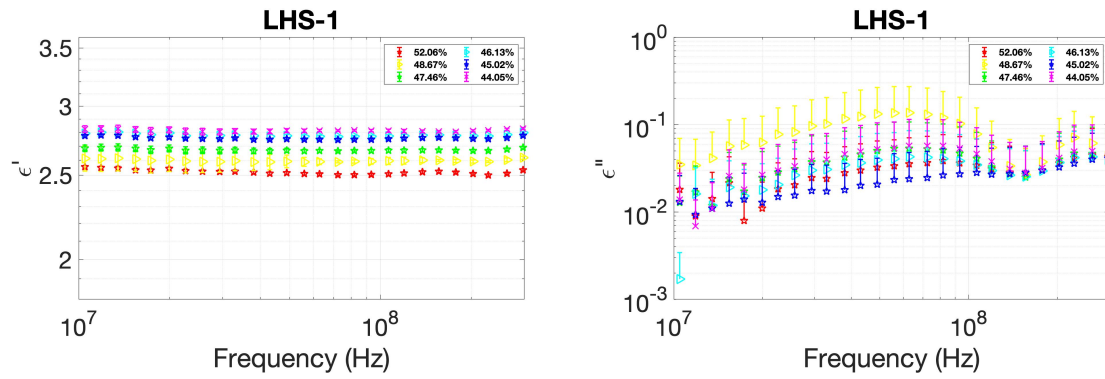


Figure 6.5: Real and imaginary part of permittivity of LHS-1 in the frequency spectrum tested at selected porosity .

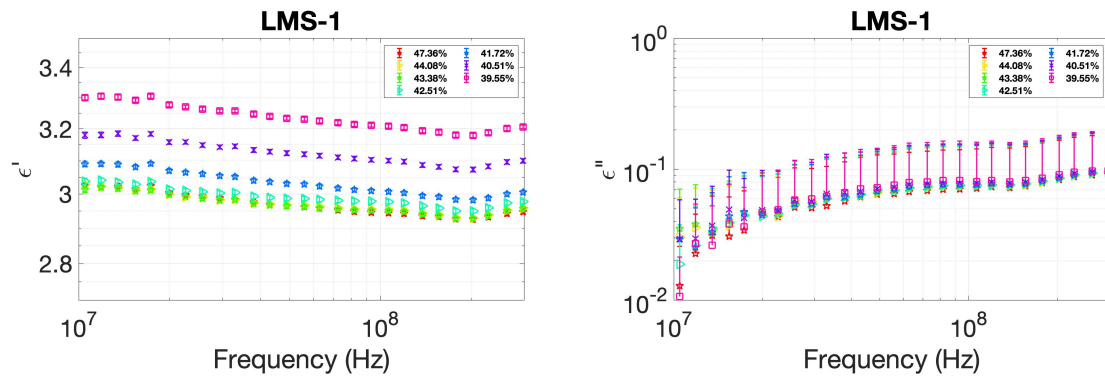


Figure 6.6: Real and imaginary part of permittivity of LMS-1 in the frequency spectrum tested at selected porosity.

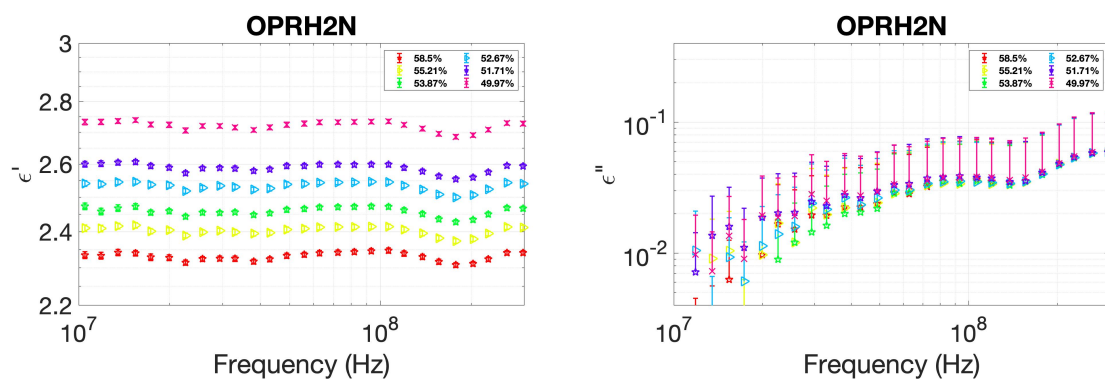


Figure 6.7: Real and imaginary part of permittivity of OPRH2N in the frequency spectrum tested at selected porosity.

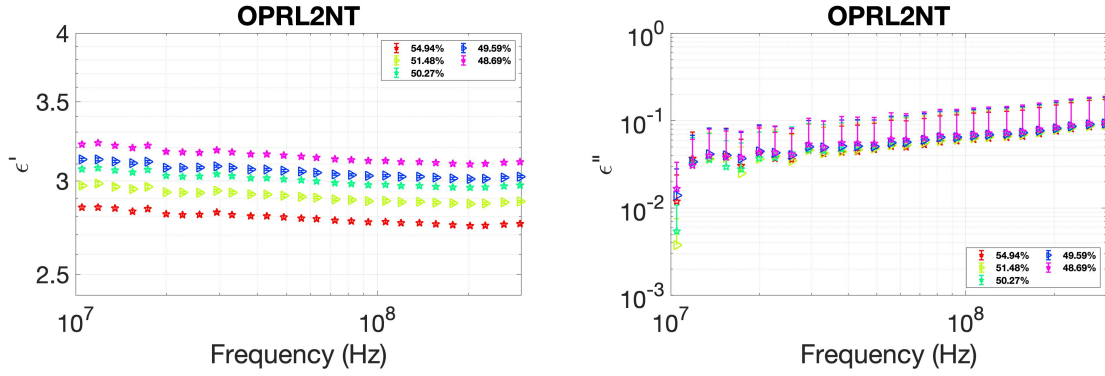


Figure 6.8: Real and imaginary part of permittivity of OPRL2NT in the frequency spectrum tested at selected porosity.

6.5.2 Magnetic permeability

All tested samples present no relevant magnetic behavior. Fig.(6.9) illustrates the complex magnetic permeability of four analogues under test in this work (LHS-1, LHS-1D, LMS-1, LMS-1D). The value of real part of magnetic permeability is ~ 1 as highlighted in the following table. This fact confirm that the assumption made at the beginning for the application of the methodology for non magnetic material are correct. Tab(6.1) shows complex magnetic permeability of the nine simulants selected and averaged over the frequency range 100 – 200 MHz.

| SIMULANT | μ' | $\sigma \mu'$ | μ'' | $\sigma \mu''$ |
|----------|--------|---------------|---------|----------------|
| LHS-1 | 1.0113 | 0.0056 | 0.0269 | 0.0020 |
| LHS-1D | 1.0136 | 0.0053 | 0.0305 | 0.0019 |
| LMS-1 | 1.0150 | 0.0047 | 0.0022 | 0.0028 |
| LMS-1D | 1.0068 | 0.0063 | 0.0026 | 0.0004 |
| OPRH2N | 1.0076 | 0.0053 | 0.0044 | 0.0018 |
| OPRH3N | 1.0050 | 0.0053 | 0.0022 | 0.0011 |
| OPRL2N | 1.0062 | 0.0053 | 0.0042 | 0.0027 |
| OPRL2NT | 1.0079 | 0.0048 | 0.0025 | 0.0017 |
| LCATS-1 | 1.0163 | 0.0058 | 0.0296 | 0.0036 |

Table 6.1: Complex magnetic permeability selected and averaged over the frequency spectra 100 – 200 MHz. All nine samples present non-magnetic behavior as expected.

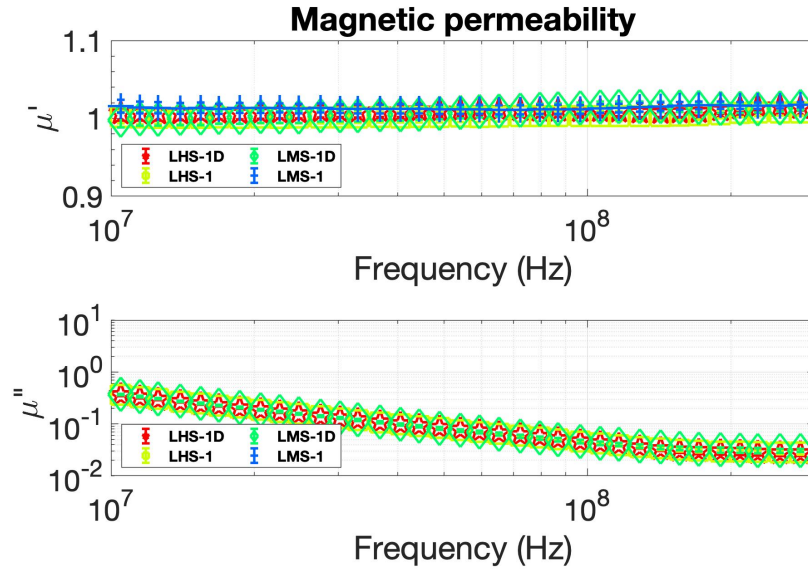


Figure 6.9: *The magnetic permeability of 4 samples tested at varying frequency. All nine samples are non-magnetic material. The imaginary part μ'' of LMS-1 is lower than 10^{-2} and it doesn't appear on the plot. Measurement uncertainties are less than few percent of the data and it might be difficult to see in the plot.*

6.5.3 Bulk density effect

Fig.(6.10) and Fig.(6.11) show the effect of porosity and bulk density on dielectric parameters of regolith samples. Data are averaged over the frequency range 100 – 200 MHz to smooth the trend and to eliminate spurious spikes caused by the measurement set-up. Powder samples are heterogeneous mixtures; when the porosity is varying, also the volume of air trapped within the solid grains is changing, leading to a variation of the dielectric behavior of the whole sample. In fact, the real part of permittivity increases when the sample is being compacted (lower porosity). This effect is also visible in Fig.(6.5) to (6.7) where some measurements at different porosity are shown. In this work, the average starting porosity (prior to the compaction) is around 55% for the analogues that present higher average grain size while for the dusty simulants like LMS-1D and LCATS-1 the starting porosity is 71% and 67% respectively. The total variability of real part obtained with more than 190 measurement is 1.8 – 3.3. In Fig.(6.11) the imaginary part of 3 samples (LHS-1, LHS-1D and OPRH3N) is not reported since it's lower than 10^{-2} which is the VNA operational limit. It is important to highlight that the imaginary part also exhibits a slight trend with porosity. This fact was never highlighted in previous works where the analyses of real and imaginary part were always discussed separately. In this work is presented a new approach where the behavior of the complex quantity (both real and imaginary part) is discussed as function of bulk density.

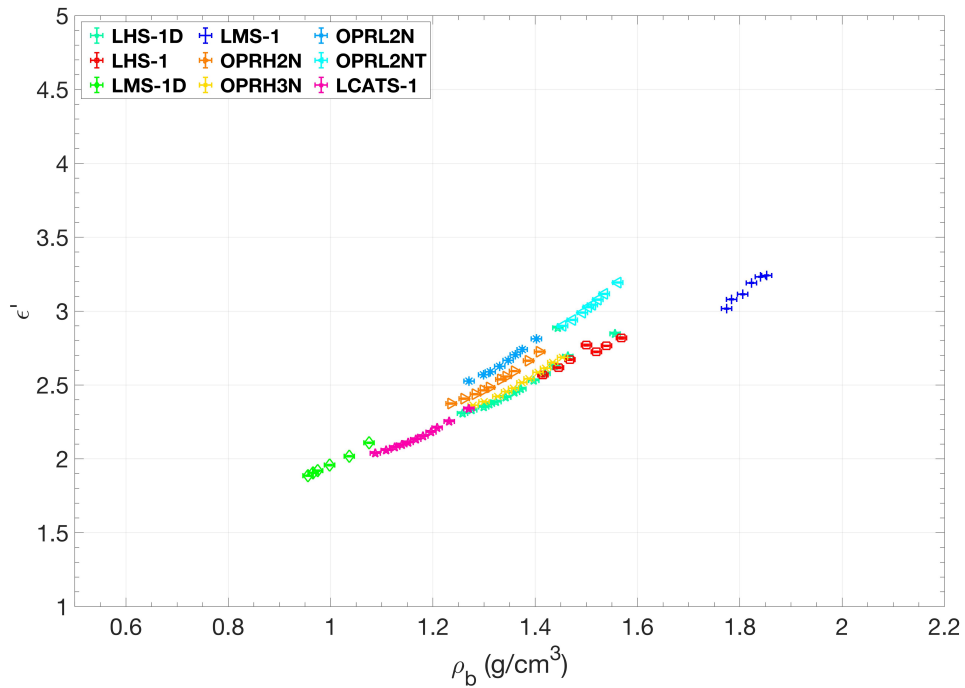


Figure 6.10: Real part of permittivity of nine analogues plotted against bulk density. These are more than 190 dielectric measurements obtained varying the compaction of each sample. Data are selected and averaged over the frequency interval 100 – 200 MHz to smooth data from spurious spikes.

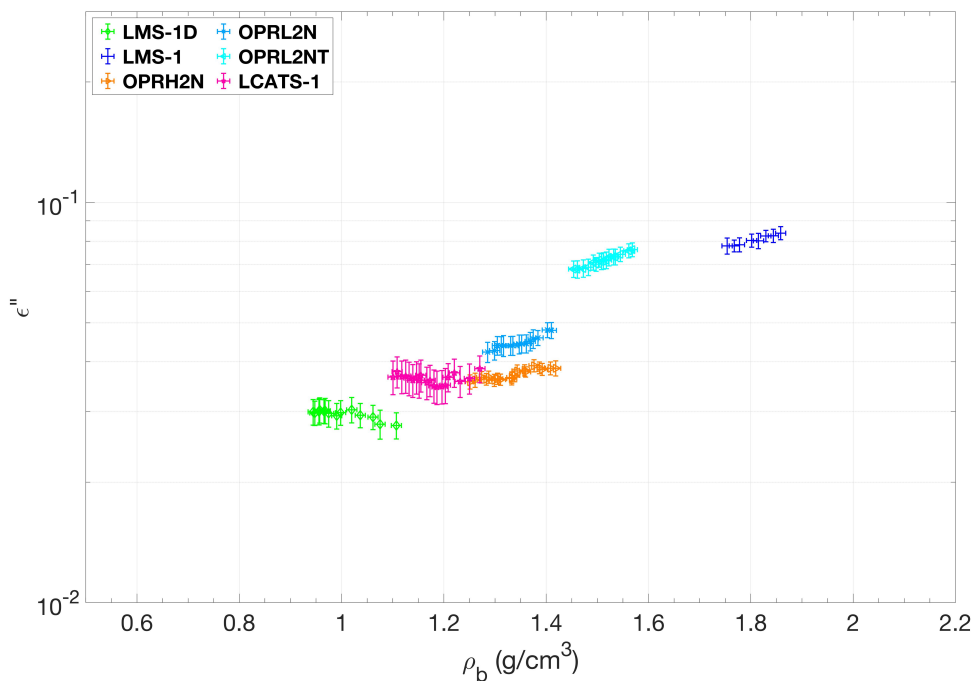


Figure 6.11: Imaginary part of permittivity of six analogues plotted against bulk density. These data are obtained varying the compaction of each sample. Data are selected and averaged over the frequency interval 100 – 200 MHz to smooth data from spurious spikes. The imaginary part of 3 samples (LHS-1, LHS-1D and OPRH3N) is not reported since it's lower than 10^{-2} which is the VNA operational limit.

6.6 Discussion

6.6.1 Models and mixing formulas

Heterogeneous mixtures are complex natural systems and it's difficult to model their physical properties. The dielectric parameters of loose material obtained by laboratory activities are defined “effective” properties of the heterogeneous mixture, which are also averaged over selected wavelength of investigation. In this context, the dielectric parameters of lunar material (i.e., grains of lunar rocks) can be extrapolated applying several mixing formulas, as deeply discussed in chapter 4. We used the Lichtenecker formula reported in eq.(6.27), which is a particular case of the power-law model, to estimate the permittivity of the rock ε_g (when $\Phi = 0$) from powder data. In fact in eq.(6.27) ε_b is the complex permittivity measured at varying bulk density (porosity). The analyses as a function of bulk density presented in this work are a novelty in the context of lunar material (both analogues and apollo samples). In fact, there are plenty of past works that estimate the dielectric parameters of lunar regolith but none of those presents a deep discussion over porosity variability. This makes difficult to compare the results of this work with the literature. A range of values of dielectric parameters is obtained for each analogue, like the case shown in Fig.(6.10), while the measurements on the Apollo samples were made for a single value of porosity that is typically not declared or it is difficult to retrieve. Mixing formulas allow to extrapolate a single value of dielectric parameters to associate to a single sample in order to make coherent comparisons with literature. Hence, the complex dielectric parameters of regolith analogues are extrapolated as they were solid material, and compared with lunar rocks data.

$$\varepsilon_b = \varepsilon_g^{\frac{\rho_b}{\rho_g}} \quad (6.27)$$

The probability density functions of the complex dielectric parameters of solid material are determined by applying non-linear least square regression on powder data. The results of the regression fit are reported in Tab.(6.2). In Fig.(6.12) is shown an example of the fit application for simulant OPRH2N and OPRL2NT, from which we retrieve the real and imaginary part of permittivity for the solid sample. The non-linear regression method is applied on dielectric data averaged over the frequency range 100 – 200 MHz as prior discussed.

| SIMULANT | ε'_g | $\sigma \varepsilon'_g$ | ε''_g | $\sigma \varepsilon''_g$ |
|----------|------------------|-------------------------|-------------------|--------------------------|
| LHS-1 | 6.4332 | 0.0085 | 0.1350 | 0.0041 |
| LHS-1D | 6.414 | 0.015 | 0.1395 | 0.0048 |
| LMS-1 | 6.775 | 0.011 | 0.3041 | 0.0041 |
| LMS-1D | 6.816 | 0.013 | 0.3491 | 0.0030 |
| OPRH2N | 7.1162 | 0.0088 | 0.22320 | 0.00060 |
| OPRH3N | 6.3572 | 0.0074 | 0.1709 | 0.0017 |
| OPRL2N | 8.187 | 0.015 | 0.2968 | 0.0018 |
| OPRL2NT | 8.990 | 0.010 | 0.4303 | 0.0039 |
| LCATS-1 | 7.815 | 0.016 | 0.3524 | 0.0058 |

Table 6.2: Results of the least square regression with Lichtenecker formula to retrieve the complex dielectric permittivity of the samples at virtually zero porosity.

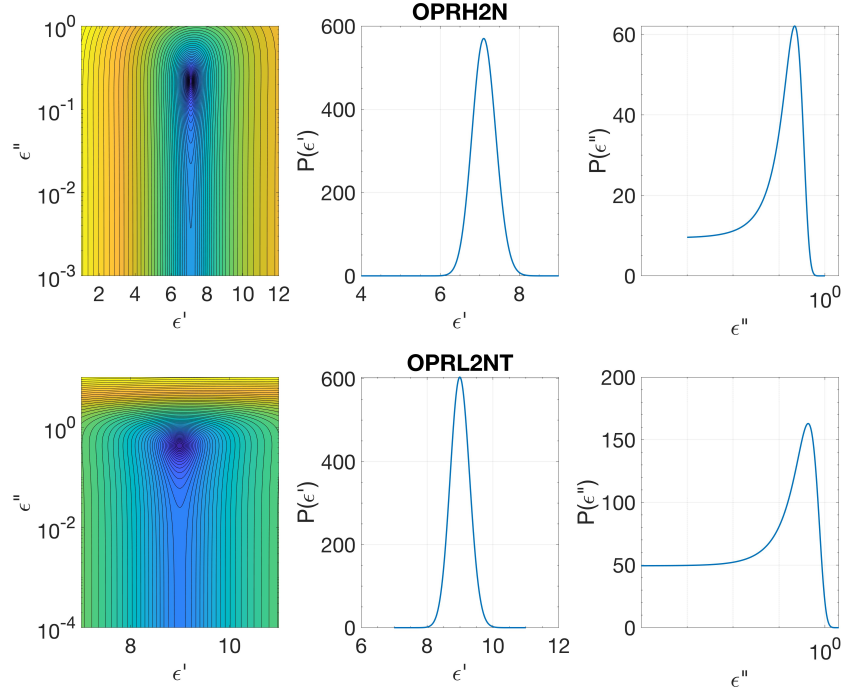


Figure 6.12: Probability density functions for real and imaginary part of permittivity applying the Lichtenecker formula on regolith data as a function of porosity to estimate the dielectric parameters of the solid material (when the porosity is equal to zero).

The values of ε'_g , listed in Tab.(6.2), range between 6 to 9. This confirms the results reported and summarized in [59], where the permittivity of Apollo lunar rocks ranges from 6 to 8. In Tab.(6.3) are reported the dielectric measurements of lunar rocks that are present in the literature that are used in this work. The OPRL2NT simulant shows the highest value of complex ε_g , which is an expected result since OPRL2NT present the highest %wt of oxide content, whose particles are heavier than the others. LMS-1D presents ε_g values that are slightly higher than LMS-1. Such a discrepancy is thought to be caused by the anomalous value of grain density. The two maria simulants are characterized by the same chemical composition, they only differ on the grain size and the expected values of ε_g must be the same. We replicated the measure of grain density with the pycnometer, and we obtained different results as discussed in chapter 5, see Tab.(5.6). We think the discrepancy is caused by the sieving process, that the dust simulant undergoes to obtain a finer powder, that blocks some heavier particles. Fig.(6.10) and (6.11) clearly show that each simulant data set present its own trend as a function of bulk density due to the variations in terms of grain size and chemical and mineralogical composition of each samples. Based on these considerations we applied the mixing formula separately for each analogue. It is important to note that the discussion in terms of porosity and density is virtually identical if we consider eq.(6.25). Rocks data are retrieved for porosity equal to zero that is the equivalent of density of the sample equal to the grain density. In the reality, the discussion in terms of bulk density is preferred when comparing dielectric results with apollo rocks data because a rock sample may present voids and cracks into the matrix, hence its porosity might be different from zero. Results reported in Tab.(6.2) have to be considered the maximum values that these samples could present if they were rocks. The real part of permittivity for lunar regolith exhibits exponential trend as a function of bulk density. This is well highlighted in Fig.(6.13) and described by eq.(6.28) from [100]. The bulk

density is derived from gravimetric measurements previously discussed and compared the real part ε' of regolith simulants with Apollo data from [53] [51] [50]. In Fig.(6.13) the dashed black line represents eq.(6.28), the pink solid line is the Lichtenecker trend, eq.(6.27), that is calculated using the whole simulants data set as a function of bulk density that yields to an average permittivity of the solid material equal to 7.23 ± 0.36 , which also confirms the previous results.

$$\varepsilon' = 1.92^{\rho_b} \quad (6.28)$$

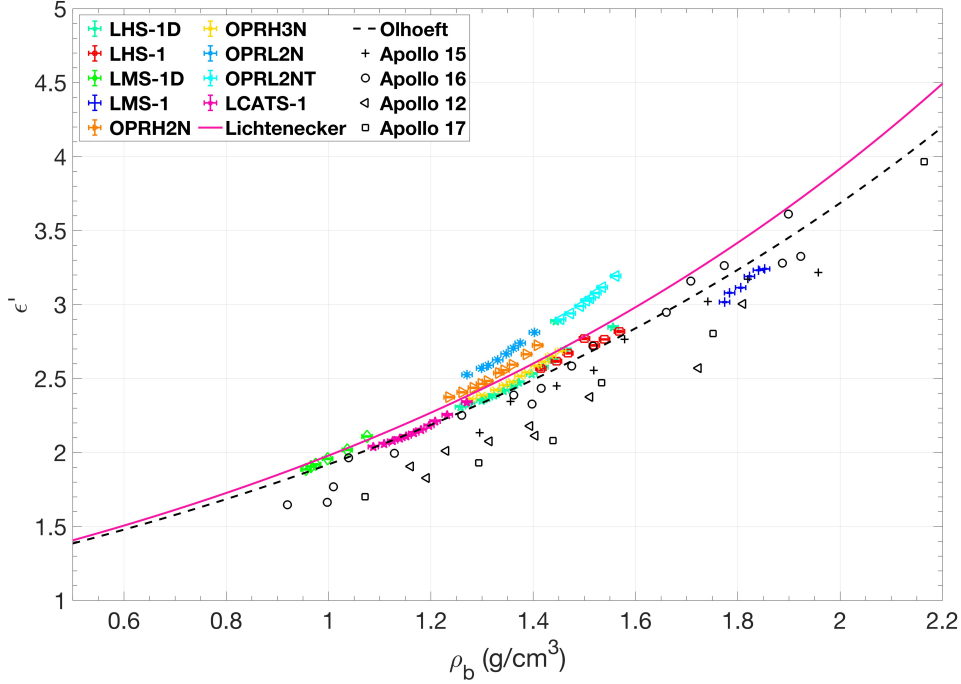


Figure 6.13: Real part of permittivity of nine analogues compared with Lichtenecker (pink line) and Olhoeft equation (black dashed line) models and Apollo 12, 15, 16 and 17 data.

6.6.2 The effect of $(FeO + TiO_2)\%$ content on loss tangent

The relation between electromagnetic energy losses and the oxide content for lunar material is still deeply debated despite several models were proposed in the past. The general idea is that the presence of TiO_2 and FeO particles can influence the energy dissipation, the higher the oxides *wt%*, the greater is the energy loss. In [59] the loss tangent of lunar material, both regolith and rocks data, are presented as a function of oxides content where some trends are extrapolated. The exponential model reported in eq.(6.29) is also from [59]. The idea proposed is that the dielectric behavior of regolith and rocks should be discussed separately. The loss tangent of the solid material is extrapolated for each of the nine simulants through eq.(6.30). In order to produce a coherent comparison, we selected only literature data with a bulk density $\rho > 2.6 \text{ g/cm}^3$ that are reported in Tab.(6.3).

$$\tan\delta = 10^{0.045(\%TiO_2 + \%FeO) - 2.754} \quad (6.29)$$

$$\tan\delta_g = \frac{\varepsilon''_g}{\varepsilon'_g} \quad (6.30)$$

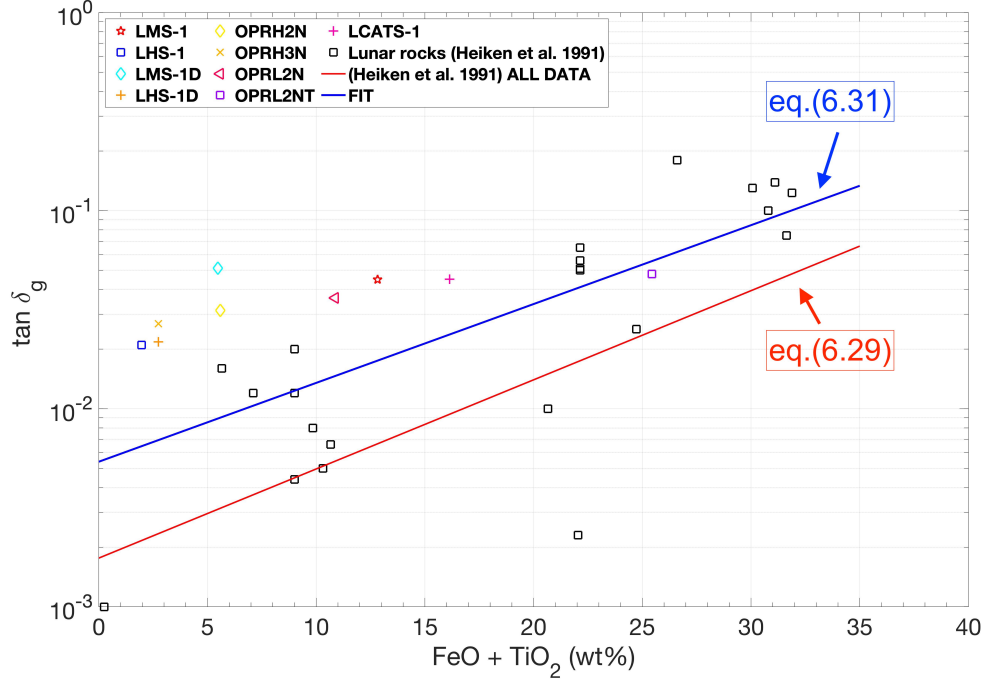


Figure 6.14: Loss tangent of regolith simulants calculated using data in Tab.(6.2) through eq.(6.30) and compared to the loss tangent of rocks data from [59]. The red line represents the equation (6.29), that was obtained by fitting the entire data set of lunar soil and rocks while the blue line is the best fit obtained in this work (using both lunar data from literature and retrieved values obtained with simulant samples).

$$\tan\delta_g = 10^{0.0398(\%TiO_2 + \%FeO) - 2.2675} \quad (6.31)$$

The eq.(6.29) from [59] doesn't describe the loss tangent of the lunar rocks data because it was obtained by fitting the entire data set where soil data are the majority. Furthermore, data used for the analysis were acquired by several authors at different frequencies that makes even harder to assess the existence of oxide-loss tangent relation. Samples were also tested at different environmental conditions (i.e. air, vacuum, nitrogen) and the procedures that were used for samples preparation and the measurements are not always well explained. This fact is also highlighted in Tab.(6.3) where the same samples were analyzed by different authors that reported different values of bulk density and dielectric parameters. In light of this, eq.(6.31) is here presented as a new model only for lunar rocks data (both lunar data from literature and retrieved values obtained with simulant samples) that is reported in Fig.(6.14) where the blue line is the new model, eq.(6.31), compared with eq.(6.29) which is the red line. They both exhibit a similar trend but the exclusion of powder samples from data set lead to a new model that highlights higher values of loss tangent for lunar rock samples.

| SAMPLE | ρ_g (g/cm^3) | frequency (MHz) | env. | ϵ' | $\tan\delta$ | TiO_2 | FeO | Ref. |
|--------|-----------------------|-----------------|------|-------------|--------------|---------|-------|-------|
| 10017 | 3.10 | 1 | N | 8.80 | 0.07500 | 11.74 | 19.89 | [72] |
| 10020 | 3.18 | 1 | AN | 10.00 | 0.13000 | 10.72 | 19.35 | [26] |
| 10022 | 3.10 | 450 | AN | 4.17 | 0.13900 | 12.20 | 18.90 | [53] |
| 10057 | 2.88 | 1 | AN | 11.00 | 0.10000 | 11.44 | 19.35 | [26] |
| 12002 | 3.30 | 1 | AN | 9.00 | 0.05000 | 2.76 | 19.38 | [25] |
| 12002 | 3.1 | 1 | N | 8.30 | 0.05100 | 2.76 | 19.38 | [72] |
| 12002 | 3.04 | 1 | N | 7.8 | 0.05600 | 2.76 | 19.38 | [72] |
| 12002 | 3.04 | 1 | V | 8.0 | 0.06500 | 2.76 | 19.38 | [103] |
| 12022 | 3.32 | 1 | AN | 11.00 | 0.18000 | 4.9 | 21.7 | [25] |
| 14310 | 2.86 | 1 | AN | 6.00 | 0.02000 | 1.30 | 7.70 | [24] |
| 14310 | 3.30 | 1 | AN | 6.40 | 0.02000 | 1.30 | 7.70 | [24] |
| 14310 | 3.30 | 1 | AN | 7.00 | 0.01200 | 1.30 | 7.70 | [24] |
| 14310 | 2.76 | 450 | AN | 6.58 | 0.00440 | 1.30 | 7.70 | [52] |
| 15065 | 2.86 | 1 | N | 6.70 | 0.01000 | 1.48 | 19.18 | [23] |
| 15415 | 2.70 | 1 | N | 4.2 | 0.00100 | 0.02 | 0.23 | [23] |
| 15459 | 2.76 | 1 | N | 6.62 | 0.00500 | 0.91 | 9.40 | [23] |
| 15555 | 3.1 | 1 | N | 6.15 | 0.02520 | 2.26 | 22.47 | [23] |
| 15597 | 2.84 | 450 | AN | 6.16 | 0.00230 | 1.87 | 20.17 | [51] |
| 60015 | 2.76 | 1 | N | 6.60 | 0.00020 | 0.06 | 0.35 | [23] |
| 61016 | 2.79 | 1 | N | 7.82 | 0.01600 | 0.69 | 4.97 | [23] |
| 62235 | 2.78 | 1 | N | 6.52 | 0.00660 | 1.21 | 9.45 | [23] |
| 62295 | 2.83 | 1 | N | 6.20 | 0.01200 | 0.70 | 6.40 | [73] |
| 65015 | 2.70 | 1 | V | 7.00 | 0.00800 | 1.26 | 8.59 | [37] |
| 65015 | 2.70 | 1 | V | 7.70 | 0.00800 | 1.26 | 8.59 | [103] |
| 70215 | 3.27 | 0.1 | V | 7.50 | 0.12300 | 12.48 | 19.40 | [2] |

Table 6.3: Lunar rocks data from Apollo landing sites used in this work to assess a relation between oxide content and energy losses. We selected only data with bulk density greater than $2.6 g/cm^3$ to discuss the loss tangent of lunar rocks. The fourth column express the environmental condition of the dielectric measurements. A=air, N=nitrogen, AN= measured in nitrogen but previously exposed to air. V=vacuum.

6.6.3 The effect of mineralogy on dielectric losses

In the previous section is reported the analysis of loss tangent and its relation with oxides content ($\%TiO_2 + \%FeO$). The connection between the rocks oxide content and dielectric energy losses has often been debated in scientific literature, particularly in lunar measurements, as demonstrated in [59]. To date, unfortunately, the relationship is not yet clear, and it certainly requires more laboratory data to improve statistical significance. Nevertheless, it would be very intriguing to determine if there is a correlation between dielectric properties and the mineralogy of the samples. Obtaining the mineral composition for Apollo samples can be somewhat challenging. Chemical analysis is available in the literature, while mineralogical analysis is often lacking. For our simulant samples, we have conducted mineralogical analyses, as summarized in chapter 5, and we have used them to investigate any relationship with the loss tangent. In the following graphs are reported the trend as a function of pyroxene, plagioclase, ilmenite and olivine content. It is important to note that more data are needed to assess a

strong correlation but data seems to suggest a linear trend as a function of pyroxene and olivine. The ilmenite content that is also strongly related to the ($\%TiO_2 + \%FeO$) content is mostly concentrated between 0 and 2 vol% and it makes difficult to assess a relation with the $\tan\delta$. Also in this case, more laboratory measurements are needed to improve the statistics. The complete discussion for chemical and mineralogical composition is found in chapter 5.

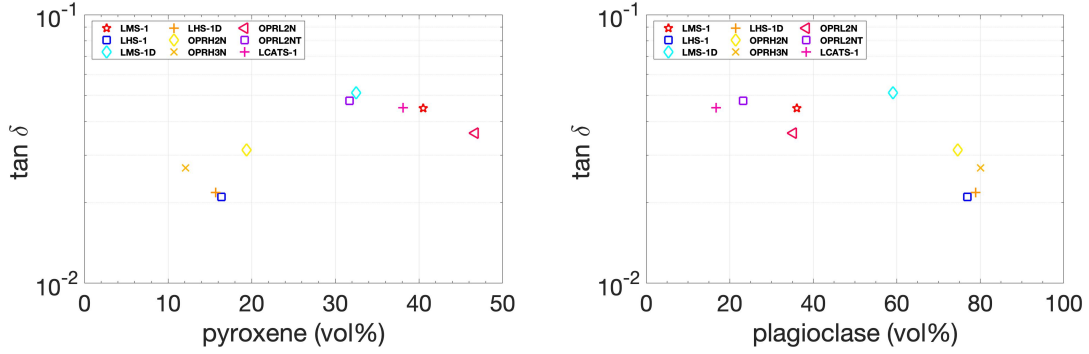


Figure 6.15: Loss tangent vs pyroxene (left panel) and plagioclase (right panel) of regolith simulants. The loss tangent values are the one retrieved for virtually zero porosity of each samples as discussed above.

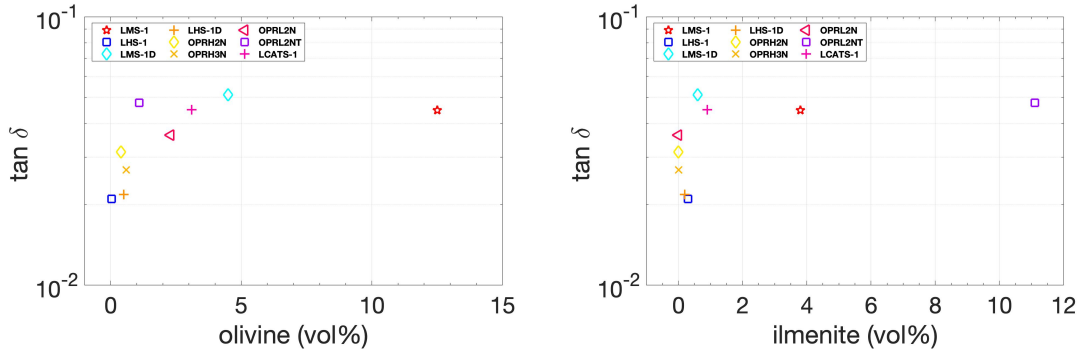


Figure 6.16: Loss tangent vs olivine (left panel) and ilmenite (right panel) of regolith simulants. The loss tangent values are the one retrieved for virtually zero porosity of each samples as discussed above.

6.6.4 Attenuation models vs depth

From the estimation of the loss tangent, attenuation curves were derived as a function of depth to compare the outcomes with the curves obtained from lunar data. The attenuation is key parameter in the context of radar analyses, as it provides information on the extent to which electromagnetic energy can penetrate the subsurface of interest. Consequently, this parameter can offer valuable insights for the design of future lunar missions and radar instruments.

The reduction in signal intensity, known as attenuation, occurs when EM signals traverse a medium. The attenuation is related to the signal's frequency, the path's length, and the material properties encountered during signal propagation, among the other mechanisms. The attenuation coefficient α is principally given by the sum of two terms: the intrinsic and the scattering contributions [33]. In this case, the

regolith material is considered almost homogeneous and thus the parameter can be approximated with the only contribution of the intrinsic attenuation $\alpha \simeq \alpha_i$, that is linear and isotropic given by eq.(6.32) [136]. In eq.(6.32) the quantity $\omega = 2\pi/\nu$ is the angular frequency, c the speed of light in a vacuum, $v = c/\sqrt{\varepsilon'}$ is the phase velocity.

$$\alpha = \frac{\omega}{c} \Im m\{\sqrt{\varepsilon}\} \simeq \frac{\omega}{2v} \tan\delta \quad (6.32)$$

The variation of bulk density with depth for lunar material was extensively studied using the drill-core from apollo missions resulting in a model reported in eq.(6.33) from [59]. For the regolith analogues, using eq.(6.33) and substituting it into the mixing model eq.(6.27) it is possible to obtain the variation of complex permittivity with depth z . The signal attenuation (two-way attenuation), eq.(6.34), is calculated for the first 40 m at two frequencies: 60 and 500 MHz which are the central frequencies of the two lunar penetrating radar missions (Chang'e3 and Chang'e4) operating on the Moon (see chapter 3, section 3.8).

$$\rho_b(z) = 1.92 \frac{z + 12.2}{z + 18} \quad (6.33)$$

$$A = \exp\left(-2 \int_{z_0}^z \alpha dz\right) \quad (6.34)$$

The two-way attenuation curves for regolith simulants are compared with models obtained from lunar data. The attenuation coefficient α is retrieved using loss tangent curves as a function of density proposed in [59]. In this case there are several model proposed: for all lunar data (both soil and rocks data) eq.(6.35), a model obtained only for lunar regolith (soil) eq.(6.36), for data obtained at 450 MHz eq.(6.37) and a subset of Apollo 15-17 data eq.(6.38). Each of these models were substituted in eq.(6.32) to calculate $\alpha(\rho)$ and then using eq.(6.34) the parameter A is retrieved.

$$\tan\delta(\rho)_{all\ data} = 10^{(0.440\rho - 2.943)} \quad (6.35)$$

$$\tan\delta(\rho)_{soil} = 10^{(0.420\rho - 2.903)} \quad (6.36)$$

$$\tan\delta(\rho)_{450MHz} = 10^{(0.398\rho - 2.871)} \quad (6.37)$$

$$\tan\delta(\rho)_{Apollo15-17} = 10^{(0.231\rho - 2.738)} \quad (6.38)$$

For the Apollo data, the quantity v into eq.(6.32) is calculated for each curve (6.35) to (6.38) using the appropriate model of $\varepsilon'(\rho)$ proposed in [59]:

$$\varepsilon'(\rho)_{all\ data} = 1.919\rho \quad (6.39)$$

$$\varepsilon'(\rho)_{soil} = 1.871\rho \quad (6.40)$$

$$\varepsilon'(\rho)_{450MHz} = 1.843\rho \quad (6.41)$$

$$\varepsilon'(\rho)_{Apollo15-17} = 1.908\rho \quad (6.42)$$

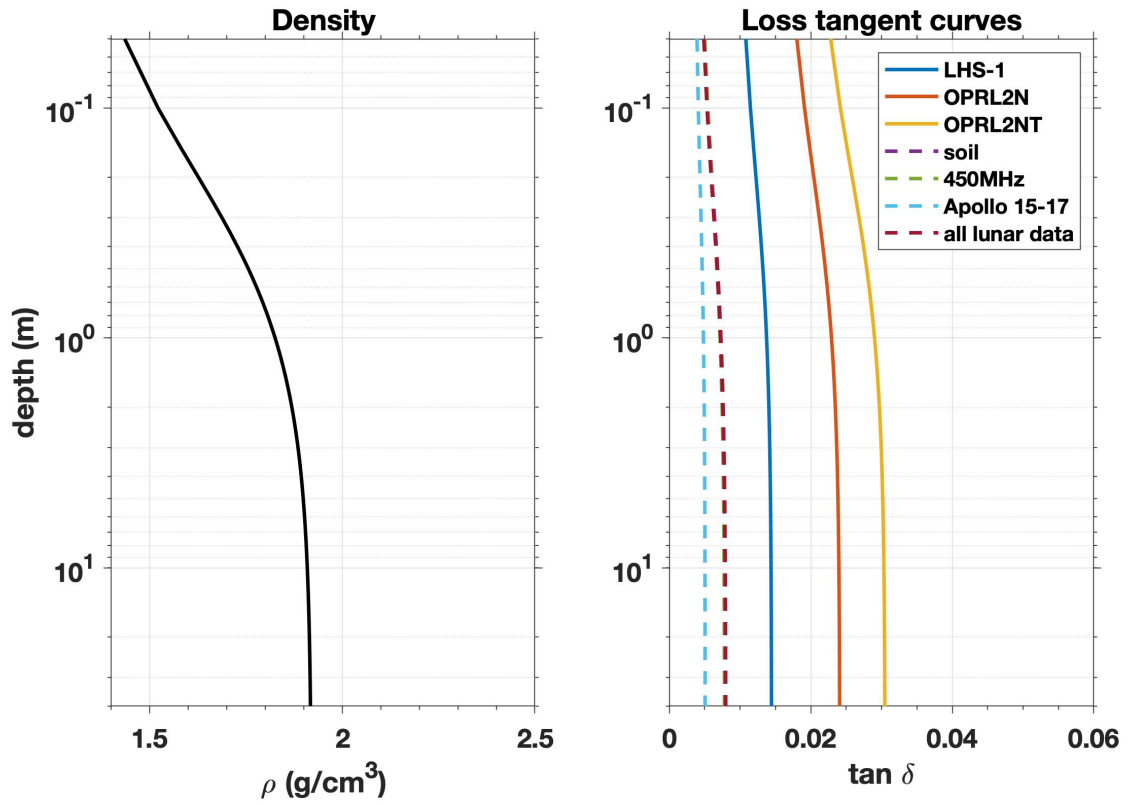


Figure 6.17: Density profile vs depth eq.(6.33) from [59] (left panel). On the right panel are reported loss tangent curves for regolith simulants and lunar data calculated using the density profile eq.(6.33).

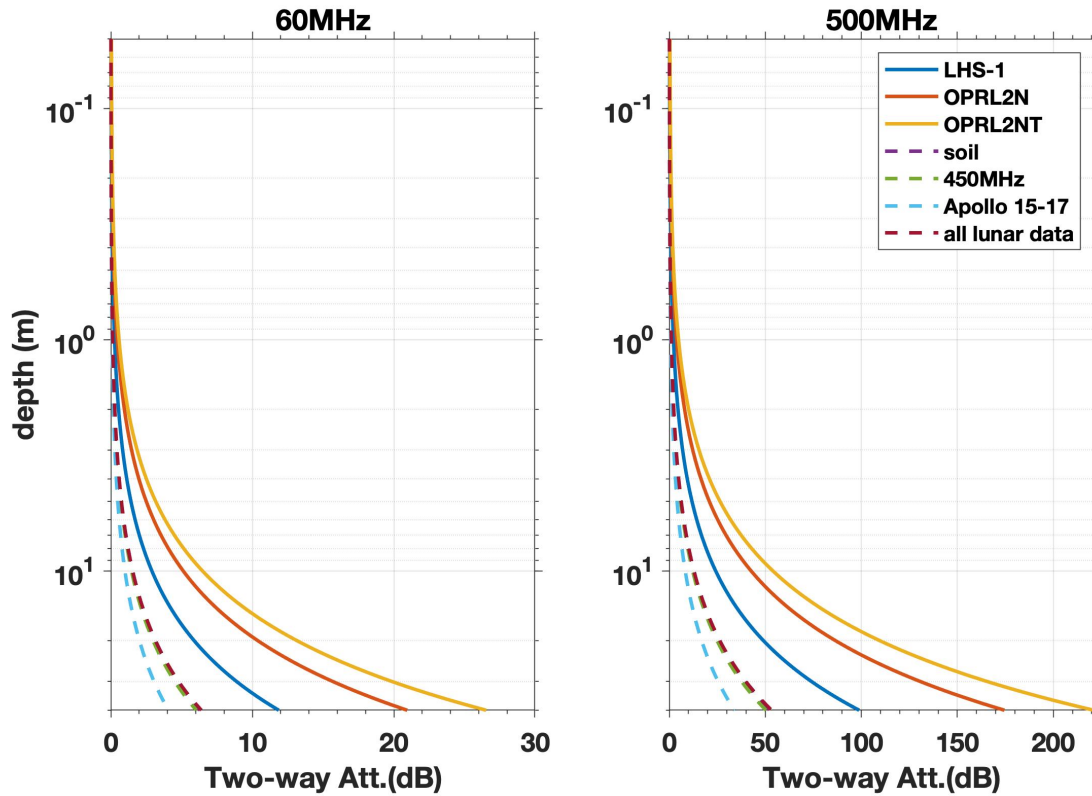


Figure 6.18: Attenuation curves calculated for the first 40 meters at two operational radar frequencies 60 and 500 MHz for regolith simulants and apollo data based on models of [59].

In Fig.(6.17) is reported the curve of density for the first 40 m reported in eq.(6.33) (left panel) and the loss tangent models for lunar simulants and lunar data (right panel). Some curves for lunar data are very similar and thus appear superimposed on the graph. This is the case of soil data eq.(6.36), data at 450 MHz eq.(6.37) and all data eq.(6.35). The curves superimposition underlying the fact that the main contribution of lunar dielectric dataset from [59] is given by lunar soil data; the set of measurements conducted at 450 MHz were carried out on soil data that is consequently a subset of soil data. On the contrary, data from Apollo 15-17 missions give a lower estimation of $\tan\delta$ but this fact is well explained in [59]. The Apollo samples from missions 11-14 underwent a different treatment compared to those from missions 15-17 to preserve Earth from potential extraterrestrial contamination. Perhaps due to inexperience, the samples were inadvertently contaminated with terrestrial atmosphere, leading to dielectric measurements affected by moisture contamination and resulting in overestimations of the dielectric parameters. In contrast, the Apollo 15-17 samples were treated differently specifically to avoid moisture contamination. As a result, the loss tangent curve for these samples deviates from the others. The $\tan\delta$ curves of the simulants range from a minimum of approximately 0.014 to 0.030 ($\pm 20\%$), remaining constant with increasing depths. These curves indicate that dielectric losses are considerably higher than those calculated from lunar data. In addition to the Apollo data results, data from the Chinese Chang'e-4 mission yielded an estimated loss tangent averaged for the initial 35-40m of depth, of $5 \pm 2 \cdot 10^{-3}$ [81], which is in perfect agreement with the Apollo 15-17 curve.

The two-way attenuation calculated at 60 and 500 MHz is reported in Fig.(6.18). The attenuation is calculated only for three simulants: LHS-1, OPRL2N and OPRL2NT

that are the three samples that represent the end-members and intermediate values of complex permittivity in Tab(6.2). The attenuation results show that between the two frequencies there is a factor 10 in terms of signal attenuation, assuming that the analogues are representative of lunar material. The lunar penetrating radar on board Chang'è 3 and 4 missions present a dynamic range of about $80 - 90 \text{ dB}$ [41]; if the analogues properly simulate the Chang'è 3 and 4 landing sites, the information retrieved by the GPR would be effective only for the first $\sim 30 \text{ m}$ below the surface that is in contrast with the results proposed by Li et al. [81], where they were able to show subsurface features into the lunar radargram up to the first 40 m after the application of specific processing techniques.

6.7 Conclusions

This chapter presents the measurements carried out on the 9 regolith analogues with the VNA set-up in function of frequency and varying the compaction of the sample inserted into the measurement cell. In section 6.5.1, the data of the real ε' and imaginary part ε'' of permittivity as a function of frequency are reported. These results are then compared with the extensive literature available on dielectric measurements performed on Apollo samples. The real part of permittivity reported in Fig.(6.5) to (6.8) shows no dependence with frequency like the Apollo regolith samples that were dielectrically tested and reported in several works [72][129][2][102] while the imaginary part slightly increases with frequency, and it ranges between 10^{-1} to 10^{-2} which is the typical range of value for powder samples [2]. The effect of porosity on dielectric properties of loose material were also conducted and reported in [117][60][9] where a strong dependence of ε' with compaction stands out. The total variability of ε' obtained in this work with more than 190 measurement is $1.8 - 3.3$ which is in good agreement with dielectric measurements conducted on lunar regolith samples [2].

Starting from the frequency spectra, data are selected in order to extrapolate dielectric parameters and applying models. Data are averaged over the frequency range $100 - 200 \text{ MHz}$ to smooth data from spurious spikes. Through the application of mixing models, dielectric parameters were extrapolated as the powder samples were solid rocks (at virtually zero porosity) see Tab(6.2) and Fig.(6.14). The extrapolation of solid data was made to conduct separate analysis on powder and rock samples, while in the major literature the results are always discussed together [59]. The powder data of ε' were compared to the literature data in Fig.(6.13) and also compared to the well-known models as a function of density like the Olhoeft equation eq.(6.28). The results confirm that the powders have an exponential trend with bulk density but the Apollo samples appears constantly below the curve while the simulants data are above eq.(6.28). This outcome is attributed to the fact that eq.(6.28) was obtained fitting the whole data set of lunar regolith and lunar rocks data; in fact in [59] other curves were presented in order to obtain a more accurate description of regolith data, using the model 1.87^{ρ} and other curves for subsets like Apollo 15-17 data and data at 450 MHz measured by Gold [53][51][50].

Starting from these considerations, the next natural step within the analysis was the study of oxide ($\%TiO_2 + \%FeO$) content and $\tan\delta$ in section 6.6.2. In this case the values of permittivity at $\Phi = 0$ are used to calculate $\tan\delta_g$ using eq.(6.30) and make a comparison with lunar rocks data. This result represents a novelty in this context since there is no models and study of oxide content and energy losses for rocks data. In fact,

eq.(6.29) from [59] was retrieved for the entire data set of soil and rocks data where soil data are the majority of the data sets, posing a different weights on the final result. The curve shown in eq.(6.31) is obtained in this work fitting the results of the regolith analogues and the selected data of lunar rocks reported in Tab.(6.3). The $\tan\delta_g$ from regolith data are retrieved at $\Phi = 0$, like the powder samples were totally compacted as a rock sample. In the reality, rocks are not characterized by porosity equal to zero since they may present cracks and bubbles within the matrix. In fact in Fig.(6.14) the lunar rocks data are slightly below the values of the regolith analogues, highlighting that the real rocks might present internal cracks and $\Phi \sim 0$. The $\tan\delta_g$ results have to be considered as end-member values, since in the reality the loss tangent of rocks can be lower.

In chapter 5 are summarized the mineralogical analysis of the regolith analogues. The *vol%* of plagioclase, pyroxene, olivine and ilmenite of simulants are used to plot the complex permittivity in function of these quantities in Fig.(6.15) and (6.16). The mineralogical composition of analogues (see table 5.7) is strongly different from the real Apollo samples since the simulants are made with no agglutinates. In this context a comparison with Apollo samples is not presented and just a qualitative description is made. It is important to emphasize that an analysis of EM properties in terms of mineralogy of Apollo samples has not been previously presented and may be more accurate than an analysis based on chemical composition, as done so far considering parameters such as the loss tangent, iron, and titanium oxides. The lunar analogue samples used in this work, while significantly different from the actual Apollo samples in terms of mineralogy, exhibit dielectric properties consistent with existing literature [129][102][2][24][50][51]. The literature is extensive but lacks uniformity, and it can also be quite complex to obtain full comprehension of the phenomena. A clear example of this can be seen in Tab.(6.3), where dielectric measurements for various Apollo samples are conducted by different authors under varying environmental conditions and at different frequencies. While it is true that dielectric properties appear to be frequency-independent, comparing data at frequencies with differences of one or two orders of magnitude may not be entirely accurate. It is crucial to underline that the purpose of this study is not to determine whether these samples are reliable lunar analogues or not. A more comprehensive analysis would require a larger samples set and, most importantly, a systematic evaluation of all Apollo samples using data at the same frequency and consistent sample preparation methods. Hence, a thorough and meticulous review of the literature is necessary to gain a clear and precise understanding of the overall context.

The attenuation profile shown in Fig.(6.18) is of particular interest due to its interpretive implications, which lead to a clear dichotomy. In one scenario, we can infer that the lunar simulators used in this work do not accurately replicate the lunar zones investigated during Apollo missions and with Chinese Lunar Penetrating Radar (LPR), thus yielding samples that are excessively attenuating in comparison to lunar regolith. Alternatively, the graph in Fig.(6.18) indicates an issue with the density curve. This curve was derived from data obtained from the sole drilling operation conducted during the Apollo missions, and the authors themselves assert its validity only up to a depth of approximately 10 meters [59]. Stratigraphic models proposed in [86] [81] show a more complex scenario than the one described in [114] and [142]. Beneath the regolith layer, a transition zone begins, characterized by a mixture of regolith, rock and blocks. In this context, the density variation below the initial 10 – 15 meters is considerably

more complex than what is described by a nearly constant linear trend, as presented in Eq.(6.33).

Chapter 7

Dielectric measurements in function of temperature on dry and saturated regolith analogues

7.1 Introduction

In this chapter are reported the measurements conducted at varying temperature using a capacitive measurement cell (filled with powder samples) connected to a LCR meter. This apparatus covers the frequency spectrum $20\text{ Hz} - 1\text{ MHz}$ (AgilentHP4284A). The set-up was also integrated to explore the dielectric behavior as a function of temperature $200\text{ K} - 350\text{ K}$ via means of a climatic chamber (Angelantoni DY340C). The analogues were tested in dry conditions but also mixed with distilled water ice, in order to assess the dielectric differences of the two scenarios. The next sections describe the characteristics of the equipment and the methodology used to perform the measurements samples preparation and the experimental results.

7.2 LCR meter set-up

The LCR meter instrument allows to study the dielectric property by measuring the resistance, capacitance and inductance of the Material Under Test MUT. This technique is suitable to test material in the low frequency range ($10 - 10^7\text{ Hz}$).

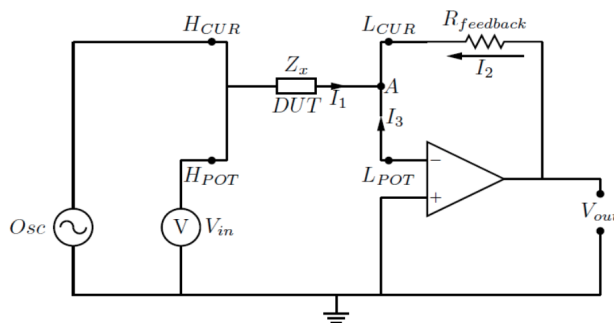


Figure 7.1: The LCR meter equivalent electric circuit can be represented by an operational amplifier in inverted configuration where the oscillator sends a sinusoidal input to the Device Under Test DUT and the feedback resistor can vary the current range that flows through the DUT.

The circuit can be represented as an operational amplifier set on the inverted configuration. The system is excited by the oscillator (Osc) that sends sinusoidal voltage inputs and the feedback resistor $R_{feedback}$ enables to change the measuring range of the current that flows through the DUT.

The instrument measures the Amplitude and Phase of the output voltage V_{out} , while the voltmeter measures the same parameters of the input voltage V_{in} , that is generated by the oscillator.

The MUT is placed into a capacitive cell and connected to the circuit by four coaxial cables that are denominated H_{cur} , H_{pot} , L_{cur} and L_{pot} in Fig.(7.1) that stand for high and low current/potential. Considering the circuital approach, the MUT is marked by the impedance Z_x that can be estimated through the Kirchhoff's junction rule over the A node:

$$\sum_i I_i = 0 \quad \rightarrow \quad I_1 + I_2 + I_3 = 0 \quad (7.1)$$

The current I_1 that flows through the MUT is given by the ratio of the input voltage and the MUT impedance, eq.(7.2); the current I_2 that flows through the feedback resistance is also given by the ratio of the output voltage and the $R_{feedback}$ itself, eq.(7.3) and the current I_3 is equal to zero assuming infinite input impedance of the operational amplifier, recalling the principal of the virtual mass, eq.(7.4). After substituting all the correct terms into eq.(7.1), the MUT characteristic impedance Z_x is given by eq.(7.5).

$$I_1 = \frac{V_{in}(\nu)}{Z_x(\nu)} \quad (7.2)$$

$$I_2 = \frac{V_{out}}{R_{feedback}} \quad (7.3)$$

$$I_3 = 0 \quad (7.4)$$

$$Z_x = -\frac{V_{in}(\nu)}{V_{out}} R_{feedback} \quad (7.5)$$

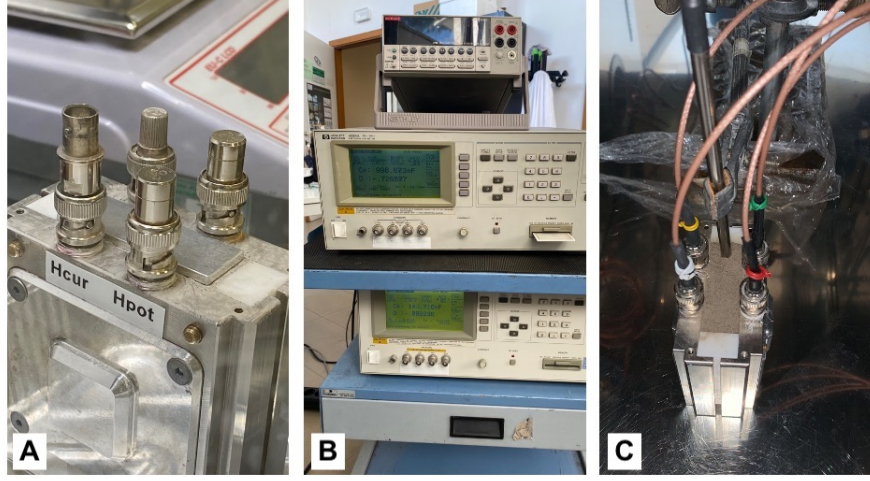


Figure 7.2: LCR meter experimental set-up emplaced to test the dielectric properties as function of temperature between 20 Hz and 1 MHz. A) shows the parallel plate cell, B) the LCR meters and C) shows the cell filled with analogue into the climatic chamber and the PT 100 to measure the temperature of the sample.

7.2.1 Capacitive cell dielectric measurements

The DUT is placed in a flat parallel plate capacitor that is connected to the LCR meter. The dielectric parameters of the DUT are retrieved via means of the study of the equivalent circuit of the system set in a parallel configuration. The equivalent circuit shown in Fig.(7.3) and the following discussion are the same reported in Chapter(2) to define the complex dielectric permittivity, see pag.(30). To avoid redundancy, here are only reported the essential steps to retrieve the dielectric parameters from the LCR meter measurements.

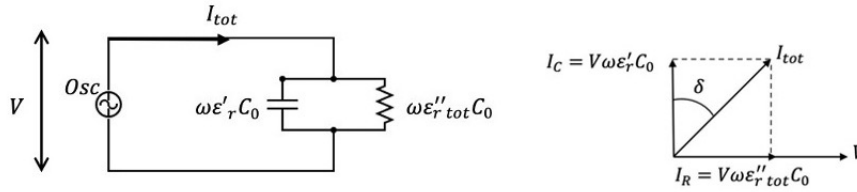


Figure 7.3: Equivalent circuit system (parallel configuration) of a flat capacitor powered by an alternating current. The resolution of the system allows to evaluate the dielectric parameters of the DUT inserted into the capacitive cell. On the right side is reported the vectorial current diagram of the system.

The total current that flows through the system is given by the sum of the charge and loss current, eq.(7.6) is expressed in terms of the relative permittivity ϵ_r . Tanking into account that $\epsilon''_{r\ tot} = \epsilon''_r + \sigma/\omega\epsilon_0$, we can simplify the formula and express it in terms of resistance and reactance, see eq. (7.7).

$$I_{tot} = I_c + I_r = V(j\omega C + G) = V(j\omega C_0 \epsilon'_r + \omega C_0 \epsilon''_r + \frac{\sigma}{\epsilon_0}) \quad (7.6)$$

$$I_{tot} = V(j\omega C_0 \varepsilon'_r + \omega C_0 \varepsilon''_{r_{tot}}) \quad (7.7)$$

Since the LCR meter directly measure the capacitance $C_p(\nu)$ and $\tan\delta(\nu)$ at varying frequency, we can simply calculate the real part of permittivity as follow:

$$C = \varepsilon'_r C_0 \rightarrow \varepsilon'_r = \frac{C_p(\nu)}{C_0} \quad (7.8)$$

where ν is the selected frequency and C_0 is the air capacitance that is obtained acquiring the measurement of the empty parallel plate cell. The quantity C_0 can also be retrieved through the capacitive cell formula, eq.(7.9), that contains the geometrical factor of the cell itself and this value is used to check the measured quantity C_0 after the calibration procedure.

$$C_0 = \varepsilon_r \varepsilon_0 \frac{\pi r^2}{d} = 8.85 \cdot 10^{-12} (F/m) \frac{\pi (0.027 m)^2}{0.0035 m} = 5.79 \pm 0.04 pF \quad (7.9)$$

where d and r are the distance between the plates of the cell and the radius of the plates respectively. The associated uncertainty is given by the error propagation law given by:

$$\Delta C_0 = \pm \sqrt{\left(\frac{\partial C_0}{\partial r}\right)^2 (\Delta r)^2 + \left(\frac{\partial C_0}{\partial d}\right)^2 (\Delta d)^2} \quad (7.10)$$

The imaginary part of permittivity can be retrieved through the loss tangent which express the ratio between loss current and charge current as shown in diagram in Fig.(7.3).

$$\tan\delta = \frac{1}{\omega C_p(\nu) R_p(\nu)} \quad (7.11)$$

$$\tan\delta = \frac{I_r}{I_c} = \frac{\omega C_0 \varepsilon''_{r_{tot}}}{\omega C_0 \varepsilon'_r} \rightarrow \varepsilon''_{r_{tot}} = \tan\delta(\nu) \varepsilon'_r \quad (7.12)$$

The uncertainties associated to ε'_r and $\varepsilon''_{r_{tot}}$ are calculated via mean of the error propagation law and assuming uniform distribution for the errors dividing for a factor $\sqrt{3}$:

$$\Delta \varepsilon'_r = \pm \frac{1}{\sqrt{3}} \sqrt{\left(\frac{\partial \varepsilon'_r}{\partial C_p}\right)^2 (\Delta C_p)^2 + \left(\frac{\partial \varepsilon'_r}{\partial C_0}\right)^2 (\Delta C_0)^2} \quad (7.13)$$

$$\Delta \varepsilon'_r = \pm \frac{1}{\sqrt{3}} \left(\frac{\Delta C_p}{C_0} + \frac{C_p \Delta C_0}{C_0^2} \right) \quad (7.14)$$

$$\Delta \varepsilon''_{r_{tot}} = \pm \frac{1}{\sqrt{3}} \sqrt{\left(\frac{\partial \varepsilon''_{r_{tot}}}{\partial D}\right)^2 (\Delta D)^2 + \left(\frac{\partial \varepsilon''_{r_{tot}}}{\partial \varepsilon'_r}\right)^2 (\Delta \varepsilon'_r)^2} \quad (7.15)$$

$$\Delta \varepsilon''_{r_{tot}} = \pm \frac{1}{\sqrt{3}} (\varepsilon'_r \Delta D + D \Delta \varepsilon'_r) \quad (7.16)$$

where $D = \tan\delta$.

Calibration

The zeroing calibration procedure is performed prior to each measurement. This operation allows to measure the stray parameters which are then used to correct data, ensuring the correct measurement of the DUT parameters without fixture errors or adaptor capacitance. The resulting calibration is stored into the LCR internal memory.

The open circuit measurements is carried out to determine the stray admittance $Y_{open} = 1/Z_{open}$, which corrects high impedance measurements. The short circuit measurement returns the so called residual impedance Z_{short} that compensates low impedance measurements. Eq.(7.17) shows how the actual impedance measure Z_{meas} is corrected to obtain the real parameter of the DUT.

$$Z_x = \frac{Z_{meas} - Z_{short}}{1 - (Y_{open} \cdot Z_{meas})} \quad (7.17)$$

7.3 Samples preparation

Dry samples

Prior to each measurement for the dielectric testing of dry regolith, the analogues were dried in a vacuum oven (SalvisLab) at $105^\circ C$ for 24 hours, to remove any residual moisture that strongly affects data. For the dry tests were conducted two separated measurements with the climate chamber denominated *cooling* and *heating* cycle as explained in detail in the following section. For both measurements were applied the sample treatment for the sample and the measurement cell was filled with almost the same mass of simulant in order to obtain a comparable data for the whole temperature cycle under test. It is important to note that filling the cell with the exactly same quantity of powder is very difficult due to the high porosity and small grain size of samples.



Figure 7.4: The dry samples were tested at varying temperature and they were placed in a vacuum oven (left panel) for 24 hours to eliminate residual moisture. On the right panel is reported the capacitive cell connected to the LCR meter and filled with dry analogue.

| Cooling cycle | | | | | | | | |
|---------------|------------|-------------------|----------------------------------|---|----------------------------------|---|---------------|----------------------|
| Simulant | m (g) | σm (g) | ρ_b (g/cm ³) | $\sigma \rho_b$ (g/cm ³) | ρ_g (g/cm ³) | $\sigma \rho_g$ (g/cm ³) | Φ (%) | $\sigma \Phi$ (%) |
| LHS-1 | 32.920 | 0.003 | 1.206 | 0.009 | 2.7850 | 0.0008 | 56.70 | 0.42 |
| LHS-1D | 27.580 | 0.003 | 1.010 | 0.007 | 2.7744 | 0.0067 | 63.59 | 0.49 |
| LMS-1 | 44.300 | 0.003 | 1.623 | 0.012 | 3.0506 | 0.0013 | 46.81 | 0.34 |
| LMS-1D | 21.140 | 0.003 | 0.774 | 0.006 | 2.8334 | 0.0021 | 72.67 | 0.54 |
| OPRH2N | 27.500 | 0.003 | 1.007 | 0.007 | 2.8154 | 0.0014 | 64.22 | 0.47 |
| OPRH3N | 29.640 | 0.003 | 1.086 | 0.008 | 2.7844 | 0.0016 | 61.01 | 0.45 |
| OPRL2N | 29.780 | 0.003 | 1.091 | 0.008 | 2.8860 | 0.0015 | 62.20 | 0.46 |
| OPRL2NT | 31.790 | 0.003 | 0.000 | 0.000 | 3.0108 | 0.0030 | 61.32 | 0.45 |
| LCATS-1 | 23.150 | 0.003 | 0.000 | 0.000 | 3.1245 | 0.0140 | 72.86 | 0.63 |

Table 7.1: Cooling cycle measurements preparation for the dry analogues tests.

| Heating cycle | | | | | | | | |
|---------------|------------|-------------------|----------------------------------|---|----------------------------------|---|---------------|----------------------|
| Simulant | m (g) | σm (g) | ρ_b (g/cm ³) | $\sigma \rho_b$ (g/cm ³) | ρ_g (g/cm ³) | $\sigma \rho_g$ (g/cm ³) | Φ (%) | $\sigma \Phi$ (%) |
| LHS-1 | 33.540 | 0.003 | 1.229 | 0.009 | 2.7850 | 0.0008 | 55.89 | 0.41 |
| LHS-1D | 28.230 | 0.003 | 1.034 | 0.008 | 2.7744 | 0.0067 | 62.73 | 0.48 |
| LMS-1 | 43.600 | 0.003 | 1.597 | 0.012 | 3.0506 | 0.0013 | 47.65 | 0.35 |
| LMS-1D | 21.190 | 0.003 | 0.776 | 0.006 | 2.8334 | 0.0021 | 72.61 | 0.53 |
| OPRH2N | 27.580 | 0.003 | 1.010 | 0.007 | 2.8154 | 0.0014 | 64.12 | 0.47 |
| OPRH3N | 29.990 | 0.003 | 1.099 | 0.008 | 2.7844 | 0.0016 | 60.55 | 0.44 |
| OPRL2N | 30.250 | 0.003 | 1.108 | 0.008 | 2.8860 | 0.0015 | 61.61 | 0.45 |
| OPRL2NT | 34.760 | 0.003 | 0.000 | 0.000 | 3.0108 | 0.0030 | 57.71 | 0.43 |
| LCATS-1 | 23.080 | 0.003 | 0.000 | 0.000 | 3.1245 | 0.0140 | 72.94 | 0.63 |

Table 7.2: Heating cycle measurements preparation for the dry analogues tests.

Saturated samples

The dry regolith analogues are saturated with distilled water in order to obtain a ice/regolith mixture with the climatic chamber. Once the grain density of the sample is noted it is possible to retrieve the volume of voids (porosity). In eq.(7.18) V is the total volume, m is the mass of dry powder and ρ_g the grain density of given sample measured with the pycnometer that are reported for each analogues in Tab.(5.6). Φ is the porosity of the dry powder, which indicate the volume of voids between powder particles. Φ is filled with distilled water up to the saturation of the sample. Conversely to the measurement of dry analogues, in this case the powders are not dried-out in the vacuum oven since it is saturated with distilled water. In Tab.(7.3) is reported the details of measurements, the estimated porosity, volume fractions and related uncertainties. For the measurements of saturated regolith 2 samples were omitted due to their dusty nature. The grain size distribution of LHS-1D and LMS-1D is so low that is difficult to estimate properly the porosity and thus the quantity of water to use in order to obtain saturated mixtures.

$$\Phi = 1 - \frac{m/V}{\rho_g} \quad (7.18)$$

| SAMPLE | Φ (%) | $\sigma\Phi$ (%) | f | σf | $(1-f)$ | $\sigma(1-f)$ |
|---------|------------|------------------|-------|------------|---------|---------------|
| LHS-1 | 46 | 7 | 0.531 | 0.077 | 0.469 | 0.068 |
| LMS-1 | 42 | 4 | 0.583 | 0.047 | 0.417 | 0.034 |
| OPRH2N | 51 | 5 | 0.490 | 0.051 | 0.510 | 0.053 |
| OPRH3N | 53 | 6 | 0.465 | 0.052 | 0.535 | 0.060 |
| OPRL2N | 50 | 5 | 0.506 | 0.050 | 0.494 | 0.049 |
| OPRL2NT | 52 | 6 | 0.480 | 0.048 | 0.520 | 0.052 |
| LCATS-1 | 65 | 9 | 0.349 | 0.046 | 0.651 | 0.086 |

Table 7.3: Details of sample preparation of ice/regolith mixtures. The tab reports the estimated porosity the volume fraction f and $(1-f)$ related to environment and inclusions (water ice and regolith).



Figure 7.5: The left panel shows the capacitive cell filled with the saturated mixture of distilled water and regolith analogue. The right panel shows the measurement cell into the climatic chamber connected to the LCR meter.

7.4 Temperature cycles

To investigate the dielectric properties of dry regolith analogues under lunar-like conditions, temperature-dependent tests were performed using a climatic chamber (Angelantoni DY340C) over the temperature range of 200 K to 350 K. Due to humidity contamination, the temperature cycle was divided into two parts. The cooling cycle involved lowering the temperature from 300 K to 200 K, while the heating cycle involved raising the temperature from room temperature to 350 K at a rate of 0.05 K/min Fig.(7.6). The collected data from both cycles were combined to obtain the overall temperature trend. For the cooling cycle, data during the descent stage (300 K \rightarrow 200 K) were selected, as the analogue remained dry. In the ascent stage (200 K \rightarrow 300 K) data present moisture contamination. Fig.(7.7) shows the ascent and descent stages of the cycle and the effect of humidity on dielectric parameter ϵ'' . The heating cycle was first set to reach a temperature of 450 K but the experimental set-up and cables are not supposed to reach that temperature; to avoid any damage to the set-up was decided to reach 350 – 370 K. Dielectric tests were also conducted for regolith samples

that are completely saturated with distilled water. In this case the temperature range that was tested is 200 K to 300 K at a rate of 0.05 K/min right panel in Fig.(7.6). The temperature variation of samples was monitored using a PT100 (Platinum Resistance Thermometer) connected to a multimeter (Keithley 2700) and directly inserted into the powder Fig.(7.2C). The PT100 provides accurate temperature measurements considering the thermal inertia between the climatic chamber and the simulant inserted into the cell. This fact is well highlighted by the difference of the red and black curve in Fig.(7.6).

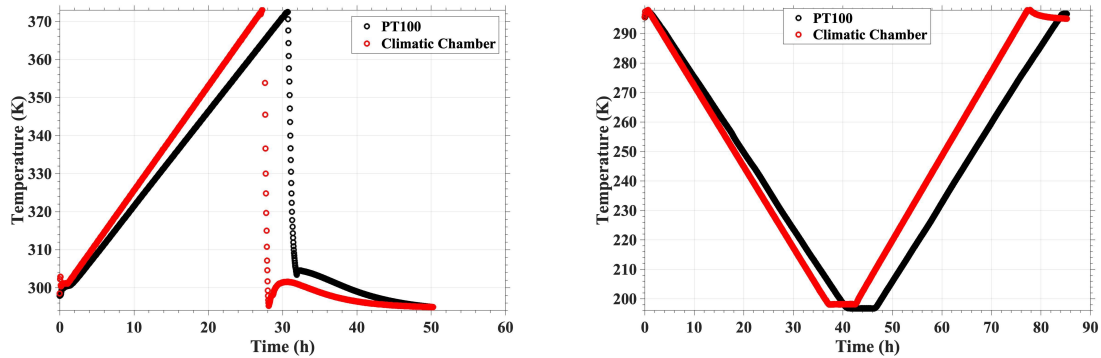


Figure 7.6: Temperature cycles emplaced for testing dielectric properties of analogues samples. The left panel shows the heating cycle involves raising the temperature from 300 K to 370 K at a constant rate of 0.05 K/min. The right panel shows the cooling cycle includes lowering the temperature from 300 K to 200 K at a rate of 0.05 K/min. In both graphs is also shown the thermal inertia observed between the climatic chamber and the lunar analogue within the cell. While the climatic chamber reaches a specific temperature, there is a delay for the lunar analogue to reach the same temperature. The temperature recorded by the climatic chamber is the red red curve and the temperature of the analogue within the cell, measured using a PT100 sensor is reported with the black curve.

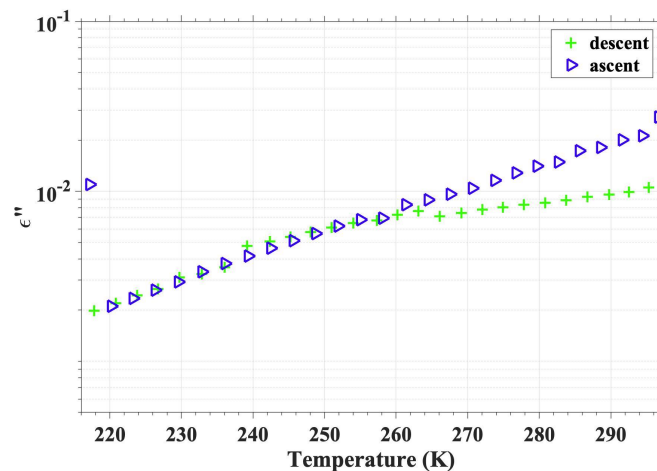


Figure 7.7: Comparison of the descent and ascent stages of the cooling cycle of sample measurement. During the ascent stage, which takes place after 50 hours, the dry sample experiences humidity contamination, leading to an impact on the dielectric parameters (indicated by the red circle). For temperatures between 200 K and 250 K, data from both stages perfectly overlap. We utilized the descent stage of the cooling cycle and the ascent stage of the heating cycle, ensuring comprehensive analysis and correlation of the experimental results.

7.5 Measurement results

7.5.1 Dielectric properties as a function of frequency

In Fig.(7.8) are reported the real and imaginary part of dry simulants measured in the frequency range $20 - 10^6 \text{ Hz}$. Real part of permittivity ϵ' on the left panel appears frequency independent for frequencies above 10^4 Hz . Some polarization effects may occur for frequency below 10^3 Hz producing data distortion, that doesn't affect much the results since for radar applications we are interested in higher frequencies results. The right panel shows the imaginary part ϵ'' that ranges between $10^{-2} - 10^1$ exhibiting descent trend at increasing frequency. Data were selected at temperature of 273 K .

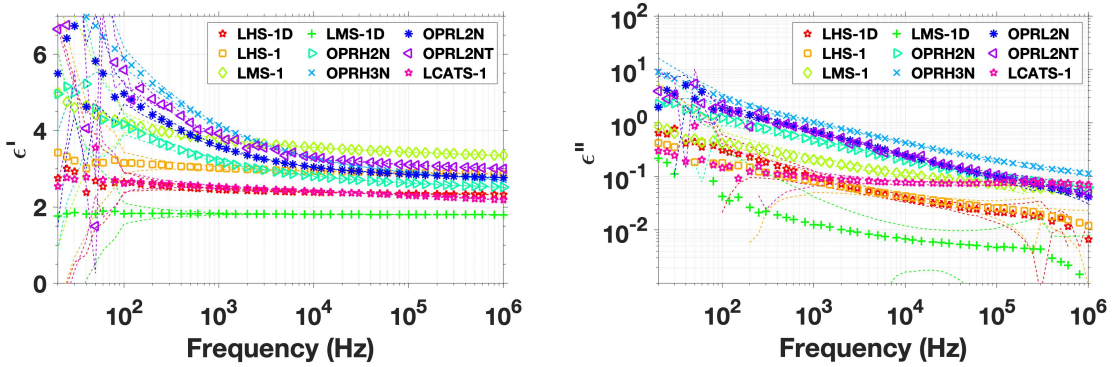


Figure 7.8: Dielectric properties of dry regolith analogues in the frequency range $20 \text{ Hz} - 1 \text{ MHz}$ at 273 K . Left panel reports the real part of permittivity, right panel reports the imaginary part.

Due to the presence of water/ice, which has a major impact on the dielectric characteristics, the behavior of a saturated mixtures is fundamentally different. Temperature has a considerable impact on frequency spectra in this second case. Figures (7.9) and (7.10) show six panels with frequency spectra of complex permittivity at various temperatures: $200, 220, 250, 273, 290,$ and 300 K . The real part ϵ' reveals that at frequencies below 10^4 Hz , temperature has a considerable impact, becoming practically flat and constant at lower temperatures, as seen in the upper row of Fig.(7.9). The frequency spectra above 10^4 Hz , on the other hand, exhibit a consistent trend at any temperature that is under test. The imaginary part ϵ'' decreases at increasing frequency presenting a very sharp trend occurring from room temperature to 273 K . Below the freezing point the frequency spectra below $3 \cdot 10^3 \text{ Hz}$ begin to fluctuate, becoming rather flat for lower frequencies.

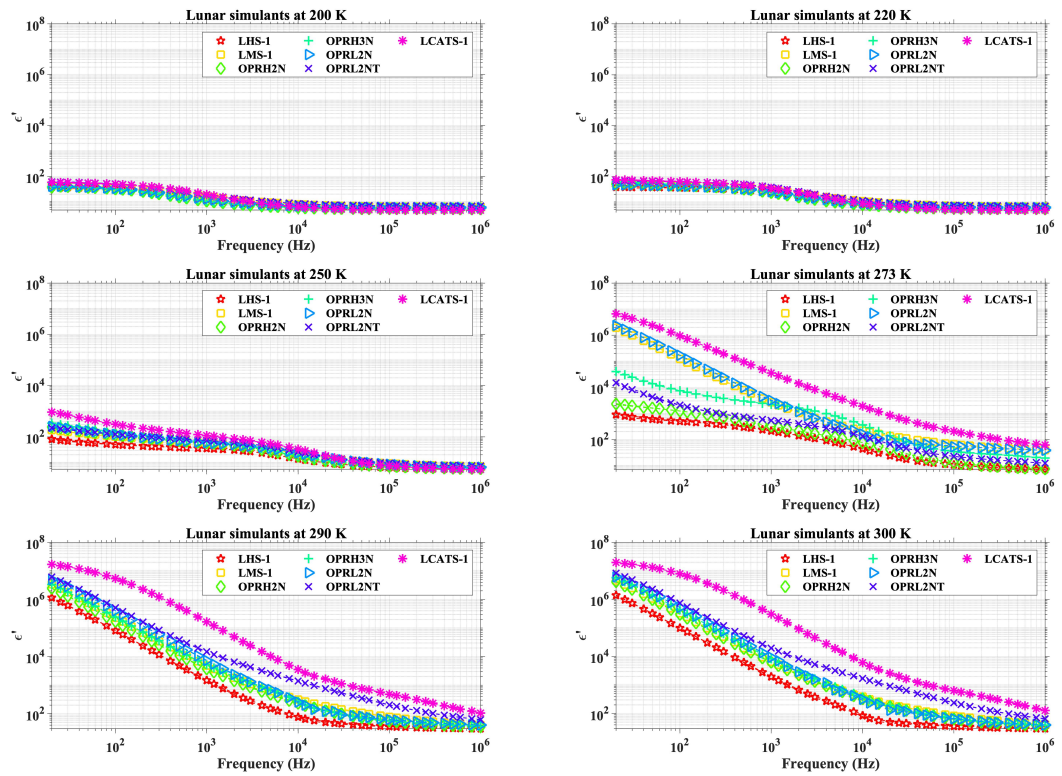


Figure 7.9: Frequency spectra of real part of permittivity of saturated mixtures at varying temperature between 200 K to 300 K.

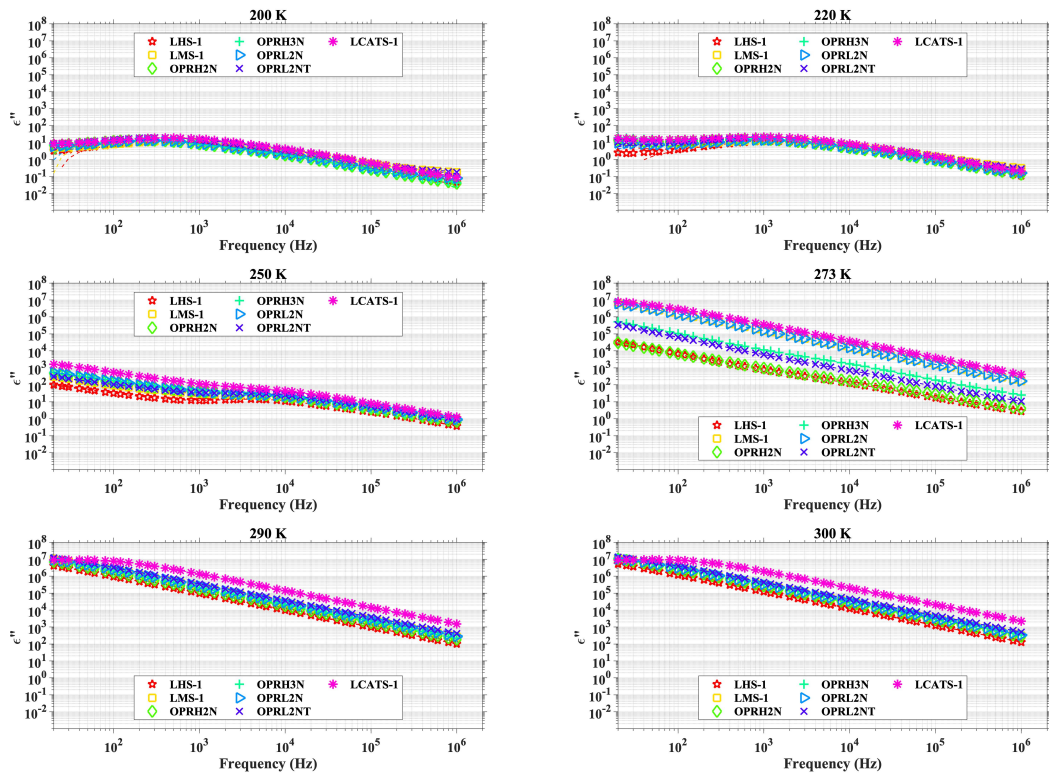


Figure 7.10: Frequency spectra of imaginary part of permittivity of saturated mixtures at varying temperature between 200 K to 300 K.

The conductivity σ of the two scenarios is reported in Fig.(7.11) at two different temperatures: 200 and 300 K. The upper row shows σ (S/m) of dry analogues (left panel) and saturated mixtures on the right panel at 200 K, respectively. The presence of water ice slightly impact the conductivity for frequencies over $2 \cdot 10^3$ where it seems to be almost flat in frequency. At 300 K the distilled water still increases the conductivity if compared to the dry scenario, in fact in the right panel σ (S/m) ranges between $4 \cdot 10^{-3}$ to 10^{-1} but is constant over the frequency spectrum, while the dry analogues present the same conductivity of the frozen case. The LCATS-1 sample when saturated shows dielectric behavior similar to clays, in fact the conductivity is 1 order of magnitude higher than the other saturated mixtures, but also the real part at room temperature reaches values above 120 at 1 MHz and at very low frequencies it can reach $\epsilon' \sim 10^3$.

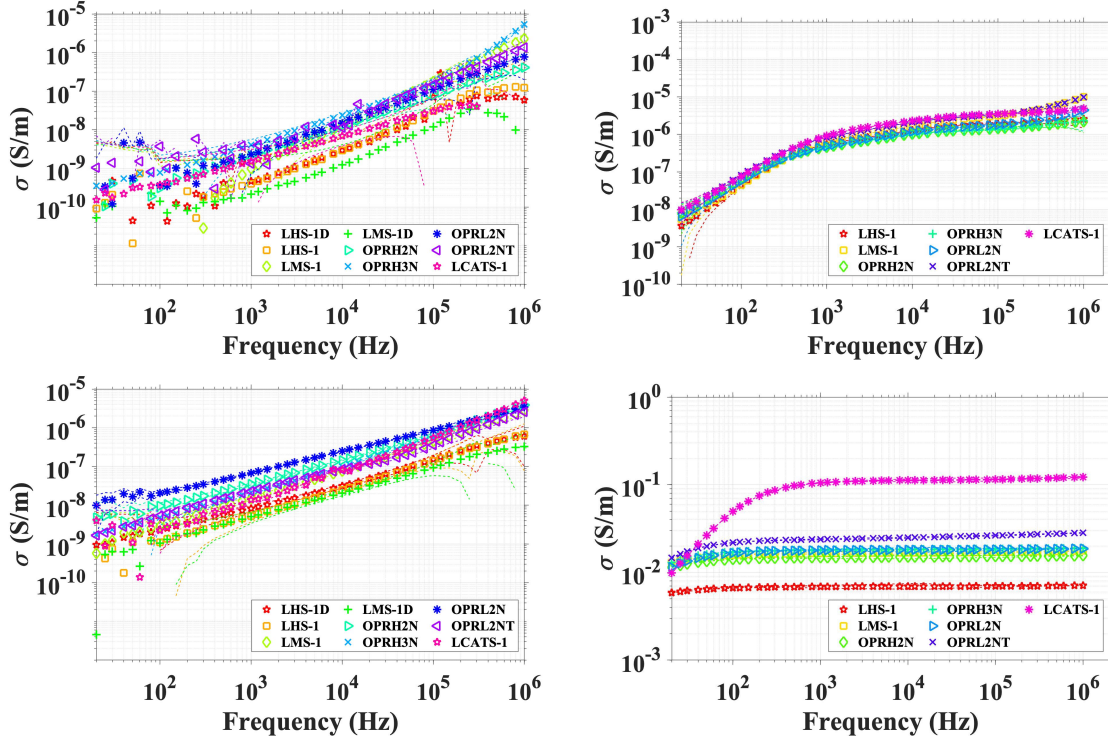


Figure 7.11: *Electrical conductivity of the two scenarios. In the upper row is reported the comparison of electrical conductivity measured at 200 K for dry simulants (left panel) and the ice/regolith mixtures (right panel) In the bottom row there is the same comparison but the conductivity is measured at 300 K.*

From the frequency spectra of both scenarios data were selected at 1 MHz in order to discuss in the following sections the trends as a function of temperature. All graphs reported also include measurement uncertainties that were determined based on the specifications provided by the instrument. Uncertainties were calculated using a type B standard model with a uniform distribution.

7.5.2 The effect of temperature

The dielectric behavior of dry analogues at varying temperature was tested with a climatic chamber and the dielectric parameters are reported in Fig.(7.12). ϵ' can be assumed constant over the temperature under test range since the percentage variation of data is around 3–4%. The imaginary part ϵ'' reported in the bottom row of Fig.(7.12) increases at increasing temperature in the range 200 – 300 K and it becomes constant over the temperature range for T above 300 K. Note that at a very low temperature the measure of the imaginary part can't be considered much reliable due to the instrument limitations. Results of LHS-1D, LMS-1D, OPRH3N and LCATS-1 were omitted since the imaginary part in below 10^{-2} and in some cases the measurements were corrupted by noise, broken cell connector and/or laboratory electrical problems that occurred during the laboratory activities.

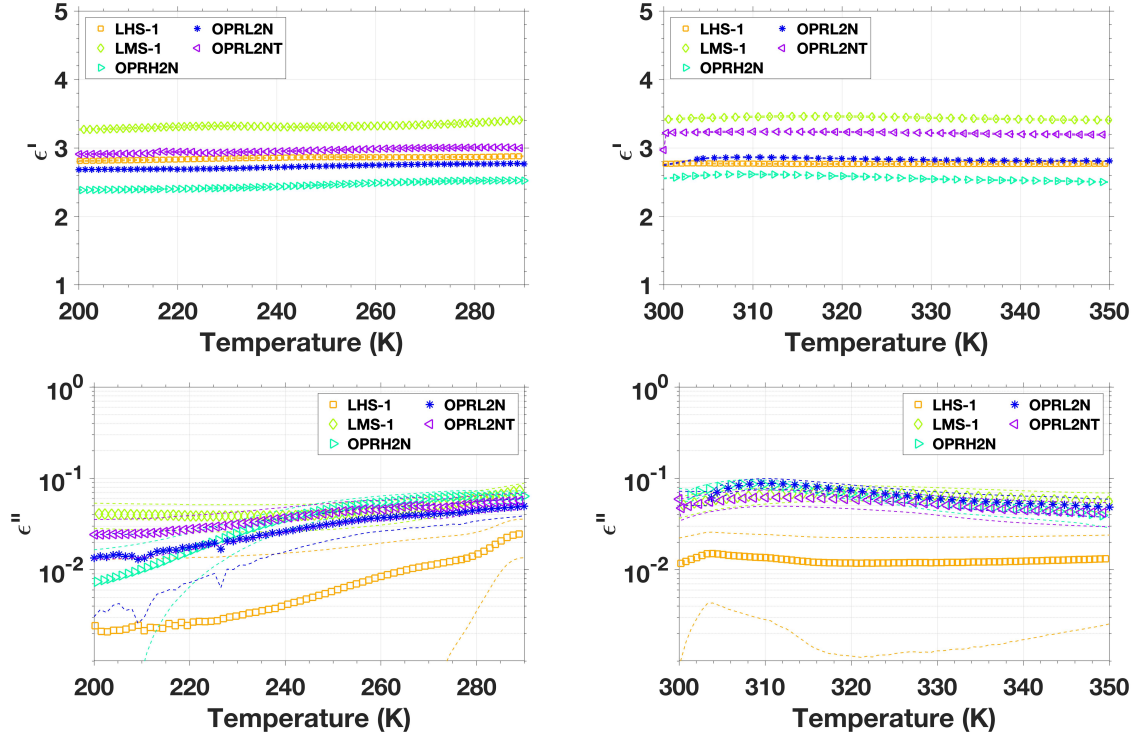


Figure 7.12: Dielectric properties of dry regolith analogues selected at 1MHz at varying temperature. The upper row reports the real part of permittivity, the bottom panels report the imaginary part.

The saturated mixtures exhibit a more complicated behavior. In Fig.(7.13) is reported the phase angle of the samples in the frequency domain at six selected temperatures between 200 – 300 K. The phase angle is a parameter that highlights the typical Debye relaxation processes occurring at varying temperature. In fact, the maximum of the phase angle typically occurs at relaxation frequency and lowering the temperature it moves towards lower frequencies as shown in the upper row of Fig.(7.13). The trend of ϵ' is plotted against temperature in the left panel of Fig.(7.14). The freezing point occurs at about $\sim 273 K$, for all samples dropping the real part of permittivity from 30 – 100 to values of the order of 5 – 8. Below the freezing point the real part appears flat and constant over the temperature range of interest. Regarding the imaginary part ϵ'' , it shows a decreasing trend with temperature in 200 – 300 K range, see right panel of Fig.(7.14). It is important to note that in Fig.(7.14) the complex permittivity is shown over the entire temperature cycle under test explained in previous section.

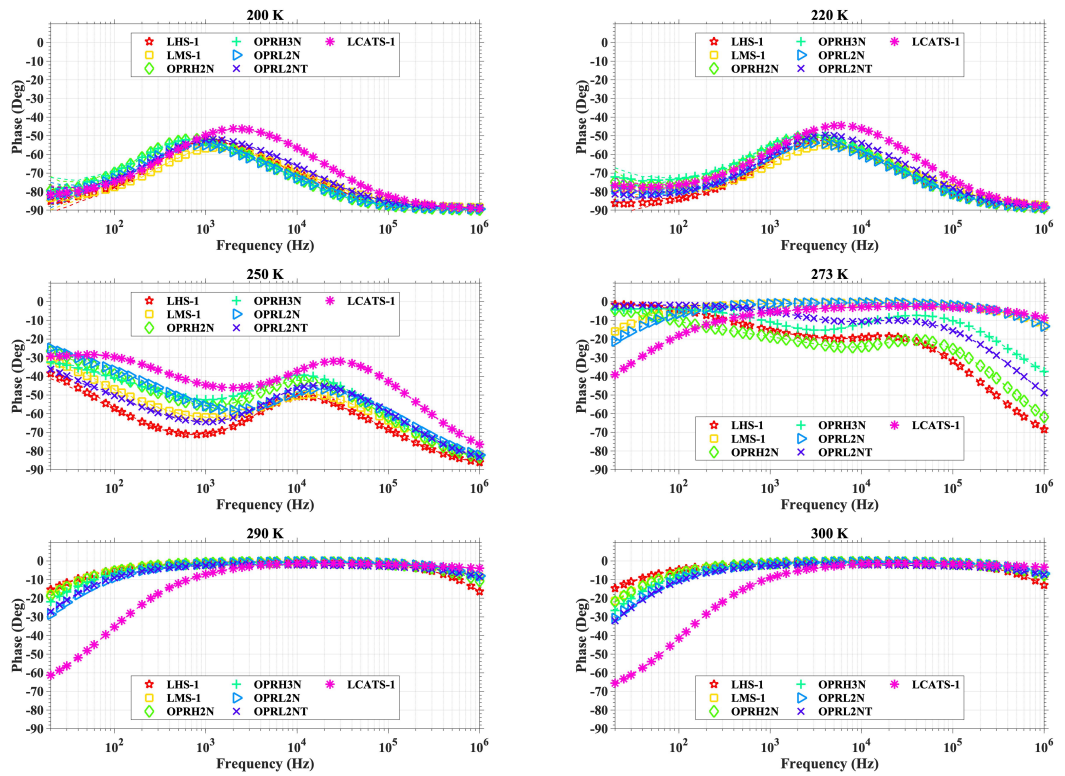


Figure 7.13: Frequency spectra of the Phase angle of saturated samples. Data is selected at varying temperature between 200 K to 300 K to highlight the temperature effect.

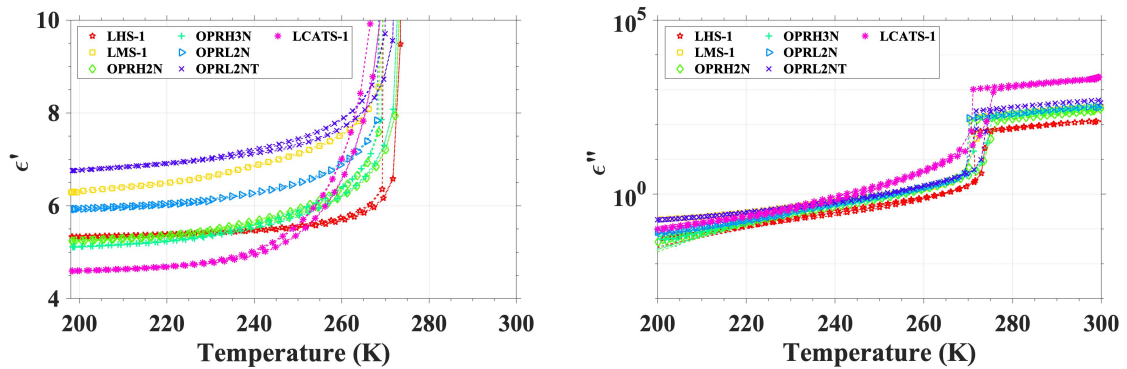


Figure 7.14: Dielectric properties of saturated samples selected at 1MHz at varying temperature. The real part ϵ' is on the left panel, on the right there is the imaginary part ϵ'' that has a clear variation with temperature below the freezing point that occurs at ~ 273 K.

7.5.3 Attenuation estimation

The obtained dielectric parameters are used to derive the attenuation A (dB/km) vs frequency, which may be portrayed as in the case of non-magnetic materials as eq.(7.19) given by [135]. For low loss material the attenuation can also be approximated using eq.(7.20). Fig.(7.15) reports a comparison of the attenuation parameter for the dry samples and ice/regolith mixtures.

$$A_{dB/km} = 8.68 \times 10^3 \left[\frac{2\pi\nu}{c} \sqrt{\frac{\varepsilon'}{2}} \sqrt{\sqrt{1 + \tan^2\delta} - 1} \right] \quad (7.19)$$

$$A_{dB/km} \cong 8.68 \times 10^3 \left[\frac{\sqrt{2}\pi\nu}{c} \frac{\varepsilon'(\nu)}{\sqrt{\varepsilon''(\nu)}} \right] \quad (7.20)$$

The attenuation is calculated using eq.(7.20) over the frequency spectrum $20Hz - 1MHz$ and at 10 different temperatures between $198 - 300 K$. The dry samples present very low level of signal attenuation ranging between $1 - 10^{-4}$ presenting a linear trend with frequency and slight increase at increasing temperature. On the other hand, the presence of ice into the matrix of ice/regolith mixtures change the attenuation parameter where for frequency above $10^4 Hz$ seems to have a more flat trend at increasing frequency. When for temperature above $273 K$ the presence of liquid water increases the attenuation of nearly 3 orders of magnitude compared to the frozen samples. In this section are reported only 3 samples since all the analogues present the same behavior in terms of attenuation and showing them won't add any information. The attenuation uncertainties is nearly $10 - 12\%$ of data and the error bars are not reported in the plot.

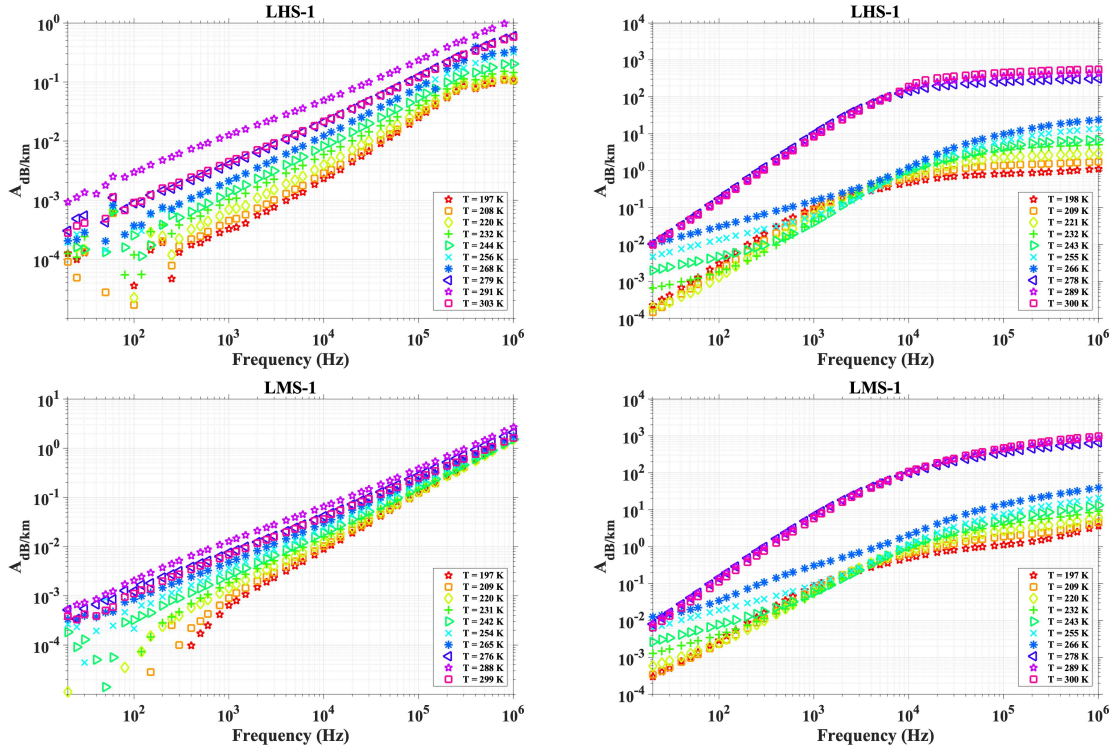


Figure 7.15: Attenuation of dry samples and ice/regolith mixtures in the temperature range $198 - 300 K$ over the frequency spectrum. Left panel shows attenuation calculated for dry samples while the right panel shows ice/regolith mixtures results. First row shows LHS-1 and the bottom row the LMS-1 results.

7.6 Discussion

7.6.1 Activation energy

The lunar surface temperature at the equator varies between $100 K$ and $400 K$. At the polar regions the surface vary between $150 - 200 K$ and $50 - 100 K$, due to the low

incident angle of sunlight [143][122]. The dielectric analyses were conducted replicating the lunar-like conditions, as far as possible considering the operational limitations of the laboratory equipment. The temperature dependence of sample properties can reveal some processes that contribute to the EM behavior at high and low temperatures. ϵ'' of both dry analogues and saturated mixtures shows a slight temperature dependence in the frequency range investigated. Particularly, the dry analogues for temperature below 300 K in the left panel of Fig.(7.12) and the ice/regolith mixtures when the temperature is below the freezing point 273 K showed in Fig.(7.14). We evaluated the activation energy through the Arrhenius model that is shown in eq.(7.21), in the temperature range 198–270 K for both scenarios and the results are listed in Tab.(7.4) and (7.5). The selected data for the application of regression model is at 1 MHz. The activation energy obtained is $E \sim 0 \text{ eV}$ suggesting that the dielectric properties can be tested in a limited temperature range and the data can be extrapolated through the application of models and linear regressions. The presence of water ice appears to introduce a variation with temperature and, generally, when mixed with water ice the activation energy is more than doubled except for the case of LMS-1 where the ϵ'' of the dry sample is almost flat in temperature but when mixed with ice its activation energy registered is $\sim +3500\%$. The regression fit of selected samples are shown in Fig.(7.16), where on the left panel is reported results for dry samples and the right panel shows the ice/regolith mixtures results. The activation energy is not calculated for all samples; some data are affected by noise or corrupted and the estimation of activation energy is not well constrained.

$$\epsilon'' = A \exp\left(-\frac{E}{k_b T}\right) \quad (7.21)$$

| Dry regolith samples | | |
|----------------------|----------|-----------------|
| Simulant | E (eV) | σE (eV) |
| LHS-1D | 0.070 | 0.017 |
| LHS-1 | 0.036 | 0.012 |
| LMS-1 | 0.0020 | 0.0012 |
| OPRH2N | 0.071 | 0.017 |
| OPRL2N | 0.035 | 0.012 |
| OPRL2NT | 0.024 | 0.010 |

Table 7.4: Activation energy of dry regolith samples calculated on data extrapolated at a frequency of 1 MHz and in the temperature range 198–270 K. The parameter is calculated only for samples that present a clear linear trend at varying temperature.

| Ice/regolith mixtures | | |
|-----------------------|----------|-----------------|
| SAMPLE | E (eV) | σE (eV) |
| LHS-1 | 0.087 | 0.019 |
| LMS-1 | 0.069 | 0.017 |
| OPRH2N | 0.115 | 0.022 |
| OPRH3N | 0.116 | 0.022 |
| OPRL2N | 0.097 | 0.020 |
| OPRL2NT | 0.078 | 0.018 |

Table 7.5: Activation energy of ice/regolith mixtures calculated on data extrapolated at a frequency of 1 MHz and in the temperature range 198–270 K. The parameter is calculated only for samples that present a clear linear trend at varying temperature.

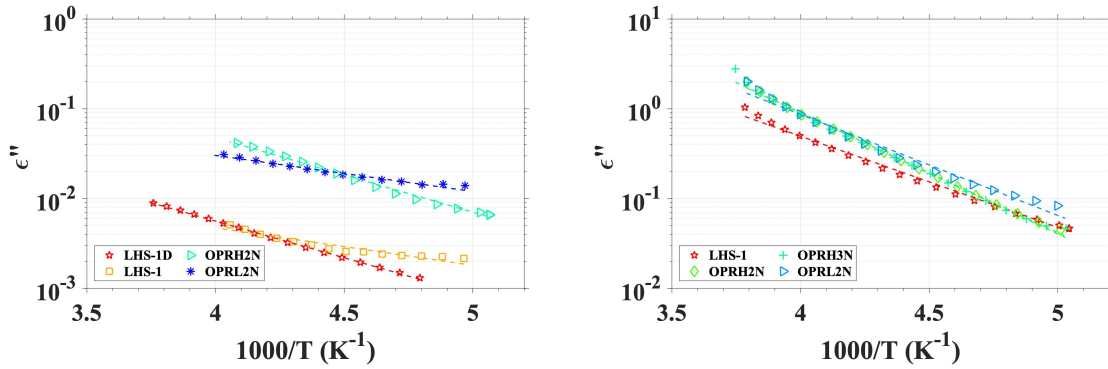


Figure 7.16: Activation energy estimation using the Arrhenius model. The left panel reports the results for dry simulants, the right panel the regression lines obtained on ice/regolith mixtures.

7.6.2 Ice/regolith mixing formula and models

This paragraph reports the analysis of the composite permittivity of the mixture using theoretical models. The dielectric properties of heterogeneous mixtures can be approximated using the so-called mixing formulas, described in [126] and all well summarized in chapter 4. The complex permittivity of the mixture is calculated, both real and imaginary part, and compared to the results of dielectric data measured in the laboratory. In this work the inclusion phase is the powder described by ε_i and volume fraction f and the environment is the water ice (ε_e and volume fraction $(1 - f)$). Input data used for the mixing formulas consisted of the complex permittivity of water ice selected from the Kawada model at frequency of 1 MHz and temperature 200 K ($\varepsilon_{ice} = 3.1 - i0.0012$) [75], as well as the complex permittivity of the simulants' grains ε_g detailed in Tab.(6.2). The permittivity value of the simulants ε_g was estimated using the non-linear regression method from powder data as presented in Chapter 6. The application of mixing formulas was exclusively applied to the imaginary part ε'' for simulants reported in Fig.(6.11). These simulants were chosen due to their distinct trend of imaginary part with bulk density ρ_b , offering a reliable estimation of ε'' of the solid material (permittivity of rocks). The real part ε' of the mixtures measured at 200 K and frequency of 1 MHz is compared to the retrieved values from mixing formulas in Fig.(7.17 and 7.18). The comparison is made with the power laws (Lichtenecker, Linear, CRIM and LLL eq.(7.22)) and the Maxwell-Garnett eq.(7.23). The Wiener bounds were also reported on graphs as the vertical black dotted lines. These bounds

constrain the min a max values that can be obtained via means of mixing formulas. In Fig.(7.19) are also reported the imaginary part ε'' of selected mixtures with the mixing models. The details of samples preparation, samples porosity and volume fractions are summarized in Tab.(7.3).

$$\varepsilon_{eff}^{\beta} = f\varepsilon_i^{\beta} + (1-f)\varepsilon_e^{\beta} \rightarrow \beta = [0; 1; \frac{1}{2}; \frac{1}{3}] \quad (7.22)$$

$$\varepsilon_{eff} = \varepsilon_e + 3f\varepsilon_e \frac{\varepsilon_i - \varepsilon_e}{\varepsilon_i + 2\varepsilon_e - f(\varepsilon_i - \varepsilon_e)} \quad (7.23)$$

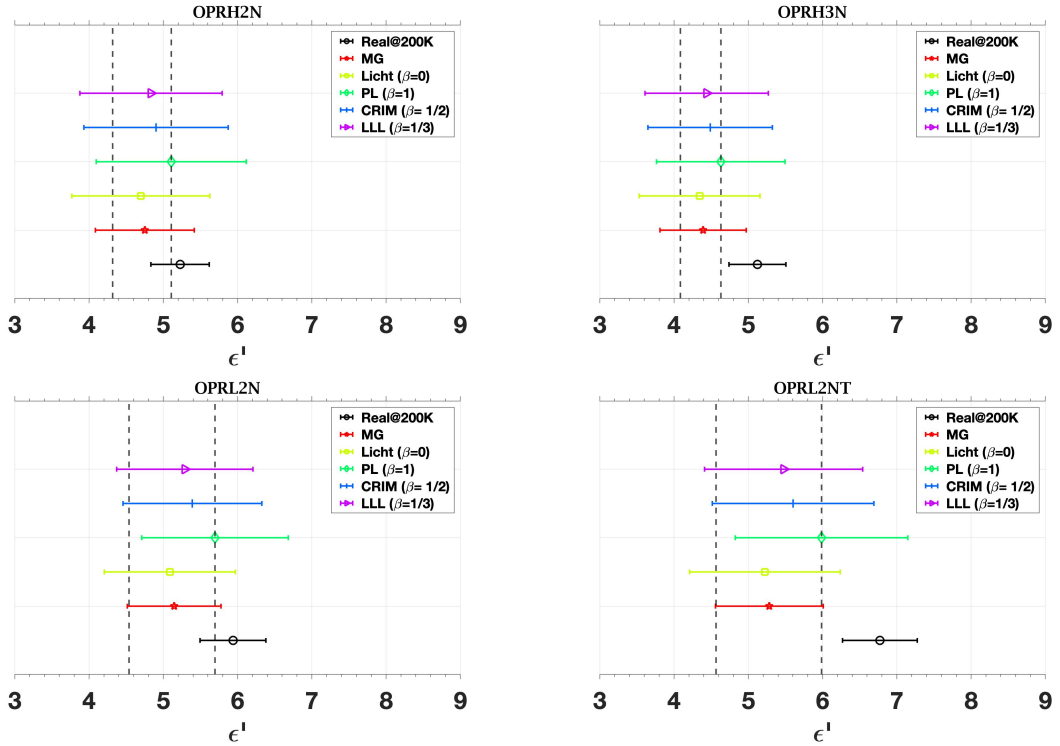


Figure 7.17: Comparison of real part of permittivity estimated using the mixing formulas and the laboratory data selected at 1 MHz and 200 K for the ice/regolith mixtures made with Off Planet Research analogues.

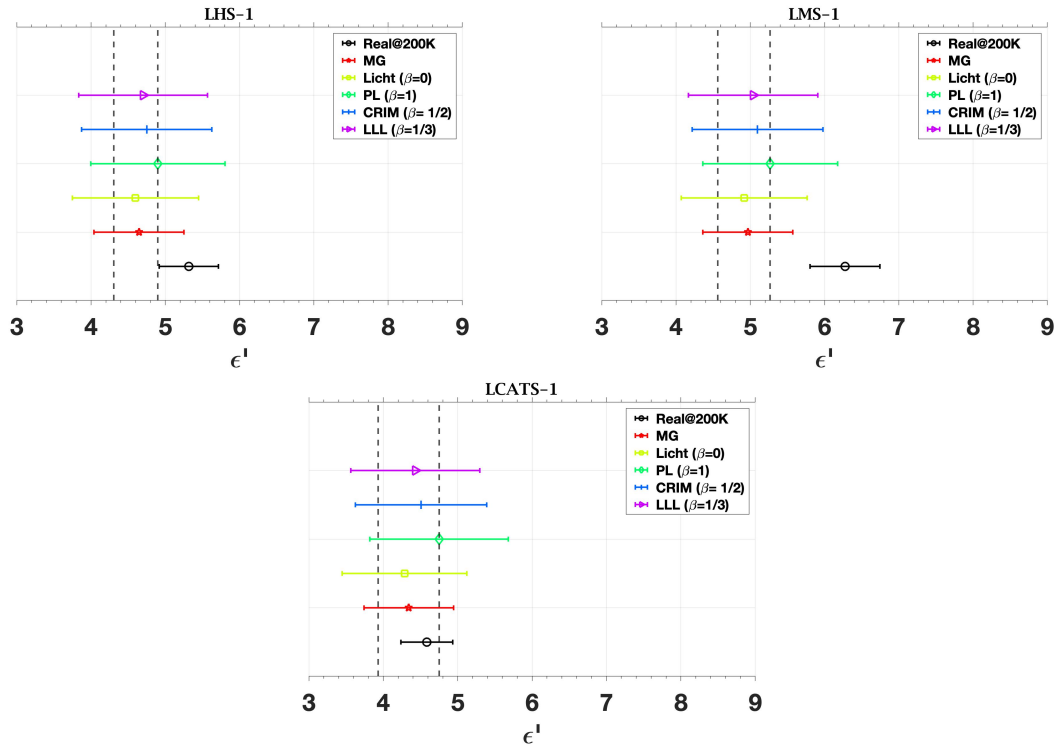


Figure 7.18: Comparison of real part of permittivity estimated using the mixing formulas and the laboratory data selected at 1 MHz and 200 K for the ice/regolith mixtures made with LHS-1, LMS-1 and LCATS-1.

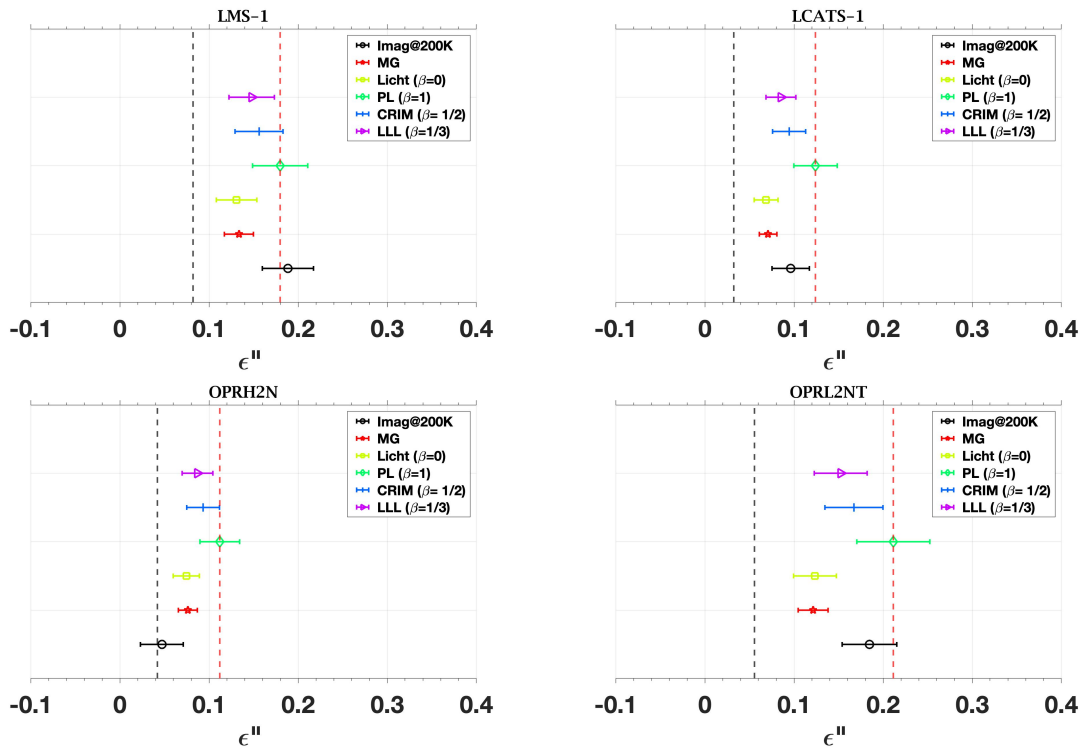


Figure 7.19: Comparison of imaginary part of permittivity estimated using the mixing formulas and the laboratory data selected at 1 MHz and 200 K for the ice/regolith mixtures made with LMS-1, LCATS-1, OPRH2N and OPRL2NT.

| Simulant | ε' | $\sigma \varepsilon'$ |
|-----------------|----------------|-----------------------|
| LHS-1 | 5.32 | 0.40 |
| LMS-1 | 6.27 | 0.47 |
| OPRH2N | 5.23 | 0.39 |
| OPRH3N | 5.12 | 0.38 |
| OPRL2N | 5.94 | 0.44 |
| OPRL2NT | 6.77 | 0.50 |
| LCATS-1 | 4.58 | 0.35 |

Table 7.6: Real part of permittivity ε' of the ice/regolith mixtures measured at 200 K and 1 MHz and compared with the results of mixing formulas.

| Simulant | ε'' | $\sigma \varepsilon''$ |
|-----------------|-----------------|------------------------|
| LMS-1 | 0.189 | 0.029 |
| OPRH2N | 0.047 | 0.024 |
| OPRL2NT | 0.185 | 0.031 |
| LCATS-1 | 0.096 | 0.021 |

Table 7.7: Imaginary part of permittivity ε'' of selected ice/regolith mixtures measured at 200 K and 1 MHz and compared with the results of mixing formulas.

The application of the mixing formulas was performed on the complex quantity of permittivity (both real and imaginary parts). The dielectric parameters obtained using the mixing formulas in Fig.(7.17) and (7.18) reveal an underestimation of ε' of the heterogeneous mixtures. The Wiener limits, represented by the dashed vertical lines, indicate the minimum and maximum values achievable with these models. However, uncertainties associated with individual model estimates exceed these limits due to errors propagated during the preparation of finely ground saturated samples and the estimation of porosity Φ . Notably, the maximum Wiener limit aligns with the calculation obtained from the linear PL model ($\beta = 1$), as expected. The only mixture whose measured value falls within the bounds is that obtained with LCATS-1. The laboratory measurements of ε' consistently exceed the model values. The underestimation of ε' by the models could indicate an overestimation in porosity estimation, implying that the input data have a higher % of water than actually present within the created mixture. The consistent overestimation of real measurements in comparison to the models could indicate a systematic error in porosity estimation. Regarding the comparison of models for estimating ε'' , the results appear more reassuring, with 3 out of 4 results falling within the Wiener bounds. It is essential to emphasize that the models' input data differs fundamentally. The permittivity of inclusions (regolith grains) is detailed in Tab.(6.2), derived from extrapolated data averaged between 100 and 200 MHz at room temperature. The permittivity of the host environment is sourced from the Kawada model for water ice at 1 MHz and temperature of 200 K. The results of dielectric properties for dry regolith samples shown in the previous sections and previous chapter demonstrates that ε' remains nearly constant with temperature but exhibits minor variations on the order of 3 – 4% between 200 and 300 K. Additionally, the measured imaginary part between 200 and 300 K displays a clear decreasing trend with reducing temperature, in Fig.(7.12). Despite these numerous factors, the results are still within 1σ agreement, indicating that the mixing formulas can be considered a valid tool for preliminary estimations of permittivity.

7.7 Conclusions

The aim of this work is not to declare what is the most accurate model among the mixing formulas employed. Consequently, It was decided to utilize the mixing bounds presented in Chapter 4 as error bars for a more appropriate comparison within the range. The complexity involved in mixing formulas, related to grain shape, grain size, and friction, etc, extends beyond the primary focus of this study. The composition of the shallow subsurface on planetary bodies comprises various components and fragments with differing densities, collectively represented by macroscopically averaged physical property values [126]. When considering radar and remote sensing applications, the electromagnetic properties of surface-covering powders notably contrast with those of solid samples. The interaction of EM radiation is intricately associated with multiple factors, such as grain size, shape, orientation, and incident wavelength. Investigating the dielectric properties of heterogeneous mixtures holds crucial importance in comprehending how radiation interacts with these planetary mixtures. The dielectric measurements of ice/regolith mixtures are pivotal for refining the interpretation of radar data, particularly in detecting subsurface water ice [87] [43]. The measurements of the anhydrous simulants demonstrate that they possess dielectric properties comparable to those of real lunar samples previously measured [103] [72]. Once the dielectric properties of the simulants were tested across varying porosity, temperature, and frequency, the subsequent step involved creating ice/regolith mixtures to characterize these samples and assess whether the permittivity changes with the presence of ice within the host environment. The results obtained from the mixtures indicate that the presence of water ice increases the sample's permittivity compared to the permittivity of dry analogues. Hence, under certain conditions, a sufficient dielectric contrast is expected to be present, enabling the potential identification of water ice within the regolith using radar measurements. It is important to note that this study has produced preliminary results, and further exploration through additional measurements and different configurations will be necessary. The experimental set-up used is suboptimal for measuring icy mixtures due to the cell's small volume and the narrow opening for filling the cell, posing challenges for sample saturation and accurate porosity estimation. Subsequent chapter present the results of laboratory measurements using ground penetrating radar on a layer of dry regolith analogue and various icy targets to observe the conditions under which a dielectric contrast is generated and observable in the radargram.

Chapter 8

GPR investigation for water ice detection within the lunar regolith layer

8.1 Introduction

The presence of water ice in permanently shadowed regions of the Moon has been confirmed over the past 30 years [45][29][82]. Water ice is expected to be found within the first 3 meters beneath the lunar surface [125]. Given these facts, a series of laboratory experiments employing the Ground Penetrating Radar were carried out using a dielectric box filled with regolith simulants and buried targets of water ice in order to study the response of the GPR to the lunar-like environment for the detection of water ice for ISRU. Unraveling the origin, age, and distribution patterns of subsurface water ice in the lunar polar and sub-polar regions necessitates employing in-situ geophysical techniques capable of measuring parameters such as depth, lateral and vertical extent, physical distribution within the regolith, and ice volume. Among various geophysical methods, GPR emerges as the most suitable for planetary shallow subsurface exploration due to its capacity for non-contact operation, lightweight design, non-destructive nature, low power consumption, and adaptability for rover-based missions. However, the potential of GPR to distinctly identify the contrast between regolith and water ice remains unexplored. In this chapter are reported preliminary results from a laboratory-scale experiment, introducing ice lenses or pockets of icy mixtures within a regolith simulant layer, aiming to assess GPR's capability in discerning these materials. The characteristics of the equipment and the methodology used for performing the measurements are described in the following sections.

8.2 Experimental set-up

A set of GPR measurements were conducted in a lab test site constituted by a dielectric box made of fiberglass. The box has approximate dimensions $150 \times 100 \times 30$ cm (length, width, and height), which can be filled by different background materials (host material). The box was filled with a synthetic mixture of glass beads, a non magnetic material that mimic the lunar regolith in terms of EM properties [115]. On the top of the test site, a GPR bistatic-antenna instrument is placed with the aim of a complete

surface scanning. A transmitting antenna emits an electromagnetic impulse that is reflected by an intrinsic impedance discontinuity in the ground and received by the receiving antenna in the basic GPR configuration. Radar images are similar to ultrasound images, except that the boundaries between objects are evident in the former due to differences in dielectric permittivity and/or magnetic permeability [4]. The full discussion related to the theory of GPR and radar theory is reported in chapter 3. The measurements were performed using a commercial, GPR PulseEkko PRO TR1000 system (“PulseEkko Pro,” Sensors and Software, Inc, Canada [55]), equipped with a pair of 1000 MHz antennas contained in a single shielding case. The survey was conducted along an $X - Y$ grid with a 5 cm line separation, 1 cm step size (controlled by an odometer), and a time window of 10 ns. Different targets (ice lenses/pockets of icy mixtures) were buried inside the glass beads at about 10/20 cm of depth. The ice was confined in a plastic bag having dimension of about 15×15 cm and several cm of thickness (simulating a lens). In addition to the X-Y grid mode acquisition, also the free-run mode acquisition was conducted for both targets; collecting GPR traces every 5 minutes starting from the frozen target until it was melted. With the free run mode acquisition the melting process and the variation of the response of permittivity contrast is characterized.

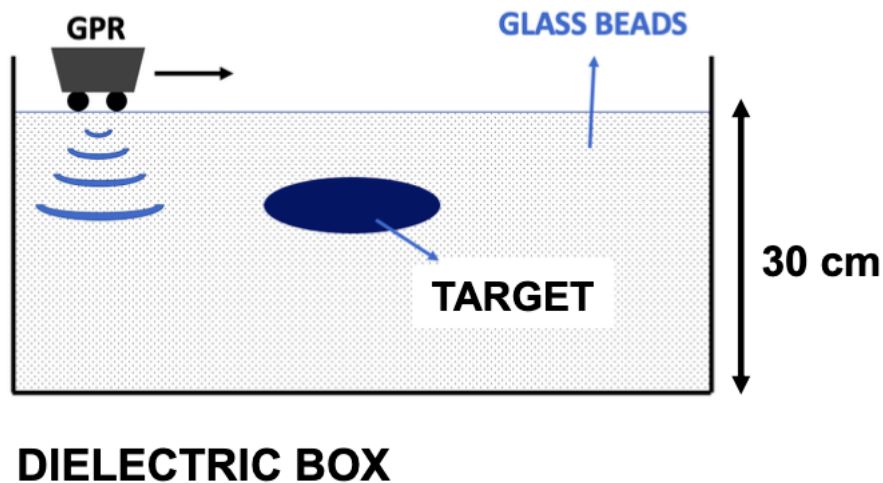


Figure 8.1: GPR experimental set-up: dielectric box made of fiberglass filled with glass beads to simulate the lunar regolith. Measurements were conducted with GPR PulseEkko PRO TR1000 system.

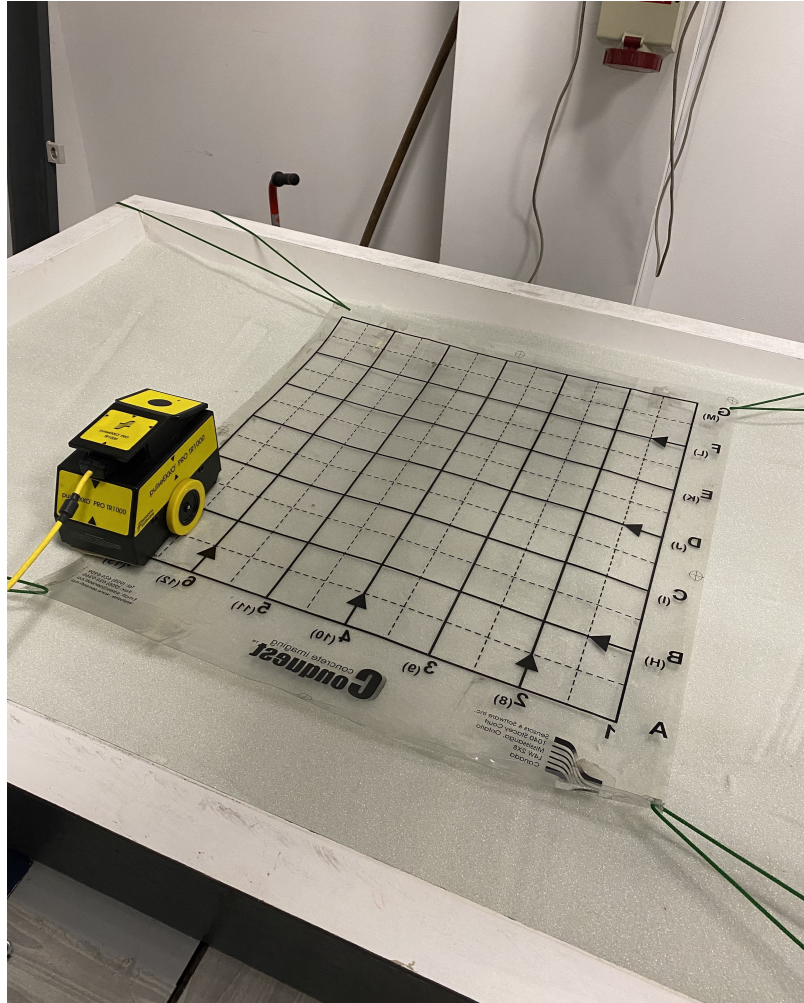


Figure 8.2: Picture of the dielectric box made of fiberglass filled with glass beads and GPR PulseEKKO PRO TR1000 system emplaced for the tests.

8.3 Environment material: Glass-beads

The dielectric box was filled with glass beads to simulate lunar regolith. This material was chosen due to the substantial quantity required to fill the entire tank, and known dielectric properties. Extensive analyses were conducted on the glass beads in order to completely characterize the permittivity also using the Time Domain Reflectometry TDR methods [132] [111]. These measurements set the relative dielectric permittivity of the glass beads equal to 3.2 [89] [137]. The decision to employ glass beads is also linked to the fact that the dielectric properties of glass beads align with measurements obtained from the nine lunar simulants under anhydrous conditions where the real part of permittivity ranges between 2 and 3.5. In this context, glass beads can be used as a lunar simulant. Before conducting GPR tests, various samples of glass beads were extracted from the tank to undergo testing with the Vector Network Analyzer (VNA) set-up (refer to Chapter 6) to determine the real part of the permittivity ϵ' and test their dry state. In Fig.(8.3), the 12 measurements conducted are presented, revealing that all measurements fluctuate between 3.15 and 3.46 in the frequency range $10^8 - 2 \cdot 10^9$ Hz, considering the error bars. Therefore, the glass beads are devoid of water/moisture content within them.

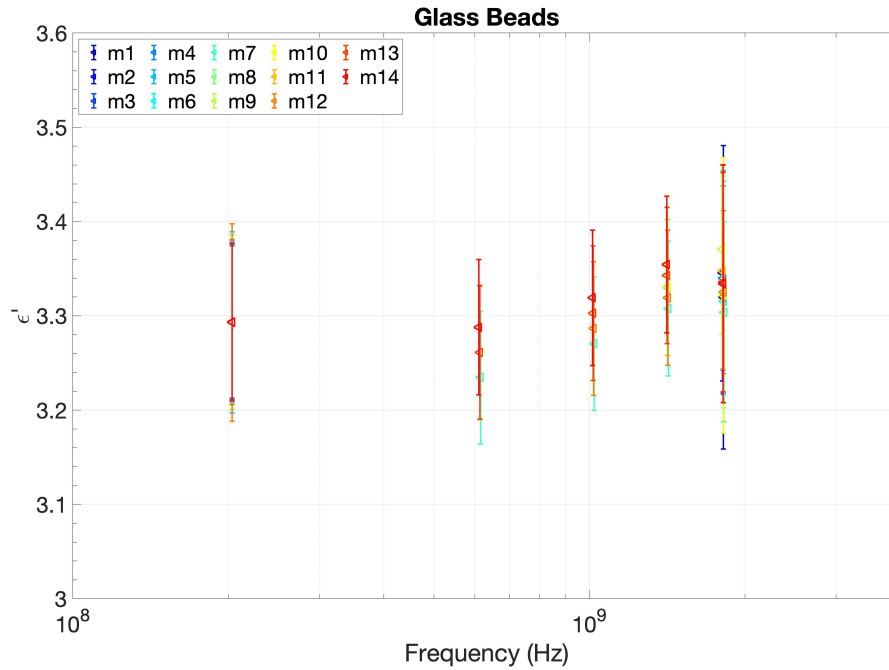


Figure 8.3: *Glass beads dielectric permittivity test. The Glass beads were used as environment material into the dielectric box to simulate the regolith layer. 12 samples of glass beads were collected from the dielectric box and tested with the VNA set-up in order to check the dry state of the material.*

8.4 Frozen targets

In this preliminary study, two distinct targets were created for burial within the layer of glass beads. The first target consisted of distilled water ice, formed by filling a plastic bag and subsequently freezing it below -20°C . This type of target introduced into the dielectric box represents the scenario of an 'ice lens' or a layer of pure ice buried beneath dry lunar regolith. The second target, on the other hand, comprised glass beads saturated with distilled water and then frozen. This target represents a different scenario of a regolith layer whose pores are entirely filled with ice, all packed and covered by anhydrous regolith. This second scenario can be labeled as 'icy soil'. This target was also frozen below -20°C . For both targets, dielectric tests were conducted to characterize the permittivity of the two targets and the surrounding environment (illustrated in the preceding paragraph). The permittivity of distilled water-ice measured at 1 MHz is 3.2469 ± 0.0083 , while that of the ice/glass-beads mixture is approximately 4.88 ± 0.12 , measured at around 10 MHz . The results of the dielectric parameters are presented in the following plots.



Figure 8.4: Icy targets used for the GPR measurements. The picture on the left is the distilled water ice target realized to replicate the ice lens. The right picture shows the ice/regolith mixture realized with frozen saturated glass beads.

| water ice lens target | | |
|-----------------------|-------------|-------------------|
| physical state | ϵ' | $\sigma\epsilon'$ |
| Frozen | 3.2469 | 0.0083 |
| Melted (T room) | 78 | 2 |

Table 8.1: Permittivity of the water-ice lens target measured when it was frozen and melted.

| ice/glass-beads mixture target | | |
|--------------------------------|-------------|-------------------|
| physical state | ϵ' | $\sigma\epsilon'$ |
| Frozen | 4.88 | 0.12 |
| Melted (T room) | 32 | 4 |

Table 8.2: Permittivity of the ice/glass-beads mixture target measured when it was frozen and melted.

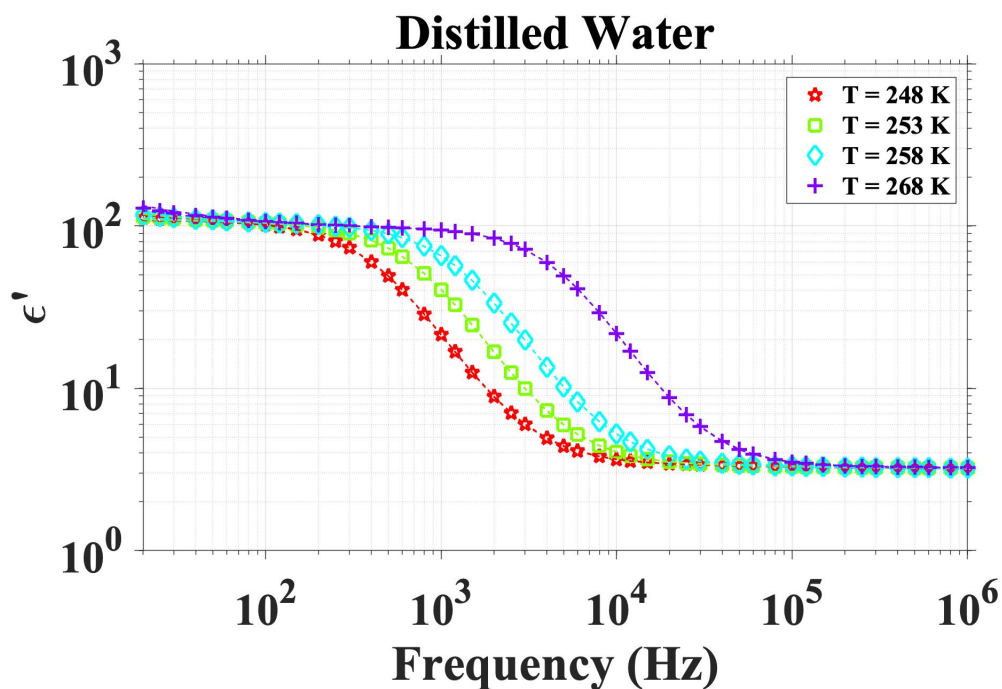


Figure 8.5: Distilled water ice dielectric permittivity tested with the climatic chamber at 4 selected temperatures between 248 – 268 K.

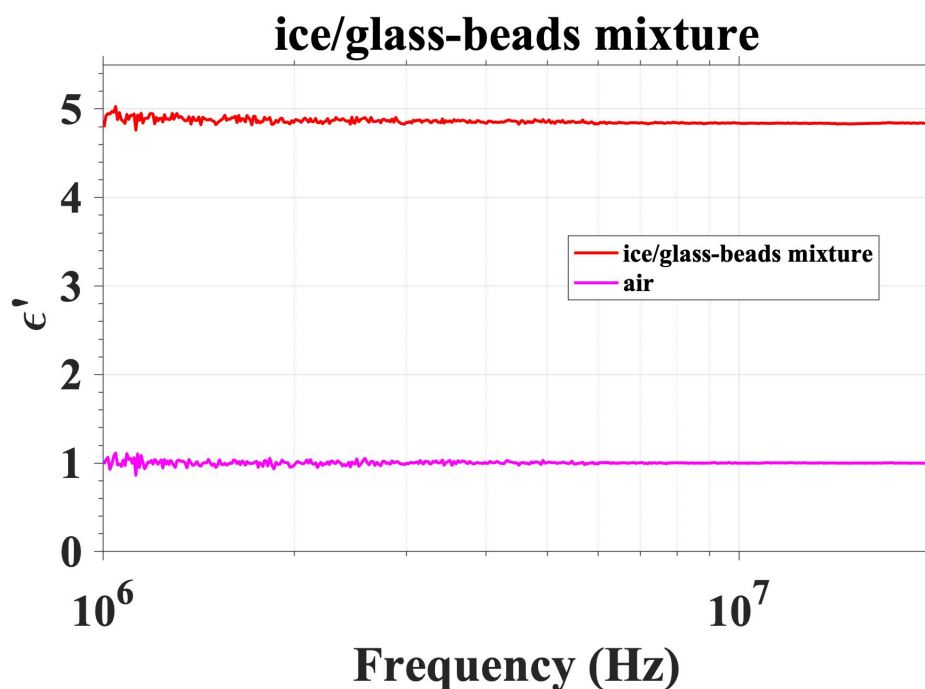


Figure 8.6: Ice/glass-beads mixture dielectric permittivity.

8.5 Experimental results

Below, the results of GPR measurements for the two scenarios, namely, 'ice lens' and 'ice/glass-beads mixture', are presented. For each scenario, two radargrams will be provided: the first acquired with the frozen target, and the second radargram acquired

24 hours later when the target is partially or totally melted. Prior to the main GPR activity for target detection also the background acquisition is acquired. The background acquisition consists of GPR trace collected with no target inserted into the dielectric box. Such a radargram image, shown in the following section, allows to easily spot target anomaly when present. The black horizontal arrows indicates the reflection given by the bottom of the dielectric box taken as a reference.

8.5.1 Background acquisition

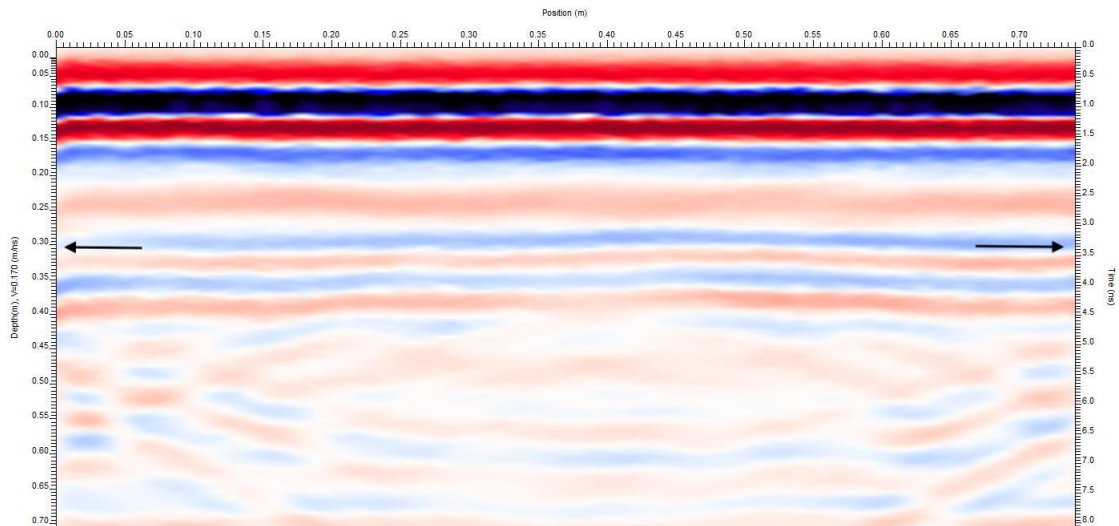


Figure 8.7: Background acquisition of the dielectric box filled with glass beads that act as the host environment for the targets.

8.5.2 Ice lens

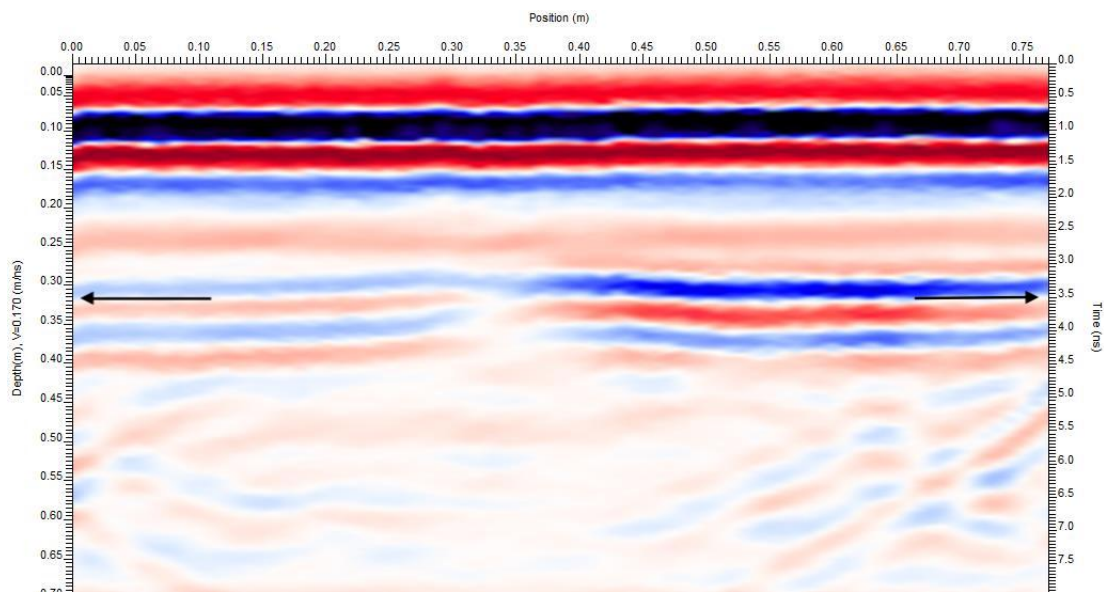


Figure 8.8: Ice lens scenario: radargram of the water ice target. The target is not detected within the glass beads.

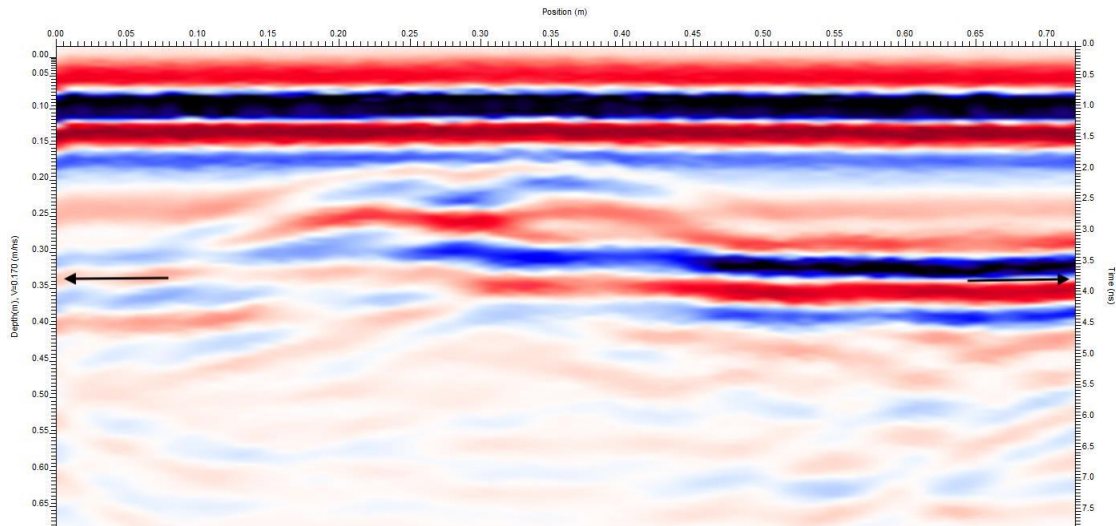


Figure 8.9: *Ice lens scenario: radargram of the melted water ice target. The bright hyperbola indicates the target within the glass beads.*

8.5.3 Ice/glass-beads mixture

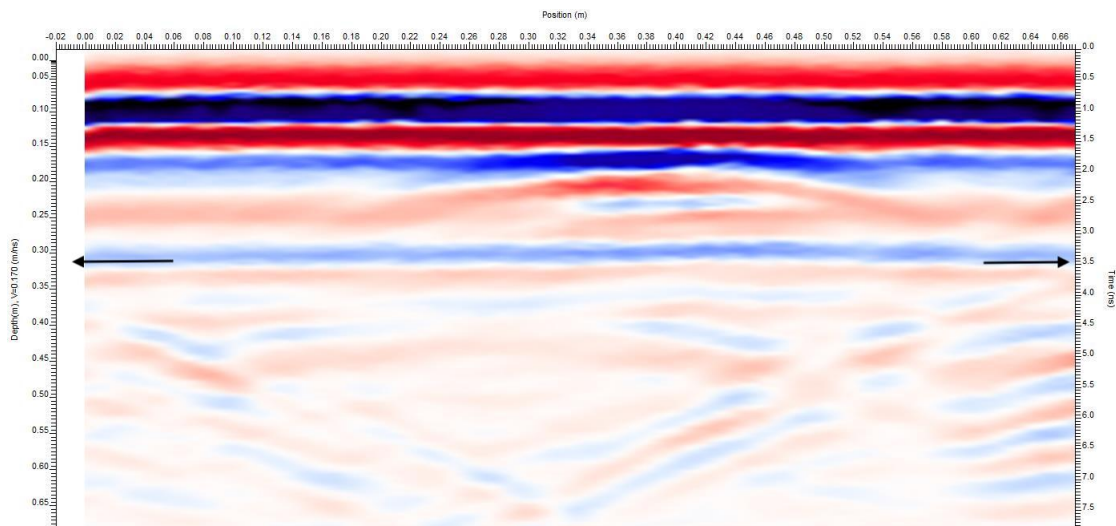


Figure 8.10: *Ice lens scenario: radargram of the ice/glass-beads mixture. The target is clearly detectable within the glass beads.*

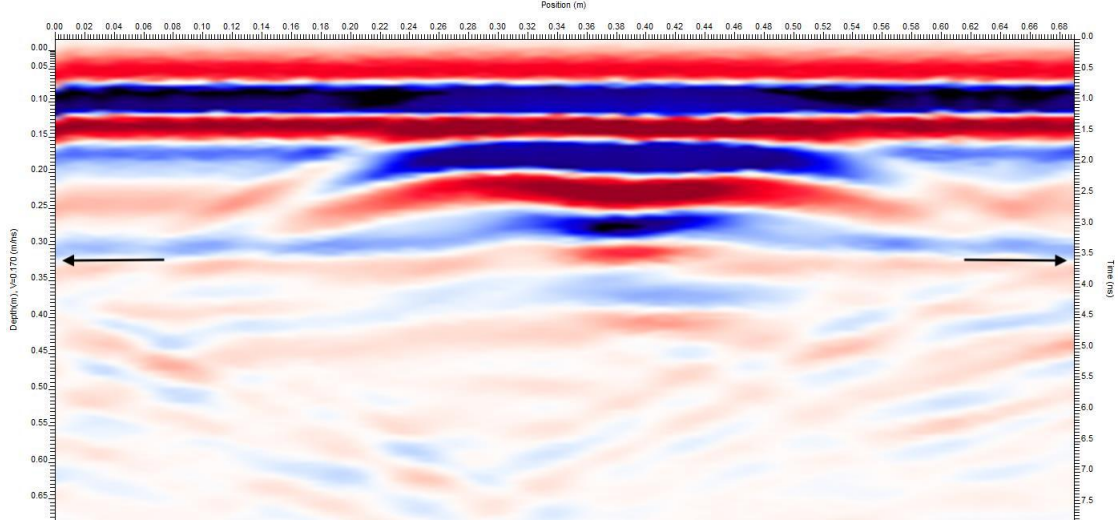


Figure 8.11: Ice lens scenario: radargram of the melted ice/glass-beads mixture. The target is more evident since the strong dielectric contrast generates a very bright signal.

8.6 Inversion approach

The radar signals obtained in the free-run acquisition mode were utilized for geophysical data inversion to estimate the permittivity of the target within the box based on the amplitude of the reflected signals. For operational convenience, the envelope of the radar traces was computed to facilitate the identification of peaks generated by the target. Refer to Fig.(8.12). In the free-run mode, the GPR is positioned on the surface of the box directly above the target. Every 5 minutes, a GPR trace is acquired, allowing the assessment of dielectric contrast variations as the properties of the melting target change over time. The dielectric contrast can be quantified by the reflection coefficient Γ expressed in eq.(8.1)¹, where ε'_T represents the permittivity of the target inserted and ε'_E is the permittivity of the environment, the glass-beads. The amplitude of the maximum peak is modulated by the reflection coefficient Γ ; the closer the Γ coefficient approaches 1, the closer the signal amplitude is to the maximum peak eq.(8.2).

$$\Gamma(\xi) = \frac{\sqrt{\varepsilon'_T} - \sqrt{\varepsilon'_E}}{\sqrt{\varepsilon'_T} + \sqrt{\varepsilon'_E}} \quad (8.1)$$

$$A_{max}(\xi) = A_0\Gamma(\xi) \quad (8.2)$$

The experiment was conducted in a controlled environment, there are no disturbances, the environment material was dry and homogeneous (both horizontally and vertically); the permittivities of the target and environment are known. Given these premises, the approach used to estimate the permittivity of the frozen target involved starting from the data obtained with the melted target. In both scenarios, when the target is melted, the peak is clearly visible within the traces due to higher dielectric contrast, as evidenced in right panels of Fig.(8.12) and (8.13). Thus, inverting eq.(8.2), the retrieved value of A_0 is normalized, imposing into the Γ equation the permittivity

¹Eq.(8.1) is valid only for rays perpendicular to the target (this is highlighted by the fact that there is no angular dependency into the formula). In the experiment setting the target is at 20-30 cm depth while the offset is of about 10cm, so we disregard this behavior and consider the system as monostatic.

values of both the glass-beads (environment) and the melted target (see tables (8.3) and (8.4) for the parameters of the water ice lens and ice/glass-beads mixture targets). Once the parameter A_0 is known, the permittivity of the target corresponding to the peak amplitude A_{max} can be estimated using eq.(8.3).

$$\sqrt{\epsilon'_T} = -\sqrt{\epsilon'_E} \frac{A_{max} + A_0}{A_{max} - A_0} \quad (8.3)$$

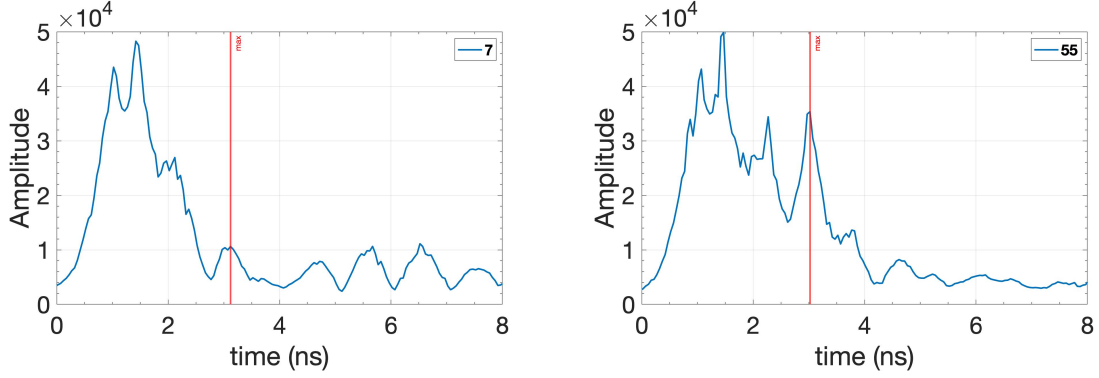


Figure 8.12: Envelopes of free run test over the ice lens target. The left panel shows the envelope of the signal acquired when the target is still frozen and the reflection produced by the target is of the same order of the noise. The right panel shows the acquisition taken after 4 hours when the ice is melted and the reflection is evident.

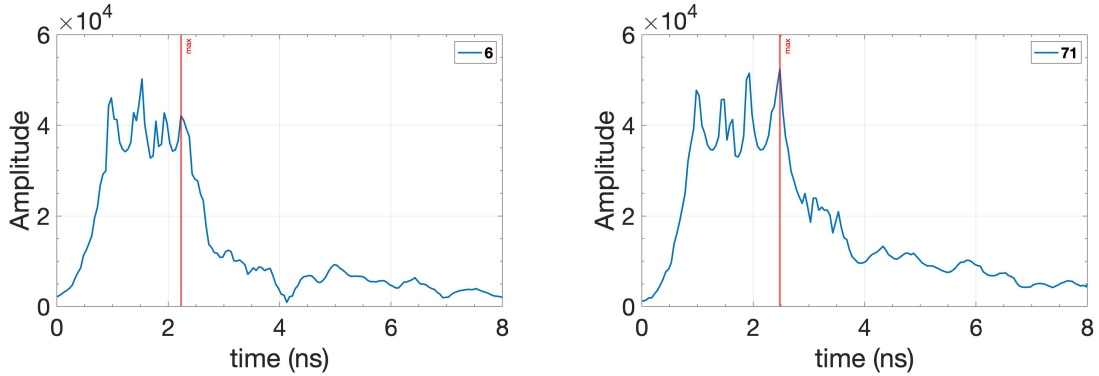


Figure 8.13: Envelopes of free run test over the ice/glass-beads mixture target. The left panel shows the envelope of the signal acquired when the target is still frozen and the reflection produced by the target visible and higher than the noise. The right panel shows the acquisition taken after 5 hours when the ice is melted and the reflection amplitude is higher.

In Fig.(8.14), the top panels illustrate the trend of the maximum amplitude A_{max} over time. This approach enables tracking the target's melting process over time, allowing the study of permittivity evolution over time using eq.(8.3) and obtaining the permittivity estimation when the target is frozen. In Fig.(8.14), the lower panels depict the variation of the target's permittivity calculated with eq.(8.3) over time. Since the measurement in free-run mode was conducted after the XY grid measurements, it is reasonable to assume that the target had already initiated melting. Therefore, a linear fit was applied to the A_{max} vs time graph, to obtain the amplitude value at virtually time zero. The amplitude values extrapolated from the regression method are then used into the eq.(8.3) to determine the permittivity value of the frozen target ϵ'_T .

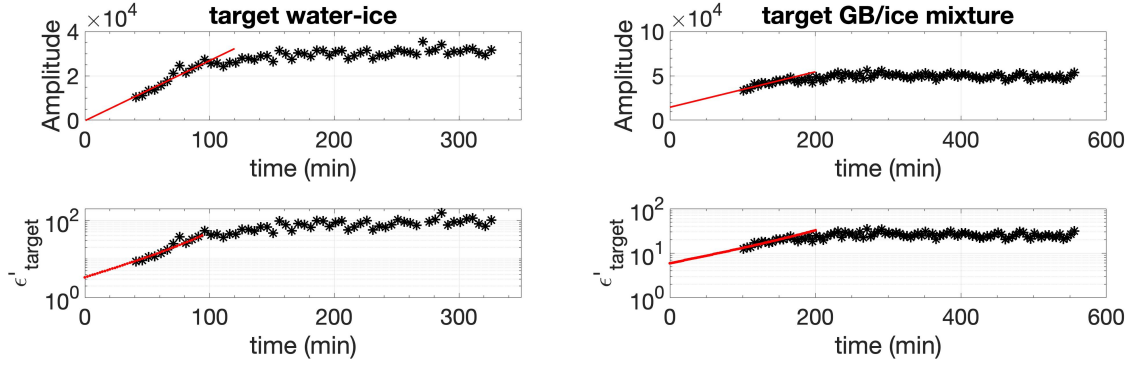


Figure 8.14: Inversion methods to estimate permittivity of the frozen target. Left panel reports the results for the water ice target, the right panel the ice/glass-beads mixture target. From the estimation the amplitude the permittivity of the target is obtained.

Tab.(8.3) and (8.4) summarize the results of the inversion approach for both targets reporting the estimation of parameters and the corresponding uncertainties in the column σ . The estimation of ε'_T is in good agreement within 1σ with the measured values of both targets (see Tab.(8.1) and (8.2) for measured values). Through the inversion method, was estimated not only the permittivity of the frozen target ε'_T but also the corresponding envelope amplitude value, reported in the table as A_T . The A_T value can be compared with the background noise signal amplitude, denoted as A_{noise} . The noise value was extracted from the signal envelope with a time delay greater than $4 ns$ using the GPR traces acquired in XY grid mode, when the target was still frozen.

| Target water ice (lens) | | |
|-------------------------|------------|----------|
| Parameter | estimation | σ |
| Γ | 0.65 | 0.15 |
| A_0 | 53991 | 12651 |
| A_{max} | 35341 | 2473 |
| ε'_T | 3.33 | 1.04 |
| A_T | 262 | 13 |
| A_{noise} | 8000 | 400 |

Table 8.3: Inversion parameters results for water ice target.

| Target ice/glass-beads mixture | | |
|--------------------------------|------------|----------|
| Parameter | estimation | σ |
| Γ | 0.53 | 0.12 |
| A_0 | 106870 | 25041 |
| A_{max} | 56083 | 3925 |
| ε'_T | 5.95 | 1.85 |
| A_T | 14863 | 743 |
| A_{noise} | 10000 | 500 |

Table 8.4: Inversion parameters results for ice/glass-beads mixture target.

It is observed that in the case of the ice-lens target, $A_T < A_{noise}$, indicating that the target peak is obscured by the noise, making it undetectable in the envelope. The

dielectric contrast generated is insufficient to highlight the electromagnetic anomaly, and as a result, no anomaly is evident in the radargram, as depicted in Fig.(8.10). On the other hand, for the ice/glass-beads mixture target, $A_T > A_{noise}$, indicating that the target peak surpasses the background noise and remains visible even when the target is frozen. In this case, the target signal is clearly visible within the radargram, as illustrated in Fig.(8.10).

8.6.1 Frequency content analysis

The following paragraph presents the frequency content analysis of the peak generated by the target. For each GPR trace acquired in free-run mode, the target peak $\chi(t)$ was selected by multiplying the radar signal with a suitably constructed Gaussian function eq.(8.5), centered on the corresponding time delay peak, see Fig.(8.15).

$$\chi(t) = f(t) \cdot \gamma(t) \quad (8.4)$$

$$f(t) = A \exp \left[-\frac{(t - t_{max})^2}{2\sigma^2} \right] \quad (8.5)$$

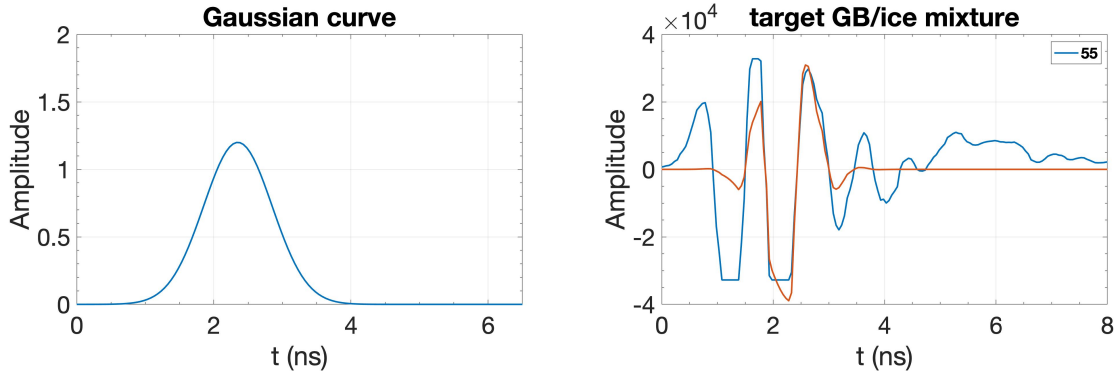


Figure 8.15: Selection of reflection peaks for the FFT analysis. The left panel shows the gaussian curve obtained for each trace peaked over the arrival times of each maximum of the amplitude. In the right panel the gaussian curve is multiplied by the corresponding waveform measure (blue line) in order to isolate the reflection waveform (orange curve).

The Fast Fourier Transform (FFT) was performed on the extrapolated signal to obtain the frequency content, reported in Fig.(8.16) and (8.17). It is noteworthy that, in the case of the ice/glass-beads mixture target, a frequency shift toward lower frequencies is observed with increasing dielectric contrast (as the target melts). This phenomenon is not as pronounced for the ice-lens target; in fact, the maximum value of the FFT does not exhibit a clear trend. Eq.(8.6) presents the results of the linear fit obtained from the data of the ice/glass-beads mixture target.

$$\nu = -3.17 \cdot 10^5 A_{FFT} + (7.78 \cdot 10^5) \quad (8.6)$$

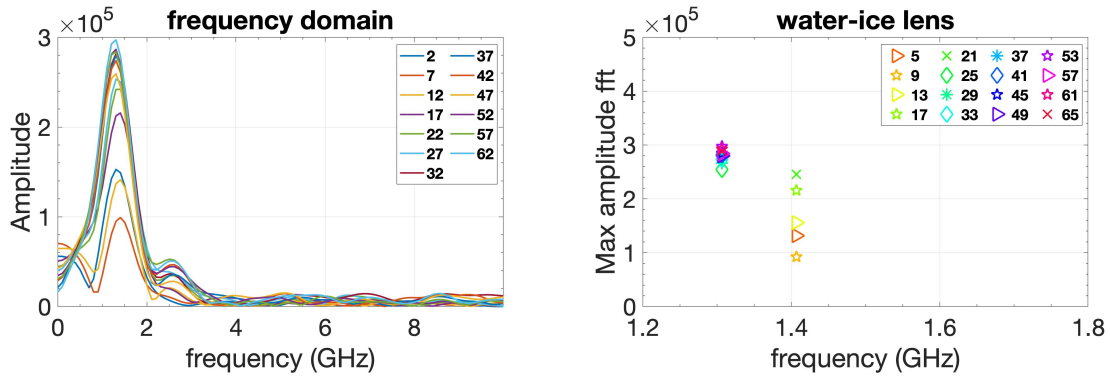


Figure 8.16: Variation of FFT peaks with frequency and time for the water-ice lens target. The legend reports the acquisitions through time (i.e. line 5 is the acquisition taken at $t = t_1$ while line 9 is taken at $t = t_1 + \Delta t$ and so on).

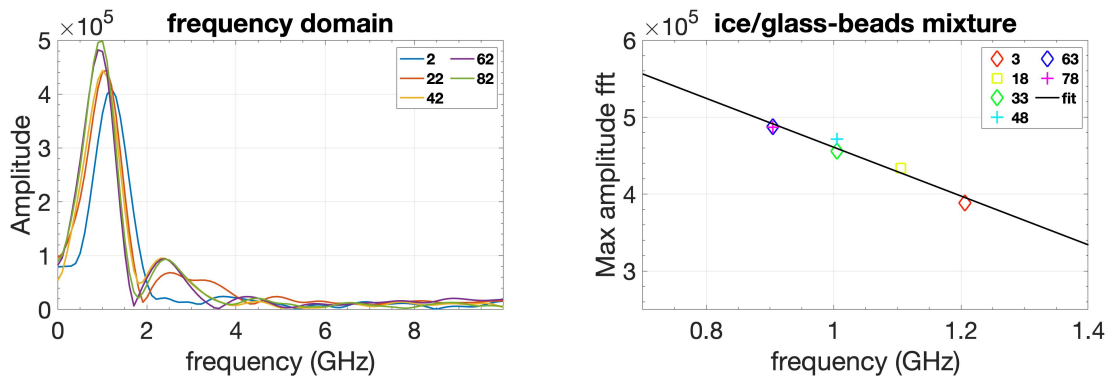


Figure 8.17: Variation of FFT peaks with frequency and time for the ice/glass-beads mixture target. The legend reports the acquisitions through time (i.e. line 2 is the acquisition taken at $t = t_1$ while line 22 is taken at $t = t_1 + \Delta t$ and so on).

8.7 Discussion

GPR measurements were conducted in the laboratory to assess the conditions under which lunar water ice could be detected beneath the surface using radar techniques. Two different small-scale scenarios were recreated in the laboratory. The first scenario involves a layer of ice (ice lens) buried within a layer of anhydrous regolith. The second scenario features a layer of saturated and frozen regolith enveloped by an anhydrous regolith layer (ice/glass-beads mixture). Literature reports various evidences regarding lunar water ice in polar and sub-polar regions [45][29][82]. Ice accumulation is particularly noted in cold traps within permanently shadowed areas such as craters and surface depressions. Existing evidence primarily pertains to data above the surface, although thermal neutron techniques provide some subsurface evidence, albeit within a few centimeters [43][44][45].

What remains unclear is whether ice has accumulated in substantial quantities, but its accumulation is expected within the first 3 m of lunar regolith [125]. For this reason, two very preliminary laboratory scenarios were created to study the feasibility of radar applications for lunar water ice detection for future ISRU.

Figure (8.7) illustrates the background acquisition of the dielectric box filled with anhydrous glass beads. This acquisition enables the understanding of the response of

the host environment that will accommodate the two targets, aiding in the accurate identification of electromagnetic anomalies generated by the targets. The x-axis in this acquisition represents the displacement made by the GPR to collect the radar trace, while the y-axis denotes depth. At approximately 30 cm depth, a reflection from the bottom of the tank is evident, characterized by a series of parallel bands. Data below this depth must be disregarded as it originates from beneath the floor. With the insertion of targets, if they generate an electromagnetic anomaly, it must necessarily be located above the reflection from the bottom of the dielectric box. The reflection generated by the bottom of the box is indicated by two black arrows into the radargrams as a reference.

Figures (8.8) and (8.9) show acquired radargrams of the ice lens scenario, respectively when the target is frozen and when it is partially melted. Comparing the two images reveals that the frozen target does not produce an electromagnetic anomaly. In contrast, the radar trace acquired 24 hours later clearly shows a signal generated by the partially melted target. The difference in results can be explained by host-target permittivity contrasts. In the ice lens scenario, there is no distinct dielectric contrast since both target and environment material show similar permittivity values of around 3. In the second case, when the target is partially melted, a strong contrast arises due to the presence of liquid water, with a permittivity close to 80.

Regarding the second proposed scenario, the results shown in Fig.(8.10) and (8.11) highlight a different situation from the previous case. In this case, the target is clearly visible within the radargram even when frozen because the target's permittivity is around 4.8, higher than the permittivity of the host environment. The differences of the two scenarios is also highlighted in the inversion approach where the peak envelope amplitude of the frozen target is compared with the signal amplitude of the background noise. For the ice-lens target, $A_T < A_{noise}$ making the target undetectable when frozen; while for the ice/glass-beads mixture target, $A_T > A_{noise}$, and the frozen target is visible. The frequency content analysis of the reflection peak also show the difference between the two cases. In fact, for the ice/glass-beads mixture target the maximum of the FFT shifts towards lower frequency values as the permittivity contrast increases.

8.8 Conclusions

Detecting ice on the Moon is a complex challenge, influenced by the specific conditions on the lunar surface and these early GPR tests highlight some factors that could play a crucial role for the detection of water ice.

One critical variable in this context is the variability in the composition and porosity of lunar regolith. Under certain conditions, regolith may exhibit permittivity values comparable to those of water ice. This presents a potential obstacle, as it diminishes the probability of effectively detecting buried water ice through GPR if it is present in the form of buried ice lenses.

Conversely, buried deposits characterized by ice/regolith mixtures, particularly when saturated, emerge as distinctive targets that are discernible through GPR.

The dielectric contrast generated by fully saturated ice/regolith mixture and the dry host environment creates a detectable GPR signature, providing a positive indicator and higher probability for the ice detection on the Moon.

The detectability of lunar ice represents a dynamic frontier in space exploration, demanding ongoing and rigorous investigations. The preliminary results presented in

this chapter demonstrate how, under specific environmental conditions, the detection of water ice on the Moon could be more difficult than originally thought using radar techniques. Such findings underline the importance of studying the GPR responses and recognizing the unique challenges and opportunities that lunar regolith presents in the quest to detect and extract water ice on the Moon.

Chapter 9

Summary and conclusions

This final chapter synthesizes key insights obtained from three main experimental activities conducted in this research, shedding light on the intricate electromagnetic properties of lunar regolith analogues under varying physical conditions and water ice detectability with radar technique on the Moon. The investigation involved a comprehensive exploration, covering dielectric measurements, temperature-dependent responses, and the feasibility of GPR for lunar subsurface exploration.

In chapter 6, the dielectric properties of lunar regolith analogues were meticulously examined under varied compaction conditions. Using a Vector Network Analyzer (VNA), the study explored real and imaginary permittivity values across a frequency spectrum up to 3 GHz .

Results reveal that ε' is frequency-independent, mirroring patterns observed in Apollo samples, and ε'' present slight frequency dependence but still presenting dielectric behavior of powder materials. The dielectric response of simulants exhibited a strong dependence on porosity and bulk density, (the variability of ε' with ϕ of all regolith analogues ranges between 1.8 to 3.3) corroborating findings from previous studies on loose lunar material.

Application of mixing models facilitated the extrapolation of dielectric parameters of the lunar simulants at $\phi = 0$ to study their dielectric behavior as they were solid rocks. The results discussion was made separately for soil data and solid samples, revealing trends in contrast to previous results of Apollo samples, indicating the necessity for a systematic assessment across all Apollo samples, and also the necessity to separate the discussion of regolith data and rocks data for more appropriate comprehension.

The comparison of attenuation profiles calculated using the $\tan\delta$ of simulants and lunar samples lead to a dichotomy: in one scenario we can infer that the lunar analogues are excessively attenuating in comparison to lunar regolith and thus they do not accurately replicate the lunar materials. On the other hand, the density curve eq.(6.33) used to retrieve the attenuation profiles vs depth, that was derived from data of Apollo drilling operation, it's not an appropriate bulk density model for depth below 10-15 meters, where the transition zone begins, made of regolith mixed with rocks.

The dielectric measurements conducted at varying temperatures are extensively discussed in Chapter 7. Through the LCR meter set-up it was possible to investigate the dielectric properties of lunar simulants under anhydrous conditions, varying temperature and frequency (up to 1 MHz), to conclude their electromagnetic charac-

terization alongside the measurements in Chapter 6. The dielectric measurements were also conducted on saturated mixtures of simulants with water ice. Measurements of these specific samples serve to characterize how the dielectric response of lunar material changes when water ice is present. The characterization of these specific samples aims at detecting water ice on the Moon using radar techniques, underscoring the importance of understanding their dielectric properties and discerning differences from anhydrous regolith. Detecting water ice with radar techniques is possible if a sufficient dielectric contrast is generated within the investigated area to produce a reflection visible in the radar signal. Hence, this study extensively characterizes simulants under anhydrous conditions, varying temperature, compaction, and frequency, to understand the variability of their dielectric properties of the "host" environment and the ice/regolith mixtures to study the dielectric properties when water ice is present.

The real part of permittivity ϵ' of dry simulants is temperature and frequency independent as the lunar soil samples; the imaginary part ϵ'' present a variation for $T < 300 K$ indicating a lower EM signal attenuation at lower temperatures.

Preliminary results of the mixtures indicated that the presence of water ice within the matrix raises the permittivity (ϵ' ranges between ~ 4.5 to 6.8), hinting at the potential for identifying subsurface water ice through radar measurements under specific conditions.

The mixing models presented in Chapter 4 describe and reproduce, within 1σ , the dielectric properties of the various mixtures. These models demonstrate that Wiener's bounds can be employed as *min* and *max* values, ensuring that the dielectric properties of the mixtures fall within these limits. However, it is systematically observed that ϵ' estimated with the mixing models consistently tends to be underestimated. This fact may indicate an overestimation of sample's porosity, implying that the input data have a higher % of water than actually present within the created mixture, leading to a systematic error in ϕ estimation. Challenges arising from the experimental set-up for icy mixtures were acknowledged, emphasizing the need for further exploration and refinements in set-up configurations.

Chapter 8 examined the potential of GPR for subsurface exploration on the Moon. Preliminary findings from a laboratory-scale experiment introduced ice lenses and ice/regolith mixtures targets within a regolith simulant layer, assessing GPR's efficacy. The laboratory work with GPR serves as the concluding segment of this study. The results of dielectric properties of anhydrous lunar simulants and ice/regolith mixtures were used to design the experiment activities with the dielectric box and frozen targets. The glass beads used as the host material exhibit a permittivity value of ~ 3.4 , aligning with the measured lunar simulants and literature values for Apollo regolith samples. The two created targets consist of a distilled water ice lens with a known permittivity of 3.2; and a target made of ice/glass beads saturated mixture, similar to those measured in Chapter 7, with a permittivity of 4.88.

The dielectric contrast between host material and target emerged as pivotal factor influencing GPR detection capabilities. While acknowledging the potential obstacle of regolith exhibiting permittivity values comparable to water ice, buried deposits characterized by ice/regolith mixtures, particularly when saturated, emerged as discernible targets for GPR. The dielectric contrast produced by fully saturated ice/regolith mixtures and the dry host environment generates a detectable GPR signature, serving as a positive indicator and increasing the probability of ice detection on the Moon.

This work presents preliminary results and analyses that lay the foundation for future research efforts related to the utilization of radar techniques for lunar exploration, specifically focusing on the detection of water ice reservoirs for ISRU. The techniques to detect water ice is rapidly advancing, constituting a new frontier in space exploration. This calls for ongoing and thorough studies, with a particular emphasis on constraining and assessing the origin, accumulation, and age of lunar ice; enhancing and expanding lunar ice mapping efforts.

Bibliography

- [1] W Ali and SR Shieh. “Exploring shallow subsurface of Mars and introducing the GPR technique for planetary sciences (exploring Mars beyond the surface features)”. In: *Journal of Geology and Geosciences* 3 (2014), p. 142.
- [2] Roman Alvarez. “Electrical properties of sample 70215-Low-frequency corrections”. In: *Lunar and Planetary Science Conference Proceedings*. Vol. 5. 1974, pp. 2663–2671.
- [3] Roman Alvarez. “Lunar powder simulator under lunarlike conditions: Dielectric properties”. In: *Journal of Geophysical Research* 78.29 (1973), pp. 6833–6844.
- [4] AP Annan. “Electromagnetic principles of ground penetrating radar”. In: *Ground penetrating radar: theory and applications* 1 (2009), pp. 1–37.
- [5] Andrew Assur. *Composition of sea ice and its tensile strength*. Vol. 44. US Army Snow, Ice and Permafrost Research Establishment, 1960.
- [6] James Baker-Jarvis, Michael D Janezic, and Robert B Stafford. “Shielded open-circuited sample holders for dielectric and magnetic measurements of liquids and powders”. In: *NASA STI/Recon Technical Report N 94* (1993), p. 14687.
- [7] M Barmatz et al. “Microwave permittivity and permeability measurements on lunar simulants”. In: *43rd Annual Lunar and Planetary Science Conference*. 1659. 2012, p. 1050.
- [8] Niels Bjerrum. “Structure and properties of ice”. In: *Science* 115.2989 (1952), pp. 385–390.
- [9] Alessandro Brin et al. “Electromagnetic characterization of a crushed L-chondrite for subsurface radar investigations of solar system bodies”. In: *Icarus* 374 (2022), p. 114800.
- [10] Yann Brouet et al. “Characterization of the permittivity of controlled porous water ice-dust mixtures to support the radar exploration of icy bodies”. In: *Journal of Geophysical Research: Planets* 121.12 (2016), pp. 2426–2443.
- [11] Bryan J Butler. “The migration of volatiles on the surfaces of Mercury and the Moon”. In: *Journal of Geophysical Research: Planets* 102.E8 (1997), pp. 19283–19291.
- [12] Dwain K Butler. *Near-surface geophysics*. Society of Exploration Geophysicists, 2005.
- [13] Om Prakash Narayan Calla and Inder Singh Rathore. “Study of complex dielectric properties of lunar simulants and comparison with Apollo samples at microwave frequencies”. In: *Advances in space research* 50.12 (2012), pp. 1607–1614.

- [14] OPN Calla, Shubhra Mathur, and Kishan Lal Gadri. “Study of variability of complex permittivity of terrestrial analogue of lunar soil (TALS) having different percentage of water at microwave frequencies”. In: *IEEE Geoscience and Remote Sensing Letters* 13.2 (2016), pp. 123–126.
- [15] Bruce A Campbell. “Comment on “Regolith layer thickness mapping of the Moon by radar and optical data,” by YG Shkuratov and NV Bondarenko”. In: *Icarus* 158.2 (2002), pp. 560–561.
- [16] Malcolm J Campbell and Juris Ulrichs. “Electrical properties of rocks and their significance for lunar radar observations”. In: *Journal of Geophysical Research* 74.25 (1969), pp. 5867–5881.
- [17] Kevin M Cannon. “A lunar soil classification system for space resource utilization”. In: *Planetary and Space Science* 237 (2023), p. 105780.
- [18] Kevin M Cannon and Daniel T Britt. “A geologic model for lunar ice deposits at mining scales”. In: *Icarus* 347 (2020), p. 113778.
- [19] Lin-Feng Chen et al. *Microwave electronics: measurement and materials characterization*. John Wiley & Sons, 2004.
- [20] Mou-Shan Chen et al. “Hopping of ions in ice”. In: *The Journal of Chemical Physics* 60.2 (1974), pp. 405–419.
- [21] Yi Chen et al. “Chang’e-5 lunar samples shed new light on the Moon”. In: *The Innovation Geoscience* 1.1 (2023), pp. 100014–1.
- [22] Gordon Chin et al. “Lunar reconnaissance orbiter overview: The instrument suite and mission”. In: *Space Science Reviews* 129 (2007), pp. 391–419.
- [23] DH Chung and WB Westphal. “Dielectric spectra of Apollo 15 and 16 lunar solid samples”. In: *Proceedings of the Lunar Science Conference, vol. 4, p. 3077*. Vol. 4. 1973, p. 3077.
- [24] DH Chung, WB Westphal, and GR Olhoeft. “Dielectric properties of Apollo 14 lunar samples”. In: *Proceedings of the Lunar Science Conference, vol. 3, p. 3161*. Vol. 3. 1972, p. 3161.
- [25] DH Chung, WB Westphal, and Gene Simmons. “Dielectric behavior of lunar samples: Electromagnetic probing of the lunar interior”. In: *Proceedings of the Lunar Science Conference, vol. 2, p. 2381*. Vol. 2. 1971, p. 2381.
- [26] DH Chung, WB Westphal, and Gene Simmons. “Dielectric properties of Apollo 11 lunar samples and their comparison with earth materials”. In: *Journal of Geophysical Research* 75.32 (1970), pp. 6524–6531.
- [27] FH Cocks et al. “Lunar ice: Adsorbed water on subsurface polar dust”. In: *Icarus* 160.2 (2002), pp. 386–397.
- [28] Anthony Colaprete et al. “An overview of the lunar crater observation and sensing satellite (LCROSS)”. In: *Space Science Reviews* 167 (2012), pp. 3–22.
- [29] Anthony Colaprete et al. “Detection of water in the LCROSS ejecta plume”. In: *science* 330.6003 (2010), pp. 463–468.
- [30] JE Colwell et al. “Lunar surface: Dust dynamics and regolith mechanics”. In: *Reviews of Geophysics* 45.2 (2007).

- [31] Michael R Cooper, Robert L Kovach, and Joel S Watkins. “Lunar near-surface structure”. In: *Reviews of Geophysics* 12.3 (1974), pp. 291–308.
- [32] David J Daniels. “Surface-penetrating radar”. In: *Electronics & Communication Engineering Journal* 8.4 (1996), pp. 165–182.
- [33] John L Davis and A Peter Annan. “Ground-penetrating radar for high-resolution mapping of soil and rock stratigraphy 1”. In: *Geophysical prospecting* 37.5 (1989), pp. 531–551.
- [34] Debye and Peter Josef William. *Polar molecules*. Vol. 172. New York: Dover, 1929.
- [35] Myron C Dobson et al. “Microwave dielectric behavior of wet soil-Part II: Dielectric mixing models”. In: *IEEE Transactions on geoscience and remote sensing* 1 (1985), pp. 35–46.
- [36] FK Duennebier, J Watkins, and R Kovach. “Results from the lunar surface profiling experiment”. In: *Lunar and Planetary Science Conference*. Vol. 5. 1974.
- [37] AR Duncan et al. “Composition and inter-relationships of some Apollo 16 samples”. In: *Lunar Science-IV* (1973), pp. 190–192.
- [38] Charles Elachi and Jakob J Van Zyl. *Introduction to the physics and techniques of remote sensing*. John Wiley & Sons, 2021.
- [39] Edwin Ethridge and William Kaukler. “Extraction of water from polar lunar permafrost with microwaves-dielectric property measurements”. In: *47th AIAA Aerospace Sciences Meeting including the New Horizons Forum and Aerospace Exposition*. 2009, p. 1342.
- [40] Wenzhe Fa et al. “Regolith stratigraphy at the Chang’E-3 landing site as seen by lunar penetrating radar”. In: *Geophysical Research Letters* 42.23 (2015), pp. 10–179.
- [41] Guang-You Fang et al. “Lunar Penetrating Radar onboard the Chang’e-3 mission”. In: *Research in astronomy and astrophysics* 14.12 (2014), p. 1607.
- [42] WM Farrell et al. “The young age of the LAMP-observed frost in lunar polar cold traps”. In: *Geophysical Research Letters* 46.15 (2019), pp. 8680–8688.
- [43] W C Feldman et al. “Fluxes of fast and epithermal neutrons from Lunar Prospector: Evidence for water ice at the lunar poles”. In: *Science* 281.5382 (1998), pp. 1496–1500.
- [44] WC Feldman et al. “Polar hydrogen deposits on the Moon”. In: *Journal of Geophysical Research: Planets* 105.E2 (2000), pp. 4175–4195.
- [45] William C Feldman et al. “Evidence for water ice near the lunar poles”. In: *Journal of Geophysical Research: Planets* 106.E10 (2001), pp. 23231–23251.
- [46] Jianqing Feng, Matthew A Siegler, and Mackenzie N White. “Dielectric properties and stratigraphy of regolith in the lunar South Pole-Aitken basin: Observations from the Lunar Penetrating Radar”. In: *Astronomy & Astrophysics* 661 (2022), A47.
- [47] Elizabeth A Fisher et al. “Evidence for surface water ice in the lunar polar regions using reflectance measurements from the Lunar Orbiter Laser Altimeter and temperature measurements from the Diviner Lunar Radiometer Experiment”. In: *Icarus* 292 (2017), pp. 74–85.

- [48] Garcia et al. “Lunar Seismology: An Update on Interior Structure Models”. In: *Space Science Reviews* 215.8 (2019), p. 50.
- [49] Allen Glisson. “Advanced engineering electromagnetics, by constantine a. balanis [book review]”. In: *IEEE Antennas and Propagation Society Newsletter* 31.6 (1989), pp. 24–26.
- [50] T Gold, E Bilson, and RL Baron. *Electrical properties of Apollo 17 rock and soil samples and a summary of the electrical properties of lunar material at 450 MHz frequency*. Tech. rep. 1976.
- [51] T. Gold, E Bilson, and M Yerbury. “Grain size analysis and high frequency electrical properties of Apollo 15 and 16 samples”. In: *Proceedings of the Lunar Science Conference, vol. 4, p. 3093*. Vol. 4. 1973, p. 3093.
- [52] T Gold, E Bilson, and M Yerbury. “Grain size analysis, optical reflectivity measurements, and determination of high-frequency electrical properties for Apollo 14 lunar samples”. In: *Proceedings of the Lunar Science Conference, vol. 3, p. 3187*. Vol. 3. 1972, p. 3187.
- [53] T. Gold, BT others O Leary, and M Campbell. “Some physical properties of Apollo 12 lunar samples”. In: *Proceedings of the Lunar Science Conference, vol. 2, p. 2173*. Vol. 2. 1971, p. 2173.
- [54] JN Goswami and M Annadurai. “Chandrayaan-1: India’s first planetary science mission to the moon”. In: *Current science* (2009), pp. 486–491.
- [55] PulseEkko Pro User Guide. “Sensors and Software”. In: *Inc., Canada* (2006).
- [56] Shin-Chan Han et al. “Global characteristics of porosity and density stratification within the lunar crust from GRAIL gravity and Lunar Orbiter Laser Altimeter topography data”. In: *Geophysical Research Letters* 41.6 (2014), pp. 1882–1889.
- [57] Craig Hardgrove et al. “The lunar polar hydrogen mapper CubeSat mission”. In: *IEEE Aerospace and Electronic Systems Magazine* 35.3 (2020), pp. 54–69.
- [58] Paul O Hayne et al. “Evidence for exposed water ice in the Moon’s south polar regions from Lunar Reconnaissance Orbiter ultraviolet albedo and temperature measurements”. In: *Icarus* 255 (2015), pp. 58–69.
- [59] Grant H Heiken, David T Vaniman, and Bevan M French. *Lunar Sourcebook, a user’s guide to the Moon*. 1991.
- [60] DC Hickson et al. “Modeling the dielectric properties of minerals from crystals to bulk powders for improved interpretation of asteroid radar observations”. In: *Journal of Geophysical Research: Planets* 125.7 (2020), e2019JE006141.
- [61] Harald Hiesinger and Ralf Jaumann. “Chapter 23 - The Moon”. In: *Encyclopedia of the Solar System (Third Edition)*. Ed. by Tilman Spohn, Doris Breuer, and Torrence V. Johnson. Third Edition. Boston: Elsevier, 2014, pp. 493–538. ISBN: 978-0-12-415845-0. DOI: <https://doi.org/10.1016/B978-0-12-415845-0.00023-2>.
- [62] Arthur Robert von Hippel. *Dielectric Materials and Applications: Papers..* Technology Press of MIT, 1954.

- [63] DM Hooper et al. “Introduction of LCATS-1, a Geotechnical Lunar Regolith Simulant for Multi-Purpose Utilization”. In: *51st Annual Lunar and Planetary Science Conference*. 2326. 2020, p. 2548.
- [64] Demidova S. I. et al. “Chemical composition of lunar meteorites and the lunar crust”. In: *Petrology* 15.4 (2007), pp. 386–407.
- [65] Wing-Huen Ip et al. “Preface: The Chang’e-3 lander and rover mission to the Moon”. In: *Research in Astronomy and Astrophysics* 14.12 (2014), p. 1511.
- [66] Alexander M Jablonski. “Technical aspects of seismicity on the moon”. In: *Apollo The International Magazine Of Art And Antiques* 613 (2010), pp. 1–25.
- [67] Claude Jaccard. “Thermodynamics of irreversible processes applied to ice”. In: *Physik der kondensierten Materie* 3 (1964), pp. 99–118.
- [68] Harry M Jol. *Ground penetrating radar theory and applications*. elsevier, 2008.
- [69] Brant M Jones et al. “Solar wind-induced water cycle on the Moon”. In: *Geophysical Research Letters* 45.20 (2018), pp. 10–959.
- [70] Piotr Kaniewski and Tomasz Kraszewski. “Estimation of Handheld Ground-Penetrating Radar Antenna Position with Pendulum-Model-Based Extended Kalman Filter”. In: *Remote Sensing* 15.3 (2023), p. 741.
- [71] Manabu Kato et al. “The Kaguya mission overview”. In: *Space science reviews* 154 (2010), pp. 3–19.
- [72] TJ Katsube and LS Collett. “Electrical properties of Apollo 11 and Apollo 12 lunar samples”. In: *Proceedings of the Lunar Science Conference, vol. 2, p. 2367*. Vol. 2. 1971, p. 2367.
- [73] TJ Katsube and LS Collett. “Measuring techniques for rocks with high permittivity and high loss”. In: *Geophysics* 38.1 (1973), pp. 92–105.
- [74] Shuji Kawada, Ru Gui Jin, and Mituru Abo. “Dielectric properties and 110 K anomalies in KOH-and HCl-doped ice single crystals”. In: *The Journal of Physical Chemistry B* 101.32 (1997), pp. 6223–6225.
- [75] Syuji Kawada. “Dielectric anisotropy in ice Ih”. In: *Journal of the Physical Society of Japan* 44.6 (1978), pp. 1881–1886.
- [76] M Kobayashi et al. “Laboratory measurements show temperature-dependent permittivity of lunar regolith simulants”. In: *Earth, Planets and Space* 75.1 (2023), pp. 1–9.
- [77] Takao Kobayashi et al. “Nadir detection of lunar lava tube by Kaguya lunar radar sounder”. In: *IEEE Transactions on Geoscience and Remote Sensing* 59.9 (2020), pp. 7395–7418.
- [78] Exolith Labs and University of Central Florida. *LHS-1 Lunar Highland Simulant Spec Sheet*. 2021.
- [79] Exolith Labs and University of Central Florida. *LMS-1 Lunar Mare Simulant Spec Sheet*. 2021.
- [80] Chunlai Li et al. “Overview of the Chang’e-4 mission: Opening the frontier of scientific exploration of the lunar far side”. In: *Space Science Reviews* 217 (2021), pp. 1–32.

- [81] Chunlai Li et al. “The Moon’s farside shallow subsurface structure unveiled by Chang’E-4 Lunar Penetrating Radar”. In: *Science advances* 6.9 (2020), eaay6898.
- [82] Shuai Li et al. “Direct evidence of surface exposed water ice in the lunar polar regions”. In: *Proceedings of the National Academy of Sciences* 115.36 (2018), pp. 8907–8912.
- [83] David Long and Fawwaz Ulaby. *Microwave radar and radiometric remote sensing*. Artech, 2015.
- [84] Lucey et al. “Relative magnitudes of water sources to the lunar poles”. In: *LPI Contributions* (2020), p. 2319.
- [85] PG Lucey et al. “Evidence for water ice and temperature dependent space weathering at the lunar poles from LOLA and Diviner”. In: *45th Annual Lunar and Planetary Science Conference*. 1777. 2014, p. 2325.
- [86] Chloe Helene Martella et al. “Combining active seismic data from Apollo 14 and 16 with ground penetrating radar results to examine the shallow lunar subsurface”. In: *Planetary and Space Science* 214 (2022), p. 105460.
- [87] E Mattei et al. “Dielectric measurements and radar attenuation estimation of ice/basalt sand mixtures as martian Polar Caps analogues”. In: *Icarus* 229 (2014), pp. 428–433.
- [88] Elisabetta Mattei et al. “Coaxial-cage transmission line for electromagnetic parameters estimation”. In: *IEEE transactions on instrumentation and measurement* 62.11 (2013), pp. 2938–2942.
- [89] Elisabetta Mattei et al. “Time domain reflectometry of glass beads/magnetite mixtures: A time and frequency domain study”. In: *Applied Physics Letters* 86.22 (2005).
- [90] Christian Matzler and Urs Wegmuller. “Dielectric properties of freshwater ice at microwave frequencies”. In: *Journal of Physics D: Applied Physics* 20.12 (1987), p. 1623.
- [91] H. Jay Melosh. “Why the Moon is so like the Earth”. In: *Nature Geoscience* 12.6 (2019), pp. 402–403.
- [92] Motomaro et al. *The Kaguya Lunar Atlas*. Jan. 2011. DOI: 10.1007/978-1-4419-7285-9.
- [93] Yosio Nakamura et al. “Deep lunar interior inferred from recent seismic data”. In: *Geophysical Research Letters* 1.3 (1974), pp. 137–140.
- [94] Nasa. *Handbook of lunar materials*. 1980.
- [95] AM Nicolson and GF Ross. “Measurement of the intrinsic properties of materials by time-domain techniques”. In: *IEEE Transactions on instrumentation and measurement* 19.4 (1970), pp. 377–382.
- [96] F Nimmo and Robert T Pappalardo. “Ocean worlds in the outer solar system”. In: *Journal of Geophysical Research: Planets* 121.8 (2016), pp. 1378–1399.
- [97] Stewart Nozette et al. “Integration of lunar polar remote-sensing data sets: Evidence for ice at the lunar south pole”. In: *Journal of Geophysical Research: Planets* 106.E10 (2001), pp. 23253–23266.

- [98] Stewart Nozette et al. “The Clementine mission to the Moon: Scientific overview”. In: *Science* 266.5192 (1994), pp. 1835–1839.
- [99] Mark A Nurge. “In situ dielectric spectroscopy for water detection on the lunar surface”. In: *Planetary and Space Science* 65.1 (2012), pp. 76–82.
- [100] Gary Olhoeft and DW Strangway. “Dielectric properties of the first 100 meters of the Moon”. In: *Earth and Planetary Science Letters* 24.3 (1975), pp. 394–404.
- [101] Gary R Olhoeft et al. “Electrical properties of rocks”. In: *Physical properties of rocks and minerals* 2 (1981), pp. 257–297.
- [102] GR Olhoeft, AL Frisillo, and DW Strangway. “Electrical properties of lunar soil sample 15301, 38”. In: *Journal of Geophysical Research* 79.11 (1974), pp. 1599–1604.
- [103] GR Olhoeft et al. “Electrical properties of lunar solid samples”. In: *Abstracts of the Lunar and Planetary Science Conference, volume 4, page 575, (1973)*. Vol. 4. 1973.
- [104] Lissa Ong et al. “Volatile retention from cometary impacts on the Moon”. In: *Icarus* 207.2 (2010), pp. 578–589.
- [105] Takayuki Ono and Hiroshi Oya. “Lunar Radar Sounder (LRS) experiment on-board the SELENE spacecraft”. In: *Earth, planets and space* 52.9 (2000), pp. 629–637.
- [106] Takayuki Ono et al. “Lunar radar sounder observations of subsurface layers under the nearside maria of the Moon”. In: *Science* 323.5916 (2009), pp. 909–912.
- [107] Eleonora Ivanovna Parkhomenko. *Electrical properties of rocks*. Springer Science & Business Media, 2012.
- [108] Victor F Petrenko and Robert W Whitworth. *Physics of ice*. OUP Oxford, 1999.
- [109] Elena Pettinelli et al. “An overview of GPR subsurface exploration of planets and moons”. In: *The Leading Edge* 41.10 (2022), pp. 672–680.
- [110] Elena Pettinelli et al. “Dielectric properties of Jovian satellite ice analogs for subsurface radar exploration: A review”. In: *Reviews of Geophysics* 53.3 (2015), pp. 593–641.
- [111] Elena Pettinelli et al. “Time domain reflectometry: Calibration techniques for accurate measurement of the dielectric properties of various materials”. In: *Review of Scientific Instruments* 73.10 (2002), pp. 3553–3562.
- [112] Leonard J Porcello et al. “The Apollo lunar sounder radar system”. In: *Proceedings of the IEEE* 62.6 (1974), pp. 769–783.
- [113] OFF Planet Research. “Simulants, Feedstocks, and Additives”. In: *WWW Document*. 2021, pp. –. URL: <https://www.offplanetresearch.com/simulants-feedstocks-and-additives>.
- [114] Abramov Richardson. “Modeling the Formation of the Lunar Upper Megaregolith Layer”. In: *The Planetary Science Journal* 1 (Mar. 2020), p. 2. DOI: 10.3847/PSJ/ab7235.

- [115] DA Robinson and SP Friedman. “The effective permittivity of dense packings of glass beads, quartz sand and their mixtures immersed in different dielectric backgrounds”. In: *Journal of Non-Crystalline Solids* 305.1-3 (2002), pp. 261–267.
- [116] Lior Rubanenko, Jaahnavee Venkatraman, and David A Paige. “Thick ice deposits in shallow simple craters on the Moon and Mercury”. In: *Nature Geoscience* 12.8 (2019), pp. 597–601.
- [117] AC Rust, JK Russell, and RJ Knight. “Dielectric constant as a predictor of porosity in dry volcanic rocks”. In: *Journal of Volcanology and Geothermal Research* 91.1 (1999), pp. 79–96.
- [118] M. Saint-Amant and David W. Strangway. “Dielectric properties of dry, geologic materials”. In: *Geophysics* 35.4 (1970), pp. 624–645.
- [119] Jürgen H Schön. *Physical properties of rocks: Fundamentals and principles of petrophysics*. Elsevier, 2015.
- [120] Norbert Schörghofer and Raluca Rufu. “Past extent of lunar permanently shadowed areas”. In: *Science Advances* 9.37 (2023), eadh4302.
- [121] Norbert Schorghofer and Jean-Pierre Williams. “Mapping of ice storage processes on the moon with time-dependent temperatures”. In: *The Planetary Science Journal* 1.3 (2020), p. 54.
- [122] David Schrank et al. *The moon: Resources, future development and settlement*. Springer Science & Business Media, 2007.
- [123] Peter H Schultz et al. “The LCROSS cratering experiment”. In: *science* 330.6003 (2010), pp. 468–472.
- [124] Laurent Sibille et al. *Lunar regolith simulant materials: recommendations for standardization, production, and usage*. Tech. rep. 2006.
- [125] MA Siegler et al. “Lunar true polar wander inferred from polar hydrogen”. In: *Nature* 531.7595 (2016), pp. 480–484.
- [126] Ari H Sihvola. *Electromagnetic mixing formulas and applications*. 47. Iet, 1999.
- [127] DE Stillman and RE Grimm. “Dielectric Spectroscopy for Scientific and Resource Characterization of Lunar Regolith”. In: *Ground-Based Geophysics on the Moon* 1530 (2010), p. 3028.
- [128] A Stogryn. “Equations for calculating the dielectric constant of saline water (correspondence)”. In: *IEEE transactions on microwave theory and Techniques* 19.8 (1971), pp. 733–736.
- [129] DW Strangway et al. “Electrical properties of lunar soil dependence on frequency, temperature and moisture”. In: *Earth and Planetary Science Letters* 16.2 (1972), pp. 275–281.
- [130] Yida Tan et al. “Image Reconstruction and Interpretation of Chang’e-5 Lunar Regolith Penetrating Radar Data”. In: *2022 45th International Conference on Telecommunications and Signal Processing (TSP)*. IEEE. 2022, pp. 242–245.
- [131] Lawrence A Taylor, Carle M Pieters, and Daniel Britt. “Evaluations of lunar regolith simulants”. In: *Planetary and Space Science* 126 (2016), pp. 1–7.

- [132] G Clarke Topp, JL Davis, and Aa P Annan. “Electromagnetic determination of soil water content: Measurements in coaxial transmission lines”. In: *Water resources research* 16.3 (1980), pp. 574–582.
- [133] Fabio Tosti and Lara Pajewski. “Applications of radar systems in Planetary Sciences: an overview”. In: *Civil Engineering Applications of Ground Penetrating Radar* (2015), pp. 361–371.
- [134] Orenthal J Tucker et al. “Lifetime of a transient atmosphere produced by lunar volcanism”. In: *Icarus* 359 (2021), p. 114304.
- [135] Fawwaz T Ulaby et al. “Textural information in SAR images”. In: *IEEE Transactions on Geoscience and Remote Sensing* 2 (1986), pp. 235–245.
- [136] Fawwaz Tayssir Ulaby and Umberto Ravaioli. *Fundamentals of applied electromagnetics*. Vol. 7. Pearson Upper Saddle River, NJ, 2015.
- [137] Guido Valerio et al. “GPR detectability of rocks in a Martian-like shallow subsoil: A numerical approach”. In: *Planetary and Space Science* 62.1 (2012), pp. 31–40.
- [138] MR Vant, RO Ramseier, and V Makios. “The complex-dielectric constant of sea ice at frequencies in the range 0.1–40 GHz”. In: *Journal of Applied Physics* 49.3 (1978), pp. 1264–1280.
- [139] Kenneth Watson, Bruce Murray, and Harrison Brown. “On the possible presence of ice on the Moon”. In: *Journal of Geophysical Research* 66.5 (1961), pp. 1598–1600.
- [140] Mark Wieczorek Benjamin Weiss et al. “Lunar magnetism”. In: *Brown University* (2013).
- [141] Mark A Wieczorek et al. “The constitution and structure of the lunar interior”. In: *Reviews in mineralogy and geochemistry* 60.1 (2006), pp. 221–364.
- [142] Saunders Wilhelms and Strom. *The Geology of the Terrestrial Planets*. Nasa, 1984.
- [143] J-P Williams et al. “The global surface temperatures of the Moon as measured by the Diviner Lunar Radiometer Experiment”. In: *Icarus* 283 (2017), pp. 300–325.
- [144] Yazhou Yang et al. “Impact remnants rich in carbonaceous chondrites detected on the Moon by the Chang’e-4 rover”. In: *Nature Astronomy* 6.2 (2022), pp. 207–213.